APPLICATION OF DIFFRACTIVE OPTICAL ELEMENT ON SPECTROSCOPY AND IMAGING

Zhenkun Guo

A dissertation submitted to the faculty at the University of North Carolina at Chapel Hill in partial fulfillment of the requirements for the degree of Doctor of Philosophy in the Department of Chemistry in the College of Arts and Sciences.

Chapel Hill
2018

Approved by:

Yosuke Kanai

Andrew Moran

Wei You

James Cahoon

Joanna Atkin

ABSTRACT

Zhenkun Guo: Application of Diffractive Optical Element on Spectroscopy and Imaging
(Under the direction of Andrew Moran)

Diffractive optical elements (DOE) are optical components that manipulate light by diffraction, interference, and other phase control methods. The application of DOE in multi-dimensional spectroscopy could significantly reduce the efforts required for conducting experiments and enhance the signal-to-noise ratio with high efficiency. In this dissertation, DOE-based two-dimensional resonance Raman spectroscopy was developed and implemented in two model systems, triiodide and myoglobin. This new technique uncovers new dimensions of information, which were not available with previous one-dimensional spectroscopy techniques. The DOE was also applied to the wide-field transient absorption microscopy. Conducting a large number of experiments simultaneously is possible in this configuration. Analysis of parallel measurements provides statistical information essential to comprehensively study heterogeneous samples.

After absorbing an ultraviolet photon, triiodide undergoes photodissociation to produce diiodide and radical iodine on a time scale comparable to the period of triiodide's nuclear motion, which could impulsively activate a vibrational coherence in the diiodide. In this dissertation, the ability of 2DRR to capture coherent reaction mechanisms is demonstrated by directly establishing a correlation, for the first time, between the nonequilibrium geometry of triiodide at photodissociation and the stretching frequency of diiodide.

Ligand binding and dissociation processes are crucial to the functions of heme proteins. The recovery of the protein matrix involves fast energy dissipation from the heme group to solvent, facilitated by the propionic acid side chains as an effective "gateway". In this dissertation, we found that the propionic chains possess significant structural heterogeneity, which could be induced by the thermal fluctuation in geometries. It is interesting to consider whether the variation in conformation could relate to the vibrational cooling rate distributions.

Carrier diffusion is imaged in a perovskite film and crystal using a newly developed DOE-based wide-field transient absorption microscopy technique. The function of the instrument is illustrated with 41 parallel measurements conducted on methylammonium lead iodide perovskite films and single crystals in a single experiment. Obvious carrier diffusion is observed in the crystal. However, results indicate that the carrier dynamics in the film are dominated by many-body interactions instead. The grain boundaries in the film contribute to this difference in behavior.

To my parents, Jianting Guo and Liping Wu, and to my friends, I couldn't have done this without your supporting.

ACKNOWLEDGEMENTS

TABLE OF CONTENTS

LIST OF TABLES

LIST OF FIGURES

LIST OF ABBREVIATIONS AND SYMBOLS

1D	one-dimensional
2D	two-dimensional
3D	three-dimensional
2DRR	two-dimensional resonance Raman spectroscopy
4WM	four-wave-mixing
6WM	six-wave-mixing
α	absorption coefficient or a time constant used to suppress noise
A	linear scaling parameter or absorption
a	lowering ladder operator or path length
$a^{\dagger}$	raising ladder operator
atm	atmosphere
$\tilde{A}(z,t)$	real slowly varying amplitude envelope
Å	angstrom
BBO	beta barium borate
B_m	Boltzmann population of level m
C	concentration
c	speed of light
°C	Celsius temperature
$c.c.$	conjugate to the previous function
CCD	charge-coupled device image sensor
cm	centimeter
cm^{-1}	wavenumber
CMOS	complementary metal–oxide–semiconductor image sensor

CO	carbon monoxide
comb	Dirac comb function
cos	cosine trigonometric function
CSRS	coherent Stokes Raman scattering
ΔA	change of absorption
$\Delta\Delta A$	transient pump-repump probe absorption
$\Delta_\perp E$	electric field in the transverse direction
Δk	wavevector mismatch
$\Delta k^{(n)}$	wavevector mismatch for the nth-order signal
$\Delta\nu$	pulse bandwidth in frequency
$\Delta\tau$	pulse duration in time
$\delta\omega$	frequency variation in wavenumber
D	diameter or Debye
D_0	diffusion constant
$D_{gk,gm}(\tau_1)$	doorway function
d_j	dimensionless potential energy minimum displacement for mode j
DOE	diffractive optical elements
DMF	Dimethylformamide
ε_0	vacuum permittivity
η	the period of grating
η_a	the deviation of the harmonic mode frequency from its mean value
ξ	laser electric field amplitude
E	energy
E	electric field

$E^{(n)}$	electric field of the nth-order signal
E_n	electric field of the nth pulse
e	base of natural logarithm or elementary charge
EH_{nm}	hollow core fiber hybrid laser beam mode, nm
ESA	excites state absorption
ESE	excited state emission
eV	electron volt
exp	exponential function with base of natural logarithm
ϕ	phase shift or wavefunction
φ	phase shift or wavefunction
ϕ_{NL}	nonlinear phase shift
$\mathfrak{F}$	two-dimensional Fourier transform
$f_{m,n}^{N}$	unit cell phase modulation at a pixel with indexes m, n of a diffractive optical element design at Nth iteration
$f_{m,n}^{'N}$	constrained unit cell phase modulation at a pixel with indexes m, n of a diffractive optical element design at Nth iteration
$F_{m,n}^{N}$	generated intensity distribution at a pixel with indexes m, n of a diffractive optical element design at Nth iteration
$F_{m,n}^{'N}$	constrained generated intensity distribution at a pixel with indexes m, n Fe iron
Fe^{2+}	ferrous cation
F_n	focal length of the nth lens
fs	femtosecond
FSRS	Femtosecond stimulated Raman spectroscopy
FTO	Fluorine doped Tin Oxide

FWHM	full width at half maximum
Γ	coherence dephasing time constant or relaxation time constant
GDD	group delay dispersion
$G(\eta_a, \eta_b)$	correlated two-dimensional Gaussian function
GSB	ground state bleach
H	Hamiltonian
H_0	non-perturbated Hamiltonian
h	Planck's constant
$\hbar$	reduced Planck's constant
h	hour
HCF	hollow core fiber
His	histidine
HWHM	half width at half maximum
Hz	hertz
I	light intensity
$I^{(n)}$	n^{th}-order signal intensity
I_0	intensity constant or incoming intensity
i	imaginary unit
I_2	iodine
$I\bullet$	radical iodine
I_2^-	diiodide ion
I_3^-	triiodide ion
IR	infrared spectroscopy
$J_{gu,gm}(\omega_2)$	describes vibrational wavepacket motion in ω_2

K	required number of photons to ionize gas atom or molecule
k	wavevector
k_0	center wavevector
kHz	kilohertz
KI	potassium iodide
k_n	wavevector of the nth pulse
k_{sig}	wavevector of the emitted signal
Λ	bath fluctuation relaxation rate
λ	wavelength
λ_0	center wavelength
L	interacting length
l	path length
LEPS	London-Eyring-Polanyi-Sato
$L_{en,gm}(\omega)$	Lorentzian line shapes
log	natural logarithm
M	molarity
m	mass
m	meter
MAI	methylammonium iodide
max	maximum
MbO_2	oxymyoglobin
MD	molecular dynamics simulation
m_e	mass of electron
MEM	maximum entropy method

metMb	metmyoglobin (water-ligated myoglobin)
mg	milligram
MHz	megahertz
ml	milliliter
mJ	millijoule
mM	millimole
mm	millimeter
mOD	milli optical density
ms	millisecond
∇	gradient differential operator
n	total refractive index
$\vec{n}$	normal vector of the plane
n_0	linear refractive index
n_2	nonlinear refractive index
$N.A.$	numerical aperture
nJ	nanojoule
nm	nanometer
NO	nitric oxide
$N(x, \tau)$	carrier density
O_2	oxygen
OD	optical density
π	ratio of a circle's circumference to its diameter
ρ	plasma density, density operator or correlation parameter
ρ_c	critical plasma density

P	induced polarization
p	product ground state
p^*	product excited state
P_{cr}	critical power to induce beam collapse
p_g	ground state population
PbI_2	lead iodide
PCBM	phenyl-C61-butyric acid methyl ester
pH	potential of hydrogen
pm	picometer
$P^{(n)}$	n^{th}-order nonlinear polarization
PP	pump-probe
ps	picosecond
psi	pound per square inch
q	reaction coordinator
R	resolution determined by Raleigh criteria
$R^{(n)}$	n^{th}-order response function
r	reactant ground state index
r^*	reactant excited state index
R_{ab}	bond length between atoms a and b
$rect$	rectangle function
RPM	revolutions per minute
θ	Heaviside step function or angle
σ_a	width of the inhomogeneous distribution
S_n	measurement under n^{th} condition

s	second
sin	sine trigonometric function
Spiro-MeOTAD	$N^2,N^2,N^{2'},N^{2'},N^7,N^7,N^{7'},N^{7'}$-octakis(4-methoxyphenyl)-9,9′-spirobi[9H-fluorene]-2,2′,7,7′-tetramine
SRS	stimulated Raman scattering
$S(\tau_1, \omega_2)$	signal in time and frequency domains
$S(\omega)$	energy spectrum or signal in frequency domain
$S(\omega_1, \omega_2)$	signal in two time domains
τ	time delay or characteristic time constant of variation envelope
t	time point or interval
TA	transient absorption
TEM_{nm}	Gaussian laser beam mode, nm
TG	transient grating
μ_I	transition dipole
μ_{eg}	transition dipole between the excited state and ground state
μ_{eg}^*	conjugate transition dipole between the excited state and ground state
μL	microliter
μm	micrometer
U_i	ionization potential
U_{jkl}	cubic expansion coefficient
UV	ultraviolet
$U(x, y, z)$	radiative field
V	volume

v	frequency or ratio of external and internal media refractive indices
ω	frequency in wavenumbers
ω_0	center frequency in wavenumber
ω_{eg}	frequency in wavenumber between the excited state and ground state
$\left\langle \omega_{vib}\left(\tau_1\right)\right\rangle$	expectation value of vibrational frequency at τ_1
ϖ_a	mean of the harmonic mode frequency
$\chi^{(n)}$	n^{th}-order susceptibility
$\otimes$	convolution

CHAPTER 1. INTRODUCTION

1.1. Applications of Diffractive Optical Elements

Diffraction and interference, phenomena that result from the wave-like property of light, have been studied since the very early stage of optics. In 1665, Grimaldi noticed that light that passed through a hole took on the shape of a cone instead of following a rectilinear path.[1] He named this effect 'diffraction,' which means "break into pieces" in Latin. Since then, the wave theory of light has been gradually developed by Huygens,[2] Fresnel,[3] Young,[4] Fraunhofer,[5-6] and others. The wave theory of light successfully explained many phenomena including diffraction, interference, and Arago spot (Poisson spot),[7] and became the basis for modern optics.

Diffractive optical elements (DOE) are optical components that manipulate light by diffraction, interference, and other phase control methods. Diffractive gratings are the most widely used diffractive optical elements, which are made by closely placed periodic structures that split the incoming beam into many diffraction orders. The simplest diffractive grating is a collection of thin slits, as shown in Figure 1.1. According to grating theory, the angles between diffracted beams are controlled by the periodic frequency, and the relative distribution of magnitudes is determined by the unit cell structures.[8-10] In 1967, Lohmann and Paris performed numerical simulations and demonstrated that in theory, a DOE can generate nearly all arbitrary magnitude and phase patterns with specially designed unit cells.[11] The limiting factor is the fabrication precision and cost. Optical engineers borrowed photolithography methods from the semiconductor industry, making possible the fabrication of a diffractive optical element with a complicated unit cell pattern.[12-13] Due to its outstanding ability to control the magnitude and

phase of the diffracted beams, the diffractive optical element typically reduces the complexity of spectroscopy experiments and improves the quality of experimental data.
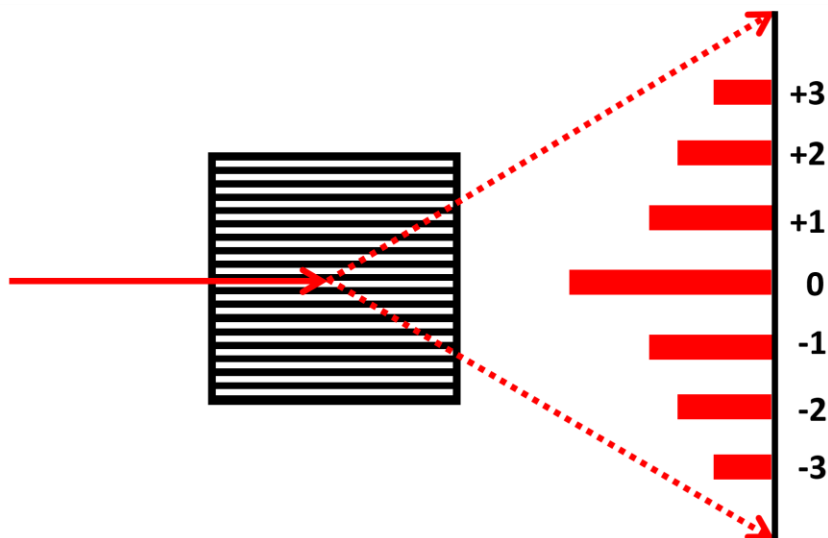
Figure 1.1. *A simple grating made by closely separated periodical slits. The incoming light can be diffracted into different orders. For a transmissive grating, the 0ᵗʰ order will be the directly transmitted light. The angle between diffraction orders and the intensity distributions can be modulated by adjusting the slit spacing and width.*

In this dissertation, we developed a DOE-based multidimensional vibrational spectroscopy experiment involving six laser beams. We demonstrated that this technique is capable of decomposing the dynamics of reactants and products into different dimensions for photo-induced reactions.[14-15] In addition, as in infrared two-dimensional spectroscopy, our technique distinguished heterogeneous and homogeneous line broadening mechanisms.[16-17] The application of a DOE improved the signal-to-noise of our measurements by enabling a background-free geometry and interferometric signal detection. The works presented herein were featured as Editor's Choice in the Journal of Chemical Physics for the years 2014 and 2015.[15, 17]

In the microscopy field, we applied the DOE in a wide-field transient absorption (TA) microscope. The DOE split the incoming pulses to excite up to 41 different spots on a sample surface simultaneously, where multiple TA measurements were conducted in parallel. Therefore,

statistical information, such as average and standard deviation, was available after a single experiment. In addition, wide-field detection captured the response of the entire field of view without scanning the position of a probe beam, which requires an extremely long time for a KHz laser system. Thus, this DOE-based approach facilitated the fast acquisition of statistical information and proved a powerful method to examine heterogeneous samples.

The key contributions of this dissertation are as follows:

- Developed two-dimensional resonance Raman spectroscopy (2DRR) for studies of fast chemical reactions.

- Showed that 2DRR reveals correlations between nuclear motions of the reactant and product in triiodide photodissociation.

- Utilized 2DRR to measure structural heterogeneity in vibrational coordinates of myoglobin responsible for energy exchange with the surrounding environment.

- Developed DOE-based wide-field TA microscopy.

- Measured and compared the diffusion processes in organic halide perovskite thin film and crystals.

1.2. Application of Diffractive Optical Elements in Spectroscopy and the Development of Two-Dimensional Resonance Raman Spectroscopy

DOEs were first implemented into transient gating spectroscopy by Miller and Nelson to stabilize the phase difference passively between the emitted signal and a reference beam, which interferes with the signal at the detector.[18-20] In this interferometric detection method, the interference fringes were measured instead of the weak intensity of the signal field to acquire high signal-to-noise data.[21-22] However, this technique was susceptible to fluctuations in the phase difference between the two pulses. Small fluctuations in the phase induce a significant amount of noise, as further discussed in Chapter 2. Previously, the phase was maintained by an

active optical phase-locked loop, which controlled the optical path of one beam in the interferometer via piezo stages and feedback circuits.[23-25] This active phase stabilizing method required high effort in daily operation and was not cost efficient. Utilizing DOE provided an excellent solution to this issue because the diffracted orders passed through the same amount of glass and were the exact replicas of each other in phase, as shown in Figure 1.2. Soon after, diffractive optical elements were also implemented for passive phase stabilization in more complicated fifth-order signal measurements.[26-28] The implementation of DOE significantly enhanced the signal-to-noise ratio and reduced the efforts involved with experimental setup.
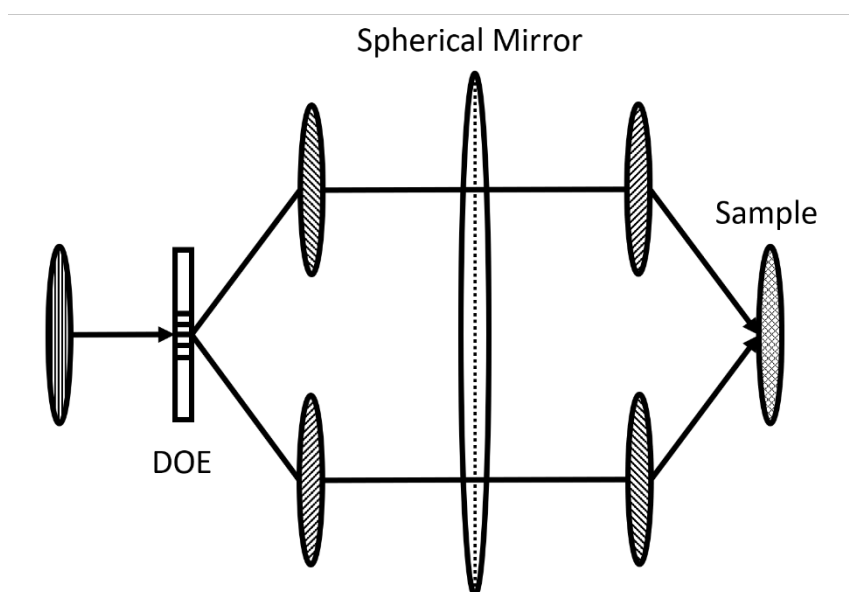
Figure 1.2. A DOE is used to generate replicas of the incoming laser pulse in both intensity and phase. The ovals represent a snapshot of the spatial pulse envelopes as they propagate through the optical system. One feature of using a DOE is that the pulse fronts are parallel in space and can entirely overlap with each other when focused on the sample (i.e., pulse front tilt is eliminated regardless of crossing angle).

The idea of two-dimensional (2D) Raman spectroscopy was rooted in the early stage of the development of multidimensional spectroscopy.[19, 29-36] It was motivated by initial attempts to determine the vibrational line broadening mechanisms and anharmonicities in liquids.[37-41] The study of 2D Raman spectroscopy was also driven by examining the coherent reaction mechanism

involved in many systems, including polymer-fullerene blends, photosynthetic complexes, and semiconductor interfaces.[42-46] As highlighted by Mukamel et al.,[29-30] a fifth-order nonlinearity needed to be measured to obtain information beyond that offered by one-dimensional (1D) Raman spectroscopy. Due to the technical challenges in measuring a weak high-order signal, it took about 10 years of exhaustive effort to conduct the first successful two-dimensional off-resonance Raman measurements with the crucial help of a diffractive optical element in 2002.[28, 47] However, further development of 2D Raman spectroscopy encountered another technical issue known as cascades.[37, 39, 47] Cascades represent a process in which the four-wave mixing response of one molecule induces a four-wave mixing response on a second molecule. The second molecule then radiates a signal field in the same direction as the desired 2D Raman response.
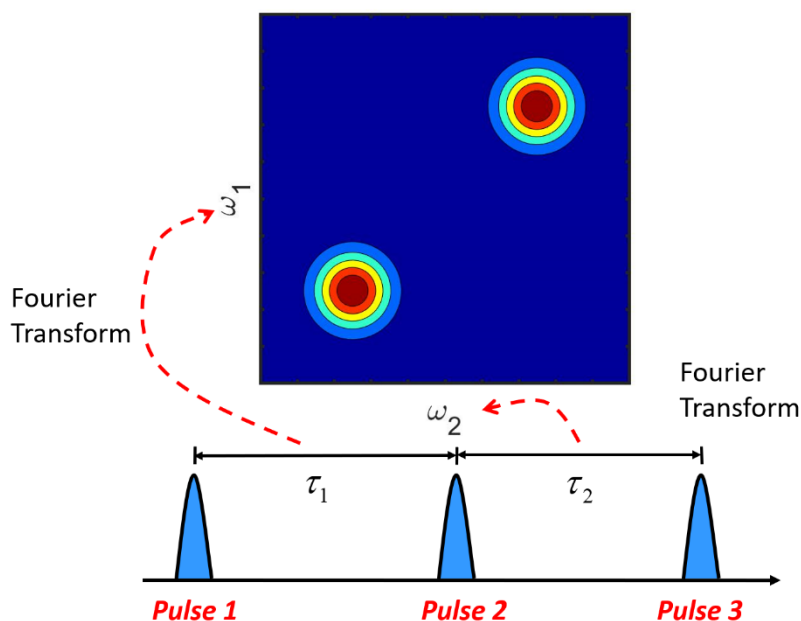
Figure 1.3. *An example of 2D Fourier transform vibrational spectroscopy. Typically, two time intervals are built by three pulses, and the measured signal oscillates in both delays, τ_1 and τ_2. Fourier transforms of the time-domain vibrations result in peaks in the frequency domain, as shown in the figure. Vibrations in the τ_1 (τ_2) dimension correspond to the signal in ω_1 (ω_2) in the 2D Fourier transform.*

Under the electronically off-resonant conditions, as in the earliest 2D Raman spectroscopy experiments, the generation of the fifth-order signal is forbidden for harmonic modes. Unfortunately, cascades are allowed for harmonic systems and are therefore able to outcompete the desired response. In contrast, the 2DRR response is permitted for all Franck-Condon active modes, whether they are harmonic or not. As a result, the 2DRR is much less susceptible to such artifacts. Details about these statements will be discussed in both theory and experiment in Chapter 3 and Chapter 4. In this dissertation, we applied the 2DRR in two model systems, triiodide and myoglobin. In the measurement of the photo-dissociation of the triiodide model, we used a diffractive optic-based six-wave mixing interferometer. We obtained the 2DRR spectrum by Fourier transforming both delay time dimensions into the frequency domain, as indicated in Figure 1.3. The two vibrational frequency dimensions distinguished the responses from the reactant and the product and established a clear correlation between the two species. In the measurement of myoglobin, we applied a pulse configuration in the six-wave mixing interferometer, similar to femtosecond stimulated Raman spectroscopy.[48-50] This approach isolated the desired fifth-order signal from background light and achieved higher signal-to-noise in less time because it scanned only one delay line. Only one vibrational frequency dimension was calculated by the Fourier transformation of the signal into the time domain. 2DRR determined the line-broadening mechanisms in myoglobin and provided valuable information about the fluctuations of the moieties relevant to energy exchange between the heme group and the environment.

1.3. Coherent Reaction Mechanism in Triiodide Photo Dissociation

Second-order perturbative theories like Forster energy transfer and Marcus theory are widely used in describing photo-induced reactions, and usually assume an initial state of vibrational equilibrium prior to the electronic reaction of interest.[51] However, this assumption is

inappropriate when the timescale of vibrational dephasing is comparable to the electronic processes of interest, as reported in polymer-fullerene blends, photosynthetic complexes, and semiconductor interfaces.[42-46] Coherent vibrational motions affect sub-picosecond energy transfer or electron transfer dynamics.[52-58] To elucidate this effect, a direct measurement of correlations between reactant and product vibrational motions is necessary.

However, it is impossible to distinguish the vibrations of a reactant and product with third-order nonlinear spectroscopy techniques unambiguously, including four-wave-mixing (4WM) and pump-probe TA spectroscopies. Both the reactants and products evolve in the single 'population time,' and ambiguities are always involved because of the difficulty in determining the exact origins of the oscillations. Besides, in the third-order nonlinear spectroscopies, the photochemistry always starts from the equilibrium geometry of the reactant. Thus, a 2D spectroscopy technique with two population times and an additional pair of pulses are necessary to deconvolve the reactant response from the product response. Under this pulse sequence, the second pair of pulses initiates the photo-induced reaction after the first population time from a non-equilibrium geometry, which is prepared by the first pair of laser pulses. The two population times are Fourier transformed and yield the two vibrational frequency dimensions, as shown in Figure 1.3. Reactant evolution corresponds to the first dimension, while the product vibration corresponds to the second dimension. The correlation between the non-equilibrium geometry of the reactant and the coherent vibration of the product is established without ambiguities in the 2D vibrational spectroscopy.
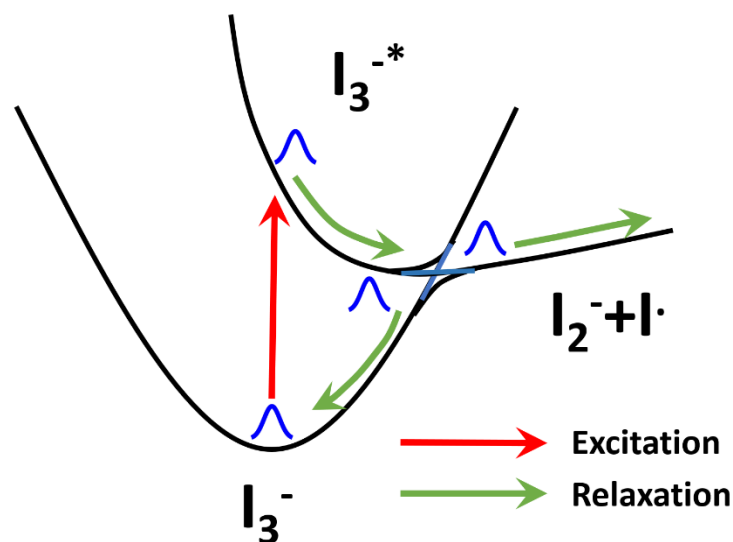
Figure 1.4. *Photo-dissociation process of triiodide after excitation. An excited state wavepacket is initiated at the excited electronic state by photo-excitation, where the steep gradient of the potential energy surface drives the motion of the wavepacket along the symmetric stretch coordinates. Dissociation of triiodide yields a diiodide ion and a free iodine atom. This entire process occurs in approximately 300 fs, at the same time scale of the period of triiodide's symmetric stretch. The non-equilibrium geometry of the reactant can have an influence on the vibrational coherence in the products. 2DRR with reactant evolution in one dimension and product evolution in the other can be used to reveal such effects.*

In this dissertation, 2DRR was applied to reveal the coherent reaction mechanism in the photo-dissociation of triiodide in solution. Triiodide is an ideal model system that has been extensively studied by one-dimensional stimulated Raman spectroscopy,[59-68] and was very suitable for developing our experimental method. A vibrational wavepacket in the excited state is initiated upon the absorption of ultraviolet (UV) light. Then, the wavepacket moves along the symmetric stretch coordinate driven by the gradient of the potential surface, as illustrated in Figure 1.4. The ensemble wavepacket quickly traverses along the symmetric stretch until a finite displacement where the bond rupture is induced to generate atomic iodine and vibrationally hot diiodide ions.[63-64, 68-69] Equation 1.1 illustrates this chemical reaction. The diiodide ions, produced directly in the electronic ground state, possess near 20 vibrational quanta of energy and dissipate mostly into the

solvent within 3-4 ps.[55, 61, 68] As shown in Figure 4, the wavepacket may also cross the intersection between the ground and the excited states, preparing a vibrationally hot ground state.[61]

$$I_3^- + h\nu \longrightarrow I_2^- + I\bullet \qquad (1.1)$$
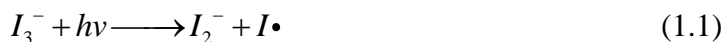
The timescale of the triiodide photo-dissociation is similar to the period of the symmetric stretch (period of 300 fs and wavenumber of 110 cm^{-1}) but shorter than the vibrational dephasing time (i.e., inverse of the line width).[64, 69-70] This key feature of the reaction determines that the non-equilibrium geometry of the reactant significantly influences the vibrational frequency of the product because the coherence of the wavepacket is preserved during the impulsive reaction. In Chapter 3, we describe how 2DRR experiments selectively detected the vibrational coherences of the reactant and product in separate population times (i.e., 'dimensions') and directly revealed the correlation without ambiguities for the first time.

1.4. Structural Heterogeneity and Vibrational Energy Exchange in Myoglobin

Heme proteins are a large family of metalloproteins that play essential roles in metabolism. They contain a porphyrin ring and a metal cofactor coordinated with four nitrogen atoms in porphyrin backbone and an amino acid residue from the protein skeleton. The remaining vacancy of the metal is usually bonded to a ligand determined by protein function, such as O_2, CO, or NO. Figure 1.5 shows the structure around the active site of myoglobin. The functions of heme proteins rely on the dissociation and binding between ligands and the metal cofactor,[71] including myoglobin,[72] hemoglobin,[73] cytochrome c oxidase,[74-75] and NO-synthase.[73] These impulsive events can induce vibrations in the protein's skeleton and cause reorganization of the conformation.[76] The ability to dissipate the vibrational energy into the surroundings quickly is crucial to recovering the proper conformation of the protein, which can determine protein activity.[76-79] Previous studies have shown that the propionic acid chains on the porphyrin

ring, as circled in Figure 1.5, are the primary channel for fast vibrational energy transfer to the solvent.[80-85] Efficient energy dissipation from the porphyrin ring prevents a significant disturbance in the protein matrix and helps to maintain functionality.
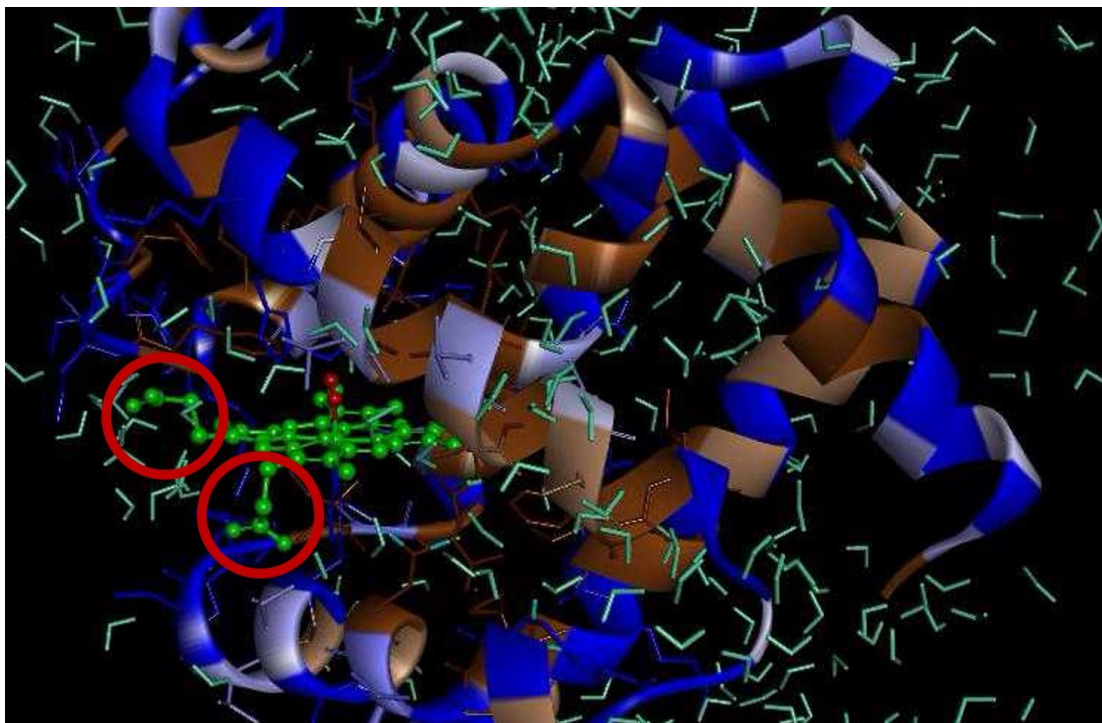
Figure 1.5. *Structure of myoglobin in water. Green spheres represent the porphyrin active site, while red spheres represent bonded oxygen. The propionic acid chains are circled in red and can form hydrogen bonds with water molecules. These side chains are the primary energy dissipation channel after ligand dissociation.*

2DRR spectroscopy is a great tool to study the exchange of vibrational energy with surroundings in a heme protein after photon-dissociation, especially in myoglobin. Myoglobin's primary biological function is to store and release molecular oxygen in muscle tissue,[79] and it only contains one active site, which simplifies the data analysis. The on-resonance excitation induces dissociation of ligand, such as water, oxygen, carbon monoxide, and nitric oxide,[71-72] and activates several vibrational modes including in-plane porphyrin stretching, iron- histidine (Fe-His) stretching, and bending and wagging of the side chains.[85-87] The vibrational energy in these modes is transferred to the surroundings within 6 ps through the propionic acid chains. With

2DRR, it is possible to extract the correlation between the two frequency dimensions for a specific vibrational mode. Such correlation between two vibrational frequency dimensions can provide information about the line broadening mechanism, as illustrated in Figure 1.6. The signatures of homogeneous and inhomogeneous line broadening mechanisms are very similar to those in well-established two-dimensional infrared measurements.[31, 88-90] Line broadening mechanisms are of central interest in condensed phase spectroscopy and shed light on the intrinsic properties of the related groups, such as conformation fluctuation[91-93] and interaction strength with surroundings.[94-95]
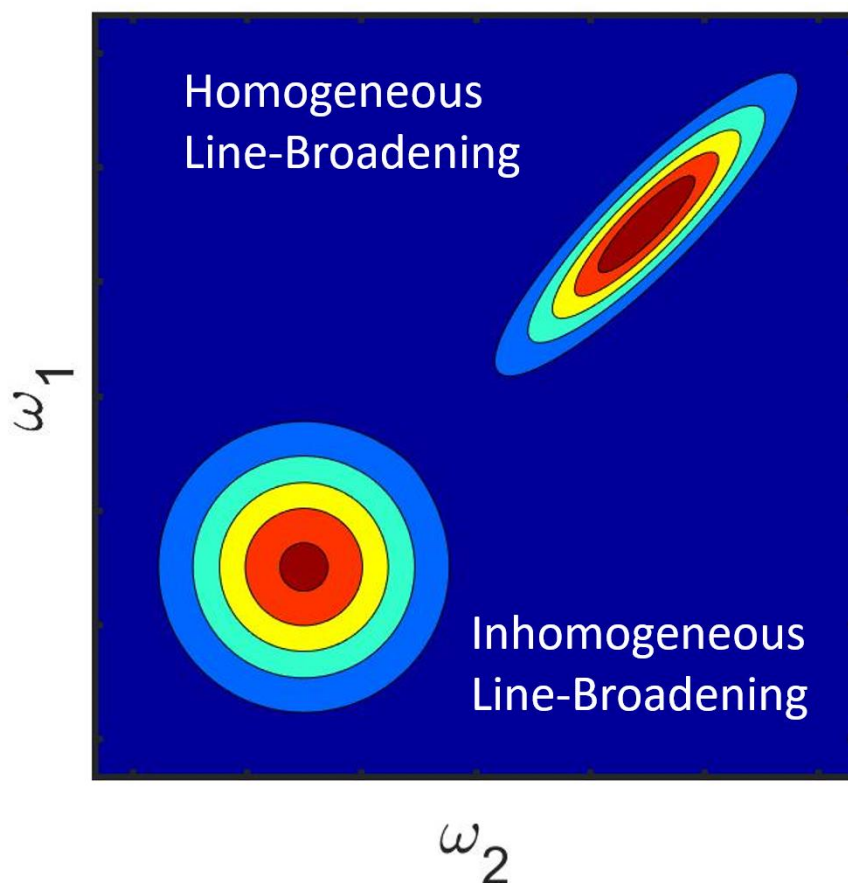
Figure 1.6. *Signatures of homogeneous and inhomogeneous line broadening mechanisms in 2DRR spectra. The inhomogeneously broadened signal is elongated with respect to the diagonal. Inhomogeneous line broadening indicates static heterogeneity in the ensemble (e.g., a difference in local environments or molecular conformations). The fluctuations of these properties occur on a time scale much longer than the measurement. The homogeneously broadened peak is circular in appearance. Homogeneous line broadening indicates fast fluctuations of the vibrational coordinates (e.g., collisions with solvent molecules). These two line broadening mechanisms are indistinguishable in one-dimensional Raman spectroscopies.*

In this dissertation, we applied an FSRS-like approach to measure the 2DRR spectrum of water- and oxygen-ligated myoglobin. In Chapter 5, we illustrate how the bending and wagging modes of propionic acid side chains exhibit significant inhomogeneous line broadening in 2DRR spectra. With knowledge about the protein structure, Figure 1.5 shows that these side chains extend to the outside of the protein matrix and are surrounded by water molecules. Together with inhomogeneous line broadening, we found that propionic acid chains are flexible and have a

large number of possible conformations in the equilibrium state. The Fe-His stretch mode also showed some amount of correlation, which reflects the variation of the Fe-His bond length determined by the number of possible conformation geometries of the protein around the active site. This work demonstrated that 2DRR is useful for investigating line broadening mechanisms in systems with multiple Franck-Condon active modes. Such spectroscopic data can be combined with structural information to provide insight into mechanisms of molecular functionality.

1.5. Application of Diffractive Optical Element in Transient Absorption Microscopy

The initial development of time-resolved microscopy was motivated by knowledge of the lifetimes of chromophores in a labeled biological sample, the delineation of local environments[96-98] progression of localized cell damage,[99-101] and the contrast between labeled chromophores and sources of background.[102] These techniques required detectors with fast responses like time-correlated single photon counters or streak cameras, which are not suitable for measurements of femtosecond dynamics. The pump-probe configuration was introduced to achieve sub-picosecond time-resolution with ultrafast femtosecond laser systems to solve this issue.[103-104] By removing the fluorophore labels and directly measuring the third-order nonlinearities, pump-probe microscopy possesses the same sensitivity to ultrafast dynamics as regular TA spectroscopy and has been widely implemented in many fields, especially nanotechnology, in recent decades. [105-109]

In these experiments, both pump and probe beams were focused onto the sample through the objective, and the probe or both of the beams were scanned in the x-y dimension to obtain a spatially resolved image. The point-to-point scanning method inflates the data acquisition time and is therefore most appropriate for a high repetition rate laser system (MHz). In contrast, a wide-field microscope can collect transient data over the entire visual field under the objective.[110-111] Unfortunately, previously reported wide-field microscopes were not suitable for

studying carrier transport, because the pump beam excited the entire field of view simultaneously, and no spatial dynamics could be observed. In this dissertation, we show how counter-propagating pump and probe beams can be used to address this drawback and resolve the carrier transport without point-to-point scanning.

To accelerate the data acquisition speed over a designated region further, multiplex excitation can be used as it is a straightforward method that excites the sample at many spots simultaneously. We applied the DOE in the multiphoton scanning fluorescence microscopy to generate multiplex excitations.[112-113] Compared to other multiplex generation techniques like an array of micro lenses[114-116] and cascades beam splitters,[117] the DOE achieved much more uniform intensity. The installation of a single customized DOE was also much more convenient than other methods. Although this DOE-based technique has previously only been applied in scanning microscopy, it was suitable for our counter-propagating wide-field microscopy. The incoming pump beam was split into 41 beams, and a typical transient signal was shown, as illustrated in Figure 1.7. With this configuration, we could conduct 41 TA experiments simultaneously. This feature of the instrument enabled the fast compilation of statistical information for heterogeneous samples.
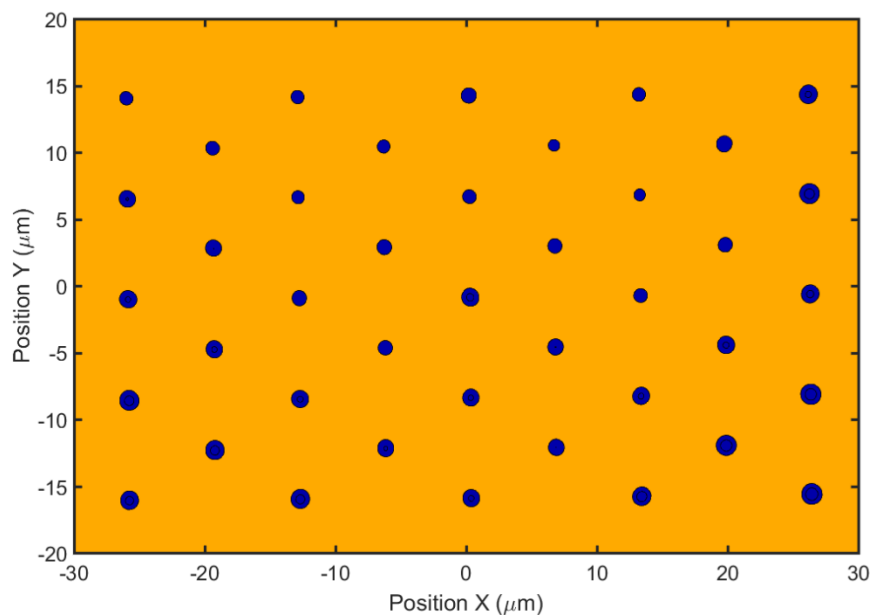
Figure 1.7. *The signals are measured simultaneously from 41 different spots on the sample surface, as shown in the figure. A DOE splits the incoming pump beam into 41 segments with equal intensity and parallel aligned wave-fronts. These beams are focused onto many spots on the sample because of the different diffraction angles. Since the probe is focused to a much larger area covering all the spots, the TA response can be measured simultaneously from all 41 positions. Statistical information is available after only a single experiment.*

1.6. Carrier Diffusion in Organic Halide Perovskite Single Crystals and Thin Films

Organohalide perovskite is a newly emerging type of solar cell material, which has achieved impressive photo-conversion efficiencies as high as 22.1%[118] and is compatible with solution processing.[119] A number of special features have been identified as crucial to its excellent performance, such as long diffusion lengths,[120-122] high tolerance to defects,[123-126] tunable absorbance spectrum by controlling the halide ratio[127] or changing the metal cation,[128] and long-lived vibrationally hot carriers.[109, 129-131] The long diffusion length and long hot carrier diffusion length may enable the harvesting of hot carriers and enhance the power conversion efficiency above the Shockley–Queisser limit.[132] Although there have been multiple studies about diffusion length in perovskite single crystals, no sufficient studies have determined to what

extent the grain boundaries influence the carrier transport, which is vital in thin film perovskite solar cells.[120, 133-134]

Many methods have been used to measure the diffusion constant of carriers in organohalide perovskite. Some indirect conventional measurements gave carrier diffusivities ranging from 0.02 cm^2/s to 0.16 cm^2/s.[122, 130, 135] These values were one order of magnitude smaller than the values yielded by TA microscopy (0.7-1.77 cm^2/s), which provided a more direct measurement.[109, 136-137] In a typical indirect measurement, an electron-PCBM or hole-quencher (Spiro-OMeTAD) is placed in contact with the perovskite to accept electrons or holes diffused to the boundary. To determine the diffusion coefficients, the key assumption that carriers will be immediately quenched once arriving at the interface must be valid. However, perfect contact between the perovskite and quencher for a relatively large area is hard to guarantee, and thus it might take some time for the carriers to cross the boundary. Moreover, interface heterogeneity could also affect the carrier transfer rate.[109, 136-137] The breakdown of this assumption may cause an underestimation of diffusion coefficients. In contrast, TA microscopy can directly image the motion of carrier within a single grain, minimizing the influence of local heterogeneity and boundaries.

Ultrafast TA microscopy is a powerful tool to image carrier dynamics directly with sub-micrometer spatial resolution and has been applied to measure carrier diffusion in organic semiconductor films,[138] silicon nanowires,[105, 108] metal dichalcogenides[139] and single-crystal gold nanobars,[140] along with perovskites.[109, 136-137] Sample heterogeneity can obscure the measurement results because TA microscopy reveals properties over a tiny area. As for perovskites, researchers have shown that heterogeneity exists even within a single grain,[141-142] and such

heterogeneity induces widely distributed diffusion constants.[136] Therefore, it is necessary to average over multiple points on the sample to characterize diffusivities correctly in the sample.

In this dissertation, we applied DOE-based wide-field TA microscopy and simultaneously measured 41 spots on the sample. Statistical distributions of diffusion constants were revealed in a single measurement, thereby yielding detailed information about the sample heterogeneity with short data acquisition time. We compared the diffusion constants in thin films and single crystals to determine to what extent the grain boundaries affected the diffusion process. According to the results, the diffusion rate in the film was one order of magnitude smaller than in crystals due to the much smaller grain size in the film (less than 1 μm) as compared to the crystal with a length scale of hundreds of μm.

1.7. Dissertation Content

The first chapter above has provided background and motivation driving the work contained in this dissertation. Technical details utilized in the dissertation are majorly discussed in Chapter 2, which includes DOE theory, pulse generation techniques, principles of nonlinear spectroscopy, third-order and fifth-order nonlinear spectroscopy techniques and the configuration of DOE based TA microscopy.

Chapter 3 focuses on a simple model system, photodissociation of triiodide, to demonstrate the ability of DOE-based 2DRR. The correlations between vibrational nuclei motions in the reactant and product are revealed for the first time. With no ambiguity, 2DRR spectra show that the nonequilibrium geometry of the reactant at the time when impulsive reaction happen directly affects the resulting vibrational frequency of the product.

Chapters 4 and 5 involve studies of myoglobin. In Chapter 4, FSRS measurement was conducted in a DOE-based six-wave-mixing geometry, which completely eliminated the undesired signal and background and guaranteed high sensitivity. The improved signal quality

and data acquisition efficiency are crucial to successfully Fourier transfer the time dimension into frequency domain, which was conducted to obtain 2DRR in Chapter 5. Signature of heterogenous line broadening in 2DRR suggested conformational fluctuation in the vibrational energy dissipation 'gateways'. Theoretical simulation and controlled experimental tests confirmed that our measurements of heme proteins are free from the technical challenges of artifacts in previous 2D Raman measurements.

In Chapter 6 the power of DOE is leveraged to measure the carrier diffusion process in organic halide perovskite film and crystal with the DOE-based multiplex excitation TA microscopy. Up to 41 measurements were performed in parallel and provided essential statistical information about the investigated property in the heterogeneous sample. The comparison between film and crystal indicated that the boundaries between grains contribute to the much lower diffusivity in the film comparing to the crystal.

Finally, Chapter 7 concludes the research highlights on the prior chapters. In addition, the future directions of 2DRR and DOE-based microscopy are discussed by presenting scientifically interesting systems which our techniques can shed new insights on.

REFERENCES

1. Grimaldi, F.-M., *Physico-mathesis de lumine, coloribus et iride, aliisque adnexis libri duo (etc.) Opus posthumum*. Haeres Victorij Benatij.

2. Huygens, C., *Traité de la lumière: Ou sont expliquées les causes de ce qui luy arrive dans la reflexion, et dans la refraction Et particulierement dans l'etrange refraction du cristal d'Islande; Avec un discours de la cause de la pesanteur*. Pierre Vander Aa: 1885.

3. Fresnel, A., Mémoire sur la diffraction de la lumière. *da p. 339 a p. 475: 1 tav. ft; AQ 210* **1819**, 339.

4. Young, T., The Bakerian Lecture: Experiments and Calculations Relative to Physical Optics. *Philosophical Transactions of the Royal Society of London* **1804,** *94* (0), 1-16.

5. Fraunhofer, J., *Neue Modificationen des Lichtes durch gegenseitige Einwirkung und Beugung der Strahlen, und Gesetze derselben*. 1824; Vol. 2.

6. Fraunhofer, J., Kurzer Bericht von den Resultaten neuerer Versuche über die Gesetze des Lichtes, und die Theorie derselben. *Annalen der Physik* **1823,** *74* (8), 337-378.

7. Arago, D., Rapport fait par M. Arago à l'Académie des Sciences, au nom de la Commission qui avait été chargée d'examiner les Mémoirs envoyés au concours pour le prix de le diffraction. *Ann. Chim. Phys.* **1819,** *11*, 5-30.

8. ERSOY, O. K., *Diffraction, Fourier Optics and Imaging*. John Wiley & Sons, Inc.: Hoboken, New Jersey, 2007.

9. Loewen, E. G.; Popov, E., *Diffraction gratings and applications*. Marcel Dekker, Inc.: New York, 1997.

10. O'Shea, D. C.; Suleski, T. J.; Kathman, A. D.; Prather, D. W., *Diffractive Optics Design, Fabrication, and Test*. SPIE Press: Bellingham, Washington, 2004; Vol. 62.

11. Lohmann, A. W.; Paris, D. P., Binary fraunhofer holograms, generated by computer. *Appl. Opt.* **1967,** *6* (10), 1739-1748.

12. Levinson, H. J., *Principles of Lithography.* SPIE Press: Bellingham, Washington, 2010; Vol. 146.

13. Sheats, J. R.; Smith, B. W., *Microlithography Science and Technology*. Marcel Dekker, Inc.: New York, 1998; Vol. 162.

14. Guo, Z.; Molesky, B. P.; Cheshire, T. P.; Moran, A. M., Elucidation of reactive wavepackets by two-dimensional resonance Raman spectroscopy. *J. Chem. Phys.* **2015,** *143* (12), 124202.

15. Molesky, B. P.; Giokas, P. G.; Guo, Z.; Moran, A. M., Multidimensional resonance Raman spectroscopy by six-wave mixing in the deep UV. *J. Chem. Phys.* **2014,** *141* (11), 114202.

16. Molesky, B. P.; Guo, Z.; Cheshire, T. P.; Moran, A. M., Two-dimensional resonance Raman spectroscopy of oxygen- and water-ligated myoglobins. *J. Chem. Phys.* **2016,** *145* (3), 034203.

17. Molesky, B. P.; Guo, Z.; Moran, A. M., Femtosecond stimulated Raman spectroscopy by six-wave mixing. *J. Chem. Phys.* **2015,** *142* (21), 212405.

18. Goodno, G. D.; Astinov, V.; Miller, R. J. D., Femtosecond Heterodyne-Detected Four-Wave-Mixing Studies of Deterministic Protein Motions. 2. Protein Response. *J. Phys. Chem. A* **1999,** *103* (49), 10630-10643.

19. Goodno, G. D.; Dadusc, G.; Miller, R. J. D., Ultrafast heterodyne-detected transient-grating spectroscopy using diffractive optics. *Journal of the Optical Society of America B* **1998,** *15* (6), 1791-1794.

20. Maznev, A. A.; Nelson, K. A.; Rogers, J. A., Optical heterodyne detection of laser-induced gratings. *Opt. Lett.* **1998,** *23* (16), 1319.

21. Eesley, G.; Levenson, M.; Tolles, W., Optically heterodyned coherent Raman spectroscopy. *IEEE J. Quantum Electron.* **1978,** *14* (1), 45-49.

22. Eichler, H. J.; Günter, P.; Pohl, D. W., *Laser Induced Dynamic Gratings*. Springer: Berlin, 1986; Vol 50.

23. Chang, Y. J.; Cong, P.; Simon, J. D., Optical Heterodyne-Detection of Impulsive Stimulated Raman-Scattering in Liquids. *J. Phys. Chem.* **1995,** *99* (20), 7857-7859.

24. de Boeij, W. P.; Pshenichnikov, M. S.; Wiersma, D. A., Short-time solvation dynamics probed by phase-locked heterodyne detected pump-probe. *Chem. Phys. Lett.* **1995,** *247* (3), 264-270.

25. Scherer, N. F.; Carlson, R. J.; Matro, A.; Du, M.; Ruggiero, A. J.; Romerorochin, V.; Cina, J. A.; Fleming, G. R.; Rice, S. A., Fluorescence-Detected Wave Packet Interferometry - Time Resolved Molecular-Spectroscopy with Sequences of Femtosecond Phase-Locked Pulses. *J. Chem. Phys.* **1991,** *95* (3), 1487-1511.

26. Khurmi, C.; Berg, M. A., Differential heterodyne detection with diffractive optics for multidimensional transient-grating spectroscopy. *J. Opt. Soc. Am. B* **2009,** *26* (12), 2357-2362.

27. Miller, R. J.; Paarmann, A.; Prokhorenko, V. I., Diffractive optics based four-wave, six-wave, ..., v-wave nonlinear spectroscopy. *Acc. Chem. Res.* **2009,** *42* (9), 1442-1451.

28. Kubarych, K. J.; Milne, C. J.; Lin, S.; Miller, R. J. D., Diffractive optics implementation of time- and frequency-domain heterodyne-detected six-wave mixing. *Appl. Phys. B: Lasers Opt.* **2002,** *74*, s107-s112.

29. Loring, R. F.; Mukamel, S., Selectivity in Coherent Transient Raman Measurements of Vibrational Dephasing in Liquids. *J. Chem. Phys.* **1985,** *83* (5), 2116-2128.

30. Tanimura, Y.; Mukamel, S., Two-dimensional femtosecond vibrational spectroscopy of liquids. *J. Chem. Phys.* **1993,** *99* (12), 9496-9511.

31. Asplund, M. C.; Zanni, M. T.; Hochstrasser, R. M., Two-dimensional infrared spectroscopy of peptides by phase-controlled femtosecond vibrational photon echoes. *Proc. Natl. Acad. Sci. U. S. A.* **2000,** *97* (15), 8219-8224.

32. Hybl, J. D.; Albrecht Ferro, A.; Jonas, D. M., Two-dimensional Fourier transform electronic spectroscopy. *J. Chem. Phys.* **2001,** *115* (14), 6606-6622.

33. Khalil, M.; Demirdöven, N.; Tokmakoff, A., Obtaining absorptive line shapes in two-dimensional infrared vibrational correlation spectra. *Phys. Rev. Lett.* **2003,** *90* (4), 047401.

34. Brixner, T.; Mancal, T.; Stiopkin, I. V.; Fleming, G. R., Phase-stabilized two-dimensional electronic spectroscopy. *J. Chem. Phys.* **2004,** *121* (9), 4221-4236.

35. Tekavec, P. F.; Lott, G. A.; Marcus, A. H., Fluorescence-detected two-dimensional electronic coherence spectroscopy by acousto-optic phase modulation. *J. Chem. Phys.* **2007,** *127* (21), 214307.

36. Shim, S.-H.; Zanni, M. T., How to turn your pump–probe instrument into a multidimensional spectrometer: 2D IR and Vis spectroscopies via pulse shaping. *Phys. Chem. Chem. Phys.* **2009,** *11* (5), 748-761.

37. Blank, D. A.; Kaufman, L. J.; Fleming, G. R., Fifth-order two-dimensional Raman spectra of CS_2 are dominated by third-order cascades. *J. Chem. Phys.* **1999,** *111* (7), 3105-3114.

38. Ivanecky, J. E.; Wright, J. C., An investigation of the origins and efficiencies of higher-order nonlinear spectroscopic processes. *Chem. Phys. Lett.* **1993,** *206* (5-6), 437-444.

39. Kubarych, K. J.; Milne, C. J.; Lin, S.; Astinov, V.; Miller, R. J. D., Diffractive optics-based six-wave mixing: Heterodyne detection of the full χ(5) tensor of liquid CS_2. *J. Chem. Phys.* **2002,** *116* (5), 2016-2042.

40. Tokmakoff, A.; Lang, M. J.; Larsen, D. S.; Fleming, G. R.; Chernyak, V.; Mukamel, S., Two-dimensional Raman spectroscopy of vibrational interactions in liquids. *Phys. Rev. Lett.* **1997,** *79* (14), 2702-2705.

41. Tominaga, K.; Yoshihara, K., Fifth-order nonlinear spectroscopy on the low-frequency modes of liquid CS_2. *J. Chem. Phys.* **1996,** *104* (12), 4419-4426.

42. Fuller, F. D.; Pan, J.; Gelzinis, A.; Butkus, V.; Senlik, S. S.; Wilcox, D. E.; Yocum, C. F.; Valkunas, L.; Abramavicius, D.; Ogilvie, J. P., Vibronic coherence in oxygenic photosynthesis. *Nat. Chem.* **2014,** *6* (8), 706-711.

43. Mohseni, M.; Omar, Y.; Engel, G.; Plenio, M. B., *Quantum Effects in Biology*. Cambridge University Press: Cambridge, 2014.

44. Song, Y.; Clafton, S. N.; Pensack, R. D.; Kee, T. W.; Scholes, G. D., Vibrational coherence probes the mechanism of ultrafast electron transfer in polymer-fullerene blends. *Nat. Commun.* **2014,** *5*, 4933.

45. Tisdale, W. A.; Williams, K. J.; Timp, B. A.; Norris, D. J.; Aydil, E. S.; Zhu, X. Y., Hot-electron transfer from semiconductor nanocrystals. *Science* **2010,** *328* (5985), 1543-1547.

46. Zimmermann, C.; Willig, F.; Ramakrishna, S.; Burfeindt, B.; Pettinger, B.; Eichberger, R.; Storck, W., Experimental fingerprints of vibrational wave-packet motion during ultrafast heterogeneous electron transfer. *J. Phys. Chem. B* **2001,** *105* (38), 9245-9253.

47. Kaufman, L. J.; Heo, J.; Ziegler, L. D.; Fleming, G. R., Heterodyne-detected fifth-order nonresonant Raman scattering from room temperature CS_2. *Phys. Rev. Lett.* **2002,** *88* (20), 207402.

48. Kukura, P.; McCamant, D. W.; Mathies, R. A., Femtosecond stimulated Raman spectroscopy. *Annu. Rev. Phys. Chem.* **2007,** *58*, 461-488.

49. McCamant, D. W.; Kukura, P.; Mathies, R. A., Femtosecond time-resolved stimulated Raman spectroscopy: Application to the ultrafast internal conversion in beta-carotene. *J. Phys. Chem. A* **2003,** *107* (40), 8208-8214.

50. McCamant, D. W.; Kukura, P.; Yoon, S.; Mathies, R. A., Femtosecond broadband stimulated Raman spectroscopy: Apparatus and methods. *Rev. Sci. Instrum.* **2004,** *75* (11), 4971-4980.

51. Nitzan, A., *Chemical Dynamics in Condensed Phases: Relaxation, Transfer and Reactions in Condensed Molecular Systems*. Oxford University Press: New York, 2006.

52. Chin, A. W.; Prior, J.; Rosenbach, R.; Caycedo-Soler, F.; Huelga, S. F.; Plenio, M. B., The role of non-equilibrium vibrational structures in electronic coherence and recoherence in pigment-protein complexes. *Nat. Phys.* **2013,** *9* (2), 113-118.

53. Christensson, N.; Kauffmann, H. F.; Pullerits, T.; Mancal, T., Origin of long-lived coherences in light-harvesting complexes. *J. Phys. Chem. B* **2012,** *116* (25), 7449-7454.

54. Fujihashi, Y.; Fleming, G. R.; Ishizaki, A., Impact of environmentally induced fluctuations on quantum mechanically mixed electronic and vibrational pigment states in

photosynthetic energy transfer and 2D electronic spectra. *J. Chem. Phys.* **2015,** *142* (21), 212403.

55.   Jun, S.; Yang, C.; Isaji, M.; Tamiaki, H.; Kim, J.; Ihee, H., Coherent oscillations in chlorosome elucidated by two-dimensional electronic spectroscopy. *J. Phys. Chem. Lett.* **2014,** *5* (8), 1386-1392.

56.   Kolli, A.; O'Reilly, E. J.; Scholes, G. D.; Olaya-Castro, A., The fundamental role of quantized vibrations in coherent light harvesting by cryptophyte algae. *J. Chem. Phys.* **2012,** *137* (17), 174109.

57.   Perlik, V.; Seibt, J.; Cranston, L. J.; Cogdell, R. J.; Lincoln, C. N.; Savolainen, J.; Sanda, F.; Mancal, T.; Hauer, J., Vibronic coupling explains the ultrafast carotenoid-to-bacteriochlorophyll energy transfer in natural and artificial light harvesters. *J. Chem. Phys.* **2015,** *142* (21), 212434.

58.   Womick, J. M.; Moran, A. M., Vibronic enhancement of exciton sizes and energy transport in photosynthetic complexes. *J. Phys. Chem. B* **2011,** *115* (6), 1347-1356.

59.   Banin, U.; Ruhman, S., Ultrafast photodissociation of I_3^-. Coherent photochemistry in solution. *J. Chem. Phys.* **1993,** *98* (6), 4391-4403.

60.   Banin, U.; Ruhman, S., Ultrafast vibrational dynamics of nascent diiodide fragments studied by femtosecond transient resonance impulsive stimulated Raman-scattering. *J. Chem. Phys.* **1993,** *99* (11), 9318-9321.

61.   Banin, U.; Waldman, A.; Ruhman, S., Ultrafast photodissociation of I_3^- in solution: Direct observation of coherent product vibrations. *J. Chem. Phys.* **1992,** *96* (3), 2416-2419.

62.   Benjamin, I.; Banin, U.; Ruhman, S., Ultrafast photodissociation of I_3^- in ethanol: A molecular dynamics study. *J. Chem. Phys.* **1993,** *98* (10), 8337-8340.

63.   Gershgoren, E.; Gordon, E.; Ruhman, S., Effect of symmetry breaking on vibrational coherence transfer in impulsive photolysis of trihalide ions. *J. Chem. Phys.* **1997,** *106* (11), 4806-4809.

64.   Hess, S.; Bursing, H.; Vohringer, P., Dynamics of fragment recoil in the femtosecond photodissociation of triiodide ions in liquid solution. *J. Chem. Phys.* **1999,** *111* (12), 5461-5473.

65.   Johnson, A. E.; Myers, A. B., Emission cross-sections and line-shapes for photodissociating triiodide in ethanol: Experimental and computational studies. *J. Chem. Phys.* **1995,** *102* (9), 3519-3533.

66.   Johnson, A. E.; Myers, A. B., Solvent effects in the Raman spectra of the triiodide ion: Observation of dynamic symmetry breaking and solvent degrees of freedom. *J. Phys. Chem.* **1996,** *100* (19), 7778-7788.

67.   Johnson, A. E.; Myers, A. B., A comparison of time- and frequency-domain resonance Raman spectroscopy in triiodide. *J. Chem. Phys.* **1996,** *104* (7), 2497-2507.

68.   Kuhne, T.; Kuster, R.; Vohringer, P., Femtosecond photodissociation of triiodide in solution: Excitation energy dependence and transition state dynamics. *Chem. Phys.* **1998,** *233* (2-3), 161-178.

69.   Kuhne, T.; Vohringer, P., Vibrational relaxation and geminate recombination in the femtosecond-photodissociation of triiodide in solution. *J. Chem. Phys.* **1996,** *105* (24), 10788-10802.

70.   Nishiyama, Y.; Terazima, M.; Kimura, Y., Ultrafast relaxation and reaction of diiodide anion after photodissociation of triiodide in room-temperature ionic liquids. *J. Phys. Chem. B* **2012,** *116* (30), 9023-9032.

71.   Vos, M. H., Ultrafast dynamics of ligands within heme proteins. *Biochim. Biophys. Acta, Bioenerg.* **2008,** *1777*, 15-31.

72.   Mizutani, Y.; Kitagawa, T., Ultrafast dynamics of myoglobin probed by time-resolved resonance Raman spectroscopy. *Chem. Rec.* **2001,** *1* (3), 258-275.

73.   Anfinrud, P. A.; Han, C.; Hochstrasser, R. M., Direct observations of ligand dynamics in hemoglobin by subpicosecond infrared spectroscopy. *Proc. Natl. Acad. Sci. U. S. A.* **1989,** *86* (21), 8387-8391.

74.   Liebl, U.; Lipowski, G.; Negrerie, M.; Lambry, J. C.; Martin, J. L.; Vos, M. H., Coherent reaction dynamics in a bacterial cytochrome c oxidase. *Nature* **1999,** *401* (6749), 181-184.

75.   Treuffet, J.; Kubarych, K. J.; Lambry, J. C.; Pilet, E.; Masson, J. B.; Martin, J. L.; Vos, M. H.; Joffre, M.; Alexandrou, A., Direct observation of ligand transfer and bond formation in cytochrome c oxidase by using mid-infrared chirped-pulse upconversion. *Proc. Natl. Acad. Sci. U. S. A.* **2007,** *104* (40), 15705-15710.

76.   Stevens, J. A.; Link, J. J.; Kao, Y. T.; Zang, C.; Wang, L.; Zhong, D., Ultrafast dynamics of resonance energy transfer in myoglobin: Probing local conformation fluctuations. *J. Phys. Chem. B* **2010,** *114* (3), 1498-1505.

77.   Debrunner, P. G.; Frauenfelder, H., Dynamics of Proteins. *Annu. Rev. Phys. Chem.* **1982,** *33*, 283-299.

78.   Miller, R. J., Vibrational energy relaxation and structural dynamics of heme proteins. *Annu. Rev. Phys. Chem.* **1991,** *42*, 581-614.

79.   Perutz, M. F.; Fermi, G.; Luisi, B.; Shaanan, B.; Liddington, R. C., Stereochemistry of cooperative mechanisms in hemoglobin. *Acc. Chem. Res.* **1987,** *20*, 309-321.

80. Bu, L.; Straub, J. E., Vibrational energy relaxation of "tailored" hemes in myoglobin following ligand photolysis supports energy funneling mechanism of heme "cooling". *J. Phys. Chem. B* **2003,** *107* (38), 10634-10639.

81. Gao, Y.; Koyama, M.; El-Mashtoly, S. F.; Hayashi, T.; Harada, K.; Mizutani, Y.; Kitagawa, T., Time-resolved Raman evidence for energy 'funneling' through propionate side chains in heme 'cooling' upon photolysis of carbonmonoxy myoglobin. *Chem. Phys. Lett.* **2006,** *429* (1-3), 239-243.

82. Koyama, M.; Neya, S.; Mizutani, Y., Role of heme propionates of myoglobin in vibrational energy relaxation. *Chem. Phys. Lett.* **2006,** *430* (4-6), 404-408.

83. Lian, T. Q.; Locke, B.; Kholodenko, Y.; Hochstrasser, R. M., Energy-flow from solute to solvent probed by femtosecond IR spectroscopy: Malachite green and heme protein solutions. *J. Phys. Chem.* **1994,** *98* (45), 11648-11656.

84. Sagnella, D. E.; Straub, J. E., Directed energy "Funneling" mechanism for heme cooling following ligand photolysis or direct excitation in solvated carbonmonoxy myoglobin. *J. Phys. Chem. B* **2001,** *105* (29), 7057-7063.

85. Zhang, Y.; Fujisaki, H.; Straub, J. E., Molecular dynamics study on the solvent dependent heme cooling following ligand photolysis in carbonmonoxy myoglobin. *J. Phys. Chem. B* **2007,** *111* (12), 3243-3250.

86. Rosca, F.; Kumar, A. T. N.; Ye, X.; Sjodin, T.; Demidov, A. A.; Champion, P. M., Investigations of coherent vibrational oscillations in myoglobin. *J. Phys. Chem. A* **2000,** *104* (18), 4280-4290.

87. Zhu, L. Y.; Wang, W.; Sage, J. T.; Champion, P. M., Femtosecond Time-Resolved Vibrational Spectroscopy of Heme-Proteins. *J. Raman. Spectrosc.* **1995,** *26* (7), 527-534.

88. Cho, M., Coherent two-dimensional optical spectroscopy. *Chem. Rev.* **2008,** *108* (4), 1331-1418.

89. Fayer, M. D., Dynamics of liquids, molecules, and proteins measured with ultrafast 2D IR vibrational echo chemical exchange spectroscopy. *Annu. Rev. Phys. Chem.* **2009,** *60*, 21-38.

90. Hamm, P.; Zanni, M., *Concepts and methods of 2D infrared spectroscopy*. Cambridge University Press: New York, 2011.

91. Demirdoven, N.; Khalil, M.; Tokmakoff, A., Correlated vibrational dynamics revealed by two-dimensional infrared spectroscopy. *Phys. Rev. Lett.* **2002,** *89* (23), 237401.

92. Ge, N. H.; Zanni, M. T.; Hochstrasser, R. M., Effects of vibrational frequency correlations on two-dimensional infrared spectra. *J. Phys. Chem. A* **2002,** *106* (6), 962-972.

93. Zanni, M. T.; Gnanakaran, S.; Stenger, J.; Hochstrasser, R. M., Heterodyned two-dimensional infrared spectroscopy of solvent-dependent conformations of acetylproline-NH$_2$. *J. Phys. Chem. B* **2001,** *105* (28), 6520-6535.

94. Gammon, D.; Snow, E. S.; Shanabrook, B. V.; Katzer, D. S.; Park, D., Homogeneous linewidths in the optical spectrum of a single gallium arsenide quantum dot. *Science* **1996,** *273* (5271), 87-90.

95. Schultheis, L.; Honold, A.; Kuhl, J.; Kohler, K.; Tu, C. W., Optical dephasing of homogeneously broadened two-dimensional exciton transitions in GaAs quantum wells. *Phys. Rev. B* **1986,** *34* (12), 9027-9030.

96. Dix, J. A.; Verkman, A. S., Pyrene eximer mapping in cultured fibroblasts by ratio imaging and time-resolved microscopy. *Biochemistry* **1990,** *29* (7), 1949-1953.

97. Kao, H. P.; Abney, J. R.; Verkman, A. S., Determinants of the translational mobility of a small solute in cell cytoplasm. *J. Cell. Biol.* **1993,** *120* (1), 175-184.

98. Keating, S. M.; Wensel, T. G., Nanosecond fluorescence microscopy. Emission kinetics of fura-2 in single cells. *Biophys. J.* **1991,** *59* (1), 186-202.

99. Koenig, K.; Schneckenburger, H., Laser-induced autofluorescence for medical diagnosis. *J. Fluoresc.* **1994,** *4* (1), 17-40.

100. Schneckenburger, H.; Gessler, P.; Pavenstadt-Grupp, I., Measurements of mitochondrial deficiencies in living cells by microspectrofluorometry. *J. Histochem. Cytochem.* **1992,** *40* (10), 1573-1578.

101. Schneckenburger, H.; Konig, K., Fluorescence decay kinetics and imaging of Nad(P)H and flavins as metabolic indicators. *Opt. Eng.* **1992,** *31* (7), 1447-1451.

102. Draaijer, A.; Sanders, R.; Gerritsen, H. C., Fluorescence lifetime imaging, a new tool in confocal microscopy. *Handbook of Biological Confocal Microscopy*, Pawley, J. B., Ed. Springer: Boston, Massachusetts, 1995; pp 491-505.

103. Dong, C. Y.; So, P. T.; French, T.; Gratton, E., Fluorescence lifetime imaging by asynchronous pump-probe microscopy. *Biophys. J.* **1995,** *69* (6), 2234-2242.

104. Feldstein, M. J.; Vöhringer, P.; Wang, W.; Scherer, N. F., Femtosecond optical spectroscopy and scanning probe microscopy. *J. Phys. Chem.* **1996,** *100* (12), 4739-4748.

105. Gabriel, M. M.; Kirschbrown, J. R.; Christesen, J. D.; Pinion, C. W.; Zigler, D. F.; Grumstrup, E. M.; Mehl, B. P.; Cating, E. E.; Cahoon, J. F.; Papanikolas, J. M., Direct imaging of free carrier and trap carrier motion in silicon nanowires by spatially-separated femtosecond pump-probe microscopy. *Nano Lett.* **2013,** *13* (3), 1336-1340.

106.   Gao, B.; Hartland, G. V.; Huang, L. B., Transient Absorption Spectroscopy of Excitons in an Individual Suspended Metallic Carbon Nanotube. *J. Phys. Chem. Lett.* **2013,** *4* (18), 3050-3055.

107.   Graham, M. W.; Shi, S. F.; Wang, Z.; Ralph, D. C.; Park, J.; McEuen, P. L., Transient absorption and photocurrent microscopy show that hot electron supercollisions describe the rate-limiting relaxation step in graphene. *Nano Lett.* **2013,** *13* (11), 5497-5502.

108.   Grumstrup, E. M.; Gabriel, M. M.; Cating, E. M.; Pinion, C. W.; Christesen, J. D.; Kirschbrown, J. R.; Vallorz, E. L.; Cahoon, J. F.; Papanikolas, J. M., Ultrafast Carrier Dynamics in Individual Silicon Nanowires: Characterization of Diameter-Dependent Carrier Lifetime and Surface Recombination with Pump-Probe Microscopy. *J. Phys. Chem. C* **2014,** *118* (16), 8634-8640.

109.   Guo, Z.; Wan, Y.; Yang, M.; Snaider, J.; Zhu, K.; Huang, L., Long-range hot-carrier transport in hybrid perovskites visualized by ultrafast microscopy. *Science* **2017,** *356* (6333), 59-62.

110.   Baiz, C. R.; Schach, D.; Tokmakoff, A., Ultrafast 2D IR microscopy. *Opt. Express* **2014,** *22* (15), 18724-18735.

111.   Ostrander, J. S.; Serrano, A. L.; Ghosh, A.; Zanni, M. T., Spatially resolved two-dimensional infrared spectroscopy via wide-field microscopy. *ACS Photonics* **2016,** *3* (7), 1315-1323.

112.   Jureller, J. E.; Kim, H. Y.; Scherer, N. F., Stochastic scanning multiphoton multifocal microscopy. *Opt. Express* **2006,** *14* (8), 3406-3414.

113.   Sacconi, L.; Froner, E.; Antolini, R.; Taghizadeh, M. R.; Choudhury, A.; Pavone, F. S., Multiphoton multifocal microscopy exploiting a diffractive optical element. *Opt. Lett.* **2003,** *28* (20), 1918-1920.

114.   Andresen, V.; Egner, A.; Hell, S. W., Time-multiplexed multifocal multiphoton microscope. *Opt. Lett.* **2001,** *26* (2), 75-77.

115.   Bewersdorf, J.; Pick, R.; Hell, S. W., Multifocal multiphoton microscopy. *Opt. Lett.* **1998,** *23* (9), 655-657.

116.   Egner, A.; Hell, S. W., Time multiplexing and parallelization in multifocal multiphoton microscopy. *J. Opt. Soc. Am. A* **2000,** *17* (7), 1192-1201.

117.   Fittinghoff, D. N.; Squier, J. A., Time-decorrelated multifocal array for multiphoton microscopy and micromachining. *Opt. Lett.* **2000,** *25* (16), 1213-1215.

118.   Yang, W. S.; Park, B. W.; Jung, E. H.; Jeon, N. J.; Kim, Y. C.; Lee, D. U.; Shin, S. S.; Seo, J.; Kim, E. K.; Noh, J. H.; Seok, S. I., Iodide management in formamidinium-lead-halide-based perovskite layers for efficient solar cells. *Science* **2017,** *356* (6345), 1376-1379.

119. Burschka, J.; Pellet, N.; Moon, S. J.; Humphry-Baker, R.; Gao, P.; Nazeeruddin, M. K.; Gratzel, M., Sequential deposition as a route to high-performance perovskite-sensitized solar cells. *Nature* **2013,** *499* (7458), 316-319.

120. Dong, Q.; Fang, Y.; Shao, Y.; Mulligan, P.; Qiu, J.; Cao, L.; Huang, J., Solar cells. Electron-hole diffusion lengths > 175 μm in solution-grown $CH_3NH_3PbI_3$ single crystals. *Science* **2015,** *347* (6225), 967-970.

121. Shi, D.; Adinolfi, V.; Comin, R.; Yuan, M.; Alarousu, E.; Buin, A.; Chen, Y.; Hoogland, S.; Rothenberger, A.; Katsiev, K.; Losovyj, Y.; Zhang, X.; Dowben, P. A.; Mohammed, O. F.; Sargent, E. H.; Bakr, O. M., Solar cells. Low trap-state density and long carrier diffusion in organolead trihalide perovskite single crystals. *Science* **2015,** *347* (6221), 519-522.

122. Stranks, S. D.; Eperon, G. E.; Grancini, G.; Menelaou, C.; Alcocer, M. J.; Leijtens, T.; Herz, L. M.; Petrozza, A.; Snaith, H. J., Electron-hole diffusion lengths exceeding 1 micrometer in an organometal trihalide perovskite absorber. *Science* **2013,** *342* (6156), 341-344.

123. Kim, J.; Lee, S. H.; Lee, J. H.; Hong, K. H., The Role of Intrinsic Defects in Methylammonium Lead Iodide Perovskite. *J. Phys. Chem. Lett.* **2014,** *5* (8), 1312-1317.

124. Saidaminov, M. I.; Abdelhady, A. L.; Murali, B.; Alarousu, E.; Burlakov, V. M.; Peng, W.; Dursun, I.; Wang, L.; He, Y.; Maculan, G.; Goriely, A.; Wu, T.; Mohammed, O. F.; Bakr, O. M., High-quality bulk hybrid perovskite single crystals within minutes by inverse temperature crystallization. *Nat. Commun.* **2015,** *6*, 7586.

125. Steirer, K. X.; Schulz, P.; Teeter, G.; Stevanovic, V.; Yang, M.; Zhu, K.; Berry, J. J., Defect Tolerance in Methylammonium Lead Triiodide Perovskite. *Acs. Energy. Lett.* **2016,** *1* (2), 360-366.

126. Wu, X.; Trinh, M. T.; Niesner, D.; Zhu, H.; Norman, Z.; Owen, J. S.; Yaffe, O.; Kudisch, B. J.; Zhu, X., Trap states in lead iodide perovskites. *J. Am. Chem. Soc.* **2015,** *137*, 2089-2096.

127. Fang, Y. J.; Dong, Q. F.; Shao, Y. C.; Yuan, Y. B.; Huang, J. S., Highly narrowband perovskite single-crystal photodetectors enabled by surface-charge recombination. *Nat. Photonics* **2015,** *9* (10), 679-686.

128. Hao, F.; Stoumpos, C. C.; Chang, R. P.; Kanatzidis, M. G., Anomalous band gap behavior in mixed Sn and Pb perovskites enables broadening of absorption spectrum in solar cells. *J. Am. Chem. Soc.* **2014,** *136* (22), 8094-8099.

129. Niesner, D.; Zhu, H.; Miyata, K.; Joshi, P. P.; Evans, T. J.; Kudisch, B. J.; Trinh, M. T.; Marks, M.; Zhu, X. Y., Persistent energetic electrons in methylammonium lead iodide perovskite thin films. *J. Am. Chem. Soc.* **2016,** *138* (48), 15717-15726.

130. Savenije, T. J.; Ponseca, C. S., Jr.; Kunneman, L.; Abdellah, M.; Zheng, K.; Tian, Y.; Zhu, Q.; Canton, S. E.; Scheblykin, I. G.; Pullerits, T.; Yartsev, A.; Sundstrom, V., Thermally activated exciton dissociation and recombination control the carrier dynamics in organometal halide perovskite. *J. Phys. Chem. Lett.* **2014,** *5* (13), 2189-2194.

131. Yang, Y.; Ostrowski, D. P.; France, R. M.; Zhu, K.; van de Lagemaat, J.; Luther, J. M.; Beard, M. C., Observation of a hot-phonon bottleneck in lead-iodide perovskites. *Nat. Photonics* **2016,** *10* (1), 53-59.

132. Huang, J.; Yuan, Y.; Shao, Y.; Yan, Y., Understanding the physical properties of hybrid perovskites for photovoltaic applications. *Nat. Rev. Mater.* **2017,** *2* (7).

133. Nie, W.; Tsai, H.; Asadpour, R.; Blancon, J. C.; Neukirch, A. J.; Gupta, G.; Crochet, J. J.; Chhowalla, M.; Tretiak, S.; Alam, M. A.; Wang, H. L.; Mohite, A. D., Solar cells. High-efficiency solution-processed perovskite solar cells with millimeter-scale grains. *Science* **2015,** *347* (6221), 522-525.

134. Reid, O. G.; Yang, M. J.; Kopidakis, N.; Zhu, K.; Rumbles, G., Grain-size-limited mobility in methylammonium lead iodide perovskite thin films. *Acs. Energy. Lett.* **2016,** *1* (3), 561-565.

135. Xing, G.; Mathews, N.; Sun, S.; Lim, S. S.; Lam, Y. M.; Gratzel, M.; Mhaisalkar, S.; Sum, T. C., Long-range balanced electron- and hole-transport lengths in organic-inorganic $CH_3NH_3PbI_3$. *Science* **2013,** *342* (6156), 344-347.

136. Hill, A. H.; Smyser, K. E.; Kennedy, C. L.; Massaro, E. S.; Grumstrup, E. M., Screened charge carrier transport in methylammonium lead iodide perovskite thin films. *J. Phys. Chem. Lett.* **2017,** *8* (5), 948-953.

137. Tian, W.; Zhao, C.; Leng, J.; Cui, R.; Jin, S., Visualizing carrier diffusion in individual single-crystal organolead halide perovskite nanowires and nanoplates. *J. Am. Chem. Soc.* **2015,** *137* (39), 12458-12461.

138. Wong, C. Y.; Penwell, S. B.; Cotts, B. L.; Noriega, R.; Wu, H.; Ginsberg, N. S., Revealing exciton dynamics in a small-molecule organic semiconducting film with subdomain transient absorption microscopy. *J. Phys. Chem. C* **2013,** *117* (42), 22111-22122.

139. Yuan, L.; Wang, T.; Zhu, T.; Zhou, M.; Huang, L., Exciton dynamics, transport, and annihilation in atomically thin two-dimensional semiconductors. *J. Phys. Chem. Lett.* **2017,** *8* (14), 3371-3379.

140. Johns, P.; Yu, K.; Devadas, M. S.; Hartland, G. V., Role of resonances in the transmission of surface plasmon polaritons between nanostructures. *ACS Nano* **2016,** *10* (3), 3375-3381.

141. Nah, S.; Spokoyny, B.; Stoumpos, C.; Soe, C. M. M.; Kanatzidis, M.; Harel, E., Spatially segregated free-carrier and exciton populations in individual lead halide perovskite grains. *Nat. Photonics* **2017,** *11* (5), 285.

142. Simpson, M. J.; Doughty, B.; Yang, B.; Xiao, K.; Ma, Y. Z., Imaging electronic trap states in perovskite thin films with combined fluorescence and femtosecond transient absorption microscopy. *J. Phys. Chem. Lett.* **2016,** *7* (9), 1725-1731.

CHAPTER 2. METHODS AND INSTRUMENTATION

2.1. Introduction

Diffractive optic elements (DOE) were applied in many types of spectroscopy in this dissertation, including two-dimensional resonance Raman spectroscopy (2DRR)[1-5] and multiplex excitation wide-field transient absorption microscopy. In this chapter, we briefly discuss some of the basic theories applied to the experiments presented herein and introduce multiple relevant nonlinear spectroscopy techniques. In the second section, we introduce the principles of scalar diffraction theory, a general strategy to design a DOE producing an arbitrary pattern. Section 2.3 is about the laser pulses implemented in 2DRR and microscopy. We describe the spectral broadening technique, which generates the 25 fs visible pulses, in the first part of Section 2.3, before explaining the white-light generation in the second. Principles of nonlinear spectroscopy and a diagrammatic method, the Feynman diagram, in Section 2.4 provide a basis to understand the following sections. In Section 2.5, we summarize two widely conducted third-order nonlinear spectroscopies, transient absorption and transient grating spectroscopy, and also emphasize the significance of applying the DOE in nonlinear spectroscopy. We review concepts about several types of fifth-order spectroscopy, especially two types of 2DRR, in Section 2.6, which comprise the primary contributions of our research group to the field. In Section 2.7, we provide the experimental details of another DOE application, multiplex wide-field transient absorption microscopy.

2.2. Basics of Diffractive Optical Elements

2.2.1. Principles of Diffracted Lights
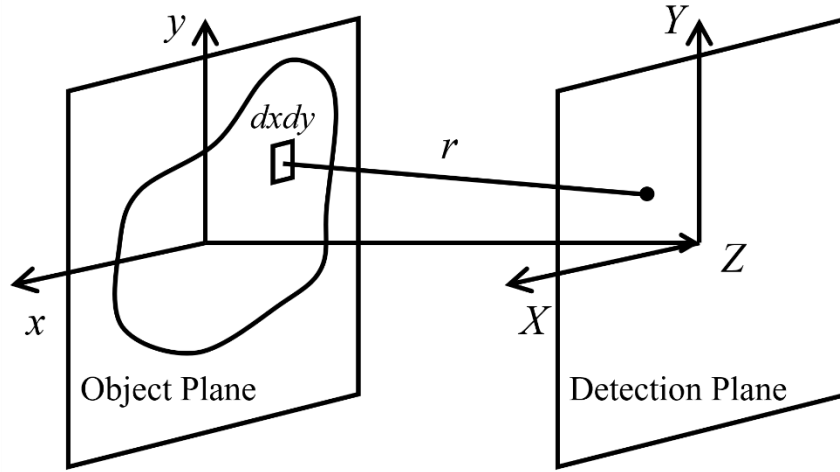
Figure 2.1. *Illustration of the symbols used in Equation 2.1 and Equation 2.2. r is the distance between a point in the object plane and a point in the detection plane,*
$r = \sqrt{(X-x)^2 + (Y-y)^2 + Z^2}$.

In scalar diffraction theory, the electronic and/or magnetic field of the propagating light is treated as a scalar field. For a complex amplitude in free space with no charges, the propagation of the field is governed by the Helmholtz equation:[6-9]

$$\nabla^2 U(x, y, z) + k_0^2 U(x, y, z) = 0 .$$
(2.1)

For a more particular case, considering a transparent pattern on an opaque input plane, which is illuminated by monochromic light as in Figure 2.1, the field on the point of the output plane with coordinates (X, Y, Z) can be determined by Fresnel-Kirchhoff's diffraction formula:[6-7, 10]

$$U(X, Y, Z) = -\frac{ik}{4\pi} \iint_{x,y} \frac{U(x, y, 0)e^{ikr}}{r} [\cos(\vec{n}, \vec{r}) + 1] dxdy .$$
(2.2)

Parameters used in the equation are illustrated in Figure 2.1, where $\vec{n}$ is the normal vector of the object plane. To simplify the equation further, several approximations can be applied. The most

important two are the paraxial approximation (Fr-esnel approximation) and the far-field

approximation (Fraunhofer approximation). The distance between the source point on the input

plane and the target point on the output plane can be expanded, shown in Equation 2.3, as the

starting point of applying these approximations:

$$r = Z \left[1 + \frac{(X-x)^2 + (Y-y)^2}{Z^2} \right]^{\frac{1}{2}} = Z + \frac{1}{2Z}\left[(X-x)^2 + (Y-y)^2 \right] - \frac{1}{8Z^3}\left[(X-x)^2 + (Y-y)^2 \right]^2 + \cdots \quad (2.3)$$

Apply the paraxial approximation:

$$Z^3 \gg \frac{k}{8}\left[(X-x)^2 + (Y-y)^2 \right]^2_{\max}. \quad (2.4)$$

The third- and higher-order terms can be truncated, and we can estimate $\cos(\vec{n}, \vec{r}) \approx 1$. Then the

Fresnel diffraction equation is given in Equation 2.5:

$$U(X,Y,Z) = \frac{\exp(ikZ)ik}{2\pi Z} \int_{aperture} U(x,y,0)\exp[\frac{ik}{2Z}(X-x)^2 + (Y-y)^2]dxdy. \quad (2.5)$$

In the next step, we consider the far-field or Fraunhofer approximation in Equation 2.6 and leave

only the linear terms in Equation 2.3:

$$Z \gg \frac{k}{2}\left(x^2 + y^2 \right)_{\max} \quad (2.6)$$

The result yields the Fraunhofer diffraction equation:

$$U(X,Y,Z) = \frac{\exp(ikZ)ik}{2\pi Z}\exp\left(ik\frac{X^2 + Y^2}{2Z} \right) \int_{aperture} U(x,y,0)\exp[-ik\frac{xX}{Z}]\exp[-ik\frac{yY}{Z})]dxdy. \quad (2.7)$$

We can further simplify Equation 2.7 by substituting X and Y with $\alpha = \dfrac{X}{R}$ and $\beta = \dfrac{Y}{R}$, and move

the phase factor outside the integral into a single function as in Equation 2.8:

$$U(\alpha, \beta) = A(X,Y,Z) \int_{aperture} U(x,y)\exp(-ik\alpha x)\exp(-ik\beta y)dxdy. \quad (2.8)$$

In Equation 2.8, the complex amplitude distribution is the product of the integral and a phase

factor. The phase factor $A(X,Y,Z)$ does not affect the amplitude distribution in which we are

interested, and the magnitude distribution after the DOE is directly proportional to the integral

portion. More importantly, the integral is in the form of a two-dimensional Fourier transform of

the field, $U(x,y)$, which can be written in a more compact way:

$$|U(\alpha,\beta)| \propto \mathfrak{F}\{U(x,y)\}. \tag{2.9}$$

2.2.2. General Diffractive Optical Element Design Strategy Based on Scalar Theory

For a typical grating, the diffractive pattern can be described by the convolution of a

periodic comb function and a unit cell function. The field passing through the DOE has a general

form, as shown in Equation 2.10, under the simplest one-dimensional condition:

$$U(x) = comb(\frac{x}{\Lambda}) \otimes rect(\frac{x}{\Lambda}) \exp[i\phi(x)]. \tag{2.10}$$

Here, Λ is the period of the grating, $rect(\frac{x}{\Lambda})$ describes the size of the unit cell, and $\phi(x)$ is the

modulation of phase by the DOE. Substituting the general function into the Fourier transform

yields:

$$U(\alpha) = \mathfrak{F}\{U(x)\} = \mathfrak{F}\left\{comb(\frac{x}{\Lambda})\right\} \times \mathfrak{F}\left\{rect(\frac{x}{\Lambda}) \exp[i\phi(x)]\right\}. \tag{2.11}$$

The first term results in another comb function, which characterizes the separation between

different diffraction orders. The second term, the Fourier transform of the unit cell pattern,

defines the diffraction pattern after the DOE.

Scalar diffraction theory in the form of a two-dimensional Fourier transform serves as a

convenient method to design the DOE pattern. It is straightforward to perform an inverse Fourier

transform on the desired output pattern and obtain the DOE design. The fast Fourier transform

and inverse fast Fourier transform are well-established algorithms, which can be efficiently executed by computers.

However, a practical fabrication issue is that the lithography etching techniques can only carve for specific discrete depths. Furthermore, partial attenuation is difficult and expensive to achieve at micrometer level. A DOE is usually constructed with binary attenuation levels, which are completely blocked and unblocked. As a result, the outgoing light cannot be modulated with infinite precision in phase and amplitude.[9, 11-12] The quantized phase and binary amplitude modulations may introduce a substantial amount of distortion in both amplitude and phase even for simple patterns. As in Figure 2.2, the desired pattern is a periodic matrix of two-dimensional Gaussian functions with uniform intensities. The direct inverse Fourier transform of this pattern yields the corresponding DOE design and then the modulations levels are quantized. The phase modulation is limited to eight different levels, while the amplitude modulation is limited to binary. The aforementioned is a general manufacturing precision widely used in modern fabrication. As in Figure 2.2(c) and 2.2(d), distortions are introduced in the unit cell, and the center dots are more significant than the target. Semicircles around the center dot are caused by the discontinuous phase and amplitude variation in the DOE unit cell. Although etching and attenuation precision can limit DOE performance, it is still possible to reduce the distortion by a better DOE design under the manufacturing limit.
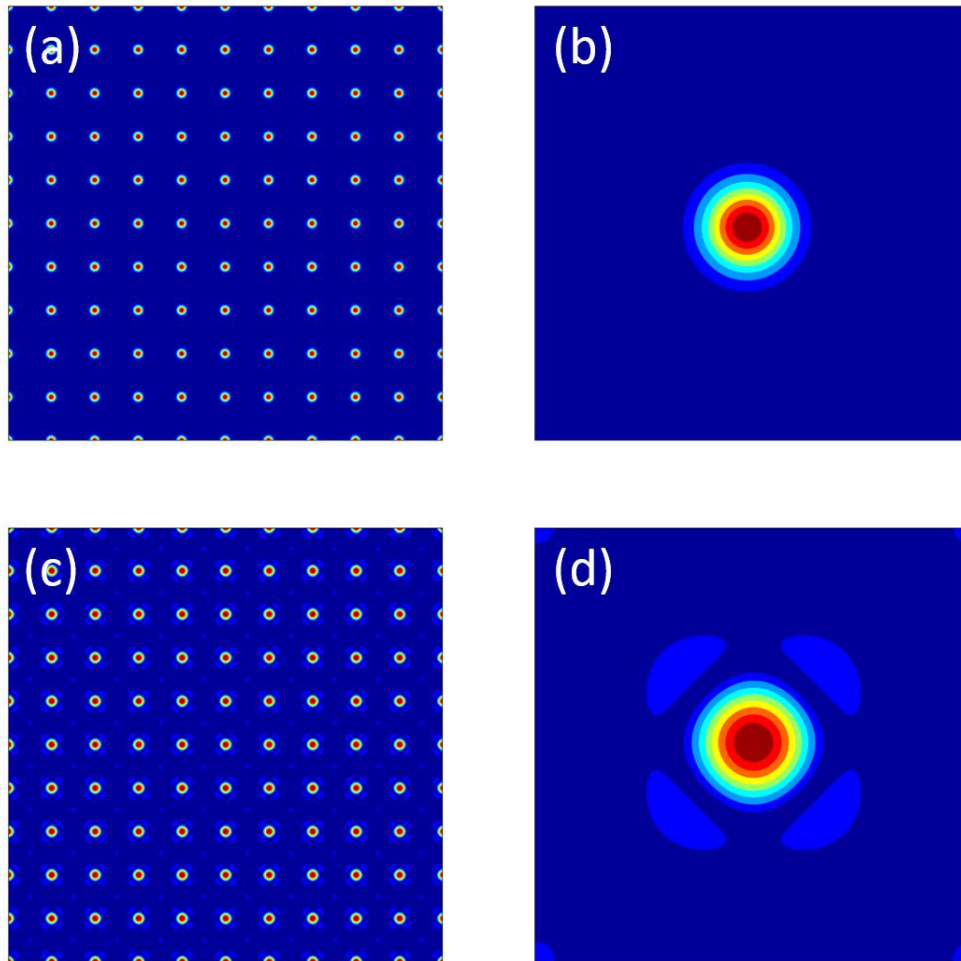
Figure 2.2. *A simple simulation to show the distortion introduced by the quantized phase and binary amplitude modulations limitations imposed by the lithography etching technique. (a) is the desired diffraction pattern and (b) is one diffraction order (unit cell) of the desired pattern. In the simplest case, one diffraction order is given by a two-dimensional Gaussian function. (c) and (d) show the diffraction pattern and unit cell obtained by DOE designed through the direct inverse Fourier transform method. The phase is quantized to eight different levels (*$0, \frac{\pi}{8}, \frac{\pi}{4}, \frac{3\pi}{8}, \frac{\pi}{2}, \frac{5\pi}{8}, \frac{3\pi}{4}, \frac{7\pi}{8}$*) and the amplitudes modulation is binary (*$0,1$*). Distortion of the unit cell pattern is clearly introduced.*

Several iterative algorithms can be used to search for the best practical DOE design. A typical iterative algorithm is usually done by following these steps[9]:

1. The first estimate of the phase plane contains random numbers for each unit cell, whose size is determined by the fabrication precision.

2. The first estimate is truncated due to the limited number of available etching depths and attenuation levels. Discrete numbers replace the continuous phase values. A threshold is set to substitute the amplitude modulation by 0 (blocked) and 1 (unblocked).

3. Two-dimensional Fourier transform (for scalar diffraction theory) or other system transform is performed on the first estimate.

4. The resulting pattern is evaluated by the difference in amplitude from the desired amplitude pattern.

5. Amplitudes of the unit cells in the resulting pattern are replaced by the desired amplitude distribution and the phase is unchanged.

6. An inverse two-dimensional Fourier transform or other inverse system transform is performed on the amplitude and phase distribution obtained from Step 5.

7. A new phase and amplitude distribution, constrained by the procedure mentioned in Step 2, enters the iteration.

Figure 2.3 summarizes the whole iterative algorithm. This iterative algorithm is still not guaranteed to converge at the best design because the optimizing destination is dependent on the first estimate and a locally optimized result is possible. Other more sophisticated algorithms can be used to reduce the possibility of ending at a locally optimized design, such as simulated annealing algorithms and genetic algorithms. These methods control the speed of minimizing the

difference between the DOE output and desired pattern to avoid locally optimized destinations. These complicated algorithms consume more computational power than the regular method described above and, as such, magnitude of performance enhancement relative to design time should be evaluated.
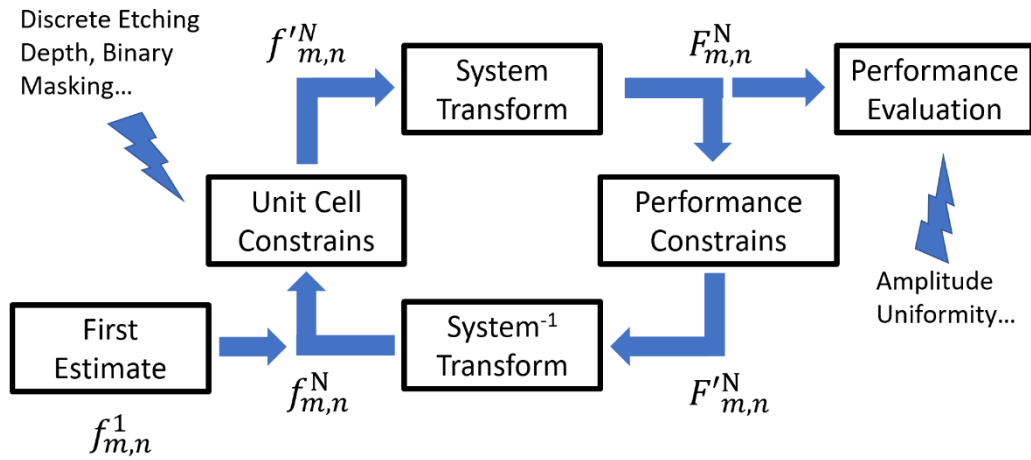
Figure 2.3. *A typical iterative algorithm to optimize the diffractive optical element design.*

2.3. Generation of the Required Laser Pulses

2.3.1. Spectral Broadening of Femtosecond Pulses Using Hollow-Core Fibers

Wide spectral width is necessary to obtain the ~25 fs duration visible pulse because of the product relation between the spectral width and the duration, $\Delta\nu\Delta\tau \geq 0.441$ for the Gaussian envelope shape. In this research, we used fused silica hollow core fiber (HCF) waveguides to broaden the spectral width of the incident femtosecond pulse.[1-5] The chamber in the middle was filled with argon providing a transparent medium for self-phase modulation. The gaseous medium is superior to solid core fibers[13] for guiding the high-intensity laser pulses because the former has much higher breakdown thresholds and weaker optical nonlinearities compared to solid media.[14-16] Although an extended interaction length is essential for the gaseous medium, it provides the tunability of self-phase modulation by changing the gas type and pressure.[13] The

lowest supported mode for a hollow-core fiber is the EH_{11} mode, which has a spatial profile very similar to the TEM_{00} laser mode for Gaussian beams.[17]

The self-phase modulation is induced by the intensity-dependent refractive index. The transmitted laser beam can be described as shown in Equation 2.12:

$$\tilde{E}(z,t) = \tilde{A}(z,t)e^{i(k_0 z - \omega_0 t - \phi_{NL})} + c.c. \ , \tag{2.12a}$$

$$\phi_{NL}(t) = -n_2 I(t)\omega_0 L / c . \tag{2.12b}$$

Here, $\phi_{NL}(t)$ is the laser-induced phase shift caused by the third-order nonlinearities, which results in the nonlinear refractive index n_2. To show just the basic concepts of self-phase modulation, here we assume that the laser does not reshape when propagating along the fiber, which was not the real case under our experimental conditions. It is possible to determine the nonlinear effects in the frequency domain by Fourier transforming Equation 2.12 and obtaining the energy spectrum given in Equation 2.13:

$$S(\omega) = \left| \int_{-\infty}^{+\infty} \tilde{A}(t)e^{-i\omega_0 t - i\phi_{NL}(t)}e^{i\omega t}dt \right|^2 . \tag{2.13}$$

The nonlinear phase shift can be considered as the induced frequency shift from the ω_0 by Equation 2.14:

$$\omega = \omega_0 + \delta\omega = \omega_0 + \frac{d\phi_{NL}(t)}{dt} . \tag{2.14}$$

For a Gaussian intensity envelope in the time domain, we have $I(t) = I_0 \exp\left(-\frac{t^2}{\tau^2}\right)$, where τ is the characteristic time for the varying envelope. The induced frequency deviation, $\delta\omega$ is:

$$\delta\omega = -n_2\omega_0 L / c \frac{dI(t)}{dt} = \frac{2n_2\omega_0 tLI_0}{c\tau^2}\exp\left(\frac{-t^2}{\tau^2}\right) . \tag{2.15}$$

Most materials except plasma retain positive n_2, for which the overall effect is illustrated in Figure 2.4. Equation 2.15 together with Figure 2.4 demonstrate how the spectrum is broadened when propagating through the transparent medium. For a medium with $n_2 > 0$, the rising edge of the pulse envelope experiences a red shift in the frequency, while the falling edge experiences a blue shift.

In this dissertation, the long hollow-core fiber was mounted in an air-tight housing charged with a noble gas. Two lenses were placed before and after the fiber focus and collimated the laser beams to ensure high transmission efficiency and suitable interaction strength. Different lengths and hollow diameters were selected to provide a balanced amount of broadening and attenuation for each wavelength. When the laser beam was carefully aligned to the fiber, the lowest fiber mode was selected and gave a Gaussian-like spatial profile. This technique was used, as discussed in Chapters 3, 4, and 5, to generate the ~25 fs visible pulses.
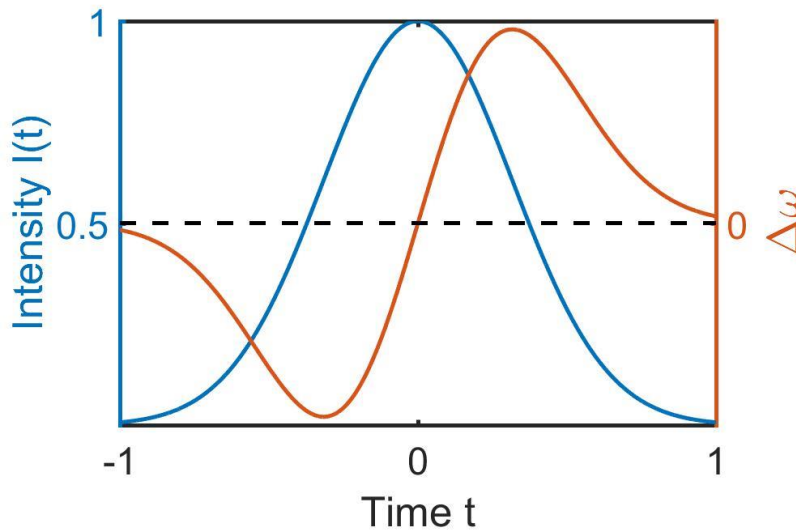
Figure 2.4. The effect of self-phase modulation in a hollow-core fiber. The plot assumes a Gaussian pulse propagating through isotropic media with positive n_2. The frequency of the pulse red-shifts at the rising edge (i.e., $t < 0$) and blue-shifts at the falling edge (i.e., $t > 0$). The frequency does not shift (i.e,. $\delta\omega = 0$) at the pulse envelope maximum.

2.3.2. White Light Generation by Filamentation in a Noble Gas

With strong enough self-phase modulation and high-order harmonic generation, it is possible to broaden the ultrashort pulse so far as to produce white light. Such an effect was reported in the condensed phase[17-21] and is well known as a white-light supercontinuum generation method. Similar results have also been observed in gaseous media,[22-26] but require higher incident intensity and longer interaction length. A phenomenon called filamentation helps stabilize the propagation of high-intensity femtosecond pulses for long distances.[27-31] The filament is produced by cycles of Kerr effect-induced self-focusing and plasma-induced defocusing.[31] Since the gas medium is not damageable under high-intensity laser beams, it is possible to apply laser pulses with high fluence and produce powerful white light.

The self-focusing process is a result of the Kerr effect. When considering the third-order nonlinearities, the intensity-dependent refractive index can be written as Equation 2.16:

$$n = n_0 + n_2 I \,, \tag{2.16}$$

where the Kerr index, n_2, is induced by the third-order susceptibility $\chi^{(3)}$ with the relation: $\chi^{(3)} = 4\varepsilon_0 c n_2 n_0^2 / 3$. For regular medium, n_2 is positive and leads to an increase of the refractive index in the presence of intense radiation field. In general, laser beams have Gaussian transverse spatial profiles where the intensity is the highest in the middle and results in a larger refractive index at the center. The overall Kerr effect influences the curvature of the incident light wave-front, which is similar to an optical lens focusing the light. When only self-focusing occurs, the propagating beam could collapse to a single point. However, it should be noted that self-focusing always needs to overcome the universal diffraction, which defocuses the laser beams. Therefore, the collapse of the laser beam requires an initial power density above the critical power for the medium as calculated in Equation 2.17:

$$P_{cr} = 3.72\lambda_0^2 / 8\pi n_0 n_2. \tag{2.17}$$

Another effect competing with the self-focusing is the photo-ionization, which defocuses the light when the power density is high enough. The ionization of the gas medium requires the simultaneous absorption of a large number of photons $\sim U_i / h\omega_0$, where U_i is the ionization potential of the gas molecule or atom and is unreachable for regular lasers. When the beam approaches the point of collapse, the power density is extremely high, and the ionization starts to generate plasma through multiphoton absorption or tunneling. The ionization rate highly depends on the power density, described as I^K , where K is the number of absorbed photons required to ionize the gas atom or molecule. The plasma could locally reduce the refractive index according to Equation 2.18:

$$n \simeq n_0 - \frac{\rho(r,t)}{2\rho_c} , \tag{2.18}$$

where $\rho(r,t)$ is the density of ionized free electrons and ρ_c is critical plasma density, defined as $\rho_c \equiv \varepsilon_0 m_e \omega_0^2 / e^2$, above which the plasma is no longer transparent.[31-32] The reduction of the refractive index works as a concave lens to diverge the laser beam with a higher power density at the center.

These two competing effects together build the filament intuitively as shown in Figure 2.5. The self-focusing effect initially dominates and shrinks the beam diameter tremendously. When the power density is high enough, gas ionization generates the plasma which defocuses the laser beam. The ionization rate decreases fast as the beam diverges and, as a result, the self-focusing dominates in the propagation again. When two such processes reach a balance, the filament is built and enables strong interaction between the high-intensity laser pulse and gas medium over a long distance. Depending on the peak power and the type of gas, the length of

filament could range from several centimeters to even kilometers. The extended interaction

length ensures the spectral width is broadened enough for white light generation. In this method,

the plasma absorption is the predominant source of energy loss.[31]

The filament is a very complicated phenomenon involving a large number of impressive

nonlinear effects that are still under investigation.[33-35] Up to now, there is not a single general

model that can include all the phenomena already observed in the propagation of a high-intensity

femtosecond laser pulse. A detailed discussion is beyond the scope of this dissertation. A

reduced scalar model, as seen in Equation 2.19, can explain the processes mentioned above,

which is enough to describe the formation of the filament:

$$\frac{\partial E}{\partial z} = \frac{i}{2k}\Delta_\perp E + ik_0 n_2 |E|^2 E - i\frac{k_0}{2n_0}\frac{\rho}{\rho_c}E, \qquad (2.19)$$

where $E(x,y,z,t)$ is a slowly varying envelope of the incident light.
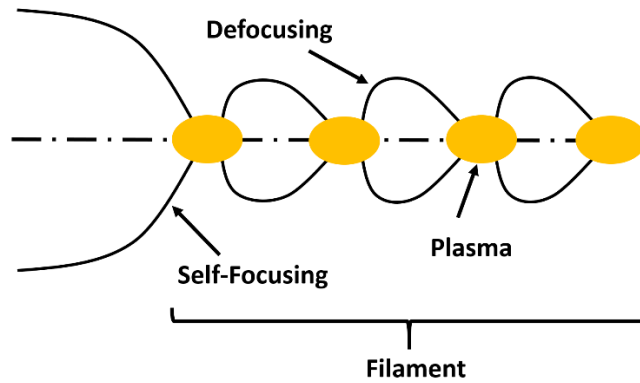
Figure 2.5. *An illustration of the focusing–defocusing cycles induced by the competing self-focusing and plasma defocusing. The solid curves indicate the diameter of the laser beam. The filament is built by a large number of these cycles, and the filament length is the distance covered by the cycles.*

2.4. Principles of Nonlinear Spectroscopy

Nonlinear spectroscopy refers to light-matter interaction under a strong radiation field when the response is nonlinearly related to the amplitude of the light field.[36-37] In nonlinear spectroscopy, the emitted signal is subject to more than one field-matter interaction and usually treated with high-order perturbation theory. From Maxwell equations, the propagation of the electronic field in a dielectric medium can be described by:

$$\nabla^2 \vec{E}(\vec{r},t) - \frac{1}{c^2}\frac{\partial^2 \vec{E}(\vec{r},t)}{\partial t^2} = \frac{4\pi}{c^2}\frac{\partial^2 \vec{P}(\vec{r},t)}{\partial t^2}. \tag{2.20}$$

Solving the equation gives $\vec{E}_{signal} \propto i\vec{P}$. The phase factor i is introduced because the emitted field is proportional to the gradient of the polarization. In nonlinear spectroscopy, the induced polarization needs to be treated by perturbation theory and can be expanded as:

$$P(t) = P^{(1)} + P^{(2)} + P^{(3)} + ..., \tag{2.21}$$

where $P^{(n)}$ refers to the polarization arising from interaction with n incident light fields.[36-38] $P^{(2)}$ and higher order terms are called the nonlinear terms. $P^{(n)}$ can be measured with suitable n^{th}-order nonlinear spectroscopic techniques. $P^{(n)}$ can be written as the convolution between the response function $R^{(n)}$, which characterizes the material response when interacting with light and the electric field.[36-37]

$$P^{(n)}(t) = \int_0^\infty d\tau_n \int_0^\infty d\tau_{n-1}...\int_0^\infty d\tau_1 R^{(n)}(\tau_n, \tau_{n-1}...\tau_1) E_1(t-\tau_n-\tau_{n-1}-...\tau_1)...E_n(t-\tau_n) \tag{2.22}$$

The response function contains all the relevant information about the response of material when interacting with the radiation field. It is possible to get the expression of $R^{(n)}$ with the commutator between the transition dipole operators and the density operator:

$$R^{(n)}\left(\tau_{1},\tau_{2},...\tau_{n}\right)=\left(\frac{i}{\hbar}\right)^{n}\theta\left(\tau_{1}\right)\theta\left(\tau_{2}\right)...\theta\left(\tau_{n}\right)$$

$$\times Tr\left\{\left[\left[...\left[\mu_{I}\left(\tau_{n}+\tau_{n-1}+...+\tau_{1}\right),\mu_{I}\left(\tau_{n-1}+\tau_{n-2}+...+\tau_{1}\right)\right]...\right]\mu_{I}\left(0\right)\right]\rho_{eq}\right\}, \tag{2.23}$$

where $\theta\left(\tau_{n}\right)$ is the Heaviside step function, which enforces the causality of the equation, μ_{I} is

the transition dipole, and ρ_{eq} is the density operator at equilibrium.[36-37]

The definition of the density operator is given in Equation 2.24 as the outer product of a

wave function and its conjugate:

$$\rho=|\psi\rangle\langle\psi| \tag{2.24}$$

If expanding the $|\psi\rangle$ in a comprehensive set, the density operator can be expressed in the format

of a matrix. For a simple two-level system, as in Equation 2.25, the diagonal elements p_{11} and p_{22}

are called populations, which describe the possibility of finding a molecule in such a state; in

contrast, the off-diagonal elements c_{12} and c_{21} are called coherences, which represent the

superposition between particular states:

$$\rho=\begin{pmatrix}p_{11}&c_{12}\\c_{21}&p_{22}\end{pmatrix}. \tag{2.25}$$

The response function is a summation over several correlation functions, which

characterize the correlation between the system before and after interacting with the radiation

field. These correlation functions differ from interacting with the *bra* or *ket* sides of the density

operator. For the nth-order response function, 2^{n} correlation function terms contribute. The

derivations of the response functions and correlation functions have not been included to avoid

too much detail in this dissertation. A graphic method called a Feynman diagram[39-41] is widely

used to write the correlation function terms representing the specific sequence of field-matter

interactions conveniently. There are several rules when drawing a Feynman diagram and translating the chart into the terms of the response function, as detailed below:

1. Two vertical lines represent the ket and bra sides of the density operator.

2. Time elapses from the bottom to the top.

3. The Feynman diagram must start and end at populations

4. Inward arrows represent absorptions, while outward arrows represent emissions.

5. Arrows on the left side interact with ket, while arrows on the right side interact with bra.

6. Absorption excites the state on its side from a lower energy to a higher energy, while the emission relaxes the state on its side from a higher energy to a lower energy.

7. For the nth-order nonlinear spectroscopy, $n+1$ arrows are included. The last arrow always represents the signal emission.

8. A transition dipole matrix element is written for each field-matter interaction including signal emission.

9. The system evolves freely under H_0 between interactions and gives a propagation function.

10. The propagation function of a coherence contains the frequency corresponding to the energy gap between the ket- and bra-side states and a damping factor.

11. Arrows pointing to the right (left) are associated with positive (negative) wavevectors and frequencies.

12. The overall wavevector (frequency) of the signal is determined by the sum of the incident field wavevectors (frequencies) reflecting the conservation of energy and momentum.

13. A constant $(-1)^k$ is multiplied to the response function where k is the number of interactions on the *bra* side.

Following these guidelines, we can write the specific terms in the response function. The whole response function is the sum over all possible Feynman diagrams obeying the above rules. Figure 2.6 and Equation 2.26 provide an example of two ground state bleach (GSB) terms in the third-order nonlinear spectroscopy of a two-level system:

$$R_1 = p_g \left(\mu_{eg} \right) \left[e^{-\left(i\omega_{eg} - \Gamma_{eg} \right)\tau_1} \right] \left(\mu_{eg} \right) \left[e^{-\Gamma_{gg}\tau_2} \right] \left(\mu_{eg} \right) \left[e^{-\left(i\omega_{eg} - \Gamma_{eg} \right)\tau_3} \right] \left(\mu_{eg} \right) \tag{2.26a}$$

and

$$R_2 = \left(-1 \right)^2 p_g \left(\mu_{eg}^* \right) \left[e^{-\left(i\omega_{eg} - \Gamma_{eg} \right)\tau_1} \right] \left(\mu_{eg}^* \right) \left[e^{-\Gamma_{gg}\tau_2} \right] \left(\mu_{eg}^* \right) \left[e^{-\left(i\omega_{eg} - \Gamma_{eg} \right)\tau_3} \right] \left(\mu_{eg} \right). \tag{2.26b}$$

Here, for convenience, the propagation functions were written under the homogeneous limit. If the spontaneous transfer $g \rightarrow e$ is not considered, the relaxation rate of the ground state Γ_{gg} equals zero. As demonstrated above, the response functions are easily obtained with the help of Feynman diagrams, which are instrumental in understanding the signal measured by nonlinear spectroscopy.
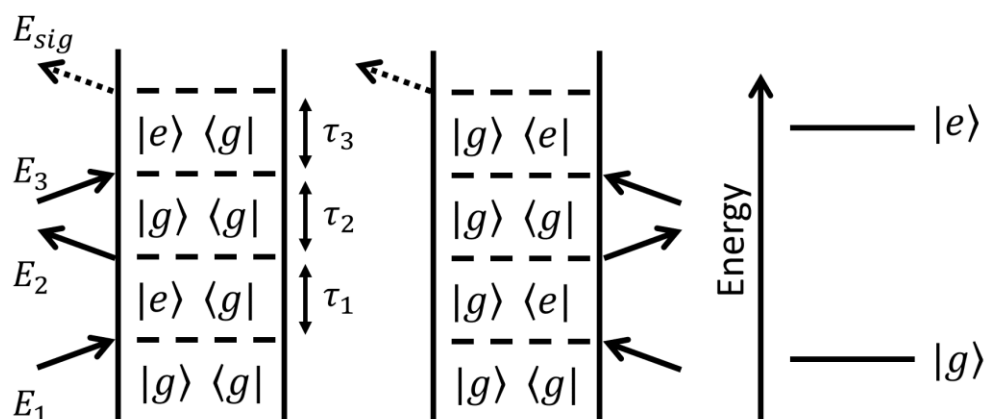
Figure 2.6. *In a third-order nonlinear spectroscopy, two Feynman diagrams for a two-level system are shown. These two Feynman diagrams are associated with the ground state bleach (GSB). The end state is not shown in the plots, which is* $|g\rangle\langle g|$ *.*

2.5. Third-Order Nonlinear Spectroscopy

2.5.1. Transient Absorption Spectroscopy

Transient absorption spectroscopy is a third-order nonlinear spectroscopic method that measures the change of the absorption spectrum induced by the pump laser pulse and can reflect the relaxation of nonequilibrium species. Firstly, a pump pulse promotes a portion of the molecules in the system from the ground state to an electronically or vibrationally excited state. The effect of the pump can be interpreted in either a classical or quantum way. In the quantum consideration, the sample absorbs a photon. In the classical consideration, two field-matter interactions are involved within the pump pulse. These two interpretations are equally valid under the particle-wave duality of light. The probe pulse then arrives after a delay τ and interacts with the excited molecules. The transmitted probe is measured by a spectrometer synchronized to the laser repetition rate to perform a pulse-by-pulse measurement. By varying the delay τ between the pump and probe pulses, spectra are acquired at different steps in the evolution of the excited species, obtaining the frequency-resolved dynamics. To measure the laser-induced

change of the absorption spectrum, an optical chopper at 500Hz, which is half of the laser

repetition rate, is placed in the path of the pump beam to produce two phases for differencing.

The transmission of the probe is measured under with pump-on conditions, representing the

excited species, and pump-off conditions, representing the ground state species. Equation 2.27 is

used to calculate the transient absorption for each delay:

$$\Delta A(\omega,\tau) = A(\omega,\tau)_{pump-on} - A(\omega,\tau)_{pump-off} = -\log\left(\frac{I_{pump-on}}{I_0}\right) + \log\left(\frac{I_{pump-off}}{I_0}\right) = \log\left(\frac{I_{pump-off}}{I_{pump-on}}\right). \qquad (2.27)$$

From the classical interpretation, the third-order nonlinear signal measured by transient

absorption spectroscopy has a phase matching condition $k_{sig} = k_1 - k_2 + k_3$, where $k_1 = k_2$ because

the first two field-matter interactions come from the same pump pulse.[42-43] Thus, the signal emits

in the same direction as k_3, the probe pulse.

The calculation of the transient absorption signal in this research for the wide-field

microscope was slightly different from the method mentioned above. When the pump pulse was

scattered by the sample and enters the spectrometer, it could introduce a large differencing signal

and overwhelm the desired response from the sample. Another optical chopper was placed in the

probe path and the frequency of the chopper in the pump was set at half of the original frequency

to remove the scattered pump. The two choppers cycled among four phases: pump-on/probe-on

(S_1), pump-on/probe-off (S_2), pump-off/probe-on (S_3), pump-off/probe-off (S_4). Equation

2.28 calculated the differencing signal:

$$\Delta A = -\log(S_1 - S_2) + \log(S_3 - S_4). \qquad (2.28)$$

There are usually three different signal components measured in transient absorption

spectroscopy: ground state bleach (GSB), excited state emission (ESE), and excited state

absorption (ESA). For the three-level system, Figure 2.7 illustrates three Feynman diagrams as

examples. It is also possible to understand these three components intuitively.[44-45] The GSB

component has a negative sign and is a result of the increase in the probe transmission. When a

fraction of the system is promoted to the excited state by the pump pulse, this population stops

absorbing the light at the ground state absorption band and the transmitted light at these

frequencies increases. According to Equation 2.27, this effect can generate a negative signal.

Instead of absorbing from the ground state, the excited molecules instead can emit light from the

bottom of the higher electronic state when stimulated by the probe. The stimulated emission is in

the same direction as the probe and increases the intensity of the transmitted probe at the

fluorescence frequencies. This contribution gives a negative signal as ESE, which is very similar

to the GSB but red-shifted due to nuclear relaxation. At short delays, the GSB and ESE are not

distinguishable.[46-47] The last component is the ESA, which is a positive component induced by

the absorption of the excited molecules. The new absorption band decreases the intensity of

transmitted light, and thus has a positive sign according to Equation 2.27. Among these three

components, ESE and ESA are directly related to the excited state population and relax when the

occupancy of specific state decreases. However, the GSB contribution is only related to the

ground state population and decays when the population of the equilibrium species recovers.
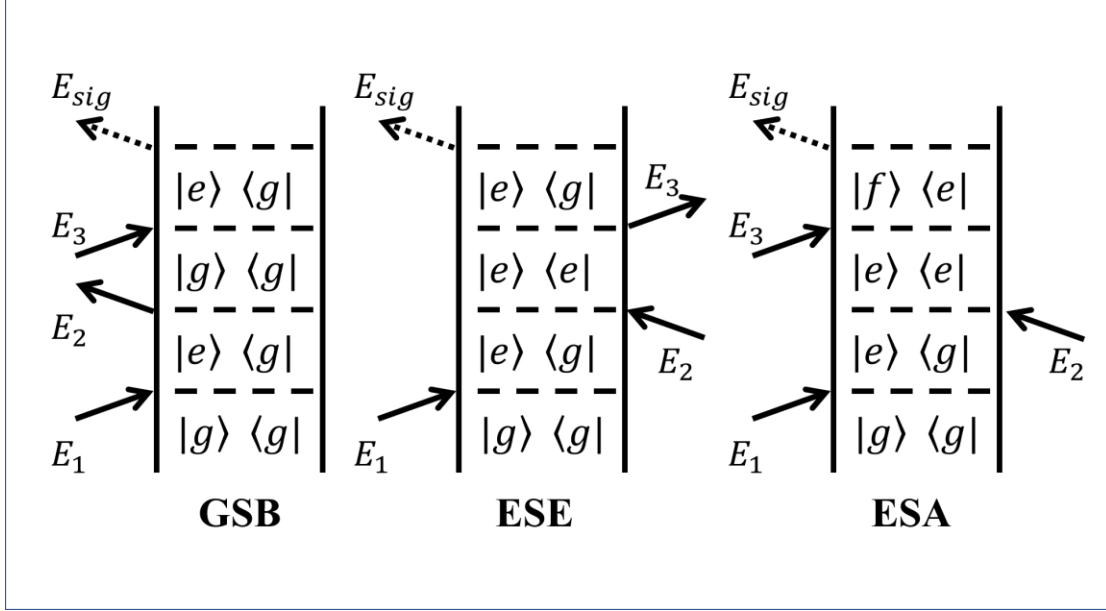
Figure 2.7. These three Feynman diagrams illustrate examples of GSB, ESE, and ESA measured by transient grating and transient absorption spectroscopy. Although not all terms contributing to these two techniques are plotted in the figure, all response function terms measured can be classified into these three categories.

2.5.2. Four-Wave-Mixing Spectroscopy and Transient Grating Spectroscopy

When counting the number of field-matter interactions, n^{th}-order nonlinear spectroscopy involves $n+1$ field-matter interactions, sometimes also referred as $n+1$ wave-mixing spectroscopy. Proposed in the 1970s, transient grating spectroscopy is a widely performed four-wave-mixing technique and measures the third-order nonlinearities of the sample.[48-49] Figure 2.8 depicts a typical geometry of a transient grating measurement. Two time-coincident laser pulses pump the sample, and after a waiting time τ, the probe beam arrives. The signal will emit in the phase-matched direction. This geometry guarantees that transient grating is a background-free technique, which increases signal-to-noise and data acquisition efficiency. The phase matching condition, which is determined by the conservation of momentum, gives the signal direction as $k_{sig} = k_1 - k_2 + k_3$. With the first two field-matter interactions, the matter only absorbs one photon, which is in a superposition of photons from the two different fields. Transient grating

spectroscopy is sensitive to ground state bleaching (GSB), excited state emission (ESE), and excited state absorption (ESA) terms in the response function. Examples for a three-level system are shown in Figure 2.7.
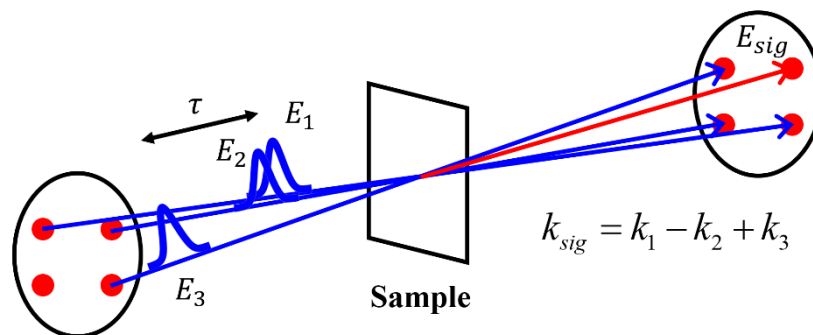
Figure 2.8. *Typical transient grating experiment geometry. Two time-coincident pump pulses arrive at the sample first. Then, after some waiting time τ, the probe pulse arrives and generates the signal. The signal is emitted in a different direction from all incoming laser beams determined by the phase match condition. Therefore, the measurement is background free and no optical chopper is necessary.*
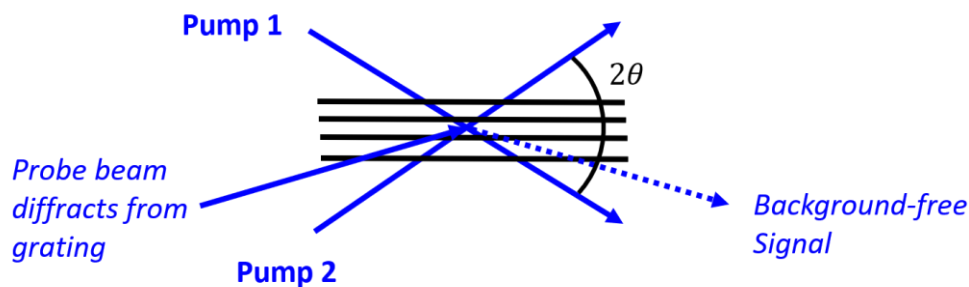
Figure 2.9. *The concept of grating formation in transient grating measurements. Two time-coincident pump beams with different wavevectors cross in the sample at an angle 2θ and interfere to form a population grating. After a delay, the probe arrives and is scattered off the grating in the signal direction $k_{sig} = k_1 - k_2 + k_3$, where k_1 and k_2 are the pump beams and k_3 is the probe.*

The mechanism of signal generation can be understood more intuitively. The two time-coincident pump pulses may form an interference pattern in the sample since they have different wavevectors, as shown in Figure 2.9. In areas of constructive interference, the molecules are

excited, whereas the molecules stay at equilibrium in regions of destructive interference. The

periodic switching between excited and ground state molecules forms a short-lived population

grating in space.[50-51] When the third probe pulse arrives at the transient population grating after a

delay τ, it can be diffracted to the particular angles determined by the period of the grating,

which is $\eta = \dfrac{\lambda}{2n\sin\theta}$. The efficiency of the diffraction depends on the sharpness of the fringes,

which reflects the fraction of molecules that stay in the excited states after delay τ. Thus, the

transient grating technique can measure relaxation processes.

The transient grating technique is sensitive to weak signals because it is background free.

The signal can be detected as long as it is stronger than the signals from random scattering and

above the detector threshold. However, when the transition dipole is small, and the sample

damage threshold limits the laser fluence, directly measuring the weak emitted signal may not

produce an excellent signal-to-noise ratio. An interferometric method, called heterodyne

detection, can be applied in this case. By overlapping the signal with a reference field of higher

intensity, it is possible to amplify the weak signal and obtain the phase information beyond just

the intensity, which is essential to separate the absorptive and dispersive parts of the emitted

field.[52-57] The signal measured in the heterodyne detection method is given by:[38, 58-60]

$$I = \left|E_{ref}\right|^2 + \left|E_S(t)\right|^2 + 2\left|E_{ref}E_S(t)\right|\cos\left(\phi_{ref} - \phi_S\right). \tag{2.29}$$

Since the reference field is much stronger than the signal, $\left|E_{ref}\right|^2 \gg \left|E_S(t)\right|^2$, the

amplification of the signal depends on the crossing term $2\left|E_{ref}E_S(t)\right|\cos\left(\phi_{ref} - \phi_S\right)$, and the

signal is amplified by a factor of $2\left|E_{ref}/E_S(t)\right|$.[53, 58] Figure 2.10(b) illustrates the interferometric

spectrum measured. A Fourier transform of the interference leads to the emission field evolution

in the time domain, where a Gaussian apodization function filters out the time independent part

E_{ref} . Finally, inverse-Fourier transform produces the complex signal in which the real part corresponds to the transient absorption,[37, 61] while the imaginary part refers to the transient dispersion.[55-57]
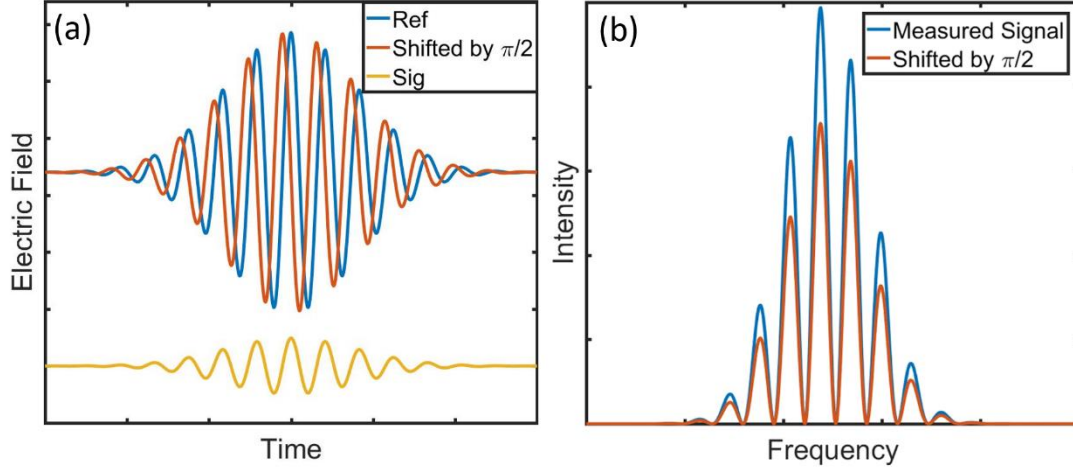
Figure 2.10. *An illustration of how the interferometric detection method magnifies the signal and why the phase fluctuation has significant influence on the measured signal. (a) The real parts of the electronic fields are shown in the time domain as a summation over all frequencies. The reference (Ref) field is five times stronger than the signal. The disturbance in the optical path on the times scale of 0.7 fs could shift the 400 nm light by π/2, as indicated by the red lines. (b) The measured signal is the square of the time-integrated sum between the reference field and the signal. Fringes are generated by the interference between the reference field and the signal. If the reference field varies by 0.7 fs in optical path, it may cause a 25% reduction of peak intensity.*

The magnitude of the crossing term is sensitive to the phase difference between the reference and the signal fields, thus a consistent phase relationship is crucial to acquire high signal-to-noise data. Figure 2.10 illustrates the influence of phase fluctuation on the measured signal. To elucidate the difficulty in maintaining the phase difference further, we can decompose it into several sources,[58]

$$\Delta\phi = \phi_{ref} - \phi_S = \frac{\pi}{2} + \phi_\chi + \left(\phi_{pump1} - \phi_{pump2}\right) - \left(\phi_{ref} - \phi_{probe}\right),$$ (2.30)

where $\pi/2$ is the phase shift between the polarization and field emitted, and ϕ_χ is the phase shift originating from the complex third-order susceptibility. The resting phase contributions, $\phi_{pump1}, \phi_{pump2}, \phi_{ref}, \phi_{probe}$, can be influenced by the air current, humidity, temperature fluctuation, and vibrations of optics. Due to the nanometer-scale wavelengths of the visible range, delicate variations of these conditions could induce significant phase shift. This factor becomes the dominant noise source in heterodyne-detected transient grating measurements. An active phase feedback loop can be applied to monitor the fluctuation and compensate the phase shift.[62-64] Another way is to apply sheer brute force to control the mechanical stability and experimental environment.[65] However, these active phase control methods are not cost-efficient and are complicated to set up. A better solution is the DOE-based passive phase-lock, which is widely used to measure weak high-order nonlinearities.[38, 52-53, 58, 60, 66-72] In transient grating experiments, the DOE splits the two incoming laser beams into ± 1 orders. Either of the two pairs contains two beams identical in intensity and phase. One pair of beams serves as the two pumps, and the other pair includes the probe and reference. The similarity in the beam proximity cancels out the phase distortion caused by temperature and humidity differences, as indicated by Equation 2.30. Furthermore, all four beams are reflected by the same set of optics. Therefore, the phase fluctuations induced by the vibrations are identical. Figure 2.11 illustrates a typical DOE-based transient grating setup.
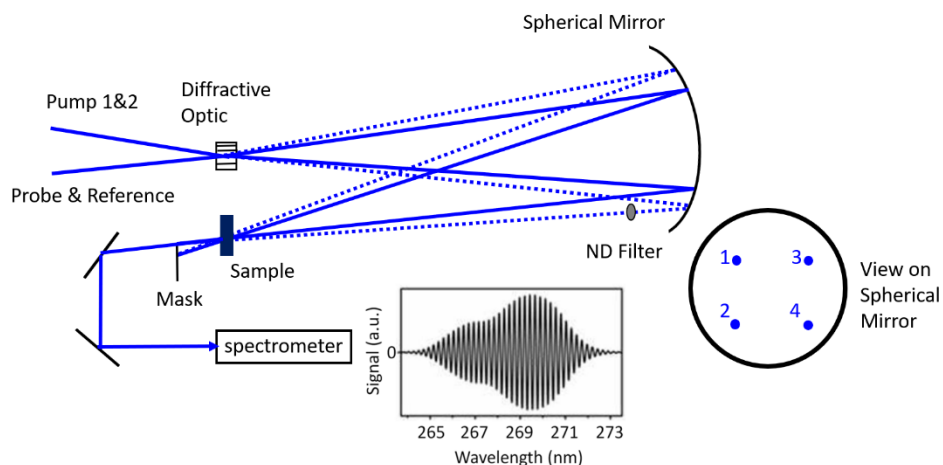
Figure 2.11. *A typical geometry for the diffractive optical element (DOE)-based transient grating setup. Two beams are focused onto the DOE and split into ±1 diffraction orders. A spherical mirror reflects and focuses the four beams. Beams 1 and 2 induce the population grating, and the transient grating diffracts beam 3 (the probe). The diffracted signal beam is collinear with beam 4, which is an attenuated reference field for heterodyne detection. A typical interferometric signal measured on the spectrometer is shown.*

2.6. Fifth-Order Nonlinear Spectroscopies

2.6.1. Diffractive Optics-Based Six-Wave-Mixing

As mentioned in Section 2.5.2 of this chapter, six-wave-mixing refers to fifth-order nonlinearities. The simplest six-wave-mixing spectroscopy is the pump-repump-probe, which adds a pump pulse to prepare a nonequilibrium state before measuring the transient absorption.[1, 73-75] Because we primarily focused on the application of DOE, we do not discuss details about this technique in this dissertation. Another avenue for developing a six-wave-mixing technique involves adding beams to the diffractive optic-based four-wave-mixing transient grating geometry shown in Figure 2.11.[38, 59-60, 71, 76] These derivations from transient grating have shown higher sensitivity and an increased signal-to-noise ratio over the pump-repump-probe, and possess a unique ability to separate absorptive and dispersive signal components. In this research, we used three different configurations to measure the two-dimensional resonance Raman spectroscopy.
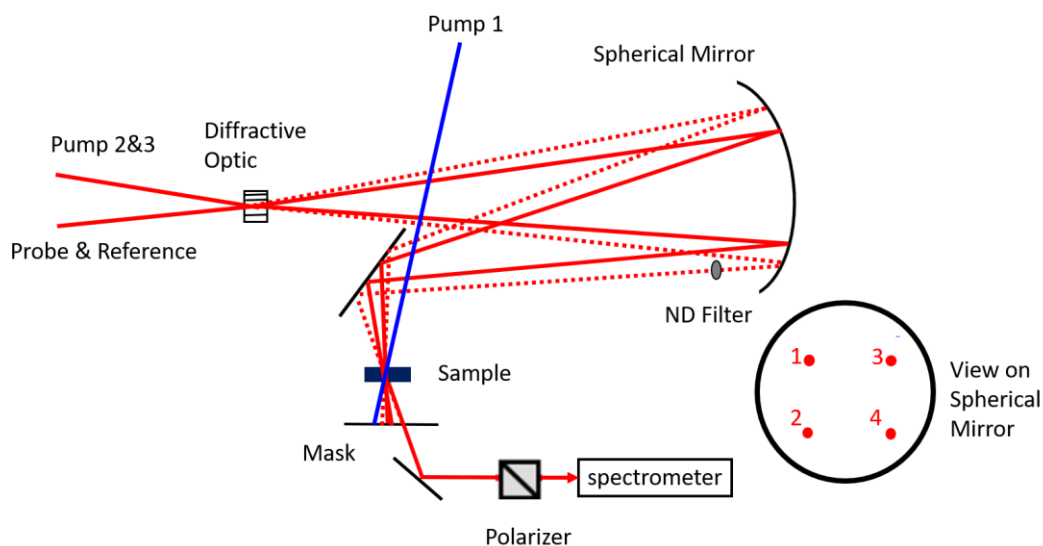
Figure 2.12. *A diffractive optic-based four-beam interferometer used to measure the six-wave-mixing signal in Chapter 3. Compared to the geometry used in the four-wave-mixing transient grating in Figure 2.11, an additional pump beam arrives before the formation of population grating. A nonequilibrium state of the sample molecules can be prepared before measuring the transient grating signal. The signal emits in the same direction as in the transient grating case, collinear to the reference field 4.*

In Figure 2.12, one additional pump beam could be added to the four-wave-mixing transient grating geometry illustrated in Figure 2.11. This four-beam geometry was used to measure the photodissociation of triiodide in this dissertation. The pump induced photochemistry processes such as photodissociation and prepares a nonequilibrium state before measuring the transient grating signal. The delay τ between this pump and the time-coincident pair of pumps in transient grating could be controlled in order to examine the relaxation processes happening during this time interval. Two field-matter interactions were involved in the first pump, and the corresponding phase matching condition was $k_{sig} = k_1 - k_2 + k_3 - k_4 + k_5$, where $k_1 = k_2$. Because the first two wavevectors canceled out, the fifth-order signal would emit in the same direction as in the transient grating measurement and overlap with the third-order response. An optical chopper must be applied to pump 1 to isolate the desired fifth-order signal. The third-order signal

background was removed by subtracting the pump1-off measurement from the pump1-on.

However, when the sample was not resonant to the wavelength used for the four transient grating

beams and possesses no third-order signal, it was possible to measure the background-free fifth-

order response without chopping directly. This situation could happen when applying 340 nm

pump1 and 680 nm pump 2, pump 3, and probe to measure the photodissociation of the triiodide.

Because the triiodide molecule was transparent at 680 nm, no third-order signal could originate

from the ground state of triiodide, and only the diiodide molecules generated by pump 1 could

react with the three 680 nm beams. In Chapter 3, we further discuss the details of this case.
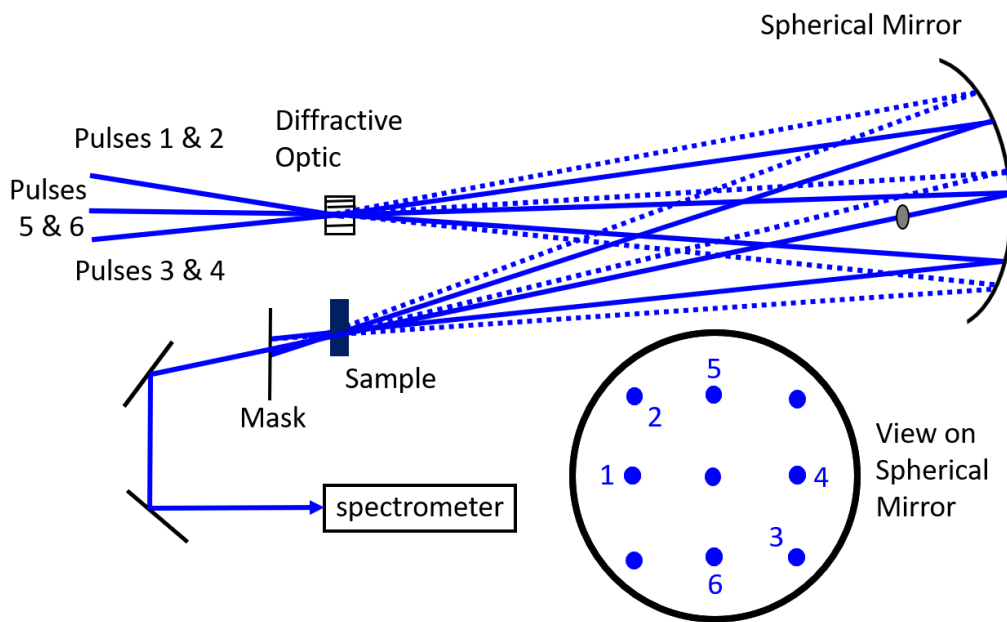
Figure 2.13. A diffractive optic-based interferometer with five-beam geometry is used to measure the six-wave-mixing signal in Chapter 3. The three incoming beams are split into -1, 0, and +1 diffraction orders with even intensity distribution. A mask on the spherical mirror blocks beams not marked with numbers. Beams 1 and 2 firstly excite the sample and produce a population grating. After a delay τ, beams 3 and 4 arrive and re-excite the sample from a prepared nonequilibrium state. These four beams generate a two-dimensional crossing grating. The last, beam 5, is diffracted by this grating in the same direction as beam 6, the attenuated reference field, for heterodyne detection.

With one more beam added in, the five-beam six-wave-mixing geometry in Figure 2.13 can separate the fifth-order response from the third-order background and still maintain a reference field automatically collinear with the signal. In this dissertation, we used this geometry to measure the degenerate two-dimensional resonance Raman spectroscopy of triiodide, as discussed in detail in Chapter 3.

In Figure 2.13, the three degenerate incoming beams are focused onto the diffractive optic and split into $0, \pm 1$ diffraction orders with identical intensities. A spherical concave mirror folds and focuses six of these nine beams onto the sample. A mask set against the mirror blocks the other three beams. The time-coincident pumps 1 and 2 arrive first and excite the sample to generate a population grating as in Figure 2.14(a). After a delay time τ_1, the second pair of time-coincident pumps 3 and 4 forms a new grating pattern and re-excites the molecules in the constructive interference regions. Figure 2.14(b) depicts the overall population grating generated by these four beams. Finally, the probe beam 5 arrives at the sample after the second delay τ_2 and is diffracted by this grating into the phase matching direction, $k_{sig} = k_1 - k_2 + k_3 - k_4 + k_5$.

Unlike the previous geometry, here $k_1 \neq k_2$. Considering the equal angles between the $0th$ order and the $+1$ or -1 order, the apparent calculation yields $k_{sig} = k_6$, which is the same direction of the attenuated reference field beam 6. The overlapped signal and reference field produce an interferrogram on the spectrometer for heterodyne detection, which needs to be processed by the method mentioned in Section 2.5.2 of this chapter. In this setup, the application of diffractive optic not only stabilizes the phase difference crucial to measuring a weak fifth-order signal, but also provides a local oscillator (beam 6) that helps find the direction of the emitted field without much effort.
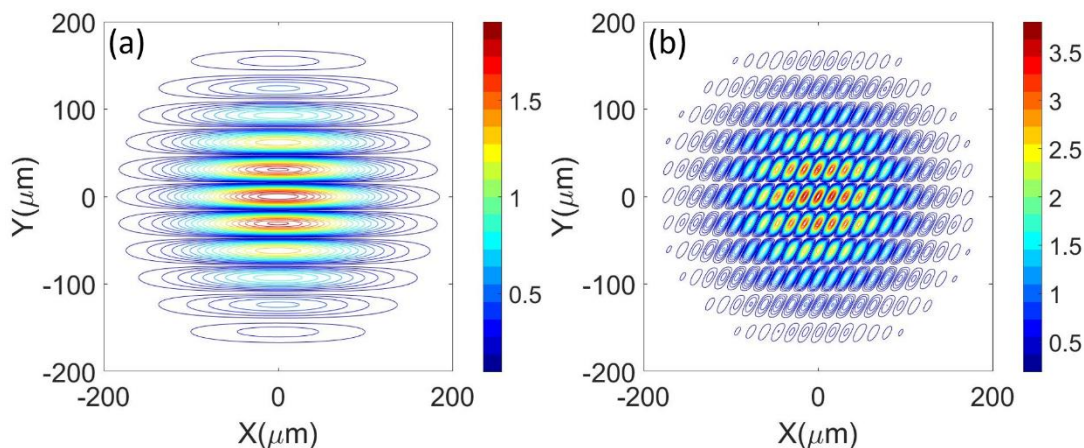
Figure 2.14. *Population grating generated by the six-wave-mixing geometry demonstrated in Figure 2.13. A 266 nm deep UV laser beam generates the patterns, as described in Chapter 3. The angle between ± 1 orders of the diffracted light is 6.1 degrees. The figures represent the views observed from a direction perpendicular to the sample surface. (a) The population grating formed by the first two pumps, beams 1 and 2. (b) The population grating formed by all four pumps, beams 1 through 4. These gratings are not moving due to the degenerate condition for all beams.*

2.6.2. Femtosecond Stimulated Raman Spectroscopy

Femtosecond stimulated Raman spectroscopy (FSRS) has been developed as a powerful method to investigate ultrafast structural dynamics in condensed phases with sub-picosecond time precision.[77-90] This new technique has shed light on systems including biological proteins[77, 79-80, 88] and organic photovoltaic materials.[78, 85] Figure 2.15 depicts the pulse sequence generally used for FSRS. The FSRS technique involves two succeeding events: (a) an electronically resonant actinic pump pulse initiates some electronic photochemical process, and (b) a stimulated Raman spectrum is obtained after a controlled delay τ using a combination of time-coincident narrowband and broadband laser pulses. The actinic pump pulse is usually < 100 fs in duration and possesses a wide bandwidth. In contrast, the Raman pump pulse is at least hundreds of femtoseconds long and is narrow enough to ensure high Raman resolution. The Stokes probe is a broadband femtosecond pulse that is red-shifted from the Raman pump to produce a broadband response that interferes with the emitted stimulated Raman scattering. As illustrated

in Figure 2.15, the actinic pump prepares a nonequilibrium state $|n\rangle$ and then a vibrational

coherence $|n\rangle\langle n+1|$ is activated by the first field-matter interaction involved in the Raman pulse

and the probe. This coherence dephases with a characteristic vibrational dephasing time. The

second field-matter interaction from anytime under the Raman pump duration envelope induces

the signal emission in the phase matching direction. The femtosecond-scale sensitivity to

ultrafast dynamics is achieved by the accuracy in the scanned delay between the short actinic

pump and the overlapped pair of Raman pump and short Stokes probe, although the vibrational

coherence can freely decay before the emission of signal.[91-93]
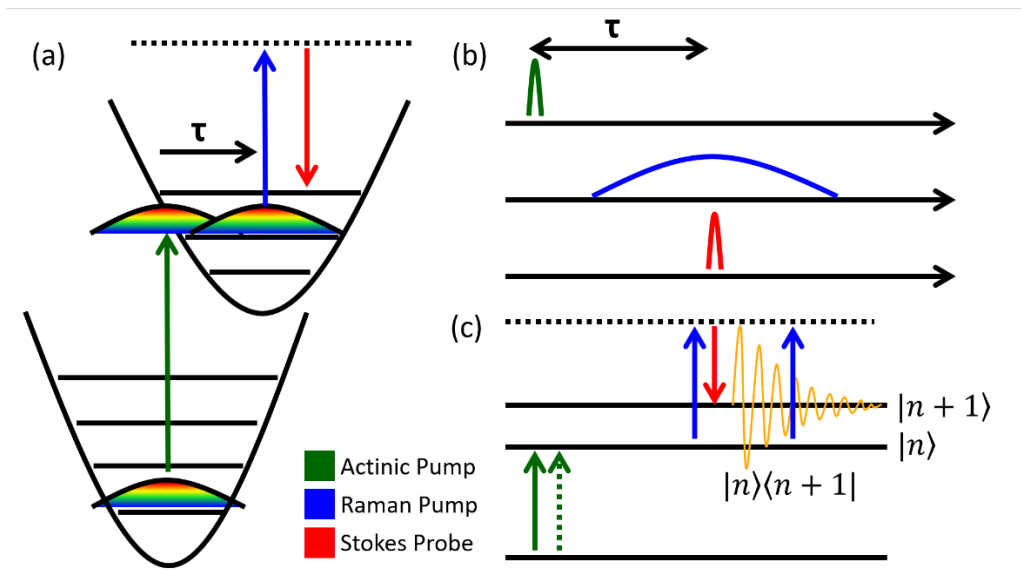
Figure 2.15. *(a) A schematic representation of time-resolved femtosecond stimulated Raman spectroscopy (FSRS). A femtosecond actinic pump pulse initiates photochemistry by promoting the system to an excited electronic state first. Then, the combination of a Raman pump pulse and a Stokes probe pulse induces the emission of the stimulated Raman signal. (b) The sequence of the actinic pump, the Raman probe, and the Stokes probe. (c) An energy diagram illustrates the key to femtosecond time precision. The actinic pump promotes the systems into an electronically excited state with two field-matter interactions. Then, the vibrational coherence $|n\rangle\langle n+1|$ is driven by the time-overlapped Raman pump and Stokes probe pulses from a prepared nonequilibrium state. The signal can actually emit anytime under the time-envelope of the Raman pump with the second field-matter interaction while the vibrational coherence is dephasing. The time precision depends on the time convolution between the actinic pump and the probe.*

In our implementation of FSRS technique, which we discuss in Section 2.6.3, a fixed delay, τ_2, was introduced between the first and second interactions involved in the long Raman pump. This 300 fs delay suppressed the broadband pump-repump-probe response, which could be very strong when the Raman pump is electronically resonant to the sample. The broadband response depended on the electronic coherence prepared by the Raman pump and Stokes probe. With increasing τ_2, both the vibrational coherence and the electronic coherence were dephasing, but the latter decayed faster due to a generally shorter dephasing time. We discuss the details of τ_2 further in Chapter 4.

2.6.3. Femtosecond Stimulated Raman Spectroscopy by Six-Wave-Mixing

Given the advantages of a background-free signal in this geometry, the data acquisition efficiency and quality can be enhanced for other fifth-order spectroscopies like FSRS in a similar setup. In this dissertation, we conducted FSRS experiments in both the four-beam and five-beam geometries described above and illustrated in Figure 2.16(a) and (b). In both geometries, the first pair of pumps, beams 1 and 2, is replaced by a pair of actinic pumps, which excites the system into a higher state. The second pair of pumps, the Raman pumps, propagate along beams 3 and 4, which induce vibrational coherence and possess narrow bandwidth and long duration. A broadband Stokes probe takes the position of beam 5. The phase matching condition $k_{sig} = k_1 - k_2 + k_3 - k_4 + k_5$ still holds, therefore the signal is emitted collinearly to beam 6. The other diffraction order of the Stokes probe is used as a local oscillator to help find the direction of the signal. Given the pulse sequence in Figure 2.16(c), one of the Raman pumps, beam 4, arrives last onto the sample and is diffracted by the population grating generated by the other beams.

Unlike the degenerate six-wave-mixing case, the grating formed by different colors is no longer static but actually moves toward a specific direction as demonstrated in Figure 2.17. In the five-beam geometry, the two degenerate actinic pumps form a static grating as in Figure 2.17(a); the first arriving Raman pump, beam 3, and the probe, beam 5, create a grating that propagates in the sample, as in Figure 2.17(b). The overall FSRS grating (Figure 2.17(c)), which is a summation of the two gratings, moves away from the detector and induces the red-shifts of the scattered Raman pump due to the 'Doppler effect.' Because of the broadband nature of the Stokes probe, the moving velocity could vary within a wide range. When the velocity matches a specific Raman mode possessed by the sample, the scattering is enhanced to generate a peak in the measured spectrum.
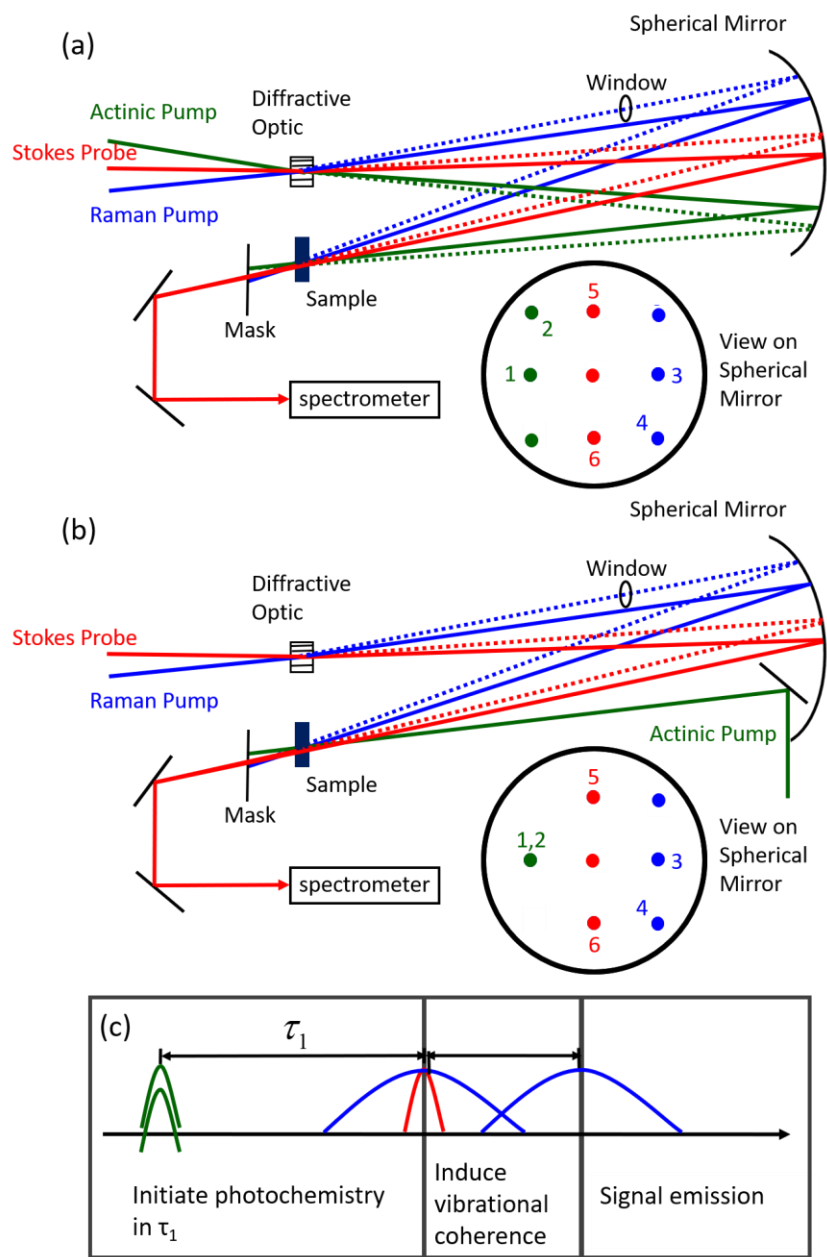
Figure 2.16. *(a) The five-beam geometry used for FSRS by six-wave-mixing (6WM) experiments in this dissertation. This design is much like the interferometer shown in Figure 2.13. However, each of the three incoming beams is a different color. (b) The four-beam FSRS geometry. (c) The pulse arrival scheme. The actinic pumps arrive first and activate some electronic process. After a controlled delay, τ_1, the first Raman pump (beam 3) and the Stokes beam (beam 5) arrive at the same time. The window shown in (a) and (b) induces a delay, τ_2, between the two Raman pumps, which suppresses the incoherent response. The final signal is formed by the diffraction of the last Raman pump (beam 4).*

As for the four-beam geometry, the wavevectors are equal, $k_1 = k_2$, because the first two field-matter interactions are from the same beam and there is no population grating formed by the actinic pump. Similar to the five-beam geometry, the first Raman pump, beam 3, and the Stokes probe, beam 5, produce a dynamic grating proceeding away from the detector as in Figure 2.17(b). This grating diffracts the last Raman pump and results in red-shifted frequency. The overall effect is very similar to the five-beam geometry case.
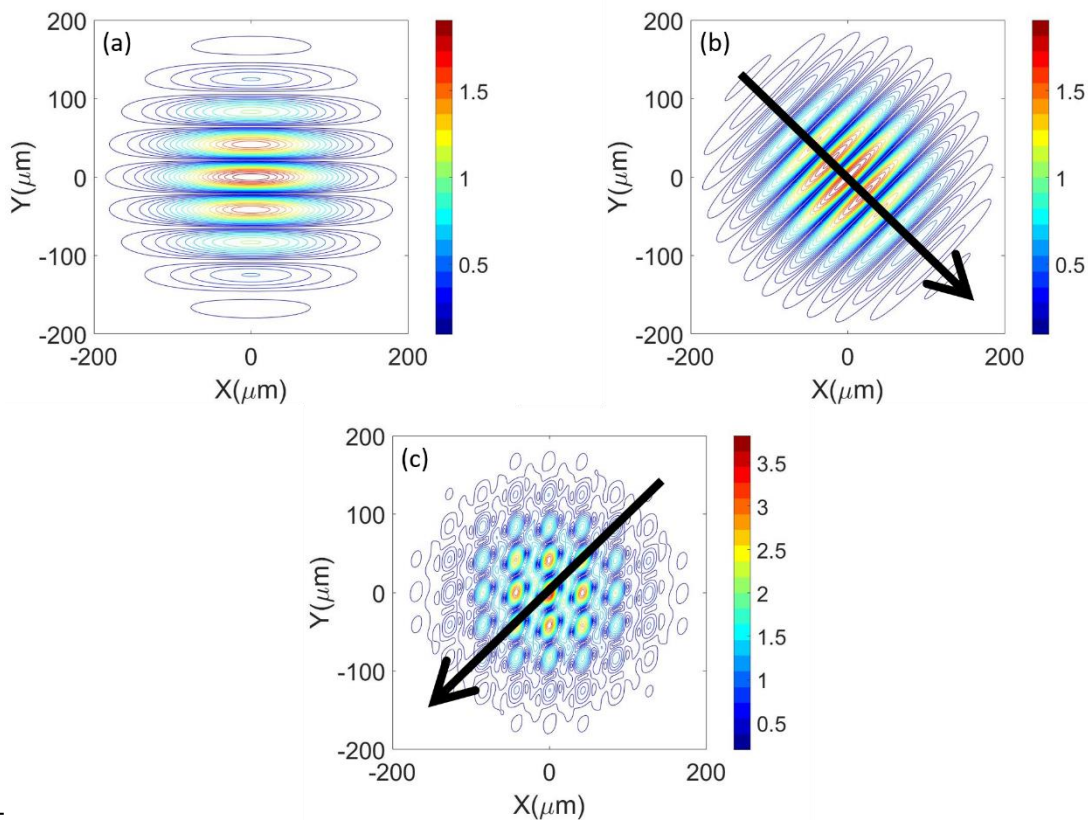
Figure 2.17. Views of gratings from the direction perpendicular to the sample surface. (a) The static grating formed by the time coincident actinic pump beams, beam 1 and 2 in the five-beam geometry experiment. However, because the first two field-matter interactions are induced by the same beam in the four-beam geometry, no grating is formed. (b) In both the four- and five-beam experiments, a dynamic population grating is generated by the Raman pump and Stokes beams because of the difference in wavelength. The interference pattern moves down and to the right. (c) In the five-beam geometry, the overall FSRS grating is the summation of the two gratings in (a) and (b) and moves down and to the left. In both four- and five-beam geometries, the moving direction of the overall population grating is opposite to the signal propagating direction. Therefore, the Doppler shifts could induce a red-shift in frequency.

2.7. Multiplex Wide-Field Transient Absorption Spectroscopy

Transient absorption microscopy is a technique that measures ultrafast dynamics with spatial resolution. It is very suitable for detecting the carrier transport in solid state materials, especially in nanostructures and film.[94-100] These experiments are usually done with a megahertz (MHz) repetition rate laser system and by spatially scanning the focused pump and probe beams on the sample. In this dissertation, we developed a new type of transient absorption microscopy with wide-field detection and multiplex excitation, which facilitates spatially- and temporally-resolved measurement using a low repetition rate laser system and access to statistical information in a single experiment. The conventional scanning transient absorption microscopy is not very suitable for use with a kHz laser system because of low data acquisition efficiency. To solve this problem, we applied a wide-field transient absorption microscopy technique[99-100] but with a counter-propagating pump and probe beams. A DOE was placed in the pump path to build multiplex excitations and obtain statistical information, which is crucial for dealing with the heterogeneity of the sample. Similar techniques have been used in scanning microscopies.[101-102]
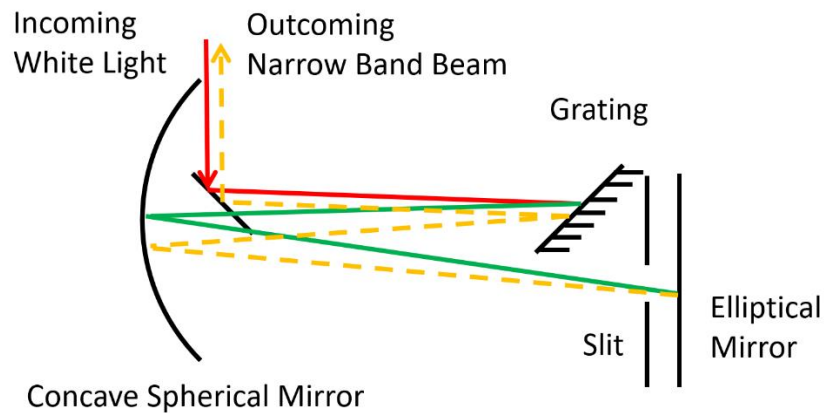
Figure 2.18. *A schematic illustration of the all-reflective 4F setup. A grating disperses the incoming broadband or super-continuum white light into a wide range of angles. The dispersed light is then focused by a concave spherical mirror to a flat mirror where different colors are spatially separated. A slit can be placed right in front of the flat mirror to select the desired wavelength range, then the flat mirror reflects the selected portion backward to the concave mirror and the grating. The distance between the concave mirror and grating as well as the distance between the concave mirror and the flat mirror are equal to the focus length of the concave mirror. The final output beam has the same beam profile as the incoming beam with frequencies selected by the slit.*
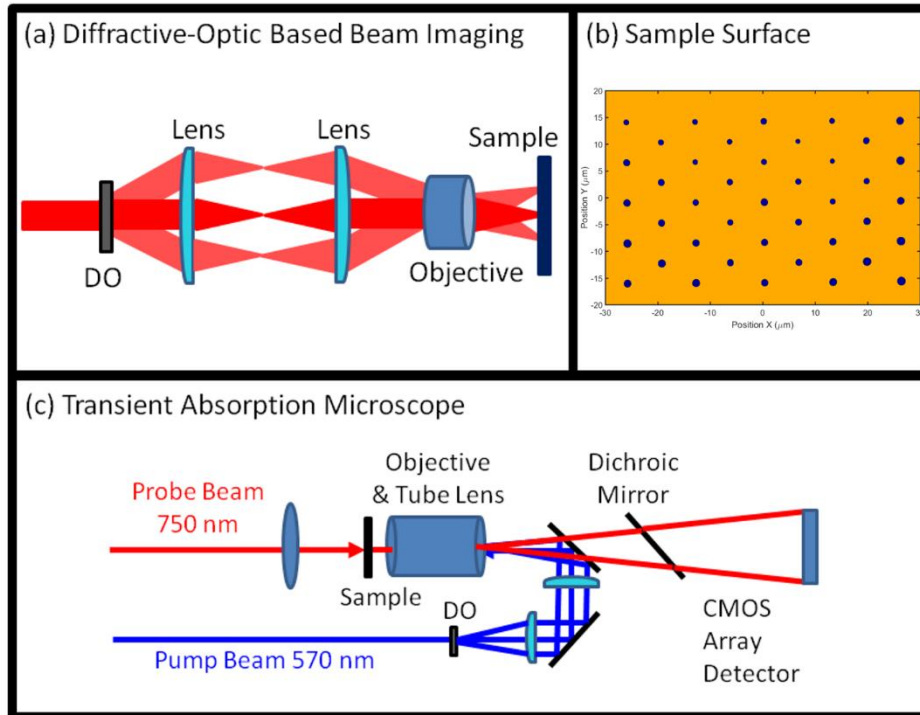
Figure 2.19. *Transient absorption microscopy experiments are conducted with a diffractive optic-based wide-field microscope. (a) A diffractive optic is used to generate a 41-point array of pump beams, which focus at different places on the sample. (b) The diffractive optic produces a 41-point matrix of laser beams, which all possess equal intensities. (c) A counter-propagating pump and probe beams are focused to full width at half maximum (FWHM) spot sizes of 0.73 and 150 μm on the sample surface, respectively.*

In this experiment, both the pump and probe beams were portions selected from the super-continuum spectrum, which was generated by focusing 1.5 mJ of a 800 nm fundamental laser beam into a 2 m long cell. This cell was pressurized by 5 psi argon, thereby creating a 6-inch long filament. In Section 2.3.2 of this chapter, we discussed the principles of the filament. A 4F setup which, as shown in Figure 2.19, uses a 1200 grooves/mm grating to disperse the white light and filters out the undesired part with a slit can select the desired frequencies. Putting the slit on a motorized stage and scanning the position achieved tunability of the pump and probe beams, thereby facilitating the spectral resolution of our microscope.

Figure 2.19 shows a schematic illustration of the microscope setup. The pump and probe beams were focused on the sample from different sides. A lens or concave spherical mirror

focused the probe beam. Because of the low numerical aperture, the probe illuminated a large area and filled the whole view under the objective lens, which enabled wide-field detection. The pump beam was split by a customized DOE into 41 collimated beams as in Figure 2.19(a). The telescope placed between the DOE along with the dichroic mirror guided the diffracted pump beams into the objective lens. The first lens focused the 41 segments onto the focal plane and the second lens recovers the collimation. If we regard the objective lens as an ideal lens, the collimated light was focused onto the focus plane with displacements from the center determined by the incident angle. Therefore, it was possible to adjust the angles between the different orders by the ratio of focal lengths according to the equation $\frac{F_1}{F_2} = \frac{\theta_o}{\theta_i}$, where F_1 and F_2 were focal lengths for the first and second lens respectively, and θ_o along with θ_i represents the angles between the diffraction orders at the DOE and objective lens. The objective lens focuses the 41 segments onto the sample surface with the pattern shown in Figure 2.19(b).

Because the signal wavevector is the same as the probe beam, as discussed in Section 2.4.1, the resolution of our transient absorption microscopy is determined in the same way as a wide-field microscope illuminated by the probe. For the 760-nm probe beam used in this dissertation, the resolution determined by Raleigh criteria is:

$$R = \frac{1.22\lambda_{probe}}{N.A._{Obj} + N.A._{Con}} = \frac{1.22 \times 0.76 \mu m}{0.95 + \frac{1cm}{30cm}} \approx 0.94 \mu m \ . \tag{2.31}$$

The objective lens can focus the pump beams into spots with diameter determined by a similar equation:

$$D = \frac{1.22\lambda_{pump}}{N.A._{Obj}} = \frac{1.22 \times 0.57 \mu m}{0.95} \approx 0.73 \mu m \ . \tag{2.32}$$

The calculation of the signal is almost the same as discussed in Section 2.4.1 of this chapter, except two laser pulses are accumulated on the camera due to the limitation of the frame rate. The camera takes images of transmitted probe under pump-off, $I_{pump-off}$, and pump on, $I_{pump-on}$, conditions. Transient absorption imaging is obtained by applying Equation 2.27 to every measured pixel of the two images.

Since a camera detected the signal instead of a spectrometer, the embedded spectral resolution of white light probing TA is lost in the experiment. However, by continuously tuning the probe, it was possible to combine the responses at different wavelengths and construct the frequency-resolved TA spectrum. Figure 2.21 demonstrates the ability with a typical measured TA spectrum of a two-dimensional perovskite film, which is not included in this dissertation.
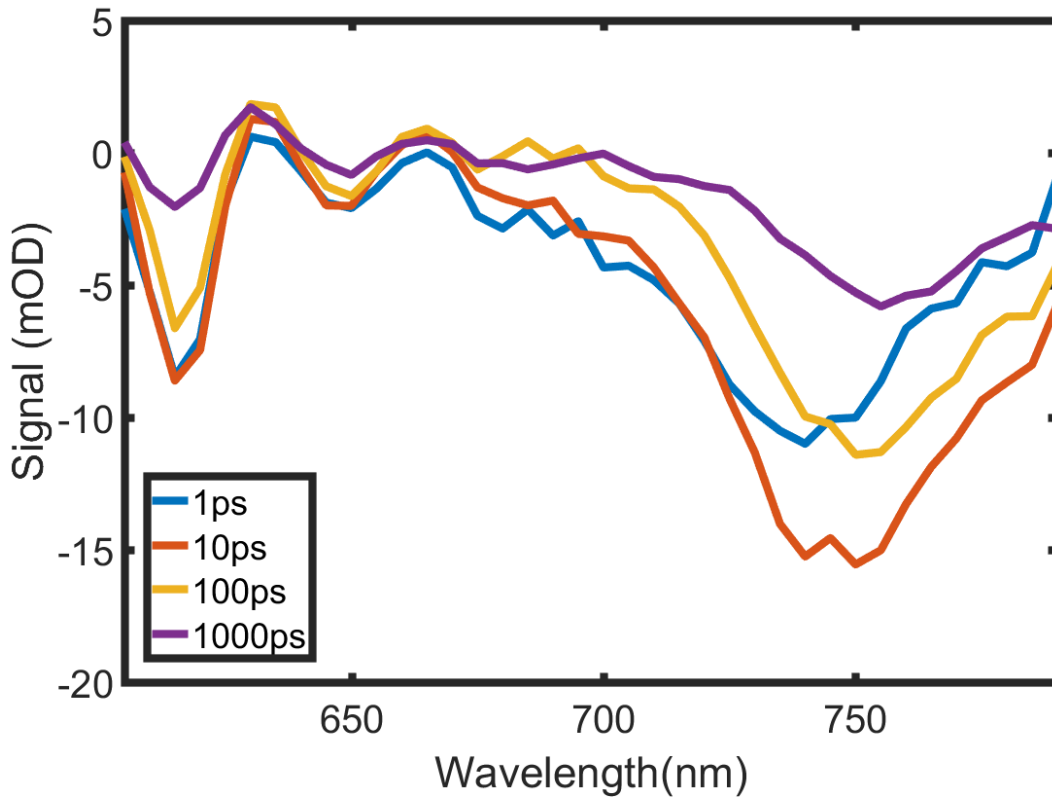
Figure 2.20. Frequency-resolved transient absorption spectrum was measured on a single spot of the two-dimensional perovskite film. The probe was scanned from 605 nm to 790 nm and resolved exciton peaks for quantum confined two-dimensional layers.

2.8. Summary

In Chapter 2, we briefly introduced basic scalar diffraction theory and DOE design strategy. We also described the techniques used to generate spectrally broad 25 fs ultrashort pulses and super-continuum white light. These pulses are used in many diffractive optic-based nonlinear spectroscopies, including transient grating, two-dimensional resonance Raman spectroscopy, femtosecond stimulated Raman spectroscopy, and multiplex excitation wide-field transient absorption microscopy with some principles in nonlinear spectroscopy.

REFERENCES

1. Guo, Z.; Molesky, B. P.; Cheshire, T. P.; Moran, A. M., Elucidation of reactive wavepackets by two-dimensional resonance Raman spectroscopy. *J. Chem. Phys.* **2015,** *143*, 124202.

2. Molesky, B. P.; Giokas, P. G.; Guo, Z.; Moran, A. M., Multidimensional resonance raman spectroscopy by six-wave mixing in the deep UV. *J. Chem. Phys.* **2014,** *141*, 114202.

3. Molesky, B. P.; Guo, Z.; Cheshire, T. P.; Moran, A. M., Two-dimensional resonance Raman spectroscopy of oxygen- and water-ligated myoglobins. *J. Chem. Phys.* **2016,** *145*, 034203.

4. Molesky, B. P.; Guo, Z.; Cheshire, T. P.; Moran, A. M., Perspective: Two-dimensional resonance Raman spectroscopy. *J. Chem. Phys.* **2016,** *145*, 180901.

5. Molesky, B. P.; Guo, Z.; Moran, A. M., Femtosecond stimulated Raman spectroscopy by six-wave mixing. *J. Chem. Phys.* **2015,** *142,* 212405.

6. Soskind, Y., *Field Guide to Diffractive Optics*. SPIE Press: Bellingham, Washington, 2011.

7. ERSOY, O. K., *Diffraction, Fourier Optics and Imaging*. John Wiley & Sons: Hoboken, New Jersey, 2007.

8. Loewen, E. G.; Popov, E., *Diffraction Gratings and Applications*. Marcel Dekker, Inc.: New York, 1997.

9. O'Shea, D. C.; Suleski, T. J.; Kathman, A. D.; Prather, D. W., *Diffractive Optics Design, Fabrication, and Test.* Spie Press: Bellingham, Washington, 2004; Vol. 62.

10. Fowles, G. R., *Introduction to Modern Optics.* Dover Publications, Inc.: New York, 1989.

11. Sheats, J. R.; Smith, B. W., *Microlithography Science and Technology*. Marcel Dekker, Inc.: New York, 1998; Vol. 162.

12. Levinson, H. J., *Principles of Lithography*. SPIE Press: Bellingham, Washington, 2010; Vol. 146.

13. Nisoli, M.; De Silvestri, S.; Svelto, O.; Szipöcs, R.; Ferencz, K.; Spielmann, C.; Sartania, S.; Krausz, F., Compression of high-energy laser pulses below 5 fs. *Opt. Lett.* **1997,** *22*, 522.

14. Kolevatova, O. A.; Naumov, A. N.; Zheltikov, A. M., Guiding high-intensity laser pulses through hollow fibers: Self-phase modulation and cross-talk of guided modes. *Opt. Commun.* **2003,** *217*, 169-177.

15. Nurhuda, M.; Suda, A.; Kaku, M.; Midorikawa, K., Optimization of hollow fiber pulse compression using pressure gradients. *Appl. Phys. B: Lasers Opt.* **2007,** *89*, 209-215.

16. Stolen, R. H.; Lin, C., Self-phase-modulation in silica optical fibers. *Phys. Rev. A* **1978,** *17*, 1448-1453.

17. Nisoli, M.; Stagira, S.; De Silvestri, S.; Svelto, O.; Sartania, S.; Cheng, Z.; Lenzner, M.; Spielmann, C.; Krausz, F., A novel-high energy pulse compression system: generation of multigigawatt sub-5-fs pulses. *Appl. Phys. B: Lasers Opt.* **1997,** *65*, 189-196.

18. Fork, R. L.; Shank, C. V.; Hirlimann, C.; Yen, R.; Tomlinson, W. J., Femtosecond white-light continuum pulses. *Opt. Lett.* **1983,** *8*, 1-3.

19. Smith, W. L.; Liu, P.; Bloembergen, N., Superbroadening in H_2O and D_2O by self-focused picosecond pulses from a YAlG:Nd laser. *Phys. Rev. A* **1977,** *15*, 2396-2403.

20. Alfano, R. R., *The Super continuum laser source.* Springer: New York, 2005.

21. Alfano, R. R.; Shapiro, S. L., Emission in the Region 4000 To 7000 Å Via Four-Photon Coupling in Glass. *Phys. Rev. Lett.* **1970,** *24*(11), 584.

22. Corkum, P. B.; Rolland, C., Femtosecond Continua Produced in Gases. *IEEE J. Quantum Electron.* **1989,** *25*, 2634-2639.

23. Corkum, P. B.; Rolland, C.; Srinivasan-Rao, T., Supercontinuum generation in gases. *Phys. Rev. Lett.* **1986,** *57* (18), 2268-2271.

24. Ilkov, F. A.; Ilkova, L. S.; Chin, S. L., Supercontinuum generation versus optical breakdown in CO_2 gas. *Opt. Lett.* **1993,** *18*, 681-683.

25. Francois, V.; Ilkov, F. A.; Chin, S. L., Supercontinuum generation in CO , gas accompanied by optical breakdown. *J. Phys. B: At., Mol. Opt. Phys.* **1992,** *25*, 2709-2724.

26. François, V.; Ilkov, F. A.; Chin, S. L., Experimental study of the supercontinuum spectral width evolution in CO_2 gas. *Opt. Commun.* **1993,** *99*, 241-246.

27. Brodeur, a.; Ilkov, F. a.; Chin, S. L., Beam filamentation and the white light continuum divergence. *Opt. Commun.* **1996,** *129*, 193-198.

28. Couairon, A.; Bergé, L., Light filaments in air for ultraviolet and infrared wavelengths. *Phys. Rev. Lett.* **2002,** *88*, 4.

29. Et Al, S. G., Self compression of millijoule pulses to 7.8fs duration in a white-light filament. *Opt. Lett.* **2006,** *31*, 274-276.

30. Aközbek, N.; Scalora, M.; Bowden, C. M.; Chin, S. L., White-light continuum generation and filamentation during the propagation of ultra-short laser pulses in air. *Opt. Commun.* **2001,** *191*, 353-362.

31. Couairon, A.; Mysyrowicz, A., Femtosecond filamentation in transparent media. *Phys. Rep.* **2007,** *441*, 47-189.

32. Feit, M. D.; Fleck, J. A., Effect of refraction on spot-size dependence of laser-induced breakdown. *Appl. Phys. Lett.* **1974,** *24*, 169-172.

33. Chekalin, S. V.; Dokukina, A. E.; Dormidonov, A. E.; Kompanets, V. O.; Smetanina, E. O.; Kandidov, V. P., Light bullets from a femtosecond filament. *J. Phys. B: At., Mol. Opt. Phys.* **2015,** *48*.

34. Mitryukovskiy, S.; Liu, Y.; Ding, P.; Houard, A.; Couairon, A.; Mysyrowicz, A., Plasma luminescence from femtosecond filaments in air: Evidence for impact excitation with circularly polarized light pulses. *Phys. Rev. Lett.* **2015,** *114*.

35. Kevrekidis, P. G.; Wang, W.; Carretero-González, R.; Frantzeskakis, D. J., Adiabatic invariant approach to transverse instability: Landau dynamics of soliton filaments. *Phys. Rev. Lett.* **2017,** *118*, 244101.

36. Tokmakoff, A., *Nonlinear Spectroscopy*. The University of Chicago, https://tdqms.uchicago.edu, 2014.

37. Mukamel, S., *Principles of Nonlinear Optical Spectroscopy.* Oxford University Press: New York, 1999.

38. Miller, R. J. D.; Paarmann, A.; Prokhorenko, V. I., Diffractive Optics Based Four-Wave, Six-Wave, ..., ν-Wave Nonlinear Spectroscopy. *Acc. Chem. Res.* **2009,** *42*, 1442.

39. Druet, S. A. J.; Taran, J. P. E., Cars spectroscopy. *Prog. Quantum Electron.* **1981,** *7*, 1-72.

40. Boyd, R. W.; Mukamel, S., Origin of spectral holes in pump-probe studies of homogeneously broadened lines. *Phys. Rev. A* **1984,** *29*, 1973-1983.

41. Yee, T. K.; Gustafson, T. K., Diagrammatic analysis of the density operator for nonlinear optical calculations: Pulsed and cw responses. *Phys. Rev. A* **1978,** *18*, 1597-1617.

42. Lepetit, L.; Chériaux, G.; Joffre, M., Linear techniques of phase measurement by femtosecond spectral interferometry for applications in spectroscopy. *J. Opt. Soc. Am. B* **1995,** *12*, 2467.

43. Gallagher, S. M.; Albrecht, A. W.; Hybl, J. D.; Landin, B. L.; Rajaram, B.; Jonas, D. M., Heterodyne detection of the complete electric field of femtosecond four-wave mixing signals. *J. Opt. Soc. Am. B* **1998,** *15*, 2338.

44. Ruckebusch, C.; Sliwa, M.; Pernot, P.; de Juan, A.; Tauler, R., Comprehensive data analysis of femtosecond transient absorption spectra: A review. *J. Photochem. Photobiol., C* **2012,** *13*, 1-27.

45. Berera, R.; van Grondelle, R.; Kennis, J. T. M., Ultrafast transient absorption spectroscopy: principles and application to photosynthetic systems. *Photosynth. Res.* **2009,** *101*, 105-118.

46. Kovalenko, S. A.; Ruthmann, J.; Ernsting, N. P., Ultrafast Stokes shift and excited-state transient absorption of coumarin 153 in solution. *Chem. Phys. Lett.* **1997,** *271*, 40-50.

47. Vos, M. H.; Lambry, J. C.; Martin, J. L.; Jones, M. R.; Hunter, C. N.; Breton, J., Coherent dynamics during the primary electron-transfer reaction in membrane-bound reaction centers of Rhodobacter sphaeroides. *Biochemistry* **1994,** *33*, 6750-6757.

48. Salcedo, J. R.; Siegman, A. E.; Dlott, D. D.; Fayer, M. D., Dynamics of energy transport in molecular crystals: The picosecond transient-grating method. *Phys. Rev. Lett.* **1978,** *41*, 131-134.

49. Phillion, D. W.; Kuizenga, D. J.; Siegman, A. E., Subnanosecond relaxation time measurements using a transient induced grating method. *Appl. Phys. Lett.* **1975,** *27*, 85-87.

50. Brown, E. J.; Zhang, Q.; Dantus, M., Femtosecond transient-grating techniques: Population and coherence dynamics involving ground and excited states. *J. Chem. Phys.* **1999,** *110*, 5772-5788.

51. Eichler, H. J.; Günter, P.; Pohl, D. W., *Laser Induced Dynamic Gratings.* Springer: Berlin, 1986; Vol 50.

52. Cowan, M. L.; Ogilvie, J. P.; Miller, R. J. D., Two-dimensional spectroscopy using diffractive optics based phased-locked photon echoes. *Chem. Phys. Lett.* **2004,** *386*, 184-189.

53. Maznev, A. A.; Nelson, K. A.; Rogers, J. A., Optical heterodyne detection of laser-induced gratings. *Opt. Lett.* **1998,** *23*, 1319.

54. Hara, T.; Hirota, N.; Terazima, M., New application of the transient grating method to a photochemical reaction: The enthalpy, reaction volume change, and partial molar volume measurements. *J. Phys. Chem.* **1996,** *100*, 10194-10200.

55. Nelson, K. A.; Casalegno, R.; Miller, R. J. D.; Fayer, M. D., Laser-induced excited state and ultrasonic wave gratings: Amplitude and phase grating contributions to diffraction. *J. Chem. Phys.* **1982,** *77*, 1144-1152.

56. Voehringer, P.; Scherer, N. F., Transient grating optical heterodyne detected impulsive stimulated Raman scattering in simple liquids. *J. Phys. Chem.* **1995,** *99*, 2684-2695.

57.   Terazima, M.; Hara, T.; Hirota, N., Reaction volume and enthalpy changes in photochemical reaction detected by the transient grating method; photodissociation of diphenylcyclopropenone. *Chem. Phys. Lett.* **1995,** *246*, 577-582.

58.   Goodno, G. D.; Dadusc, G.; Miller, R. J. D., Ultrafast heterodyne-detected transient-grating spectroscopy using diffractive optics. *J. Opt. Soc. Am. B* **1998,** *15*, 1791-1794.

59.   Cho, M., Coherent two-dimensional optical spectroscopy. *Chemical Reviews* **2008,** *108*, 1331-1418.

60.   Kubarych, K. J.; Milne, C. J.; Lin, S.; Miller, R. J. D., Diffractive optics implementation of time- and frequency-domain heterodyne-detected six-wave mixing. *Appl. Phys. B: Lasers Opt.* **2002,** *74*, 107-112.

61.   Jonas, D. M., Two-dimensional femtosecond spectroscopy. *Annu. Rev. Phys. Chem.* **2003,** *54*, 425-463.

62.   Chang, Y. J.; Cong, P.; Simon, J. D., Optical heterodyne detection of impulsive stimulated Raman scattering in liquids. *J. Phys. Chem.* **1995,** *99*, 7857-7859.

63.   de Boeij, W. P.; Pshenichnikov, M. S.; Wiersma, D. A., Short-time solvation dynamics probed by phase-locked heterodyne detected pump-probe. *Chem. Phys. Lett.* **1995,** *247*, 264-270.

64.   Scherer, N. F.; Carlson, R. J.; Matro, A.; Du, M.; Ruggiero, A. J.; Romero-Rochin, V.; Cina, J. A.; Fleming, G. R.; Rice, S. A., Fluorescence-detected wave packet interferometry: Time resolved molecular spectroscopy with sequences of femtosecond phase-locked pulses. *J. Chem. Phys.* **1991,** *95*, 1487-1511.

65.   Strauss, J.; Hundhausen, M.; Ley, L., An optical heterodyne experiment for sensitive detection of laser induced photocarrier gratings in semiconductors. *Appl. Phys. Lett.* **1996,** *69*, 875-877.

66.   Brixner, T.; Mančal, T.; Stiopkin, I. V.; Fleming, G. R., Phase-stabilized two-dimensional electronic spectroscopy. *J. Chem. Phys.* **2004,** *121*, 4221-4236.

67.   Gundogdu, K.; Stone, K. W.; Turner, D. B.; Nelson, K. A., Multidimensional coherent spectroscopy made easy. *Chem. Phys.* **2007,** *341*, 89-94.

68.   Moran, A. M.; Maddox, J. B.; Hong, J. W.; Kim, J.; Nome, R. A.; Bazan, G. C.; Mukamel, S.; Scherer, N. F., Optical coherence and theoretical study of the excitation dynamics of a highly symmetric cyclophane-linked oligophenylenevinylene dimer. *J. Chem. Phys.* **2006,** *124*.

69.   Underwood, D. F.; Blank, D. A., Ultrafast solvation dynamics: A view from the solvent's perspective using a novel resonant-pump, nonresonant-probe technique. *J. Phys. Chem. A* **2003,** *107*, 956-961.

70. Khurmi, C.; Berg, M. A., Analyzing nonexponential kinetics with multiple population-period transient spectroscopy (MUPPETS). *J. Phys. Chem. A* **2008,** *112*, 3364-3375.

71. Khurmi, C.; Berg, M. A., Differential heterodyne detection with diffractive optics for multidimensional transient-grating spectroscopy. *J. Opt. Soc. Am. B* **2009,** *26*, 2357-2362.

72. Goodno, G. D.; Astinov, V.; Dwayne Miller, R. J., Femtosecond heterodyne-detected four-wave-mixing studies of deterministic protein motions. 2. Protein response. *J. Phys. Chem. A* **1999,** *103*, 10630-10643.

73. Papagiannakis, E.; Vengris, M.; Larsen, D. S.; Stokkum, I. H. M. V.; Hiller, R. G.; Grondelle, R. V., Use of ultrafast dispersed pump-dump-probe and pump-repump-probe spectroscopies to explore the light-induced dynamics of peridinin in solution. *J. Phys. Chem. B* **2006**, 512-521.

74. Larsen, D. S.; Papagiannakis, E.; Van Stokkum, I. H. M.; Vengris, M.; Kennis, J. T. M.; Van Grondelle, R., Excited state dynamics of β-carotene explored with dispersed multi-pulse transient absorption. *Chem. Phys. Lett.* **2003,** *381*, 733-742.

75. Chen, Y. C.; Chen, Y. W.; Su, J. J.; Huang, J. Y.; Yu, I. A., Pump-probe spectroscopy of cold87Rb atoms in various polarization configurations. *Phys. Rev. A: At., Mol., Opt. Phys.* **2001,** *63*, 1-11.

76. Kubarych, K. J.; Milne, C. J.; Lin, S.; Astinov, V.; Miller, R. J. D., Diffractive optics-based six-wave mixing: Heterodyne detection of the full χ(5)tensor of liquid CS2. *J. Chem. Phys.* **2002,** *116*, 2016-2042.

77. Wende, T.; Liebel, M.; Schnedermann, C.; Pethick, R. J.; Kukura, P., Population-controlled impulsive vibrational spectroscopy: Background- and baseline-free raman spectroscopy of excited electronic states. *J. Phys. Chem. A* **2014,** *118*, 9976-9984.

78. Provencher, F.; Bérubé, N.; Parker, A. W.; Greetham, G. M.; Towrie, M.; Hellmann, C.; Côté, M.; Stingelin, N.; Silva, C.; Hayes, S. C., Direct observation of ultrafast long-range charge separation at polymer-fullerene heterojunctions. *Nat. Commun.* **2014,** *5*.

79. Oscar, B. G.; Liu, W.; Zhao, Y.; Tang, L.; Wang, Y.; Campbell, R. E.; Fang, C., Excited-state structural dynamics of a dual-emission calmodulin-green fluorescent protein sensor for calcium ion imaging. *Proc. Natl. Acad. Sci. U. S. A.* **2014,** *111*, 10191-10196.

80. Fang, C.; Frontiera, R. R.; Tran, R.; Mathies, R. A., Mapping GFP structure evolution during proton transfer with femtosecond Raman spectroscopy. *Nature* **2009,** *462*, 200-204.

81. Rhinehart, J. M.; Challa, J. R.; McCamant, D. W., Multimode charge-transfer dynamics of 4-(dimethylamino)benzonitrile probed with ultraviolet femtosecond stimulated Raman spectroscopy. *J. Phys. Chem. B* **2012,** *116*, 10522-10534.

82. Pontecorvo, E.; Ferrante, C.; Elles, C. G.; Scopigno, T., Spectrally tailored narrowband pulses for femtosecond stimulated Raman spectroscopy in the range 330-750 nm. *Opt. Express* **2013,** *21*, 6866-72.

83. Kraack, J. P.; Buckup, T.; Motzkus, M., Coherent high-frequency vibrational dynamics in the excited electronic state of all-trans retinal derivatives. *J. Phys. Chem. Lett.* **2013,** *4*, 383-387.

84. Kraack, J. P.; Wand, A.; Buckup, T.; Motzkus, M.; Ruhman, S., Mapping multidimensional excited state dynamics using pump-impulsive-vibrational-spectroscopy and pump-degenerate-four-wave-mixing. *Phys. Chem. Chem. Phys.* **2013,** *15*, 14487.

85. Yu, W.; Zhou, J.; Bragg, A. E., Exciton conformational dynamics of poly(3-hexylthiophene) (P3HT) in solution from time-resolved resonant-raman spectroscopy. *J. Phys. Chem. Lett.* **2012,** *3*, 1321-1328.

86. Weigel, A.; Dobryakov, A.; Klaumünzer, B.; Sajadi, M.; Saalfrank, P.; Ernsting, N. P., Femtosecond stimulated Raman spectroscopy of flavin after optical excitation. *J. Phys. Chem. B* **2011,** *115*, 3656-3680.

87. Frontiera, R. R.; Dasgupta, J.; Mathies, R. A., Probing interfacial electron transfer in coumarin 343 sensitized TiO_2 nanoparticles with femtosecond stimulated Raman. *J. Am. Chem. Soc.* **2009,** *131*, 15630-15632.

88. McCamant, D. W.; Kukura, P.; Mathies, R. A., Femtosecond time-resolved stimulated Raman spectroscopy: Application to the ultrafast internal conversion in β-carotene. *J. Phys. Chem. A* **2003,** *107*, 8208-8214.

89. Kukura, P.; McCamant, D. W.; Mathies, R. A., Femtosecond Stimulated Raman Spectroscopy. *Annu. Rev. Phys. Chem.* **2007,** *58*, 461-488.

90. McCamant, D. W.; Kukura, P.; Yoon, S.; Mathies, R. A., Femtosecond broadband stimulated Raman spectroscopy: Apparatus and methods. *Rev. Sci. Instrum.* **2004,** *75*, 4971-4980.

91. Mukamel, S.; Biggs, J. D., Communication: Comment on the effective temporal and spectral resolution of impulsive stimulated Raman signals. *J. Chem. Phys.* **2011,** *134*.

92. McCamant, D. W., Re-evaluation of Rhodopsin's relaxation kinetics determined from femtosecond stimulated Raman lineshapes. *J. Phys. Chem. B* **2011,** *115*, 9299-9305.

93. Dorfman, K. E.; Fingerhut, B. P.; Mukamel, S., Time-resolved broadband Raman spectroscopies: A unified six-wave-mixing representation. *J. Chem. Phys.* **2013,** *139*.

94. Guo, Z.; Wan, Y.; Yang, M.; Snaider, J.; Zhu, K.; Huang, L., Long-range hot-carrier transport in hybrid perovskites visualized by ultrafast microscopy. *Science* **2017,** *356*, 59-62.

95. Hill, A. H.; Smyser, K. E.; Kennedy, C. L.; Massaro, E. S.; Grumstrup, E. M., Screened charge carrier transport in methylammonium lead iodide perovskite thin films. *J. Phys. Chem. Lett.* **2017,** *8*, 948-953.

96. Tian, W.; Zhao, C.; Leng, J.; Cui, R.; Jin, S., Visualizing Carrier Diffusion in Individual Single-Crystal Organolead Halide Perovskite Nanowires and Nanoplates. *J. Am. Chem. Soc.* **2015,** *137*, 12458-12461.

97. Wong, C. Y.; Penwell, S. B.; Cotts, B. L.; Noriega, R.; Wu, H.; Ginsberg, N. S., Revealing exciton dynamics in a small-molecule organic semiconducting film with subdomain transient absorption microscopy. *J. Phys. Chem. C* **2013,** *117*, 22111-22122.

98. Yuan, L.; Wang, T.; Zhu, T.; Zhou, M.; Huang, L., Exciton dynamics, transport, and annihilation in atomically thin two-dimensional semiconductors. *J. Phys. Chem. Lett.* **2017,** *8*, 3371-3379.

99. Gabriel, M. M.; Grumstrup, E. M.; Kirschbrown, J. R.; Pinion, C. W.; Christesen, J. D.; Zigler, D. F.; Cating, E. E. M.; Cahoon, J. F.; Papanikolas, J. M., Imaging charge separation and carrier recombination in nanowire p-i-n junctions using ultrafast microscopy. *Nano Lett.* **2014,** *14*, 3079-3087.

100. Johns, P.; Yu, K.; Devadas, M. S.; Hartland, G. V., Role of resonances in the transmission of surface plasmon polaritons between nanostructures. *ACS Nano* **2016,** *10*, 3375-3381.

101. Jureller, J. E.; Kim, H. Y.; Scherer, N. F., Stochastic scanning multiphoton multifocal microscopy. *Opt. Express* **2006,** *14*, 3406-3414.

102. Sacconi, L.; Froner, E.; Antolini, R.; Taghizadeh, M. R.; Choudhury, A.; Pavone, F. S., Multiphoton multifocal microscopy exploiting a diffractive optical element. *Opt. Lett.* **2003,** *28*, 1918-1920.

CHAPTER 3. ELUCIDATION OF REACTIVE WAVEPACKETS BY TWO-DIMENSIONAL RESONANCE RAMAN SPECTROSCOPY[1]

3.1. Introduction

Models used to describe photoinduced electronic relaxation mechanisms in condensed phases are often based on perturbative descriptions at the level of Fermi's golden rule (e.g., Marcus equation, Forster energy transfer).[1-3] Such second-order rate theories typically assume an equilibrium initial condition in the photoexcited state of the system prior to the non-radiative transition of interest. This assumption is generally poor when applied to processes that occur on a time scale faster than solvation and/or vibrational dephasing. Recent studies show that non-trivial quantum effects may emerge when electronic and nuclear relaxation processes become time-coincident.[4] For example, in charge transfer processes that are time-coincident with vibrational dephasing, bursts of population flow have been observed in polymer-fullerene blends,[5] photosynthetic complexes,[6] and at interfaces of semiconductors.[7-8] Transient coupling between electronic and vibrational degrees of freedom has also been implicated in sub-picosecond energy transfer transitions.[9-15] The two-dimensional resonance Raman (2DRR) techniques developed in this work are motivated by new insights into these types of non-equilibrium dynamics.

In this paper, the sensitivity of 2DRR spectroscopy to coherent reaction mechanisms is demonstrated with measurements conducted on the photodissociation process of triiodide. Two-color laser pulse configurations are used to selectively detect vibrational motions of the triiodide

---

reactant and/or diiodide photoproduct in the two dimensions of the 2DRR spectrum. The unique power of the technique is ultimately realized using a pulse sequence, where vibrational resonances of triiodide and diiodide appear in separate dimensions. These "cross peaks" represent events in which a nuclear wavepacket transitions between reactant and product states without loss of coherence. Below, we explore how 2DRR spectroscopy can be used to expose non-trivial correlations between the nonequilibrium geometry of the reactant and vibrational coherence frequency of the product. Such information cannot be derived from four-wave mixing spectroscopies, which possess only one "population time" in which nuclear wavepacket motions take place.

Ultrafast spectroscopic investigations of the photodissociation process in solvated triiodide are motivated by knowledge of the extraordinary reaction mechanism in this well-defined system.[16-23] Light absorption by triiodide in the ultraviolet spectral range induces photodissociation on a time scale that is shorter than[16, 19] or comparable to[22, 24] the vibrational period of diiodide. Photodissociation of triiodide acts as an impulse that initiates vibrational coherence in the bond stretching coordinate of diiodide. Information about the geometry changes that transform the reactant to the photoproduct can be derived from oscillatory components of transient absorption signals. For example, earlier work has shown that the oscillatory amplitude reflects symmetry breaking in the excited state,[20] whereas the "chirp" in the waveform of the vibrational coherence represents time evolution of the bond strength during the reaction.[22] It has also been demonstrated that photodissociation yields distinct populations of free solvated diiodide and a contact fragment pair (diiodide and iodine).[25] Of relevance to the present 2DRR study, recent work suggests that the vibrational mode in free solvated diiodide dephases on a

time scale that is longer than the 300-fs vibrational period, whereas overdamped vibrational motion tends to take place in the contact radical pair.[24]

We recently measured 2DRR spectra of triiodide using deep UV laser pulses.[26] This approach was sensitive to ground state wavepacket motions in the triiodide molecule but did not convey detailed information about the photodissociation mechanism. Examination of this simple nonlinearity was motivated by the ability to compare experimental 2DRR spectra with those simulated using the Hamiltonian of triiodide determined in earlier spontaneous resonance Raman studies.[27-29] Together with a battery of control experiments, these simulations were essential for ruling out cascades of four-wave mixing signal fields, which are known to significantly challenge 2D Raman experiments conducted under off-resonant conditions.[30-34] We concluded that the desired 2DRR response will generally be dominant in systems with large excited state potential energy surface displacements. In effect, Franck–Condon activity obviates the selection rules that favor cascaded signal intensity under off-resonant conditions.

3.2. 2DRR Spectra Simulated for a Reactive Model System

As implemented in this work, 2DRR spectroscopy is a fifth-order technique in which vibrational coherences are detected in two delay times between laser pulses. In contrast, vibrational coherences may be investigated during only one pulse delay time in a traditional third-order pump-probe spectroscopy. The goal of the model presented in this section is to establish spectroscopic signatures corresponding to particular classes of terms in the 2DRR response function. It is important to carry out such an analysis, because the 2DRR nonlinearity is more complicated than that associated with a traditional pump-probe experiment.[1]

Vibrational motions in the ground electronic state of triiodide were detected in our earlier all-UV 2DRR experiments.[26] Here, sensitivity to the diiodide photoproduct is derived by applying laser pulses in a spectral range that is electronically off-resonant with triiodide at

equilibrium.[16-23] The patterns of 2DRR resonances associated with such two-color pulse sequences are explored with model calculations below.
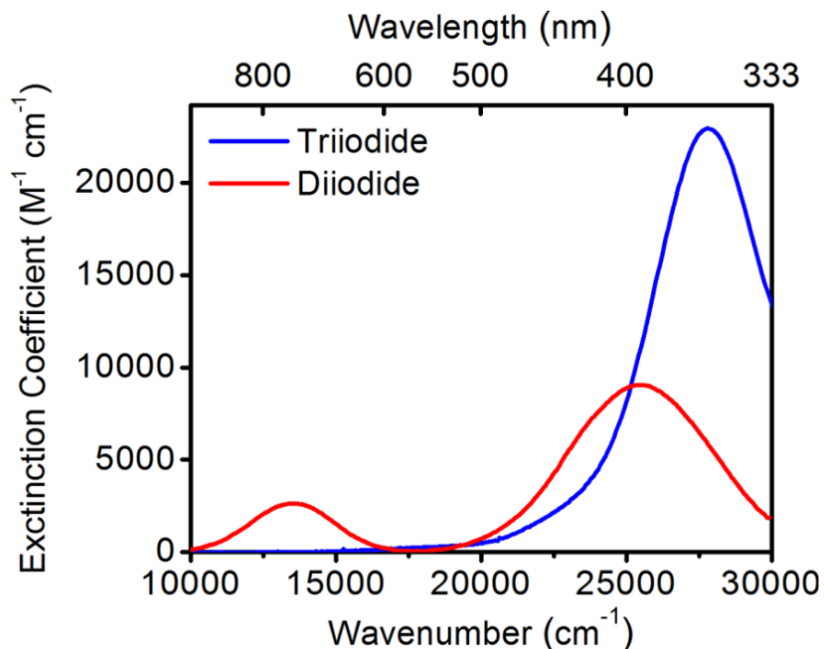
Figure 3.1. Linear absorbance spectra of triiodide and diiodide in ethanol. The absorbance spectrum of triiodide is directly measured, whereas that of diiodide is derived from Ref. 35 because it is not stable in solution. Diiodide is probed on the picosecond time scale in the present work. The electronic resonance frequencies associated with this nonequilibrium state of diiodide are likely red-shifted from those displayed above.

3.2.1. Model Hamiltonians

The electronic resonances relevant to the experiments conducted in this work are displayed in Figure 3.1. The resonance of triiodide centered near 27800 cm^{-1} is excited in all experiments. In a single experiment, either the lower- (13300 cm^{-1}) or higher-frequency (25400 cm^{-1}) electronic resonance of diiodide is probed (i.e., the 2DRR experiments presented below are two-color rather than three-color). Therefore, the nonlinear optical response associated with all measurements presented below may be simulated using a Hamiltonian in which each molecule, triiodide and diiodide, is treated as an effective two-level electronic system. Explicit inclusion of

additional off-resonant electronic states will have a negligible impact on these signals. The

effective Hamiltonian for triiodide can be written as

$$H_{triiodide} = |r\rangle\langle r|\sum_{m=0}^{\infty}|m\rangle\langle m|\big[E_r + E_m\big] + |r^*\rangle\times|r^*\rangle\langle r^*|\sum_{n=0}^{\infty}|n\rangle\langle n|\big[E_{r^*} + E_n\big],$$ (3.1)

whereas that of diiodide is given by

$$H_{diiodide} = |p\rangle\langle p|\sum_{m=0}^{\infty}|m\rangle\langle m|\big[E_p + E_m\big] + |p^*\rangle\times|p^*\rangle\langle p^*|\sum_{n=0}^{\infty}|n\rangle\langle n|\big[E_{p^*} + E_n\big]$$ (3.2)

Here, r and p represent the ground electronic states of triiodide and diiodide, whereas an

asterisk is used to denote the excited electronic state. The energies, E_r and E_{r^*} (E_p and E_{p^*}),

correspond to the ground and excited states, respectively. The dummy indices, m and n, represent

vibrational levels belonging to the ground and excited electronic states.

The transition energies of each system, $E_{r^*} - E_r$ and $E_{p^*} - E_p$, are readily derived from

the absorbance spectra presented in Figure 3.1. The two potential energy surfaces that belong to

each molecule must also be described in order to generate the vibrational energy levels, E_m and

E_n. The ground state potential energy surfaces must be modeled with a far greater level of detail

than the excited state potential energy surfaces in order for the model to generate realistic

spectroscopic signals. Insensitivity to the global excited state potential energy surfaces is taken

into account when writing the summations over quantized vibrational levels for the dissociative

excited states in $H_{triiodide}$ and $H_{diiodide}$. We next discuss the approximations made in the

descriptions of the potential energy surfaces in a qualitative way. Further technical details about

the parameterization of the potential energy surfaces are given in Section 3.8.1.

The summations over quantized levels for the ground states in $H_{triiodide}$ and $H_{diiodide}$

are clearly motivated. The previous literature can be used to guide decisions about parameters.[16,]

[19, 27] The vibrational motions of triiodide and diiodide detected in this work are known to occur in the electronic ground states, because the excited states of both systems are dissociative.[16, 19] Vibrational resonances in the ground electronic state of triiodide have been detected in both spontaneous and stimulated Raman experiments carried out with deep and near ultraviolet laser beams.[16, 27] In this work, signals will be simulated using a harmonic ground-state potential for triiodide, because only the lowest-energy vibrational states contribute to the signals. Resonance Raman experiments suggest that the harmonic approximation is indeed reasonable for these energy levels.[27] In two-color transient absorption experiments (ultraviolet pump with visible- and near-infrared probes), the relationship between the vibrational phase and detection wavelength was used to assign wavepacket motions to the electronic ground state in diiodide.[16, 19] The ground state potential energy surface of diiodide is modeled using a cubic potential in this work, because higher-energy vibrational levels (near 12 quanta) are known to contribute to the response following photodissociation.[19] Introduction of the cubic potential is required to obtain agreement between theoretical and experimental vibrational frequencies but does not impact the patterns of peaks in the 2DRR spectra.

The shapes of the excited state potentials require far less detail than those of the ground states, because the experiments presented here are sensitive only to the potential energy gradient near the Franck–Condon geometry.[36] This aspect of the response is made clear by the absence of vibronic progressions in the absorbance spectra shown in Figure 3.1. In the semiclassical perspective, this means that the wavepacket initiated on the excited state potential energy surface does not return to the Franck–Condon geometry before electronic dephasing is complete (i.e., electronic dephasing is on the order of 10-20 fs).[37] The excited state potential energy gradient near the Franck–Condon geometry primarily governs the amplitude of the wavepacket stimulated

in the ground electronic state. Here, we use the cubic fitting parameters for the London-Eyring-Polanyi-Sato (LEPS) excited state potential energy surface of triiodide in ethanol.[18, 27] Johnson and Myers used a similar displaced oscillator model for triiodide to achieve reasonable agreement with spontaneous Raman spectra.[27] The gradient of the excited state potential energy surface of diiodide at the Franck–Condon geometry is approximated by displacing a replica of the cubic ground state potential energy surface. We have chosen a set of parameters that produces a gradient which is consistent with models used in other work (see 3.8.1).[24-25]

3.2.2. Response Functions

We consider three types of 2DRR nonlinearities: (i) both dimensions correspond to the triiodide reactant; (ii) both dimensions correspond to the diiodide photoproduct; and (iii) the vibrational resonances of triiodide and diiodide appear in separate dimensions. As in Section 3.2.1., we use a notation where the indices r and r^* represent the ground- and lowest-energy excited electronic states of the triiodide reactant. Likewise, p and p^* correspond to the ground- and lowest-energy excited states of the diiodide photoproduct. Vibrational levels associated with these electronic states are specified by dummy indices (m, n, j, k, l, u, v, w). The Feynman diagrams presented in Figure 3.2 show that the vibrational coherences detected in 2DRR spectra evolve in the two time-intervals with even indices $(t_2$ and $t_4)$. Electronic (or vibrionic) coherences, which dephase in 10's of fs for solvated triiodide, evolve in the time intervals that correspond to odd indices $(t_1, t_3$, and $t_5)$. It is useful to consider that the experimentally controlled pulse delay times, τ_1 and τ_2, are good approximations to the time intervals between field-matter interactions, t_2 and t_4.

The first class of nonlinearities shown in Figure 3.2 (i.e., terms 1-4) involves vibrational motions of only the triiodide reactant.[26] In contrast to terms 1-4, the Feynman diagrams

associated with the other two classes of response functions incorporate the photodissociation process as a transfer of vibrionic coherence from triiodide to diiodide either before (terms 5-8) or after (terms 9-12) evolution of the vibrational coherence in t_2 (i.e., the delay time, τ_1). In the present model, we assume that the reaction is faster than the 300-fs period of the symmetric stretching coordinate in triiodide. This separation in time scales is consistent with the finding of vibrational coherence in diiodide (i.e., vibrational motions in the ensemble can dephase if the reaction is not impulsive). It was understood in earlier studies that photodissociation is faster than the 300-fs vibrational period.[16, 19] However, some later work suggests that the reaction takes place on nearly the same time scale as the vibrational period (i.e., a few hundred femtoseconds).[22, 24] In any case, we consider the impulsive approximation to be reasonable here, because it does not impact the pattern of peaks in the 2DRR spectra.
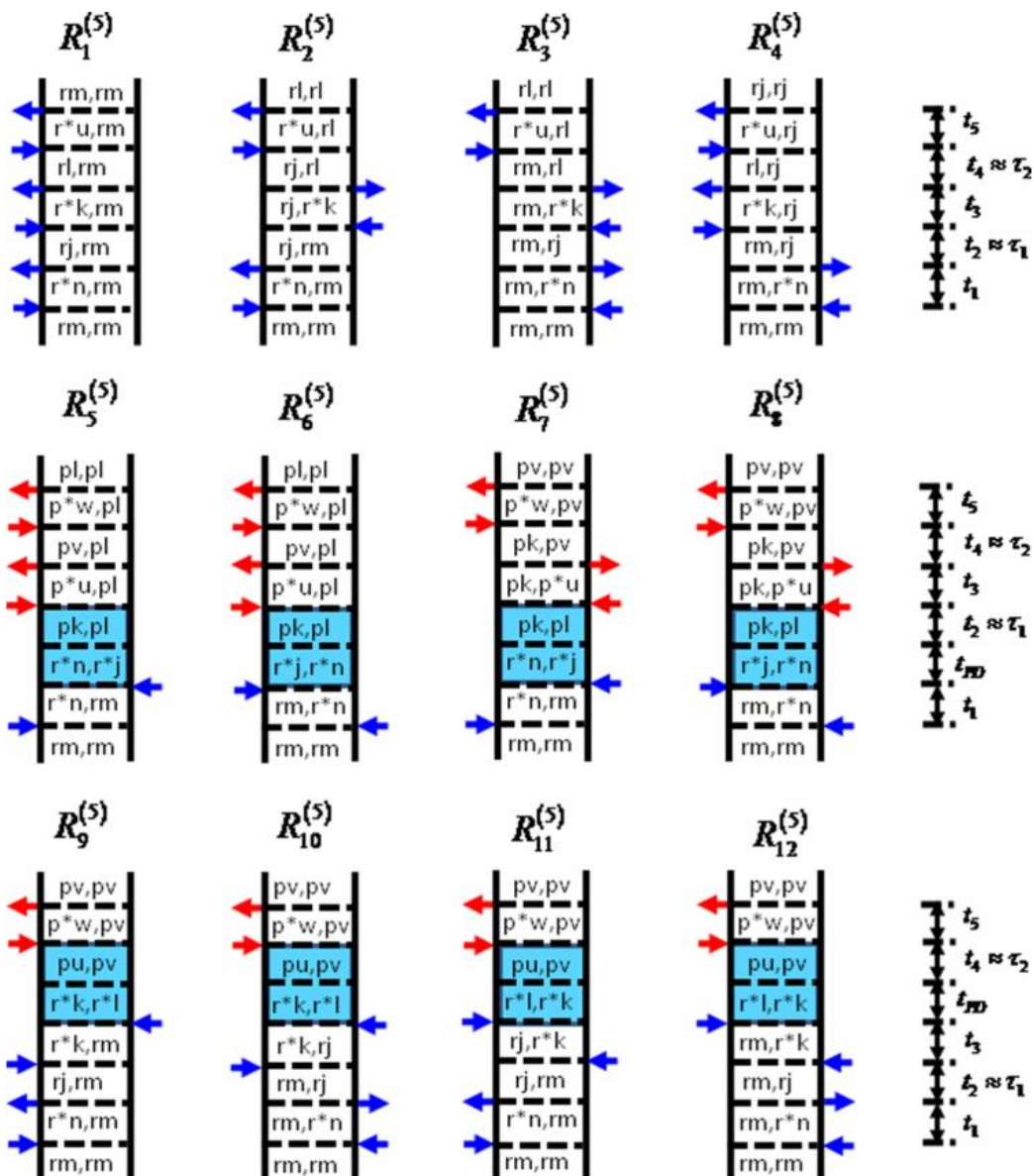
Figure 3.2. *Feynman diagrams associated with dominant 2DRR nonlinearities. Blue and red arrows represent pulses resonant with triiodide and diiodide, respectively. The indices r and r^* represent the ground and excited electronic states of the triiodide reactant, whereas p and p^* correspond to the diiodide photoproduct. Vibrational levels associated with these electronic states are specified by dummy indices (m, n, j, k, l, u, v, w). Each row represents a different class of terms: (i) both dimensions correspond to triiodide in terms 1-4; (ii) both dimensions correspond to diiodide in terms 5-8; and (iii) vibrational resonances of triiodide and diiodide appear in separate dimensions in terms 9-12. The intervals shaded in blue represent a non-radiative transfer of vibrionic coherence from triiodide to diiodide.*

As in Ref. 26, response functions are written in the "snapshot" limit, where the laser pulses are short compared to the vibrational period but long compared to electronic dephasing.[1] Both approximations are appropriate for the experiments described below. We additionally take the finite bandwidths of the laser pulses into account in the expressions for the nuclear wavepacket. Under these approximations, the polarization components consist of products of Lorentzian functions (see the supplementary material for derivation).[38] For example, the first term is given by

$$P_1^{(5)}(\omega_1, \omega_2) = -\frac{N\xi_{UV}^5 |\mu_{r^*r}|^6}{\hbar^5} \sum_{mnjklu} B_m \langle n|m \rangle \langle n|j \rangle \langle k|j \rangle \langle k|l \rangle \langle u|l \rangle \langle u|m \rangle$$
$$\times L_{r^*n,rm}(\omega_{UV}) D_{rj,rm}(\omega_1) L_{r^*k,rm}(\omega_{UV}) D_{rl,rm}(\omega_2) L_{r^*u,rm}(\omega_t)$$

, (3.3)

where

$$L_{r^*n,rm}(\omega) = \frac{1}{\omega - \omega_{r^*r} - \omega_{nm} + i\Gamma_{r^*r}},$$

(3.4)

and

$$D_{rk,rm}(\omega) = \frac{2\Gamma_{vib} + 4\Lambda_{UV}}{\omega_{km}^2 + (\Gamma_{vib} + 2\Lambda_{UV})^2} \left(\frac{1}{\omega - \omega_{km} + i\Gamma_{vib}} \right).$$

(3.5)

Here, $\langle n|m \rangle$ is a vibrational overlap integral, where the index on the left represents the vibrational level of the excited electronic state (i.e., the same notation is used in Ref. 39). The subscript of the electric field, UV, denotes an interaction with the lowest-energy electronic resonance of triiodide (VIS denotes an interaction with either electronic resonances of diiodide). The remaining 11 response functions are given in 3.8.2.

The parameters given in Table 3.1 are chosen to approximate the properties of triiodide and diiodide. The electronic and vibrational resonance frequencies of both systems have been

determined in earlier studies.[16-23, 26] We take the potential energy surface of the ground state of triiodide to be harmonic in agreement with spontaneous resonance Raman experiments.[27] The excited state potential energy surface of triiodide and both the ground and excited state potential energy surfaces of diiodide are expanded to the cubic term.[26] Cubic expansion coefficient of -1 cm^{-1} (see Equation 3.8) approximate the LEPS surface of triiodide[17] and capture the 100-cm^{-1} gap between successive energy levels in diiodide near 20 vibrational quanta.[19] Evaluation of the vibrational overlap integrals in the response function is accomplished by assuming a dimensionless displacement of 7.0 for both triiodide and diiodide. This value of the displacement is consistent with spontaneous Raman measurements[27] and our previous 2DRR study of triiodide.[26] A displacement of 7.0 also produces an excited state potential energy gradient in diiodide (225 eV/pm) that is identical to that associated with a commonly employed exponential surface at a displacement of only 9 pm from the Franck–Condon geometry.[24-25] As discussed in Section 3.2.1, this gradient is the key quantity that must be reproduced by the present model, because electronic dephasing is fast compared to the vibrational period.

Table 3.1. *Parameters of Model Used to Compute 2DRR Spectra*

[a]Parameter	Value
$\omega_{r^*r} / 2\pi c$	27,800 cm^{-1}
[b] $\omega_{p^*p} / 2\pi c$	13,300 cm^{-1} & 25,400 cm^{-1}
[c] $\omega_{r,vib} / 2\pi c = \omega_{r^*,vib} / 2\pi c$	111 cm^{-1}
[c] $\omega_{p,vib} / 2\pi c = \omega_{p^*,vib} / 2\pi c$	114 cm^{-1}
[c] $U_{3,r} / hc$	0 cm^{-1}
[c] $U_{3,r^*} / hc = U_{3,p} / hc = U_{3,p^*} / hc$	-1 cm^{-1}
$\Gamma_{r,vib} / c = \Gamma_{r^*,vib} / c = \Gamma_{p,vib} / c = \Gamma_{p^*,vib} / c$	10 cm^{-1}
$\Gamma_{r^*r} / c = \Gamma_{p^*p} / c$	2000 cm^{-1}
[d] μ_{r^*r}	2.3 D
[d] μ_{p^*p}	1.0 D
[e] $\omega_{UV} / 2\pi c$	29,400 & 25,000 cm^{-1}
[f] $\omega_{VIS} / 2\pi c$	14,705 & 18,900 cm^{-1}
$\omega_t / 2\pi c$	$\omega_{VIS} / 2\pi c$
$\Lambda_{UV} / c = \Lambda_{VIS} / c$	500 cm^{-1}

[a] The indices r and p represent triiodide and diiodide, respectively. Asterisks indicate the lowest-energy excited electronic states of the molecules.
[b] The electronic resonance of diiodide that is probed depends on the particular experiment (see Section 3). In terms 1-4 and 9-12, the resonance is located at 25400 cm^{-1}, whereas in terms 5-8 it is equal to 13300 cm^{-1}.
[c] Parameters of Equation 3.7.
[d] Magnitudes of transition dipoles do not impact line shapes of simulated 2DRR spectra.
[e] In Figure 3.3, "pump" wavenumbers are: 25000 cm^{-1} for terms 1-4; 29400 cm^{-1} for terms 5-8; 25000 cm^{-1} for terms 9-12.
[f] In Figure 3.3, "probe" wavenumbers are 14705 cm^{-1} in terms 5-8 and 20000 cm^{-1} in terms 9-12, respectively.

3.2.3. Calculated 2DRR Spectra

Figure 3.3 presents signals that are simulated for the three types of nonlinearities. Terms 1-4 yield resonances in only the upper right and lower left quadrants of Figure 3.3(a) because of interferences between components of the response function.[26] For terms 5-8 in Figure 3.3(b),

suppression of signal intensity in the upper left and lower right quadrants originates in the same types of interferences found in terms 1-4. In terms 1-8, evolution of the system in the time intervals, t_2 and t_4, is always described by a pair of coherences in which only one of the vibrational indices is modified by the third and fourth field-matter interactions (e.g., $r\,j$ in terms 2 and 4 or pl in terms 5 and 6). In contrast, calculations based on terms 9-12 yield peaks with equal intensities in all four quadrants in Figure 3.3(c). *The unique pattern of resonances found in terms 9-12 reflects independence of the vibrational coherences that evolve during t_2 and t_4.* The key issue is that the photo-dissociation process takes place between t_2 and t_4 time intervals in terms 9-12 (see Figure 3.2). Therefore, the vibrational coherence in the time interval t_4 involves a set of indices that is fully independent from those in t_2. In contrast, photodissociation occurs before vibrational coherences evolve in t_2 in terms 5-8 thereby placing constraints on the vibrational coherences that evolve in t_2 and t_4.

In summary, the model calculations presented in this section demonstrate that cross peaks between triiodide and diiodide appear in all four quadrants of the 2DRR spectrum. These 2DRR cross peaks may be induced with a pulse configuration in which UV pulses are employed before the τ_2 delay time, and a visible pulse is applied afterwards (see terms 9-12). This particular signature of cross peaks will generalize to other systems in which vibrational coherences of the reactant and product evolve in the ground electronic states. For such systems, only cross peaks between the reactant and product will yield resonances in the upper left and lower right quadrants. The key issue is that the third and fourth field-matter interactions must take place with either the ket or bra in terms 1-8, thereby allowing a difference in only one of the indices that describes the coherences in τ_1 and τ_2 (see Figure 3.2).
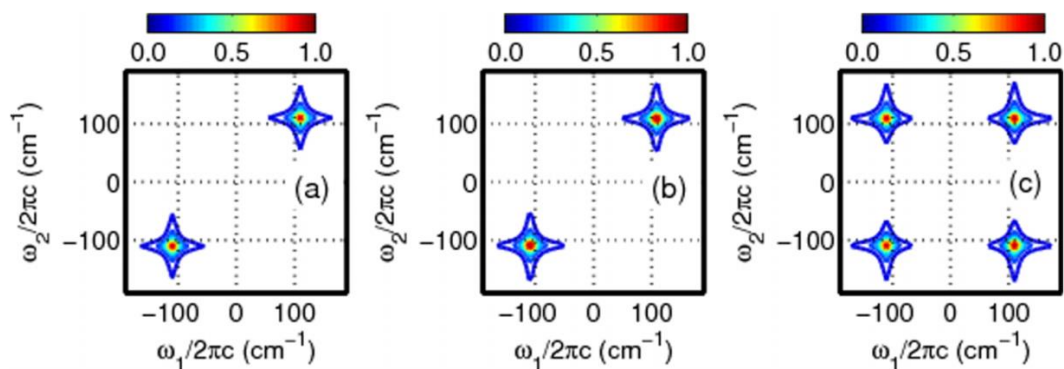
Figure 3.3. *Absolute values of 2DRR spectra computed using (a) the sum of terms 1-4 in Equation 3.22. (b) the sum of terms 5-8 in Equation 3.23 and (c) the sum of terms 9-12 in Equation 3.24. The frequency dimensions, ω_1 and ω_2, are conjugate to the delay times, τ_1 and τ_2 (see Figure 3.2). Signal components of the type shown in panel (a) are generally detected in one-color experiments. Two-color 2DRR approaches are used to detect nonlinearities that correspond to panels (b) and (c) in this work. The peaks displayed in (c) are unique in that resonances of the reactant and product are found in ω_1 and ω_2, respectively.*

3.3. Experimental Methods

The 2DRR experiments conducted in this work utilize either five or three laser beams to obtain the fifth-order response. Measurements conducted in these geometries must contend with a background of residual laser light and/or lower-order nonlinearities, because fewer than six laser beams are employed.[26] In this section, we describe the two experimental setups and discuss how sources of background are dealt with.

3.3.1. Conducting 2DRR Spectroscopy with a Five-Beam Geometry

Detection of signal components described by terms 5-8 in Figure 3.2 is accomplished with a geometry of five laser beams. In Figure 3.4, it is shown that a 340-nm laser beam is simply added to an existing diffractive optic-based transient grating setup operational at 680 nm.[40] A slightly modified version of this interferometer has been described elsewhere.[41-42] Briefly, the 680-nm beams are focused on the diffractive optic with a 20-cm focal length spherical mirror and cross at 5.4º. The angle between the +1 and −1 diffraction orders is also 5.4º. Thus, a square pattern of 680-nm beams appears on the 20-cm focal length spherical mirror.

The spherical mirror is tilted off-axis by approximately 5° (i.e., the minimum amount) in order to image the spot from the diffractive optic onto the sample. Focusing conditions of the 340-nm beam are optimized to match the 200-µm FWHM spot sizes of the 680-nm beams.
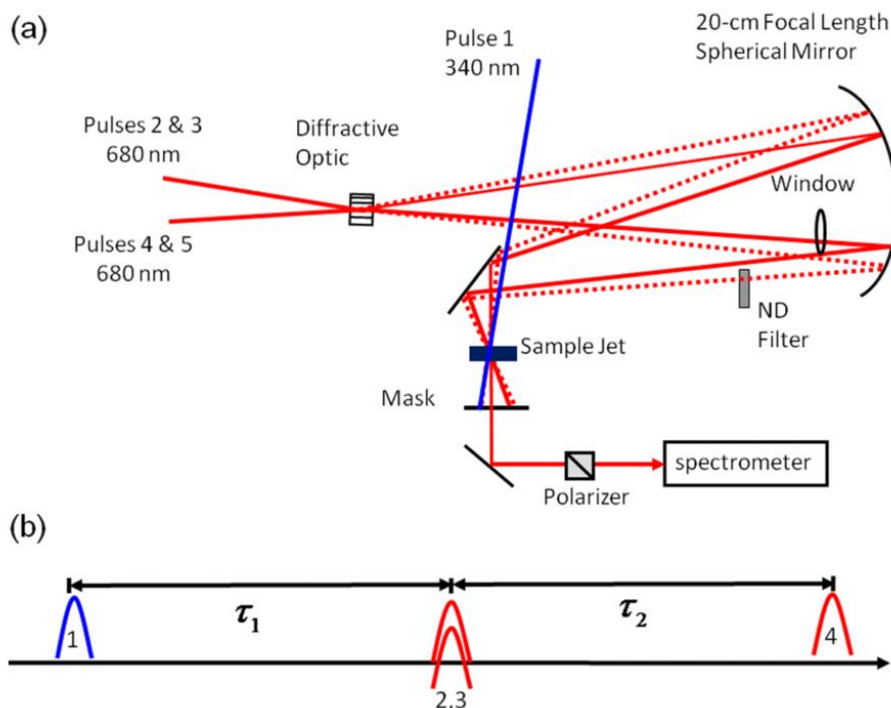
Figure 3.4. *(a) Diffractive optic-based interferometer used to detect signal components described by terms 5-8 in Figure 3.2. Each of the two 680-nm beams is split into −1 and +1 diffraction orders with equal intensities at the diffractive optic. The signal is collinear with the reference field (pulse 5) used for interferometric signal detection. (b) The 340-nm pulse induces photodissociation and vibrational coherence in the diiodide photoproduct during the delay, τ_1. The time-coincident 680-nm pulses, 2 and 3, reinitiate the vibrational coherence in diiodide during the delay, τ_2.*

The 340-nm and 680-nm laser beams are produced by focusing a 0.8-mJ, 60-fs laser beam at 800 nm into a 43-cm long hollow core fiber with a 250-µm inner diameter. The continuum produced in the fiber spans the full visible spectral range. A 4-µJ, 40-nm wide portion of the continuum centered at 680 nm is filtered in a fused silica prism compressor. Most of the 680-nm beam (65%) is used to generate 340-nm light in a 100-µm thick, Type I Beta Barium Borate (BBO) crystal. In order to minimize lossy reflections, the 340-nm beam is directly imaged

from the BBO onto the sample using a 15-cm focal length spherical mirror placed 30-cm from the BBO. Residual 680-nm light is filtered using a 1-mm thick fused silica polarizer. A lossy second compression step is not required for the 340-nm beam because of pre-compensation for dispersion in the aforementioned prism compressor; the polarizer used to filter residual 680-nm light compensates for negative chirp in the 340-nm pulse.

In this pulse sequence, the 40-fs, 340-nm pulse (pulse 1 in Figure 3.4) induces a photodissociation process that leaves the diiodide photoproduct in a vibrational coherence as suggested by terms 5-8 in Figure 3.2. A time-coincident pair of 25-fs, 680-nm laser pulses (pulses 2 and 3 in Figure 3.4) reinitiates the vibrational coherence in diiodide during the delay, τ_2. The fourth pulse (also at 680 nm) induces signal emission. The fifth pulse, which is attenuated by a factor of 1000 before the sample, is used for heterodyne detection by spectral interferometry.[43-44] The signal phase can be determined using the method devised by Turner and Scholes in this beam geometry,[45] because the 340-nm pulse does not factor into the phase calibration. Scherer and Blank have employed similar laser beam geometries and phasing schemes in related fifth-order experiments.[46-48]

An undesired four-wave mixing response may be radiated by the solvent in the same direction as the fifth-order signal in this geometry. However, because the sample is transparent at 680 nm, this four-wave mixing signal is approximately 50 times smaller than that associated with the solute at delay times greater than 80 fs. Moreover, the desired signal radiated by the solute exhibits a vibrational coherence with a period of 300 fs. Insensitivity of this setup to intramolecular vibrations of the solvent was confirmed by scanning the delay, τ_2, with the 340 nm beam blocked. Thus, the assignment of the experimentally observed 112-cm^{-1} vibrational resonance to the solute is unambiguous.[26] The 2DRR experiment may be conducted without

chopping the 340-nm beam, because the desired fifth-order nonlinearity dominates the total response of the solution. Conducting the experiment without chopping the 340-nm beam greatly speeds up data acquisition and facilitates signal averaging.

Signals are detected using a back-illuminated CCD array (Princeton Instruments PIXIS 100B) mounted on a 0.3 m spectrograph with a 600 g/mm grating. The signal generates roughly 80 counts/ms on the detector with 150-nJ, 340-nm pulses and 200-nJ, 680-nm pulses. All beams possess the same electric field polarization and are focused to 200 µm at the sample position. The two delay lines are scanned 20 times and averaged. The step sizes are 40 fs in both dimensions.

3.3.2. Conducting 2DRR Spectroscopy with a Three-Beam Geometry

Signal components of the type described by terms 9-12 are detected using a three-pulse geometry (i.e., a standard pump-repump-probe experiment).[49] As shown in Figure 3.5, the first two pulses that arrive at the sample are 25-fs, 400-nm pulses produced by self-phase modulation in a hollow core fiber,[50] whereas the third pulse is a visible continuum produced in a 3-mm thick sapphire plate. The 400-nm beams are focused onto the sample with a 30-cm focal length spherical mirror, whereas the continuum is relayed from the sapphire plate onto the sample using a single 5-cm focal length mirror (the continuum focuses 35 cm from the spherical mirror). The FWHM spot sizes of the 400-nm beams are 600 µm, whereas those of the continuum are 400 µm. Angles between the adjacent beams are 5°. Pulse energies of the 400-nm beams range from 150 to 300 nJ in various experiments, and we observe no differences in the vibrational line shapes obtained within this range of pulse energies. The phases of the two chopper wheels, which are both operated at 250 Hz, are shifted by 90° to acquire signals under the four conditions needed to produce a pump-repump-probe signal ($\Delta\Delta A$).[49] Signal detection is accomplished with a CMOS array detector that is synchronized to the 1-kHz repetition rate of the laser system. The

noise level of a pump-repump-probe signal is approximately 0.1 mOD in this setup. The delay

lines are scanned 10 times with step sizes of 40 fs and averaged.
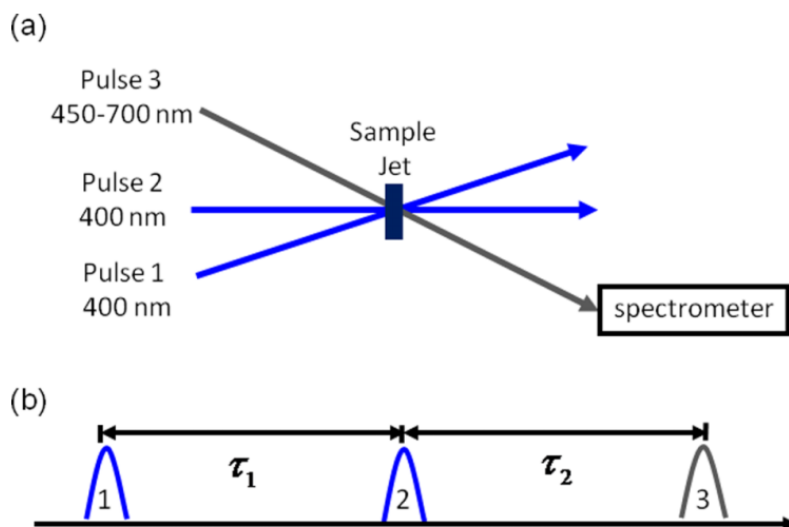
Figure 3.5. *(a) Pump-repump-probe beam geometry used to detect signal components described by terms 9-12 in Figure 3.2. (b) The first 400-nm pulse promotes a stimulated Raman response in the ground electronic state of the triiodide reactant during the delay, τ_1. The second pulse induces photodissociation of the non-equilibrium reactant, thereby giving rise to vibrational coherence in the diiodide photoproduct during the delay, τ_2. Sensitivity to diiodide is enhanced by signal detection in the visible spectral range.*

Two field-matter interactions with triiodide occur with each of the 400-nm pump pulses

in this experiment. The first pulse stimulates wavepacket motion in the ground electronic state of

triiodide as indicated in terms 9-12. The application of a second 400-nm pulse ensures that the

signals are primarily sensitive to vibrational coherences of triiodide during τ_1 (i.e., signal

contributions from diiodide are negligible during τ_1). The key issue is that the transient

electronic resonance of triiodide is dominant at 400 nm (i.e., the bleach of the ground state). The

second 400-nm pulse induces photodissociation of triiodide and leaves the diiodide photoproduct

in a vibrational coherence in τ_2. Signal detection in the visible spectral range enhances

sensitivity to the diiodide product in the delay, τ_2.

3.3.3. Sample Preparation and Handling

Triiodide solutions are prepared by mixing solid I_2 (Aldrich) with 5-fold molar excess of KI (Aldrich) in ethanol (Decon Labs, 200 proof). The solutions are stirred for 1 h to fully dissolve the solid. The absorbance of the solutions is equal to 0.5 at 400 nm in a 300-µm path length. The sample is flowed through a wire-guided jet with a thickness of 300 µm, where the volume of the reservoir is 50 ml.

3.4. Experimental Results

In this section, we present 2DRR signals obtained for triiodide using two-color pulse sequences. We begin by reviewing properties of the third-order pump-probe response to facilitate the subsequent discussion of 2DRR spectra.

3.4.1. Third-Order Stimulated Raman Response

The pump-probe signals shown in Figure 3.6 illustrate several aspects of the stimulated Raman response of triiodide. Vibrational coherences are observed throughout the visible spectral range as in earlier work on this system.[16-23] The modulation depth of the oscillations is greatest in the range, 18000-21000 cm^{-1} (475-555 nm). Coherences at detection wavenumbers below 20000 cm^{-1} (500 nm) are dominated by diiodide, whereas signals acquired at detection wavenumbers above 20000 cm^{-1} possess significant contributions from ground state wavepacket motions of triiodide. The vibrational coherences detected below 20 000 cm^{-1} are similarly assigned to the ground electronic state of diiodide, because the excited state potential energy surface is dissociative.[51]
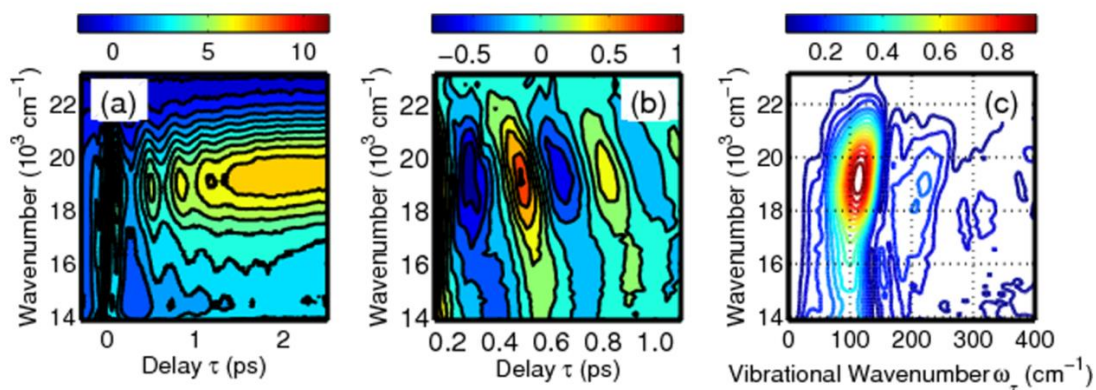
Figure 3.6. (a) Transient absorption signals (in mOD) obtained for triiodide with a 400-nm pump pulse and continuum probe pulse. (b) The coherent component of the signal is isolated by subtracting sums of 2 exponentials from the total signal presented in panel (a). (c) Fourier transformation of the signal between delay times of 0.1 and 2.5 ps shows that the vibrational frequency decreases as the detection wavenumber decreases. Dispersion in the vibrational frequency reflects sensitivity to high-energy quantum states in the anharmonic potential of diiodide.[19]

The photodissociation process is known to cause the period of vibrational motion to evolve as the delay increases.[22] In Figure 3.6(b), such "chirped" wavepacket dynamics are evidenced by time evolution in the orientations of the nodal contour lines of the signal. It has been established that the strength of the chemical bond weakens as the symmetry of triiodide breaks immediately following light absorption.[16-23] The reactive wavepacket departs from the Franck–Condon geometry as one of the bonds ruptures, thereby giving rise to the time dependence of the vibrational frequency observed in Figure 3.6(b). The dependence of the vibrational period on the detection wavenumber reflects sensitivity to highly excited states in the anharmonic potential of the diiodide product. Kühne and Vöhringer determined that experiments with visible probe pulses are sensitive to states with 10-30 vibrational quanta.[19]

3.4.2. 2DRR Response of The Diiodide Photoproduct

The 2DRR response of the diiodide photoproduct is detected using the two-color approach described in Figure 3.4. The signals shown in Figure 3.7 are Fourier transformed to

reveal peaks in the upper right and lower left quadrants of the 2DRR spectrum. The resonances appear near 100 cm^{-1} in both dimensions, which indicates that the experiment is sensitive to states of diiodide that possess roughly 20 vibrational quanta.[19] Vibrational resonances are not detected in the other two quadrants of the 2DRR spectrum as in our earlier study of ground state wavepacket motions in triiodide.[26] The locations of the peaks in the experimental 2DRR spectrum agree with the prediction made for terms 5-8 in Figure 3.3 (i.e., the terms this pulse sequence is designed to detect).
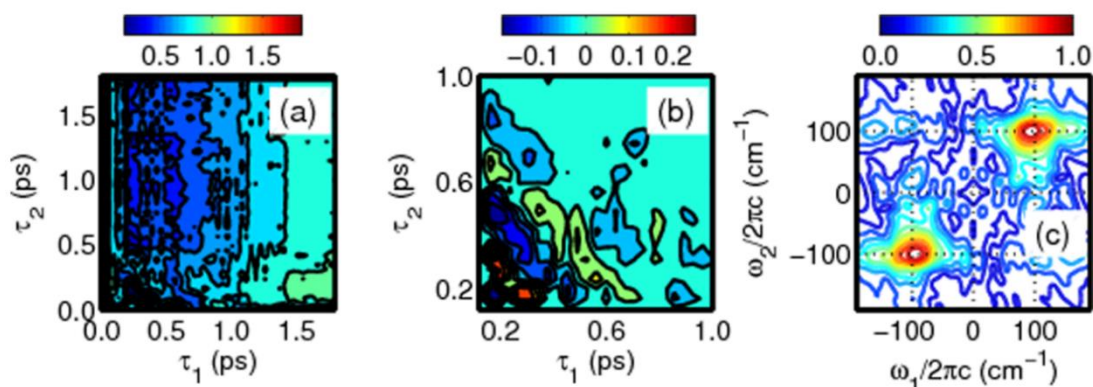
Figure 3.7. *2DRR signals associated with terms 5-8 are obtained using the two-color approach described in Figure 3.4. (a) The total signal possesses both coherent and incoherent components. (b) The coherent (Raman) component of the signal is isolated by subtracting sums of two exponentials from the total signal presented in panel (a). (c) The two-dimensional Fourier transformation of the signal in panel (b) reveals resonances in the upper right and lower left quadrants. This pattern of 2DRR resonances is consistent with calculations based on terms 5-8 (see Figure 3.3), which this experiment is designed to detect.*

The data shown in Figure 3.7(b) indicate that the vibrational dephasing rate is slightly faster in τ_1 than it is in τ_2 (i.e., the line width is slightly larger in ω_1 than it is in ω_2). We attribute this difference in line widths to intramolecular relaxation and inertial solvation processes that occur following photodissociation in τ_1. The photoproduct is likely far from equilibrium when the vibration fully damps near 2 ps; however, a significant amount of solute-to-solvent vibrational energy transfer may still take place on this time scale.[17] This view of the information

carried by each dimension of the 2DRR signals consistent with interpretations of related optical pump/Raman probe experiments.[46-48, 52-54] That is, the relaxation processes detected in the first delay time, τ_1, are related to those investigated with traditional pump-probe experiments (e.g., vibrational cooling).[16-23]16–23 Scanning the second delay time, τ_2, essentially yields a snapshot of the vibrational spectrum as the system relaxes in τ_1.[18]

3.4.3. 2DRR Cross Peaks Between Triiodide and Diiodide

The 2DRR spectra theoretically predicted in Figure 3.3 are consistent with the experimental measurements shown in Figure 3.7 (terms 5-8) and our earlier all-UV 2DRR spectra (terms 1-4).[26] In both cases, peaks are found in only the upper right and lower left quadrants because of interferences between numerous terms in the response function. In this section, we test the prediction that signal components corresponding to terms 9-12 will give rise to resonances in all four quadrants of the 2DRR spectrum (see Figure 3.3(c)). This unique pattern of resonances signifies a process in which a vibrational wavepacket transitions between reactant and product states without loss of coherence.

The 2DRR data presented in Figure 3.8 are obtained using the experimental setup described in Figure 3.5. The pump-repump-probe signals exhibit oscillations in both dimensions, which may be Fourier transformed to produce 2DRR spectra. Signals acquired at several detection wavenumbers are displayed to illustrate a transition between regimes in which motions of triiodide or diiodide dominate the second dimension, ω_2. At a detection wavenumber of 22500 cm^{-1} (444 nm), where absorption of triiodide is dominant, the pattern of resonances is consistent with terms 1-4 (see Figure 3.3(a)). However, intensities of the vibrational resonances in the upper left and lower right quadrants of the 2DRR spectrum increase as the detection wavenumber is detuned from the absorption spectrum of triiodide. At detection wavenumbers

less than 19500 cm-1 (513 nm), we observe peaks with equal intensities in all four quadrants, which is consistent with the prediction made for terms 9-12 in Figure 3.3(c).
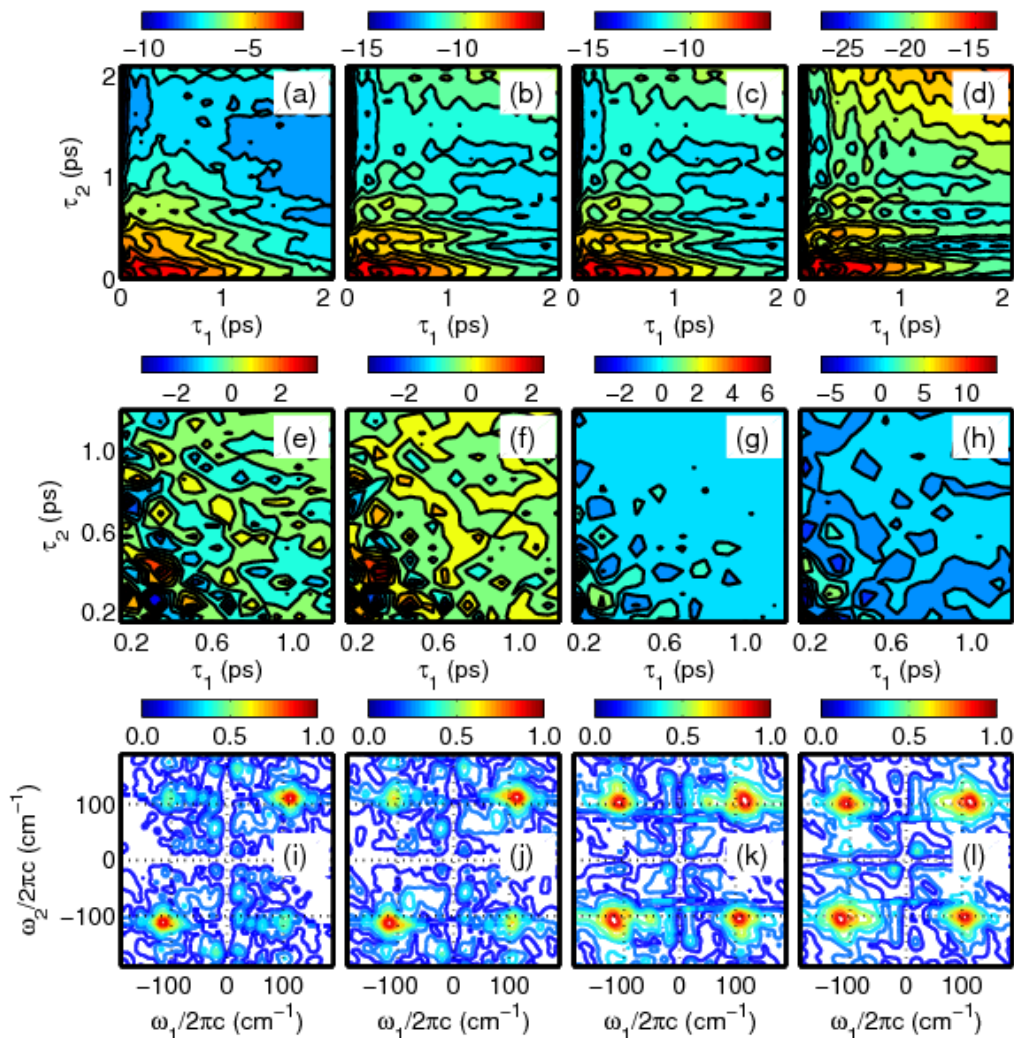
Figure 3.8. *2DRR data are obtained using the two-color approach described in Figure 3.5. Each column corresponds to a different detection wavenumber: 22500 cm^{-1} (444 nm) in column 1; 21000 cm^{-1} (476 nm) in column 2; 19500 cm^{-1} (513 nm) in column 3; 18000 cm^{-1} (555 nm) in column 4. (a)-(d) Total pump-repump-probe signal in mOD. (e)-(h) Coherent parts of the pump-repump-probe signals displayed in the first row. (i)-(l) 2DRR spectra are generated by Fourier transforming the signals shown in the second row in delay ranges, τ_1 and τ_2, between 0.15 and 2.0 ps. The data show that peaks in the upper left and lower right quadrants emerge as the detection wavenumber becomes off-resonant with triiodide. Signals acquired at detection wavenumbers above 21,000 cm^{-1} (476 nm) are dominated by stimulated Raman processes in the ground electronic state of triiodide (terms 1-4). In contrast, signals acquired at detection wavenumbers below 19,500 cm^{-1} (513 nm) are consistent with terms 9-12, where vibrational resonances in ω_1 and ω_2 correspond to triiodide and diiodide, respectively.*

The detection of peaks with equal intensities in all four quadrants is consistent with nonlinearities of the type shown in terms 9-12. The peak positions are also consistent with this assignment. The 112-cm^{-1} vibrational resonance in   is notably independent of the detection wavenumber (as it should be for the reactant). In contrast, the frequency of the vibrational resonance in   decreases as the detection wavenumber decreases. For example, we observe resonances in   at 110 cm-1 and 100 cm-1 for detection wavenumbers of 22500 cm^{-1} (444 nm) and 18000 cm^{-1} (555 nm), respectively. As discussed in Section 3.4.1, correlation between the vibrational frequency and detection wavenumber is a signature that diiodide contributes to the signal (i.e., the origin of the response transitions from terms 1-4 to terms 9-12 as the detection frequency decreases).[51] At present, 2DRR spectra cannot be measured at detection wavenumbers below 18,000 cm^{-1} (555 nm) in this setup, because of the substantial background that must be removed by chopping the pump and repump laser beams. Nonetheless, the transition between the two aforementioned regimes (i.e., terms 1-4 versus terms 9-12) is made sufficiently clear in the range of detection frequencies where adequate signal strength is obtained.

Cascades of four-wave mixing signal fields challenge the application of 2D Raman spectroscopy under off-resonant conditions. Cascades were ruled out in our previous all-UV 2DRR study of triiodide using control experiments based on the signal phase, concentration dependence of the signal intensity, and the relative phases of the vibrations detected in four and six-wave mixing signals.[26] The direct 2DRR response should be even more dominant in the present study, because lower-frequency laser beams are employed. Moreover, the direct response is favored in the present experiments for the same reasons discussed at length in Reference 26. In the Supplementary Material, we demonstrate that the sign of the 2DRR response is consistent with the direct fifth-order nonlinearity rather than a cascade.[38]

3.4.4. Summary of 2DRR Signal Components

In this section, we summarize our attainment of 2DRR spectra associated with the three types of signal components d. Figure 3.9 displays the present results alongside the 2DRR spectrum for ground state wavepacket motions of triiodide obtained in earlier work.[26] As shown in Figure 3.9(a), the application of all-UV pulses yields a 2DRR spectrum in which the vibrational resonances of triiodide appear in both dimensions (i.e., terms 1-4 in Figure 3.2). Similarly, vibrational motions of diiodide dominate both dimensions in Figure 3.9(b), because only the first pulse is resonant with equilibrium triiodide (i.e., terms 5-8 in Figure 3.2). Finally, vibrational motions of triiodide and diiodide are detected in separate dimensions in Figure 3.9(c). Here, only the final pulse to arrive at the sample is electronically off-resonant with triiodide (i.e., terms 9-12 in Figure 3.2). This type of nonlinearity is unique in that it gives rise to 2DRR spectra in which peaks with equal intensities appear in all four quadrants. The terms in the response function responsible for these peaks reflect a sequence in which a wavepacket in the symmetric stretching coordinate of triiodide transforms into a wavepacket in the bond stretching mode of diiodide without loss of coherence. 2DRR spectroscopy is specially equipped for investigations of such coherent dynamics, because it possesses two electronic "population times". In contrast, traditional third-order pump-probe experiments only have one population time.
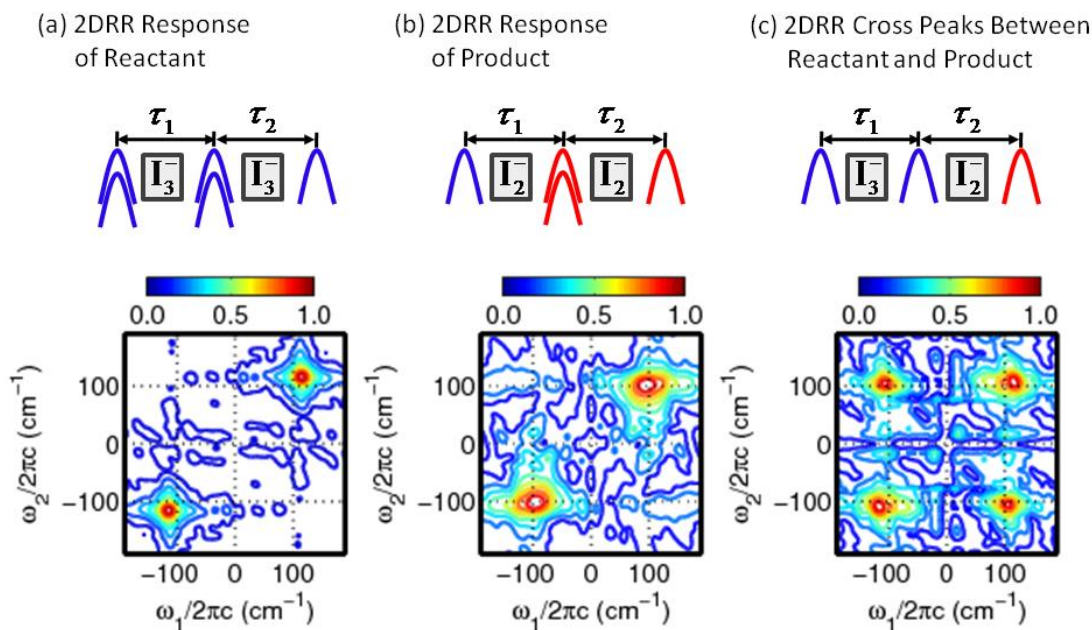
Figure 3.9. *Summary of 2DRR experiments conducted on triiodide: (a) the response of triiodide was detected in both dimensions in Reference 26; (b) the response of the diiodide photoproduct is detected in both dimensions (see Figure 3.7); (c) the response of triiodide and diiodide are detected in separate dimensions (see Figure 3.8). Blue and red laser pulses represent wavelengths that are electronically resonant with triiodide and diiodide, respectively.*

The signature of cross peaks demonstrated in Figure 3.9 will not necessarily generalize to all systems. In the photodissociation process of triiodide, the key is that the wavepacket motions take place on the ground state potential energy surfaces of both the reactant and product. For signal components associated with terms 1-8, this means that both the third and fourth field-matter interactions occur with either the ket or bra (see Figure 3.2). In contrast, the constraints that suppress intensity in the upper left and lower right quadrants in Figures 3.9(a) and 3.9(b) may be lifted in systems with bound excited states, thereby yielding peaks in all four quadrants. Nonetheless, it is likely that strategies such as three-color pulse sequences can be used in systems with bound excited states to isolate the desired signal components.

3.5. Nonequilibrium Correlation Between Reactants and Products

We have focused to this point on establishing signatures of cross peaks between triiodide and diiodide in 2DRR spectra (see Figure 3.9(c)). Of course, the vibrational resonance frequencies of both species can be determined by lower-order pump-probe experiments.[16, 19-21] The information unique to 2DRR spectroscopy pertains to the correlated vibrational motions of the reactant and product. In this section, we explore a time-frequency representation of the signal that is well-suited for physical insight into the photodissociation process of triiodide.
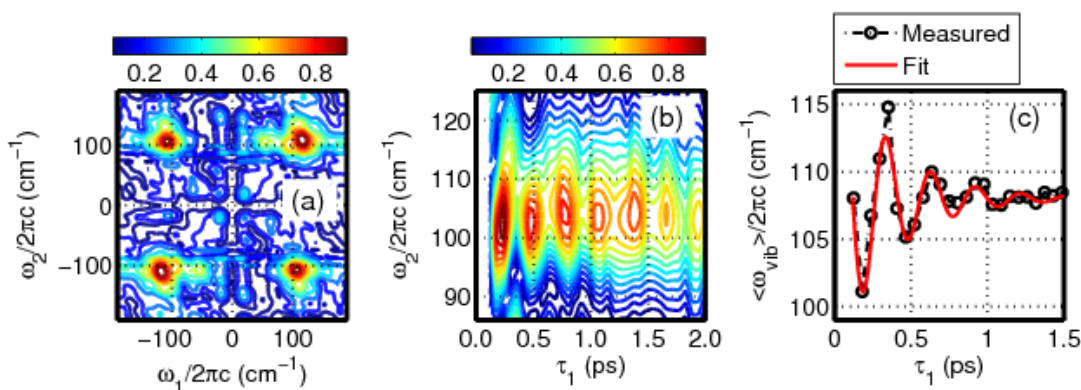
Figure 3.10. *2DRR response of triiodide in ethanol with a detection wavenumber of 19,500 cm^{-1} (513 nm). (a) Resonances in all four quadrants of the 2DRR spectrum signify cross peaks between triiodide (in ω_1) and diiodide (in ω_2). (b) Quantum beats in the Raman spectrum of diiodide are observed when the 2DRR spectrum in panel (a) is inverse Fourier transformed with respect to ω_1. (c) Oscillations in the mean vibrational frequency are analyzed using Equation 3.6. Such oscillatory behavior suggests that the vibrational coherence frequency of diiodide is sensitive to vibrational motions of triiodide in the delay time, τ_1.*

For the present system, it is our view that the frequency-domain representation of the 2DRR signal is primarily useful for confirming that the reactant and product dominate separate dimensions (see Figure 3.9). Once this is established, we suggest that the physical insight into the dissociation process is most clearly derived by leaving the first dimension in the time domain as displayed in Figure 3.10(b). Here, the τ_1 dimension represents wavepacket motion of triiodide in its ground electronic state, whereas the vibrational spectrum of diiodide is displayed in the ω_2

dimension. The mean vibrational frequency shown in Figure 10(c) is generated using the weighted average,

$$\langle \omega_{vib}(\tau_1) \rangle = \frac{\int d\omega_2 S(\tau_1, \omega_2) \omega_2}{\int d\omega_2 S(\tau_1, \omega_2)}, \tag{3.6}$$

where $S(\tau_1, \omega_2)$ denotes the signal displayed in Figure 10(b). The oscillations in $\langle \omega_{vib}(\tau_1) \rangle$ indicate that the vibrational coherence frequency of diiodide depends on the time-evolving nonequilibrium geometry of triiodide in the delay time, τ_1. The fit shown in Figure 10(c) reveals extrema in $\langle \omega_{vib}(\tau_1) \rangle$ of 99 and 111 cm^{-1} near the turning points of the wavepacket at delay times of 170 and 325 fs, respectively.

The LEPS potential energy surface of triiodide in ethanol shown in Figure 3.11 facilitates a discussion of the signal generation mechanism in terms of a microscopic picture.[17, 27] As suggested by Figure 3.11(a), the first pulse induces an electronic coherence and initiates a wavepacket in the symmetric stretching mode on the ground state potential (i.e., a stimulated Raman process). The turning points of the wavepacket can be estimated using the 300-fs period of the vibration and approximate 0.6 Å bond length displacement between the ground and excited state potential energy minima (i.e., 0.6 Å is the projection of the symmetric stretching coordinate onto the individual bond lengths).[27] We estimate that the wavepacket is stimulated in the ground state at bond lengths, $R_{ab}=R_{bc}$, near 3.06 Å by assuming a 20-fs electronic dephasing time. Here, the turning point is computed by adding 20/75×0.6 Å to the equilibrium bond length of 2.9 Å (75 fs is 1/4 of the vibrational period and 20 fs is the electronic dephasing time).[18] In other words, we estimate that the wavepacket moves approximately 0.16 Å from the equilibrium position of 2.9 Å during the electronic coherence induced by the first laser pulse before undergoing oscillations on the ground state potential energy surface in τ_1. Notably, small

changes in the numbers chosen for this analysis do not impact the physical interpretation of the

experiment.
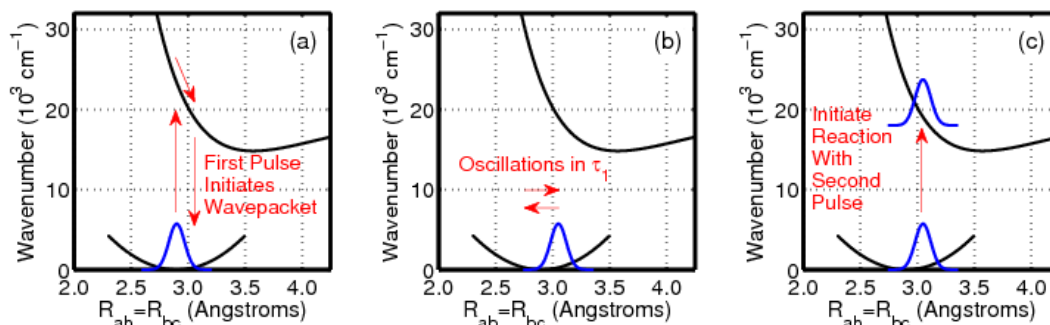
Figure 3.11. *The sequence of events associated with the 2DRR signals shown in Figure 3.10. R_{ab} and R_{bc} denote the two bond lengths in triiodide. (a) The first pulse initiates a ground state wavepacket in the symmetric stretching coordinate. Force is accumulated when both bond lengths increase during the electronic coherence induced by the first laser pulse. (b) Wavepacket motion on the ground state potential energy surface is detected in the delay between the pump and repump laser pulses, τ_1. (c) Photodissociation of triiodide is initiated from a nonequilibrium geometry by the repump laser pulse. The Raman spectrum of diiodide may then be detected by scanning the delay of a probe pulse, τ_2.*

Following ground state wavepacket initiation by the pump pulse, the application of a

repump laser pulse promotes the vibrational wavepacket in triiodide to the excited state potential

energy surface, where asymmetric motion induces dissociation of the molecule (see Figures

3.11(b) and 3.11(c)). The 20-fs pump and repump laser pulses are much shorter than the 300-fs

vibrational period, and the wavepacket moves very little along the symmetric stretching

coordinate before photodissociation.[20] For these reasons, the geometry of triiodide from which

the reaction commences is sensitive to the delay time, τ_1. By contrast, in a traditional (third-

order) transient absorption spectroscopy, the reactive wavepacket must always be promoted onto

the excited state potential energy surface from the equilibrium geometry (i.e., bond lengths of

approximately 2.9 Å).

Correlation between the wavepacket in the symmetric stretching coordinate of triiodide and the vibrational coherence frequency of diiodide can be visualized by converting the delay time, τ_1, into the position of the wavepacket in the symmetric stretching coordinate (i.e., the bond lengths in triiodide, $R_{ab}=R_{bc}$). In Figure 3.12, the inner and outer turning points of the wavepacket are taken to correspond to the minima and maxima in $\langle \omega_{vib}(\tau_1) \rangle$ shown in Figure 3.10(c). Translation between the delay, τ_1,, and the bond lengths is achieved by applying the model described above to $\langle \omega_{vib}(\tau_1) \rangle$. That is, we estimate that the wavepacket is located at 2.74 and 3.06 Å at delay times, τ_1, of 170 and 325 fs, respectively. Each revolution of the spiral in Figure 3.12 represents one period of vibrational motion in τ_1,. The spiral focuses inward towards the equilibrium bond length because of damping in $\langle \omega_{vib}(\tau_1) \rangle$. The orientation of the spiral during the first cycle of the wavepacket suggests that bond length displacements of approximately 0.1 Å in triiodide produce a 6.8-cm^{-1} shift in the vibrational coherence frequency of diiodide.
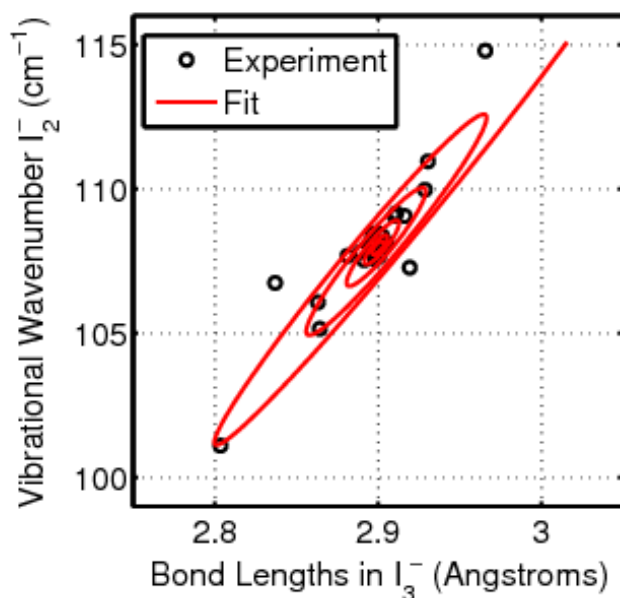
Figure 3.12. *Correlation between the vibrational wavenumber of the diiodide photoproduct and the pair of bond lengths in the triiodide reactant, $R_{ab}=R_{bc}$, is illustrated by analyzing the dynamics in the mean vibrational coherence frequency, $\langle \omega_{vib}(\tau_1) \rangle$, shown in Figure 3.10(c). The delay time, τ_1, is converted into the position of the wavepacket in the symmetric stretching coordinate using the model presented in Figure 3.11. Each revolution of the spiral corresponds to 300 fs. The wavepacket oscillates around the equilibrium bond length until vibrational dephasing is complete. The diagonal slant in the spiral suggests that a bond length displacement of 0.1 Å in triiodide induces a shift of 6.8 cm^{-1} in the vibrational coherence frequency of diiodide.*

The primary goal of the analysis presented in this section is to demonstrate the type of information that 2DRR spectroscopy can provide about nonequilibrium dynamics. Although our data suggests correlation between triiodide and diiodide, further theoretical work will be needed to draw firm conclusions about the relationship established in Figure 3.12. We have considered two possibilities. First, the geometry of the triiodide from which the reaction is initiated may influence the distribution of vibrational quanta in diiodide through a straightforward Franck-Condon mechanism as discussed in earlier work on triiodide in the gas phase.[55] Indeed, a second-order perturbative theory for photodissociation processes suggests that the populations of the vibrational states in a product may be weighted by overlap integrals involving the nuclear

coordinates of the reactant.[56] Of course, the vibrational coherence frequency of diiodide is known to be sensitive to the distribution of vibrational quanta because of anharmonicity.[19] A second possibility is that the correlation displayed in Figure 3.12 reflects interactions between dissociated fragments. Small inter-fragment distances have been suggested to influence vibrational coherence frequencies in solution on short time scales (i.e., fragment recoil).[19] Ruhman and co-workers have also recently discovered the presence of contact fragment pairs in solution (i.e., fragments in close proximity).[25] It is not yet clear if contributions from distinct relaxation channels are relevant to the present observations. Nishiyama et al. found evidence that vibrational dephasing may be faster than or comparable to the vibrational period in contact ion pairs, which suggests that 2DRR spectroscopy may be insensitive to these species.[24]

3.6. Concluding Remarks

In summary, we have demonstrated that 2DRR spectra carry unique signatures of vibrionic coherence transfer in triiodide. The patterns of resonances associated with three different types of nonlinearities are summarized in Figure 3.9. The unique pattern of resonances associated with cross peaks between triiodide and diiodide facilitates insights into the reaction mechanism. Moreover, cross peaks between triiodide and diiodide provide information about nonequilibrium behavior that cannot be derived from traditional pump-probe experiments, where reactants are always photo-initiated from the equilibrium geometry of the ground state. The present experiments suggest positive correlation between the bond lengths of the triiodide reactant and the vibrational coherence frequency of the diiodide photoproduct (see Figure 3.12). We suggest that correlation between these variables can be explained by Franck-Condon activity and/or by sensitivity to inter-fragment interactions.[24-26]

2DRR spectroscopy may reveal coherent reaction dynamics in any system where a light-activated non-radiative transition is fast compared to the period of vibrational motion. A non-

radiative transition, rather than the direct action of laser pulses, serves as an impulse that initiates

vibrational coherence in such systems. Triiodide has long been recognized as a well-defined

model system for reaction-induced wavepacket motions; however, these types of dynamics may

also be detected in larger systems that possess numerous Franck-Condon active coordinates. For

example, the photodissociation process of myoglobin is known to exhibit reaction-induced

vibrational coherences in both the doming and iron-histidine stretching coordinates.[57] Champion

and co-workers uncovered these dynamics with a sophisticated modulation scheme in third-order

stimulated Raman experiments.[58] New physical insights can be derived at fifth-order, because the

photodissociation reaction can be initiated from a well-defined nonequilibrium geometry of the

heme moiety. Fast non-radiative transitions also initiate vibrational coherences in bulk-

heterojunction systems,[5] photosynthetic complexes,[6, 9-13] and molecule-semiconductor

interfaces.[7-8] These systems may also be well-suited to 2DRR investigations.

3.7. Supplemental Information

3.7.1. Vibrational Hamiltonians

The present model assumes that both triiodide and diiodide possess two electronic levels

and one nuclear coordinate whose potential energy minimum is displaced between the ground

and excited electronic states. The rationale behind the model is discussed in Section 3.2.1. The

anharmonic vibrational wavefunctions for the Franck-Condon active bond stretching mode of

diiodide and the symmetric stretching coordinate of triiodide are generated using a Hamiltonian

with the following form:[59]

$$H_\alpha = \frac{\hbar \omega_{\alpha,vib}}{2}\left(2a^\dagger a + 1\right) + U_{3,\alpha}\left[a^\dagger a^\dagger a^\dagger + 3a^\dagger a^\dagger a + 3a^\dagger aa + aaa + 3a^\dagger + 3a\right], \qquad (3.7)$$

where

$$U_{3,\alpha} = \frac{1}{3!\sqrt{2^3 m^3 \omega^3 \hbar^{-3}}} \left(\frac{d^3V}{dq^3} \right)_0 . \tag{3.8}$$

The wavefunctions are obtained by diagonalizing this Hamiltonian in a basis set of harmonic

oscillators that includes states with up to the 40 vibrational quanta. Parameters of the vibrational

Hamiltonian are given in Table 3.1. We use a notation in which α represents the molecule (r for

triiodide or p for diiodide) and an asterisk indicates an electronically excited state.

The vibrational overlap integrals used to evaluate the response functions of diiodide are obtained

using

$$\langle n|m \rangle = \sum_{jk} \varphi_{nk} \varphi_{mj} \langle k|j \rangle , \tag{3.9}$$

where φ_{nk} is the expansion coefficient for harmonic basis vector, k, and the anharmonic excited

state vibrational wavefunction, n. Vibrational overlap integrals of triiodide are given by a

different formula,

$$\langle n|m \rangle = \sum_{k} \varphi_{nk} \langle k|m \rangle . \tag{3.10}$$

because the ground and excited states are taken to be harmonic and anharmonic, respectively

(see discussion in Section 3.2). In order to evaluate the overlap integrals, we assume a

dimensionless displacement of 7.0 based on spontaneous Raman measurements for triiodide[27]

and our earlier 2DRR study.[26] A displacement of 7.0 also produces an excited state potential

energy gradient of 225 eV/pm in diiodide which is identical to that associated with a previously

employed exponential surface at a displacement of only 9 pm from the Franck-Condon

geometry.[24-25] As discussed in Section 3.2.1, this gradient is the key quantity that must be

reproduced by the present model, because electronic dephasing is fast compared to the

vibrational period.[36] For this reason, the spectroscopic signals investigated in this work are

insensitive to features of the excited state potential energy surface that are displaced from the Franck-Condon geometry.

3.7.2. Two-Dimensional Resonance Raman Signal Components

The Feynman diagrams presented in Figure 3.2 include dummy indices for vibrational levels (m, n, j, k, l, u, v, w) associated with the ground and excited electronic states (r and r^* for triiodide, p and p^* for diiodide). Response functions are written in the Condon approximation, where the integral over electronic and nuclear degrees of freedom in the transition dipole is separated into a product of two integrals. For example, an interaction that couples vibrational level m in the ground electronic state of the reactant and vibrational level n in the excited electronic state of the reactant contributes the product, $\mu_{r^*r}\langle n|m\rangle$, to the response function, where μ_{r^*r} is the electronic transition dipole and $\langle n|m\rangle$, is a vibrational overlap integral. We use a notation in which the excited state vibrational energy level is always written in the bra.[39]

The first polarization component is given in Equation 3.3. The remaining 11 polarization components, which are derived in the Supplementary Material,[38] are given by

$$P_2^{(5)}(\omega_1,\omega_2) = -\frac{N\xi_{UV}^5 |\mu_{r^*r}|^6}{\hbar^5} \sum_{mnjklu} B_m \langle n|m\rangle\langle n|j\rangle\langle k|m\rangle\langle k|l\rangle\langle u|j\rangle\langle u|l\rangle$$
$$\times L_{r^*n,rm}(\omega_{UV})D_{rj,rm}(\omega_1)L_{rj,r^*k}(-\omega_{UV})D_{rj,rl}(\omega_2)L_{r^*u,rl}(\omega_t) \tag{3.11}$$

$$P_3^{(5)}(\omega_1,\omega_2) = -\frac{N\xi_{UV}^5 |\mu_{r^*r}|^6}{\hbar^5} \sum_{mnjklu} B_m \langle n|m\rangle\langle n|j\rangle\langle k|j\rangle\langle k|l\rangle\langle u|m\rangle\langle u|l\rangle$$
$$\times L_{rm,r^*n}(-\omega_{UV})D_{rm,rj}(\omega_1)L_{rm,r^*k}(-\omega_{UV})D_{rm,rl}(\omega_2)L_{r^*u,rl}(\omega_t) \tag{3.12}$$

$$P_4^{(5)}(\omega_1,\omega_2) = -\frac{N\xi_{UV}^5 |\mu_{r^*r}|^6}{\hbar^5} \sum_{mnjklu} B_m \langle n|m\rangle\langle n|j\rangle\langle k|m\rangle\langle k|l\rangle\langle u|l\rangle\langle u|j\rangle$$
$$\times L_{rm,r^*n}(-\omega_{UV})D_{rm,rj}(\omega_1)L_{r^*k,rj}(\omega_{UV})D_{rl,rj}(\omega_2)L_{r^*u,rj}(\omega_t) \tag{3.13}$$

$$P_5^{(5)}(\omega_1, \omega_2) = -\frac{N \xi_{UV}^2 \xi_{VIS}^3 |\mu_{r*r}|^2 |\mu_{p*p}|^4}{\hbar^5} \sum_{mnjkluvw} B_m \langle n|m \rangle \langle j|m \rangle \langle u|k \rangle \langle u|v \rangle \langle w|v \rangle \langle w|l \rangle$$
$$\times L_{r*n,rm}(\omega_{UV}) D_{pk,pl}(\omega_1) L_{p*u,pl}(\omega_{VIS}) D_{pv,pl}(\omega_2) L_{p*w,pl}(\omega_t) \quad (3.14)$$

$$P_6^{(5)}(\omega_1, \omega_2) = -\frac{N \xi_{UV}^2 \xi_{VIS}^3 |\mu_{r*r}|^2 |\mu_{p*p}|^4}{\hbar^5} \sum_{mnjkluvw} B_m \langle n|m \rangle \langle j|m \rangle \langle u|k \rangle \langle u|v \rangle \langle w|v \rangle \langle w|l \rangle$$
$$\times L_{rm,r*n}(-\omega_{UV}) D_{pk,pl}(\omega_1) L_{p*u,pl}(\omega_{VIS}) D_{pv,pl}(\omega_2) L_{p*w,pl}(\omega_t) \quad (3.15)$$

$$P_7^{(5)}(\omega_1, \omega_2) = -\frac{N \xi_{UV}^2 \xi_{VIS}^3 |\mu_{r*r}|^2 |\mu_{p*p}|^4}{\hbar^5} \sum_{mnjkluvw} B_m \langle n|m \rangle \langle j|m \rangle \langle u|l \rangle \langle u|v \rangle \langle w|k \rangle \langle w|v \rangle$$
$$\times L_{r*n,rm}(\omega_{UV}) D_{pk,pl}(\omega_1) L_{pk,p*u}(-\omega_{VIS}) D_{pk,pv}(\omega_2) L_{p*w,pv}(\omega_t) \quad (3.16)$$

$$P_8^{(5)}(\omega_1, \omega_2) = -\frac{N \xi_{UV}^2 \xi_{VIS}^3 |\mu_{r*r}|^2 |\mu_{p*p}|^4}{\hbar^5} \sum_{mnjkluvw} B_m \langle n|m \rangle \langle j|m \rangle \langle u|l \rangle \langle u|v \rangle \langle w|k \rangle \langle w|v \rangle$$
$$\times L_{rm,r*n}(-\omega_{UV}) D_{pk,pl}(\omega_1) L_{pk,p*u}(-\omega_{VIS}) D_{pk,pv}(\omega_2) L_{p*w,pv}(\omega_t) \quad (3.17)$$

$$P_9^{(5)}(\omega_1, \omega_2) = -\frac{N \xi_{UV}^4 \xi_{VIS} |\mu_{r*r}|^4 |\mu_{p*p}|^2}{\hbar^5} \sum_{mnjkluvw} B_m \langle n|m \rangle \langle n|j \rangle \langle k|j \rangle \langle l|m \rangle \langle w|u \rangle \langle w|v \rangle$$
$$\times L_{r*n,rm}(\omega_{UV}) D_{rj,rm}(\omega_1) L_{r*k,rm}(\omega_{UV}) D_{pu,pv}(\omega_2) L_{p*w,pv}(\omega_t) \quad (3.18)$$

$$P_{10}^{(5)}(\omega_1, \omega_2) = -\frac{N \xi_{UV}^4 \xi_{VIS} |\mu_{r*r}|^4 |\mu_{p*p}|^2}{\hbar^5} \sum_{mnjkluvw} B_m \langle n|m \rangle \langle n|j \rangle \langle k|m \rangle \langle l|j \rangle \langle w|u \rangle \langle w|v \rangle$$
$$\times L_{rm,r*n}(-\omega_{UV}) D_{rm,rj}(\omega_1) L_{r*k,rj}(\omega_{UV}) D_{pu,pv}(\omega_2) L_{p*w,pv}(\omega_t) \quad (3.19)$$

$$P_{11}^{(5)}(\omega_1, \omega_2) = -\frac{N \xi_{UV}^4 \xi_{VIS} |\mu_{r*r}|^4 |\mu_{p*p}|^2}{\hbar^5} \sum_{mnjkluvw} B_m \langle n|m \rangle \langle n|j \rangle \langle k|m \rangle \langle l|j \rangle \langle w|u \rangle \langle w|v \rangle$$
$$\times L_{r*n,rm}(\omega_{UV}) D_{rj,rm}(\omega_1) L_{rj,r*k}(-\omega_{UV}) D_{pu,pv}(\omega_2) L_{p*w,pv}(\omega_t) \quad (3.20)$$

$$P_{12}^{(5)}(\omega_1, \omega_2) = -\frac{N \xi_{UV}^4 \xi_{VIS} |\mu_{r*r}|^4 |\mu_{p*p}|^2}{\hbar^5} \sum_{mnjkluvw} B_m \langle n|m \rangle \langle n|j \rangle \langle k|j \rangle \langle l|m \rangle \langle w|u \rangle \langle w|v \rangle$$
$$\times L_{rm,r*n}(-\omega_{UV}) D_{rm,rj}(\omega_1) L_{rm,r*k}(-\omega_{UV}) D_{pu,pv}(\omega_2) L_{p*w,pv}(\omega_t) \quad (3.21)$$

In the above polarization components, laser pulses with the subscripts *UV* and *VIS* are taken to interact with triiodide and diiodide, respectively.

For convenience, we further group the terms into three classes of signal fields under the assumption of perfect phase-matching conditions

$$E_{r,r}^{(5)}(\omega_1,\omega_2) = \left(\frac{i\omega_t l}{2\varepsilon_0 n(\omega_t)c}\right)\sum_{m=1}^{4} P_m^{(5)}(\omega_1,\omega_2),\tag{3.22}$$

$$E_{p,p}^{(5)}(\omega_1,\omega_2) = \left(\frac{i\omega_t l}{2\varepsilon_0 n(\omega_t)c}\right)\sum_{m=5}^{8} P_m^{(5)}(\omega_1,\omega_2),\tag{3.23}$$

and

$$E_{r,p}^{(5)}(\omega_1,\omega_2) = \left(\frac{i\omega_t l}{2\varepsilon_0 n(\omega_t)c}\right)\sum_{m=9}^{12} P_m^{(5)}(\omega_1,\omega_2),\tag{3.24}$$

Here, the two subscripts of the signal fields represent sensitivity to the triiodide reactant (subscript r) and diiodide product (subscript p) in the two frequency dimensions, ω_1 and ω_2.

REFERENCES

1. Mukamel, S., *Principles of Nonlinear Optical Spectroscopy*. Oxford University Press: New York, 1999.

2. Nitzan, A., *Chemical Dynamics in Condensed Phases: Relaxation, Transfer and Reactions in Condensed Molecular Systems*. Oxford University Press: New York, 2006.

3. Valkunas, L.; Abramavicius, D.; Mancal, T., *Molecular Excitation Dynamics and Relaxation: Quantum Theory and Spectroscopy*. John Wiley & Sons: Weinheim, Germany, 2013.

4. Mohseni, M.; Omar, Y.; Engel, G. S.; Plenio, M. B., *Quantum Effects in Biology*. Cambridge University Press: Cambridge, 2014.

5. Song, Y.; Clafton, S. N.; Pensack, R. D.; Kee, T. W.; Scholes, G. D., Vibrational coherence probes the mechanism of ultrafast electron transfer in polymer-fullerene blends. *Nat. Commun.* **2014,** *5*, 4933.

6. Fuller, F. D.; Pan, J.; Gelzinis, A.; Butkus, V.; Senlik, S. S.; Wilcox, D. E.; Yocum, C. F.; Valkunas, L.; Abramavicius, D.; Ogilvie, J. P., Vibronic coherence in oxygenic photosynthesis. *Nat. Chem.* **2014,** *6* (8), 706-711.

7. Tisdale, W. A.; Williams, K. J.; Timp, B. A.; Norris, D. J.; Aydil, E. S.; Zhu, X. Y., Hot-electron transfer from semiconductor nanocrystals. *Science* **2010,** *328* (5985), 1543-1547.

8. Zimmermann, C.; Willig, F.; Ramakrishna, S.; Burfeindt, B.; Pettinger, B.; Eichberger, R.; Storck, W., Experimental fingerprints of vibrational wave-packet motion during ultrafast heterogeneous electron transfer. *J. Phys. Chem. B* **2001,** *105* (38), 9245-9253.

9. Womick, J. M.; Moran, A. M., Vibronic enhancement of exciton sizes and energy transport in photosynthetic complexes. *J. Phys. Chem. B* **2011,** *115* (6), 1347-1356.

10. Christensson, N.; Kauffmann, H. F.; Pullerits, T.; Mancal, T., Origin of long-lived coherences in light-harvesting complexes. *J. Phys. Chem. B* **2012,** *116* (25), 7449-7454.

11. Kolli, A.; O'Reilly, E. J.; Scholes, G. D.; Olaya-Castro, A., The fundamental role of quantized vibrations in coherent light harvesting by cryptophyte algae. *J. Chem. Phys.* **2012,** *137* (17), 174109.

12. Chin, A. W.; Prior, J.; Rosenbach, R.; Caycedo-Soler, F.; Huelga, S. F.; Plenio, M. B., The role of non-equilibrium vibrational structures in electronic coherence and recoherence in pigment–protein complexes. *Nat. Phys.* **2013,** *9* (2), 113-118.

13. Fujihashi, Y.; Fleming, G. R.; Ishizaki, A., Impact of environmentally induced fluctuations on quantum mechanically mixed electronic and vibrational pigment states in photosynthetic energy transfer and 2D electronic spectra. *J. Chem. Phys.* **2015,** *142* (21), 212403.

14.	Jun, S.; Yang, C.; Isaji, M.; Tamiaki, H.; Kim, J.; Ihee, H., Coherent oscillations in chlorosome elucidated by two-dimensional electronic spectroscopy. *J. Phys. Chem. Lett.* **2014,** *5* (8), 1386-1392.

15.	Perlik, V.; Seibt, J.; Cranston, L. J.; Cogdell, R. J.; Lincoln, C. N.; Savolainen, J.; Sanda, F.; Mancal, T.; Hauer, J., Vibronic coupling explains the ultrafast carotenoid-to-bacteriochlorophyll energy transfer in natural and artificial light harvesters. *J. Chem. Phys.* **2015,** *142* (21), 212434.

16.	Banin, U.; Kosloff, R.; Ruhman, S., Femtosecond Chemical dynamics in solution: photodissociation of I_3^-. *Isr. J. Chem.* **1993,** *33* (2), 141-156.

17.	Benjamin, I.; Banin, U.; Ruhman, S., Ultrafast photodissociation of I_3^- in ethanol: A molecular dynamics study. *J. Chem. Phys.* **1993,** *98* (10), 8337-8340.

18.	Banin, U.; Kosloff, R.; Ruhman, S., Vibrational relaxation of nascent diiodide ions studied by femtosecond transient resonance impulsive stimulated Raman scattering (TRISRS); experiment and simulation. *Chem. Phys.* **1994,** *183* (2-3), 289-307.

19.	Kühne, T.; Vöhringer, P., Vibrational relaxation and geminate recombination in the femtosecond-photodissociation of triiodide in solution. *J. Chem. Phys.* **1996,** *105* (24), 10788-10802.

20.	Gershgoren, E.; Gordon, E.; Ruhman, S., Effect of symmetry breaking on vibrational coherence transfer in impulsive photolysis of trihalide ions. *J. Chem. Phys.* **1997,** *106* (11), 4806-4809.

21.	Kühne, T.; Küster, R.; Vöhringer, P., Femtosecond photodissociation of triiodide in solution: Excitation energy dependence and transition state dynamics. *Chem. Phys.* **1998,** *233* (2-3), 161-178.

22.	Hess, S.; Bürsing, H.; Vöhringer, P., Dynamics of fragment recoil in the femtosecond photodissociation of triiodide ions in liquid solution. *J. Chem. Phys.* **1999,** *111* (12), 5461-5473.

23.	Yang, T. S.; Chang, M. S.; Chang, R.; Hayashi, M.; Lin, S. H.; Vöhringer, P.; Dietz, W.; Scherer, N. F., Femtosecond pump-probe study of molecular vibronic structures and dynamics of a cyanine dye in solution. *J. Chem. Phys.* **1999,** *110* (24), 12070-12081.

24.	Nishiyama, Y.; Terazima, M.; Kimura, Y., Ultrafast relaxation and reaction of diiodide anion after photodissociation of triiodide in room-temperature ionic liquids. *J. Phys. Chem. B* **2012,** *116* (30), 9023-9032.

25.	Baratz, A.; Ruhman, S., UV photolysis of I_3^- in solution-Multiple product channels detected by transient hyperspectral probing. *Chem. Phys. Lett.* **2008,** *461* (4-6), 211-217.

26.   Molesky, B. P.; Giokas, P. G.; Guo, Z.; Moran, A. M., Multidimensional resonance Raman spectroscopy by six-wave mixing in the deep UV. *J. Chem. Phys.* **2014,** *141* (11), 114202.

27.   Johnson, A. E.; Myers, A. B., Emission cross sections and line shapes for photodissociating triiodide in ethanol: Experimental and computational studies. *J. Chem. Phys.* **1995,** *102* (9), 3519-3533.

28.   Johnson, A. E.; Myers, A. B., A comparison of time- and frequency-domain resonance Raman spectroscopy in triiodide. *J. Chem. Phys.* **1996,** *104* (7), 2497-2507.

29.   Johnson, A. E.; Myers, A. B., Solvent effects in the raman spectra of the triiodide ion: Observation of dynamic symmetry breaking and solvent degrees of freedom. *J. Phys. Chem.* **1996,** *100* (19), 7778-7788.

30.   Ulness, D. J.; Kirkwood, J. C.; Albrecht, A. C., Competitive events in fifth order time resolved coherent Raman scattering: Direct versus sequential processes. *J. Chem. Phys.* **1998,** *108* (10), 3897-3902.

31.   Blank, D. A.; Kaufman, L. J.; Fleming, G. R., Fifth-order two-dimensional Raman spectra of CS_2 are dominated by third-order cascades. *J. Chem. Phys.* **1999,** *111* (7), 3105-3114.

32.   Kubarych, K. J.; Milne, C. J.; Lin, S.; Astinov, V.; Miller, R. J. D., Diffractive optics-based six-wave mixing: Heterodyne detection of the full $\chi(5)$ tensor of liquid CS_2. *J. Chem. Phys.* **2002,** *116* (5), 2016-2042.

33.   Wilson, K. C.; Lyons, B.; Mehlenbacher, R.; Sabatini, R.; McCamant, D. W., Two-dimensional femtosecond stimulated Raman spectroscopy: Observation of cascading Raman signals in acetonitrile. *J. Chem. Phys.* **2009,** *131* (21), 214502.

34.   Ivanecky, J. E.; Wright, J. C., An investigation of the origins and efficiencies of higher-order nonlinear spectroscopic processes. *Chem. Phys. Lett.* **1993,** *206* (5-6), 437-444.

35.   Herrmann, V.; Krebs, P., Temperature dependence of optical absorption spectra of solvated electrons in CD_3OD for T .ltoreq. Tc. *J. Phys. Chem.* **1995,** *99* (18), 6794-6800.

36.   Myers, A.; Rizzo, T.; Baumgartel, H., Laser techniques in chemistry. *Angew. Chem.* **1997,** *109* (10), 1172-1172.

37.   Heller, E. J., The semiclassical way to molecular spectroscopy. *Acc. Chem. Res.* **2002,** *14* (12), 368-375.

38.   See supplementary material at http://dx.doi.org/10.1063/1.4931473 E-JCPSA6-143-069536 for derivation of the response functions presented in Appendix B and an experimental test used to rule out cascades.

39. Myers, A. B.; Mathies, R. A.; Tannor, D. J.; Heller, E. J., Excited state geometry changes from preresonance Raman intensities: Isoprene and hexatriene. *J. Chem. Phys.* **1982,** *77* (8), 3857-3866.

40. Goodno, G. D.; Dadusc, G.; Miller, R. J. D., Ultrafast heterodyne-detected transient-grating spectroscopy using diffractive optics. *J. Opt. Soc. Am. B* **1998,** *15* (6), 1791.

41. West, B. A.; Womick, J. M.; Moran, A. M., Probing ultrafast dynamics in adenine with mid-UV four-wave mixing spectroscopies. *J. Phys. Chem. A* **2011,** *115* (31), 8630-8637.

42. West, B. A.; Womick, J. M.; Moran, A. M., Interplay between vibrational energy transfer and excited state deactivation in DNA components. *J. Phys. Chem. A* **2013,** *117* (29), 5865-5874.

43. Lepetit, L.; Chériaux, G.; Joffre, M., Linear techniques of phase measurement by femtosecond spectral interferometry for applications in spectroscopy. *J. Opt. Soc. Am. B* **1995,** *12* (12), 2467.

44. Gallagher, S. M.; Albrecht, A. W.; Hybl, J. D.; Landin, B. L.; Rajaram, B.; Jonas, D. M., Heterodyne detection of the complete electric field of femtosecond four-wave mixing signals. *J. Opt. Soc. Am. B* **1998,** *15* (8), 2338.

45. Turner, D. B.; Wilk, K. E.; Curmi, P. M. G.; Scholes, G. D., Comparison of electronic and vibrational coherence measured by two-dimensional electronic spectroscopy. *J. Phys. Chem. Lett.* **2011,** *2* (15), 1904-1911.

46. Underwood, D. F.; Blank, D. A., Measuring the change in the intermolecular Raman spectrum during dipolar solvation. *J. Phys. Chem. A* **2005,** *109* (15), 3295-3306.

47. Moran, A. M.; Nome, R. A.; Scherer, N. F., Field-resolved measurement of reaction-induced spectral densities by polarizability response spectroscopy. *J. Chem. Phys.* **2007,** *127* (18), 184505.

48. Park, S.; Kim, J.; Scherer, N. F., Two-dimensional measurements of the solvent structural relaxation dynamics in dipolar solvation. *Phys. Chem. Chem. Phys.* **2012,** *14* (22), 8116-8122.

49. Busby, E.; Carroll, E. C.; Chinn, E. M.; Chang, L.; Moulé, A. J.; Larsen, D. S., Excited-state self-trapping and ground-state relaxation dynamics in poly(3-hexylthiophene) resolved with broadband pump–dump–probe spectroscopy. *J. Phys. Chem. Lett.* **2011,** *2* (21), 2764-2769.

50. Molesky, B. P.; Guo, Z.; Moran, A. M., Femtosecond stimulated Raman spectroscopy by six-wave mixing. *J. Chem. Phys.* **2015,** *142* (21), 212405.

51. Chen, E. C. M.; Wentworth, W. E., Negative ion states of the halogens. *J. Phys. Chem.* **1985,** *89* (19), 4099-4105.

52. Marek, M. S.; Buckup, T.; Motzkus, M., Direct observation of a dark state in lycopene using pump-DFWM. *J. Phys. Chem. B* **2011,** *115* (25), 8328-8337.

53. Valley, D. T.; Hoffman, D. P.; Mathies, R. A., Reactive and unreactive pathways in a photochemical ring opening reaction from 2D femtosecond stimulated Raman. *Phys. Chem. Chem. Phys.* **2015,** *17* (14), 9231-9240.

54. Kukura, P.; McCamant, D. W.; Mathies, R. A., Femtosecond stimulated Raman spectroscopy. *Annu. Rev. Phys. Chem.* **2007,** *58*, 461-488.

55. Zanni, M. T.; Greenblatt, B. J.; Davis, A. V.; Neumark, D. M., Photodissociation of gas phase I_3^- using femtosecond photoelectron spectroscopy. *J. Chem. Phys.* **1999,** *111* (7), 2991-3003.

56. Band, Y. B.; Freed, K. F., Energy distribution in selected fragment vibrations in dissociation processes in polyatomic molecules. *J. Chem. Phys.* **1977,** *67* (4), 1462-1472.

57. Champion, P. M.; Rosca, F.; Ionascu, D.; Cao, W.; Ye, X., Rapid timescale processes and the role of electronic surface coupling in the photolysis of diatomic ligands from heme proteins. *Faraday Discuss.* **2004,** *127*, 123.

58. Kumar, A. T. N.; Rosca, F.; Widom, A.; Champion, P. M., Investigations of amplitude and phase excitation profiles in femtosecond coherence spectroscopy. *J. Chem. Phys.* **2001,** *114* (2), 701.

59. Moran, A. M.; Dreyer, J.; Mukamel, S., Ab initiosimulation of the two-dimensional vibrational spectrum of dicarbonylacetylacetonato rhodium(I). *J. Chem. Phys.* **2003,** *118* (3), 1347-1355.

CHAPTER 4. FEMTOSECOND STIMULATED RAMAN SPECTROSCOPY BY SIX-WAVE MIXING[2]

4.1. Introduction

Femtosecond Stimulated Raman Spectroscopy (FSRS) has emerged as a powerful method for investigating ultrafast structural dynamics in condensed phases.[1-12] Recent applications have revealed new insights into systems ranging from proteins[9-10, 12] to organic photovoltaic materials.[4, 11] The FSRS technique is essentially a sequence of two events: (i) an electronically resonant (actinic) pump pulse initiates a photochemical process; (ii) a stimulated Raman spectrum is obtained at various delay times using a combination of narrowband and broadband laser pulses. Simultaneous probing of all vibrational resonances in the fingerprint region of the spectrum and sensitivity to dynamics on the 100-fs time scale are the primary selling points for the technique. The key is that the precision in the delay between photoexcitation and initiation of the Raman response is determined by the convolution of femtosecond laser pulses in FSRS (although the vibrational frequencies can notably evolve during the free induction decay).[13-15] In contrast, precision in the delay time and spectral resolution are intrinsically coupled in experiments that employ spontaneous Raman probes, because initiation of the Raman response requires a spontaneous fluctuation of the radiation field.[16]

Foremost among the technical challenges that may be encountered in a three-beam implementation of FSRS is a substantial background associated with residual laser light and third-order processes that are radiated in the same direction as the signal. The third-order nonlinearities include a broadband pump-probe signal and a stimulated Raman scattering response (SRS). Of course, undesired signal components that are generated by subsets of the incoming beams (e.g., pump-probe and SRS) can always be eliminated by chopping the incident beams and/or by modulating the frequency of the narrowband pulse.[17-19] The magnitude of the background depends on the particular properties of the sample and the frequencies of the Raman pump and Stokes pulses. The pulses involved in the Raman probe are often tuned into pre-electronic-resonance with the photoproduct, where the equilibrium system is transparent.[1, 17, 20] The amount of background may be reduced to a non-problematic level under these conditions. In contrast, the method presented in this work is motivated by a more general situation, wherein all pulses are electronically resonant with the equilibrium system. Lower-order nonlinearities and the pump-repump-probe response may then become dominant, particularly in systems with small normal mode displacements.
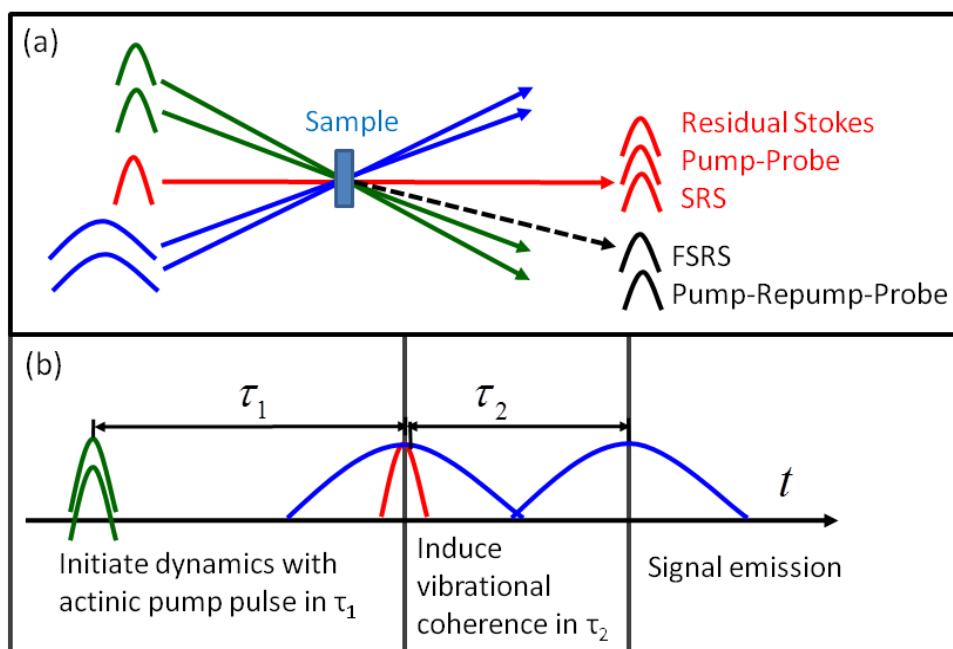
Figure 4.1. *(a) A five-beam FSRS geometry is used in this work to eliminate the portion of the background associated with residual Stokes light and third-order nonlinearities. The color code is as follows: the actinic pump is green, the Raman pump is blue, and the Stokes pulse is red. (b) Relaxation dynamics are probed in the delay between the actinic pump and Stokes pulses, τ_1. The fixed time delay, τ_2, is used to suppress a broadband pump-repump-probe response.*

In this work, we implement laser beam geometries that either reduce or fully eliminate residual laser light and the background of third-order nonlinearities present in traditional FSRS. Figure 4.1 explains how a five-beam geometry can be used to spatially separate most of the background from the FSRS signal emission. It should be noted that, while Figure 4.1 assumes detection of Stokes shifted emission, the same approach can be employed with anti-Stokes detection. Elimination of these undesired signal components greatly enhances sensitivity and reduces data acquisition times compared to a traditional approach in which three incoming beams are utilized. The broadband pump-repump-probe response of the sample is not spatially filtered in the present approach, because this undesired nonlinearity is phase-matched in the same direction as the FSRS signal. Nonetheless, the pump-repump-probe response can be suppressed

124

in the five-beam geometry by introducing a delay between the two Raman pump pulses, τ_2. This delay enforces the order of field-matter interactions unique to the FSRS response.

The present approach to FSRS is demonstrated with metmyoglobin (metMb), which is the ferric form (Fe^{+3}) of the protein. Photoexcitation induces ground state recovery within several picoseconds (rather than ligand dissociation and recombination) in metMb, because water binds to the distal side of the heme group.[21-25] Upon photoexcitation of the Soret band, the ground electronic state of metMb is repopulated through one of two relaxation mechanisms that have been delineated in recent work by Chergui and co-workers.[23] The most efficient pathway (57% efficiency) involves sub-picosecond internal conversion from a high-energy charge-transfer state formed immediately after photoexcitation. In the second pathway, the ground state is repopulated within 5 picoseconds following a cascade of transitions through iron spin states. In both processes, excess vibrational energy is dissipated within several picoseconds following ground state recovery. We employ metMb as a model system here in order to establish the validity of the present technique for investigations of heme proteins. Future studies may then focus on understanding photochemical processes in related systems (e.g., photodissociation, electron transfer).

Cascades of third-order signals have been recognized as a serious experimental complication in off-resonant fifth-order Raman experiments conducted on pure liquids and concentrated mixtures.[26-30] Cascades involve a sequence in which the third-order polarization induced on one molecule radiates a signal field that induces a third-order polarization in a second molecule. The second molecule then radiates a signal field in the same direction as the fifth-order signal of interest. The central problem in off-resonant experiments is that direct (desired) and cascaded (undesired) signals are respectively forbidden and allowed by the lowest order terms in

the polarization responses (i.e., harmonic potentials with polarizabilities that depend linearly on the vibrational coordinates).[27, 31-33] One key to the success of electronically resonant FSRS is that the signal generation mechanism does not rely on such higher-order terms in the expansion of the potential energy.[15, 34-36] Unlike off-resonant experiments, resonant FSRS signal generation is allowed for all Franck-Condon active modes (whether they are harmonic or not). Moreover, the solute concentrations employed in resonant FSRS experiments are typically more than 10,000 times smaller than those associated with samples in which cascades are known to dominate the optical response (e.g., pure CS_2). Nonetheless, we have encountered uncertainties among specialists regarding the potential for cascades in electronically resonant FSRS, which should be dealt with before studies of photochemical mechanisms are pursued. For this reason, significant effort is put forth in this work to rule out contributions from cascades with experimental tests and model calculations.

4.2. Experimental Methods

4.2.1. Laser Pulse Generation

Actinic pump, Raman pump, and Stokes pulses resonant with the Soret band of metMb are employed in the present study (see Figure 4.2). All experiments are based on a Titanium Sapphire laser system that produces 0.8 mJ, 55-fs pulses at 1 kHz. The 410-nm actinic pump pulses are obtained by second harmonic generation of 50 μJ of the fundamental beam in a 0.25-mm thick BBO crystal. Dispersion accumulated in the BBO crystal and several beam splitters, which amounts to roughly 500 fs^2 group delay dispersion (GDD), is pre-compensated for with reflections of the 800-nm pulses on mirrors that impart negative GDD before second harmonic generation. Raman pump pulses are produced by second harmonic generation of the fundamental laser beam in a 1-mm thick BBO crystal. The Raman pump is then sent through a 4F spectral

filter consisting of two 2400-g/mm gratings and two 25-cm focal length lenses. Pulses with spectral widths of 50 cm^{-1} are obtained by placing a slit with an 890-μm width at the 2F plane.
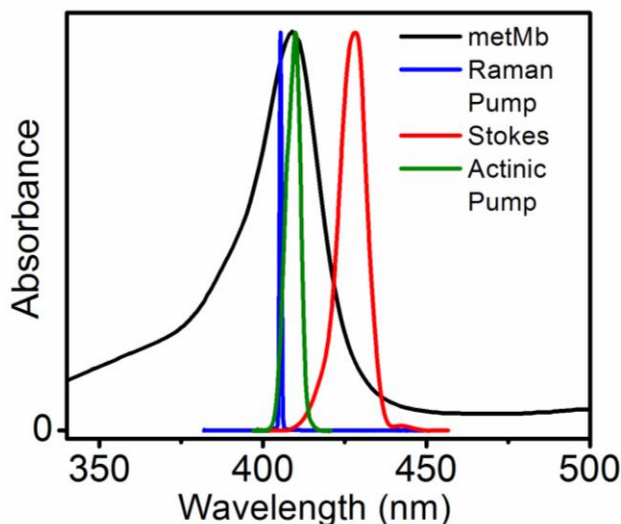
Figure 4.2. *Spectra of the actinic pump (green), Raman pump (blue), and Stokes pulses (red) are overlaid on the linear absorbance spectrum of metmyoglobin in aqueous buffer solution at pH=7.0.*

The Stokes pulse is produced by doubling the frequency of the fundamental laser beam in a 0.25-mm thick BBO crystal. The resulting 90-μJ, 410-nm second harmonic beam is then focused into a 75-cm long hollow core fiber with a 30-cm focal length lens. The 100-μm inner diameter of the fiber constitutes a suitable compromise between throughput and spectral broadening. The fiber is housed in a stainless-steel cell filled with 1.0 atm of argon gas. The spectrum of the spectrally broadened laser pulse that exits the fiber is fairly sensitive to the alignment into the fiber. For this reason, the spectrum of the output is continually monitored with an Ocean Optics spectrometer and laptop computer; adjustments are made after the laser is warmed up to reproduce the spectrum on a daily basis. The Stokes spectrum shown in Figure 4.1 is obtained by spectral filtering of the laser beam in a fused-silica prism compressor with 70-cm prism separation. The instrument response width, which was determined in a 0.25-mm thick

fused silica window, is less than 80 fs at Raman shifts ranging from 500-2000 cm^{-1} (i.e., Stokes

wavelength range of 415-440 nm).
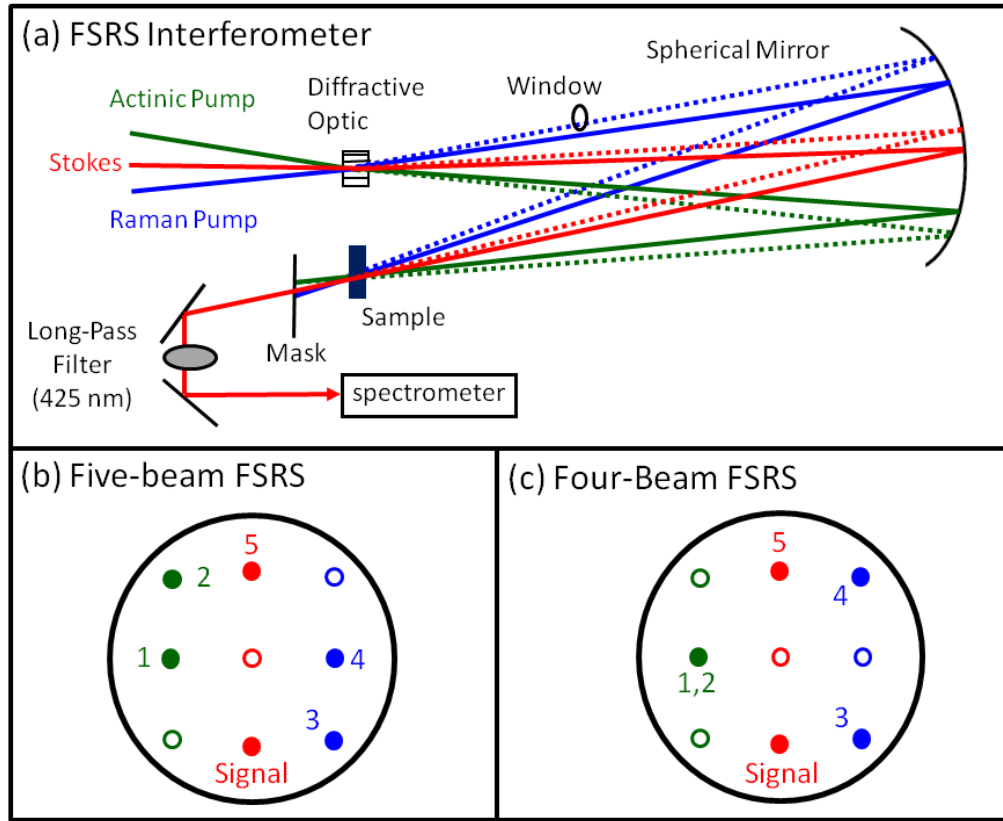
Figure 4.3. *(a) Diffractive optic-based interferometer used for FSRS measurements. The transparent fused silica window delays pulse 3 by 290 fs with respect to pulse 4 (delay τ_2 in Figure 4.1). (b) A five-beam geometry is used to detect the FSRS signal in the background-free direction, k_1-k_2+k_3-k_4+k_5. (c) The FSRS signal is also radiated in the direction, k_1-k_2+k_3-k_4+k_5 in the four-beam geometry; however, the wavevectors k_1 and k_2 cancel each other, so the signal is radiated in the same direction as a four-wave mixing signal, k_3-k_4+k_5. In the four-beam geometry, the FSRS signal corresponds to the difference between signals measured with and without the actinic pump beam (beam 1,2). Beams represented with solid circles reach the sample, whereas those represented with open circles are blocked with a mask. The same color code is applied in all panels (Raman pump is blue, actinic pump is green, Stokes beam is red).*

4.2.2. Laser Beam Geometries

Experiments are conducted with the diffractive optic-based interferometer shown in

Figure 4.3. All beams are focused onto the diffractive optic with a 50-cm focal length spherical

mirror. The 20-cm focal length imaging mirror is rotated off-axis by approximately 5° (i.e., the

minimum amount). The actinic pump and Raman pump beams cross at approximately 6.9° in the diffractive optic and are bisected by the Stokes beam. The angles between the +1 and -1 diffraction orders of the actinic and Raman pump beams are both 6.9°. The angle between +1 and -1 diffraction orders of the Stokes beam is 7.2°. Approximately 25% of each incident beam is diffracted into each of the three diffraction orders (0 and +/-1). Subsets of the 9 beams can be selected to conduct a variety of four and six-wave mixing experiments. We utilize the two beam patterns shown in Figures 4.3(b) and 4.3(c) in this work.

The laser beam geometry displayed in Figure 3(b) was developed by Mark Berg for studies of multidimensional population dynamics.[37-38] The signal is detected in the direction, $\mathbf{k}_1$-$\mathbf{k}_2$+$\mathbf{k}_3$-$\mathbf{k}_4$+$\mathbf{k}_5$. The key advantage of this geometry is that the signal is free from a background of direct third-order signal fields when the beam diameters are small compared to their separation after the sample. As discussed in our earlier study of triiodide,[35] a direct third-order signal is radiated in the direction $\mathbf{k}_1$+$\mathbf{k}_4$-$\mathbf{k}_5$ when the actinic pump and Stokes beams overlap. This response vanishes at positive delay times, τ_1, because pulses 1 and 5 establish the holographic grating in the sample; this can be proven by blocking either beam 2 or 3 at positive delay times. Notably, this undesired signal (near τ_1=0) does not possess narrow vibrational resonances due to the 250-cm^{-1} spectral width of the actinic pump pulse. It is therefore removed when the broadband baseline is subtracted in the signal processing algorithm described in Section 4.3. Beams 2 or 3 may also be chopped if dynamics at sub-100-fs delay times are of interest.

The four-beam geometry shown in Figure 4.3(c) is obtained simply by changing the mask between the diffractive optic and the sample. The signal is again radiated in the direction, $\mathbf{k}_1$-$\mathbf{k}_2$+$\mathbf{k}_3$-$\mathbf{k}_4$+$\mathbf{k}_5$; however, this direction is collinear with the vector $\mathbf{k}_3$-$\mathbf{k}_4$+$\mathbf{k}_5$, because a single actinic pump beam is employed. The actinic pump beam (beam 1,2) must be chopped in order to

remove contributions of the third-order SRS signal.[39-41] Chopping the actinic pump beam significantly increases the data acquisition time and reduces sensitivity compared to the five-beam geometry. Therefore, we use the four-beam geometry only to determine the relative signs of the third- and fifth-order signals in this work.

In both geometries, the beams are focused onto the diffractive optic with a 50-cm focal length spherical mirror. The depth of focus for each beam is approximately 7 mm given the approximate 6-mm beam diameters at the surface of the spherical mirror. The beams are imaged onto the sample with 20-cm focal length spherical mirror placed 40 cm from the diffractive optic. In the five-beam geometry, beams 1 and 2 are displaced by 2.4 cm and 3.5 cm from the center of the mirror, respectively. The difference in focal lengths induced by spherical aberration for this pair of beams is 0.2 mm (beams 1 and 2 respectively focus 40.02 and 40.04 cm from the imaging mirror). The effects of spherical aberration are minimal, because the 7-mm depth of focus is large compared to the 0.2-mm displacement in the focal position. Thus, the beams propagate through the 0.22-mm thick sample with a negligible change in diameter.

4.2.3. Signal Detection

In all experiments, signals are detected using a back-illuminated CCD array (Princeton Instruments PIXIS 100B) mounted on a 0.3-meter spectrograph with a 1200-g/mm grating. The signal beam is focused to a spot size of 100 μm at the entrance to the spectrograph to obtain hardware-limited spectral resolution of approximately 10 cm^{-1}. Ultimately, the resolution of the measurement is limited by the 50-cm^{-1} spectral width of the Raman pump beam. The FWHM spot sizes of all laser beams are 200 μm at the sample position. Pulse energies of the actinic pump and Raman pump pulses are 150 nJ and 200 nJ, respectively. The pulse energy of the Stokes beam is 50 nJ. Under these conditions, the total six-wave mixing signal produces 5000 counts on the detector with an integration time of 100 ms under our experimental conditions. The

FSRS response is typically 10-20% of the total signal strength (i.e., the majority of the signal field is a broadband pump-repump-probe response). The noise level in each spectrum is less than 20 counts.

4.2.4. Sample Handling

Myoglobin from horse skeletal muscle is purchased from Sigma-Aldrich. The protein is dissolved in 0.1-M sodium phosphate buffer at a pH of 7.0. The solution is centrifuged at 6000 revolutions per minute for 5 minutes before experiments to optimize the optical quality. In all experiments except for those described in Section 3.2, the 0.2-mM sample of metMb is flowed through a wire-guided jet with a thickness of 220 μm, where the reservoir volume is 50 mL. Absorbance spectra are measured before and after experiments to confirm the absence of sample degradation. We do not observe changes in the absorbance spectrum of the solution during experiments that require several hours.

Investigation of the concentration dependence of the signal intensity in Section 4.1 requires an approach in which the solutions are quickly exchanged without moving the sample holder. To this end, we mounted an aluminum adaptor plate with a slot for a cuvette on a spinning rotation mount (spins at a rate of 720º per second). This setup allows a cuvette with a 0.5-mm path length to be removed and put back into the same position when the samples are exchanged and/or the cuvette is cleaned. FSRS signals are readily detected in this setup; however, we find that it is more susceptible to scattered light than the jet.

4.3. Signal Processing

4.3.1. Algorithm

Figure 4.4 illustrates the signal processing algorithm used in this work with a six-wave mixing signal acquired in the five-beam geometry. The total signal intensity shown in Figure 4.4(a) exhibits dispersive line shapes, which is a signature of interference between broadband

(pump-repump-probe) and FSRS responses. The origin of the interference can be understood by considering the total signal intensity, $I_{total}(\omega)$, as a sum of three terms,

$$I_{total}(\omega) = \left| E_{BB}(\omega) + E_{FSRS}(\omega) \right|^2 = I_{BB}(\omega) + I_{FSRS}(\omega) + 2\,\text{Re}\left\{ E_{BB}(\omega) E_{FSRS}(\omega) \right\}, \quad (4.1)$$

where $E_{BB}(\omega)$ and $E_{FSRS}(\omega)$ represent the broadband and FSRS components of the signal field ($I_{BB}(\omega)$ and $I_{FSRS}(\omega)$ are signal intensities). The third term in Equation 4.1 is responsible for the dispersive vibrational line shapes in the signal spectrum. In Figure 4.4(a), the broadband baseline, $I_{BB}(\omega)$, is obtained by Fourier transforming the total signal intensity, $I_{total}(\omega)$, into the time domain and filtering the peak at 0 fs (see Figure 4b). Subtraction of the baseline isolates the third term in Equation 4.1,

$$I_{total}(\omega) - I_{BB}(\omega) \approx 2 \left| E_{BB}(\omega) \right| \left| E_{FSRS}(\omega) \right| \cos\left[\varphi_{BB}(\omega) - \varphi_{FSRS}(\omega) \right], \quad (4.2)$$

where $\varphi_{BB}(\omega)$ and $\varphi_{FSRS}(\omega)$ are the phases of the broadband and FSRS signal components. Here, we have assumed that $I_{BB} \gg I_{FSRS}$, which is a good approximation in systems with modest mode displacements such as myoglobin.[42] Dominance of the term on the right side of Equation 4.2 is consistent with the dispersive line shapes observed in the measured signals (I_{FSRS} does not possess a dispersive line shape). In systems with large mode displacements, the term linear in the field component, $E_{FSRS}(\omega)$, can be obtained using an external local oscillator that is delayed with respect to the Stokes pulse. The fringe spacing associated with $E_{FSRS}(\omega)$ will be unique in such an implementation, so it can be isolated with a Fourier filter. Such an interferometric detection scheme has been demonstrated in a previous four-wave mixing experiment.[43]

Dependence of the signal on the phase difference, $\varphi_{BB}(\omega) - \varphi_{FSRS}(\omega)$, can be eliminated

by applying a second filter function to the inverse Fourier transform of the baseline-subtracted

signal (see Figure 4.4(c)). The filter in Figure 4.4(c) is displaced from the origin by 60 fs in order

to eliminate the residual broadband response. As shown in Figure 4.4(d), Fourier transformation

of the signal back to the frequency domain yields a complex signal field in which phase

information can be eliminated by taking the absolute value,

$$\left| E_{FSRS}(\omega) \right| \propto I_{BB}^{-1/2}(\omega) \left| E_{BB}(\omega) E_{FSRS}(\omega) \exp\left[i\varphi_{BB}(\omega) - i\varphi_{FSRS}(\omega) \right] \right|. \tag{4.3}$$

In Equation 4.3, the magnitude of the FSRS response, $\left| E_{FSRS}(\omega) \right|$, is obtained by

multiplication of $\left| E_{BB}(\omega) E_{FSRS}(\omega) \right|$ and $I_{BB}^{-1/2}$. Equation 4.3 also makes clear one of the

tradeoffs associated with the present technique. The phase of the FSRS response, $\varphi_{FSRS}(\omega)$,

cannot be obtained without knowledge of $\varphi_{BB}(\omega)$, which is a τ_1-dependent quantity.

Traditional FSRS is not subject to this limitation, because the signal is heterodyne-detected with

the residual Stokes pulse.[17]
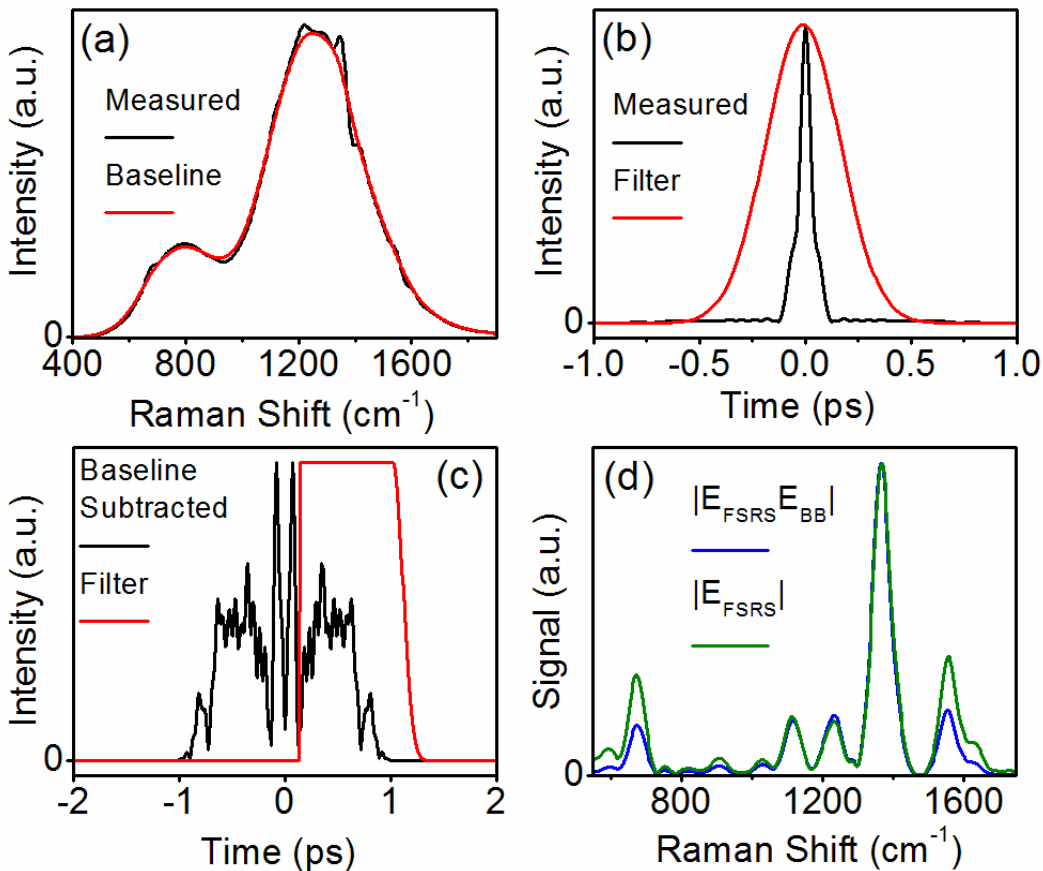
Figure 4.4. *(a) This six-wave mixing signal for metMb is obtained in the five-beam FSRS geometry with $\tau_2 = 290\,fs$. The broadband baseline is subtracted to isolate the vibrational component of the response. (b) The baseline in panel (a) is obtained by inverse Fourier transforming the measured signal into the time domain, then filtering the broadband part of the response at 0 fs. (c) The baseline-subtracted signal is filtered at positive times after inverse Fourier transformation of the difference between the measured signal and the baseline shown in panel (a). The filter is displaced from the origin by 60 fs to eliminate the residual broadband response, which is dominant at earlier times. (d) The absolute value of the FSRS spectrum is obtained by Fourier transformation of the filtered signal in panel (c).*

The Raman spectrum obtained in Figure 4(d) exhibits several known vibrational resonances of metMb.[44] The 670 and 1370-cm[-1] modes correspond to deformation and bond-stretching motions localized on the tetrapyrrole moiety, respectively. The remaining resonances are primarily localized on the vinyl substituents of the tetrapyrrole group shown in Figure 4.5. Intensities of the resonances in the 1000-1300 cm^{-1} range are enhanced in the present technique,

because they coincide with the peak of the Stokes spectrum. In contrast, the peak intensities observed in traditional FSRS are independent of the Stokes intensity.[17]
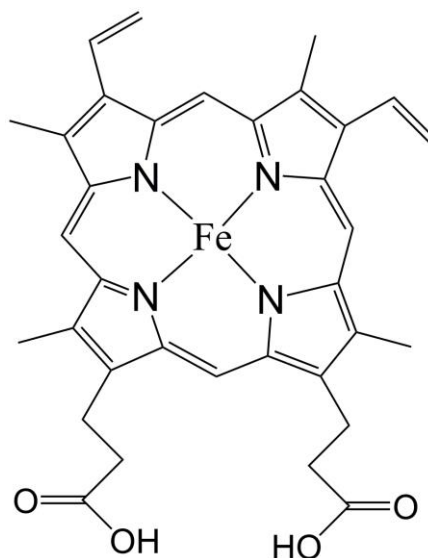
Figure 4.5. Molecular structure of iron protoporphyrin-IX.

In principle, an external (i.e., τ_1-independent) reference field may be used to eliminate $\varphi_{BB}(\omega)$ from consideration.[45] Such an approach is challenged by several technical issues. One problem particular to the present five-beam geometry is that no beam produced by the diffractive optic is perfectly collinear with the signal (there is at least a 0.5° deviation for the beam whose wavevector is most closely matched to that of the signal). Additional cross terms will also appear in Equation 4.1 if an external reference field is introduced, so a different baseline subtraction algorithm would need to be devised. We are presently working on solutions to these challenges. One key to success may be reduction of the ratio, $|E_{FSRS}(\omega)|/|E_{BB}(\omega)|$, perhaps by using shaped Raman pump pulses.[46]
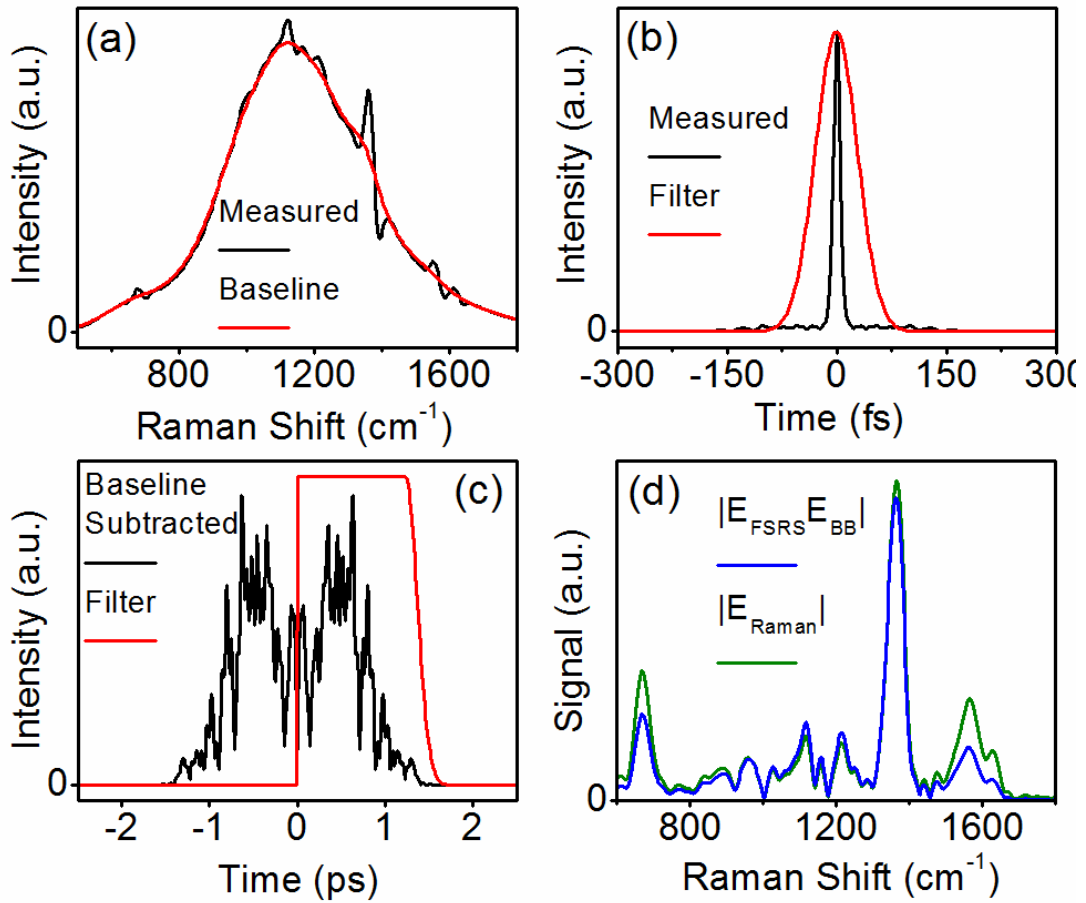
Figure 4.6. *This six-wave mixing signal for metMb is obtained in the five-beam FSRS geometry with $\tau_2 = 420\,fs$ The panels (a)-(d) are defined in the same way as those in Figure 4.4. The vibrational frequencies obtained in this measurement differ by less than 10 cm^{-1} from those found in Figure 4. This difference is 5 times less than the bandwidth of the Raman pump pulse (i.e., intrinsic frequency resolution). The vibrational line widths are roughly 25% less than those shown in Figure 4.4. This decrease in the line width with increasing delay, τ_2, is consistent with the theory outlined in Section 4.5.*

4.3.2. Adequate Suppression of the Broadband Response

The key to success of the baseline subtraction method is adequate suppression of the broadband pump-repump-probe response. This undesired nonlinearity can be suppressed by increasing the delay between Raman pump pulses, τ_2. An increase in this delay increases the probability that the final field-matter interaction occurs with the final Raman pump pulse to

136

arrive at the sample (see Figure 4.1). This order of field-matter interactions is unique to the FSRS response (see Section 4.5); the last field-matter interaction occurs with the Stokes pulse in the undesired pump-repump-probe response.[47] A compromise must be made between signal intensity and background suppression, because the amplitude of the FSRS response also increases as τ_2 increases (the FSRS signal vanishes when τ_2 is longer than the inverse of the vibrational line width).

In Figure 4.6, a FSRS signal acquired with $\tau_2 = 420$ fs is presented. The signal count rate is roughly 4 times lower than that associated with the measurement in Figure 4.4, and the integration time has been doubled to 200 ms. The contribution of the FSRS response to the total signal is approximately 3-5 times larger than that found with the delay, $\tau_2 = 290$ fs, in Figure 4.4. This reduces the magnitude of the broadband response near 60 fs in Figure 6(c), and there is no need to displace the apodization window from time-zero. The vibrational resonance frequencies displayed in Figures 4.4(c) and 4.6(c) are indistinguishable, thereby confirming the theoretically predicted independence of the resonance frequency on the delay, τ_2. Small displacements in the apodization window do not alter the frequencies of the vibrational resonances, because the information is primarily located at times greater than 60 fs (i.e., the vibrations damp as the magnitude of the time axis increases).

In the theory outlined in Section 4.5, it is predicted that the line width decreases as the delay, τ_2, increases. Consistent with this prediction, we find that the line widths decrease from approximately 60 cm^{-1} to 45 cm^{-1} when the delay, τ_2, increases from 290 and 420 fs. Related line-narrowing effects have been discussed in the context of sum-frequency generation

techniques that combine broadband and narrowband laser pulses.[48] We have also examined this

issue numerically in a study of short-lived electronic coherences in molecular aggregates.[49]

Essentially, the temporal decay of the polarization is determined by the product of the vibrational

coherence, which is initiated when the Stokes pulse arrives at the sample, and the envelope of the

final Raman pump pulse to arrive at the sample (see Figure 4.1(b)). Both quantities decay

simultaneously when $\tau_2 = 0$ fs, and the measured line width is generally broader than the

bandwidth of the Raman pump. However, the envelope of the Raman pump rises as the

vibrational coherence decays when $\tau_2 > 0$ fs. This convolution artificially inflates the duration of

the polarization, thereby reducing the vibrational line width.

It is worth noting that the suppression of the broadband response in the present

implementation is limited by the time-symmetric envelopes of the Raman pump pulses. Overlap

between the two Raman pump pulses can be further reduced significantly using etalons. Such an

approach has already been successfully demonstrated in the traditional three-beam FSRS

geometry.[46]

4.3.3. Summary of Technical Issues Involved in Signal Processing

In summary, FSRS spectra are obtained using the data processing algorithm described

above. Key points made in this section are summarized below.

(i) Success of the algorithm requires suppression of the broadband pump-repump-probe response

using a delay between the two Raman pump pulses. The ratio of the FSRS to broadband response

increase as the delay, τ_2, increases (see Figure 4.4 and 4.6); however, the overall magnitude of

the signal intensity decreases as well. Thus, a compromise between signal strength and

background suppression must be made.

(ii) An increase in the delay, τ_2, induces a line-narrowing effect. This observation is consistent with theory presented in Section 4.5.

(iii) The vibrational resonance frequencies are unaffected by the delay, τ_2. The vibrational coherences are induced before the final Raman pump pulse arrives at the sample.

(iv) In principle, the relative magnitudes of the vibrational resonances may depend on τ_2. The amplitudes of vibrational resonances with the broadest line widths (fastest dephasing times) should decrease the most as τ_2 increases. Notably, the amplitudes of the vibrational resonances reflect the intensity of the Stokes pulse in the four and five-beam geometries. In contrast, the relative amplitudes are independent of the Stokes spectrum in traditional three-beam FSRS, where the Stokes pulse is uses for heterodyne detection.

(v) Further suppression of the broadband pump-repump-probe response can likely be achieved by reducing the overlap in the Raman pump pulses using etalons. Further suppression of the broadband response will enable interferometric detection with an external local oscillator.[43] Signs of the vibrational resonances can then be determined.

4.4. Experimental Results

4.4.1. Dependence of FSRS Signal on Incident Pulse Energies

In this section, we examine the dependence of the signal strength on the intensities of the incident laser beams. As in traditional FSRS, the Raman response, $|E_{FSRS}(\omega)|$, must scale linearly with both I_{AP} and I_{RP}, where I_{AP} and I_{RP} are the intensities of the actinic and Raman pump beams (these intensities represent sums for pulse-pairs 1,2 and 3,4). The broadband response, $|E_{BB}(\omega)|$, must also scale linearly in both I_{AP} and I_{RP}, because it represents a fifth-order

nonlinearity (i.e., a pump-repump-probe signal). Unlike traditional FSRS, $\left|E_{FSRS}(\omega)\right|$ and

$\left|E_{BB}(\omega)\right|$ scale as the square root of the Stokes intensity, $I_{St}^{1/2}$, because the signal is not obtained

by differential transmission of the Stokes beam.[17]
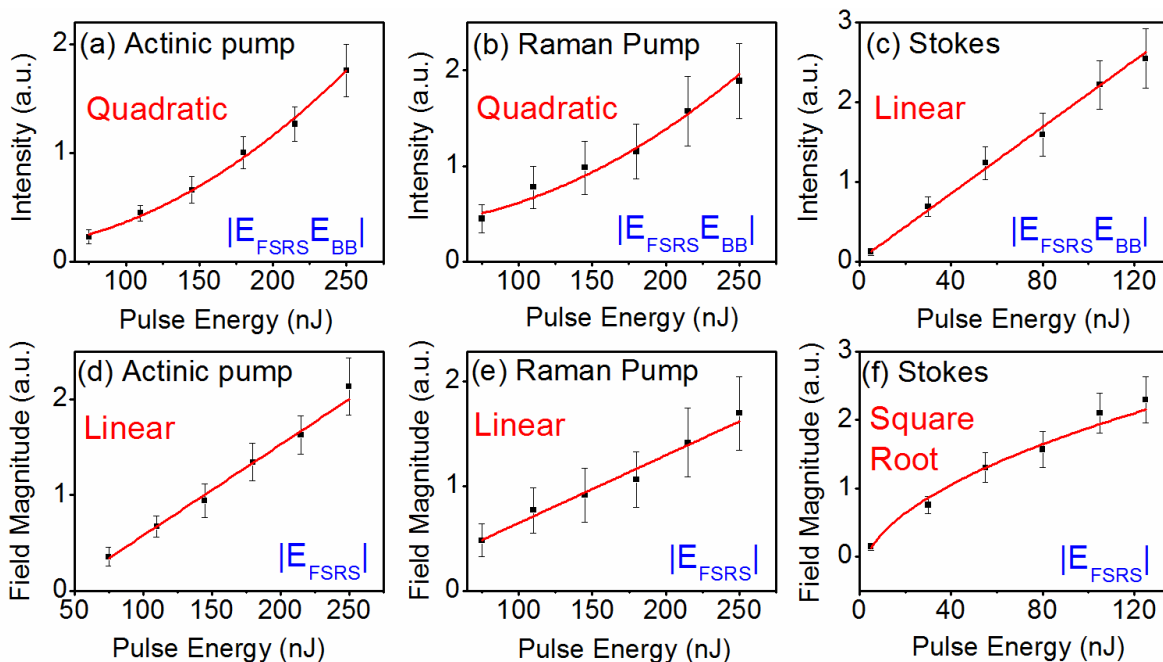
Figure 4.7. *Signal intensities corresponding to the vibrational resonance at 1370 cm^{-1} are plotted versus incident pulse energies. In the first row, the signal, $\left|E_{FSRS}(\omega)E_{BB}(\omega)\right|$, is plotted versus energies of (a) actinic pump, (b) Raman pump, and (c) Stokes beams. In the second row, the signal, $\left|E_{FSRS}(\omega)\right|$, is plotted versus energies of the (d) actinic pump, (e) Raman pump, and (f) Stokes beams. Pulse energies associated with the actinic and Raman pump represent sums for the respective pairs of beams at the sample position (i.e.,beams 1 and 2 or beams 3 and 4). The functional forms used to fit the data (red lines) are indicated in the respective panels. These data validate the signal processing algorithm described in Section 4.3 and confirm that saturation of the optical response is negligible in these ranges of the pulse energies.*

Figure 4.7 displays both $\left|E_{FSRS}(\omega)E_{BB}(\omega)\right|$ and $\left|E_{FSRS}(\omega)\right|$ obtained for the 1370-cm^{-1}

mode, which represents in-plane stretching of the tetrapyrrole moiety,[44] with respect to I_{AP},

I_{RP}, and I_{St}. The pulse energies are cycled within the respective ranges three times and 30

spectra are accumulated at each pulse energy within each cycle (i.e., each point in Figure 4.7

represents a total of 90 spectra or 9000 laser shots). The error bars are determined by computing standard deviations in the signal intensities for the 30 spectra acquired at each pulse energy then propagating the error for each of the three cycles. Experiments conducted on different days yield indistinguishable results. As expected, the measurements in Figure 4.7 suggest that $\left| E_{FSRS}\left(\omega\right) E_{BB}\left(\omega\right) \right|$ and $\left| E_{FSRS}\left(\omega\right) \right|$, scale as $I_{AP}^2 I_{RP}^2 I_{St}$ and $I_{AP} I_{RP} I_{St}^{1/2}$, respectively. The form of the function used to fit the data is indicated in each Figure panel. In all cases, fits conducted with the assumed functions are within the uncertainty ranges of the data. In principle, the functional forms may be better characterized by examination of a larger ranges in pulse energies; however, this cannot be achieved here without the potential for artifacts caused by sample degradation. We find that the sample degrades during the experiment if the upper limit of each pulse energy in Figure 4.7 is doubled.

4.4.2. Dependence of FSRS Signal on Sample Concentration

Determination of the dependence of the FSRS signal on solute concentration is one way to rule out contributions from third-order cascades.[50-51] At extremely low optical densities (less than 0.1), the direct (fifth-order) FSRS signal intensity scales as the square of concentration, whereas third-order cascades scale as the fourth power of the concentration. However, saturation effects related to absorption of the incident beams and signal take hold at the optical densities where the experiments are usually conducted (0.7-1.0). Therefore, as in our recent study of triiodide,[35] we develop a simple model in this section to capture the dependence of the signal intensity on concentration. Predictions of the model are then compared to experimental data.

The direct fifth-order signal intensity at position x in the sample is subject to the relation,

$$I_{direct}^{(5)}\left(x,C\right) \propto C^2 \left| \chi^{(5)} \right|^2 I_{AP}^2\left(x,C\right) I_{RP}^2\left(x,C\right) I_{St}\left(x,C\right), \qquad (4.4)$$

where C is concentration and $\chi^{(5)}$ is the fifth-order susceptibility. The laser intensity is given by

$$I_j(x,C) \propto \exp\left(-\alpha_j C x\right), \tag{4.5}$$

where α_j is an absorption coefficient (product of $\ln(10)$ and the molar extinction coefficient) and j denotes the type of laser pulse (RP, AP, or St). The signal intensity accumulated at the exit of the sample is obtained by integrating over x,

$$I_{direct}^{(5)}(C) \propto C^2 \int_0^a dx I_{AP}^2(x,C) I_{RP}^2(x,C) I_{St}^2(x,C) \exp\left[\alpha_{St} C(x-a)\right], \tag{4.6}$$

where a is the path length and the exponential function represents attenuation of the signal beam as it exits the sample. The susceptibility can be removed from the proportionality in Equation 4.6 because it is independent of x.

Treatment of the cascaded signal field must take into account accumulation of both the primary and secondary third-order signal intensities. For the cascaded process that the five-beam geometry is most susceptible to, the primary four-wave mixing signal intensity scales according to $I_{AP}^2(x,C) I_{St}(x,C)$. The intensity of the secondary four-wave mixing process depends on the product of $I_{RP}^2(x,C)$, which decreases exponentially with x, and the intensity of the primary four-wave mixing signal (denoted as $I_{primary}^{(3)}(x,C)$), which increases in a (slightly) sub-quadratic fashion with x at the optical densities of interest. With consideration of these factors, the cascaded signal intensity may be written as

$$I_{cas}(C) \propto C^2 \int_0^a dx I_{RP}^2(x,C) \exp\left[\alpha_{St} C(x-a)\right] I_{primary}^{(3)}(x,C), \tag{4.7}$$

where the primary four-wave mixing signal intensity at position x is proportional to

$$I_{primary}^{(3)}(C,x) \propto C^2 \int_0^x dx' I_{AP}^2(x',C) I_{St}(x',C) \exp\left[\alpha_{St} C(x'-a)\right]. \qquad (4.8)$$
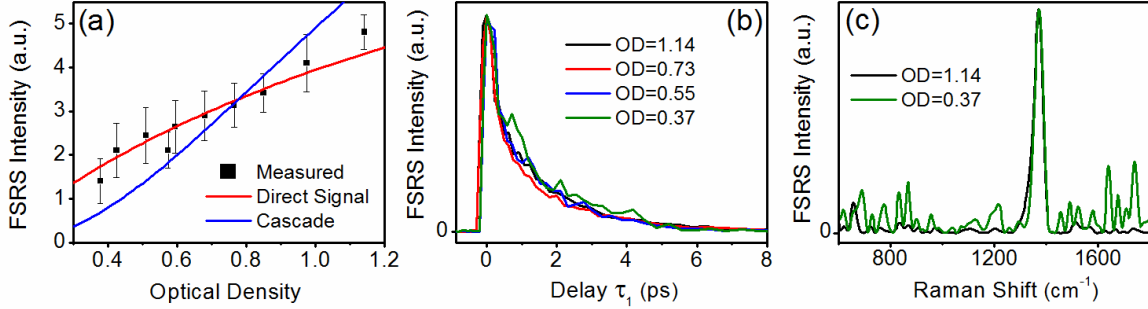
Figure 4.8. *(a) FSRS signal intensities associated with the vibrational resonance at 1370 cm^{-1} are plotted versus the optical density of the solution in a 0.5-mm path length. The functions, $I_{direct}^{(5)}(C)$ and $I_{cascade}(C)$, illustrate how the data compare to the concentration dependence predicted for (red) the direct fifth-order signal and (blue) third-order cascades. The functions, $I_{direct}^{(5)}(C)$ and $I_{cascade}(C)$, are multiplied by constants to overlay them with the measured signal intensities. (b) Dynamics in the peak intensity at 1370 cm^{-1} are experimentally indistinguishable at various sample concentrations. (c) Signal intensities are overlaid at the highest and lowest concentrations to illustrate the range in the data quality.*

The signal intensity at $\tau_1 = 1$ ps is plotted versus the optical density of the solution at 410 nm in Figure 4.8. Saturation of the measured signal intensity with increasing optical density is caused by absorption of the incident laser beams. $I_{direct}^{(5)}(C)$ and $I_{cascade}(C)$ are overlaid on the experimental data to illustrate how these functional forms compare to the measurements. The data are more consistent with the model based on the direct fifth-order signal. Figure 4.8(b) additionally shows that the dynamics are insensitive to the concentration. Notably, the dynamics in the signal observed at an OD of 0.37 are due noise (not a vibrational coherence). It should also be noted that if the direct and cascaded signals are comparable in magnitude, then signatures of destructive interference between these nonlinearities should be found in the concentration dependence, because direct and cascaded signals have opposite signs.[35] The data show no signs of such interference. FSRS spectra overlaid at the highest and lowest concentrations demonstrate

the range in signal quality in Figure 4.8(c). The best signal quality is generally obtained at optical densities near 1.0. The narrow spectral features observed at an OD of 0.37 are caused by noise. These features are not caused by the shape of the Fourier filter, which is the same for all values of the OD.

4.4.3. Relative Signs of Third- and Fifth-Order Signals

In this section, we present an experimental test for third-order cascades that takes into account the approximate 180º phase-difference between the direct third- and fifth-order signal fields under resonant conditions.[35, 51] This phase-relationship can be understood with simple bookkeeping on the numbers of field-matter interactions and light emission events. Under resonant conditions, a 90º phase-shift is accumulated in each time-interval between field-matter interactions. In a background-free experiment, the number of incoming beams is simply multiplied by 90º (270º and 450º at third- and fifth-order). Thus, approximate phase-shifts of 360º and 540º are respectively accumulated in direct third- and fifth-order processes when the signal field emission events are accounted for (field emission adds 90º). Direct third- and fifth-order nonlinearities therefore have opposite signs, because their phases differ by 180º. It is useful to consider that essentially the same idea applies to traditional experiments such as pump probe spectroscopy. For a two-level system, the sign of light transmission changes when a sample is exposed to a pump beam due to ground-state depletion (i.e., a comparison of first and third-order responses). The sign of the signal again changes if a second pump beam is introduced in a pump-repump-probe experiment (i.e., pump-repump-probe signals are absorptive in two-level systems).[52]

In a cascaded nonlinearity, a phase-shift of approximately 540º is accumulated through the total of 6 (perturbation-theoretic) time-evolution intervals involved in the process. An additional phase-shift of 180º degrees must be added for the two emission events, which results

in a total of 720°. *Thus, the phase of the absorptive component of the cascaded nonlinearity differs from those associated with the direct third- and fifth-order signals by approximately 0° and 180°, respectively.* This is a convenient relationship, because the third-order signal can serve as an "internal standard" for the signal phase.[39-41] The key is to employ a geometry in which the third- and fifth-order signals are equally phase-matched, so that significant phase-shifts are not accumulated through propagation in the medium. The four-beam geometry shown in Figure 4.3(b) satisfies this criterion, because both interactions with the actinic pump take place with a single beam. Previous experiments have similarly made use of four-beam geometries in which the signal phase is referenced to that of a background-free third-order signal.[39-41]
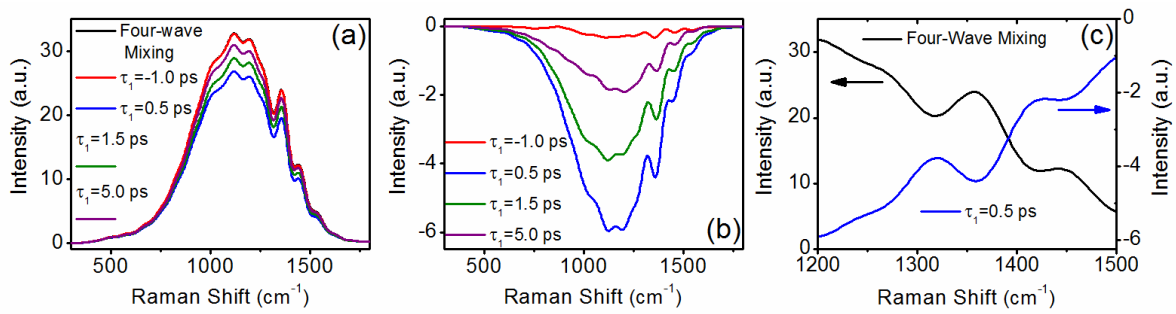
Figure 4.9. *(a) Signals acquired in the four-beam geometry at various delay times between the actinic pump and Stokes pulses, τ_1. The signal at τ_1 =-0.5 ps is indistinguishable from the four-wave mixing signal measured with actinic pump pulse blocked. (b) The fifth-order signal is obtained by computing differences between signals acquired with the actinic pump unblocked and blocked (i.e., pump on – pump off). Depletion of the ground state population with the actinic pump pulse is a signature that the direct fifth-order FSRS signal field is measured. In contrast, third-order cascades would induce an increase in the total signal intensity, because such nonlinearities are in-phase with the third-order response. (c) Oscillatory features associated with the vibrational resonances are phase-shifted by approximately 180° in third- and fifth-order measurements (these are magnified views of the data in panels (a) and (b)).*

Figure 4.9(a) presents the total signal intensity measured at various delays between the actinic pump and the Stokes pulses, τ_1, in the four-beam geometry. The four-wave mixing signal obtained with the actinic pump beam blocked is also presented as a reference. The four-beam signal is indistinguishable from the four-wave mixing signal at negative delay times, but a

decrease in the total signal intensity is observed at positive delay times. Observation of a decrease in signal intensity is expected because of the sign reversal that takes place in the direct third- and fifth-order signals. That is, Figure 4.9(a) indicates that the direct third- and fifth-order signals interfere destructively. The difference, actinic-pump-on/actinic-pump-off, shown in Figure 4.9(b) represents the direct fifth-order signal (i.e, the third-order contribution has been removed in the difference). The third- and fifth-order line shapes are additionally overlaid in Figure 4.9(c) to illustrate the reversal in the signal sign.

We interpret the data shown in Figure 4.9 by considering the following components of the total signal intensity,

$$\left|E^{(3)}+E^{(5)}+E_{cas}\right|^2 \approx \left|E^{(3)}\right|^2 + 2\left|E^{(3)}\right|\left|E^{(5)}\right|\cos\left(180^\circ\right) + 2\left|E^{(3)}\right|\left|E_{cas}\right|\cos\left(0^\circ\right), \qquad (4.9)$$

where it is assumed that the direct third-order signal field, $E^{(3)}$, is large compared to the direct fifth-order and cascaded responses, $E^{(5)}$ and E_{cas}. The second and third terms on the right side of Equation 4.9 have negative and positive signs, respectively. An actinic pump-induced decrease in signal intensity is predicted if $\left|E^{(5)}\right| >> \left|E_{cas}\right|$, whereas an increase in signal intensity is predicted if $\left|E_{cas}\right| >> \left|E^{(5)}\right|$. The 180° phase-shift associated with the second term on the right side of Equation 4.9 is generally valid, because the direct third- and fifth-order signals have the same amounts of phase mismatch in the four-beam geometry. However, the 0° phase-shift in term 3 is dependent on the sample thickness and amount of phase mismatch for particular cascades. Therefore, we have also confirmed that the same signal sign is measured at path lengths of 0.2, 0.3, and 0.5 mm.

In addition to the perspective suggested by Equation 4.9, it may also be useful to consider the signal phase in terms of the ground-state depletion induced by the actinic pump pulse. Each

molecule involved in a third-order cascade possesses independent populations. For this reason, depletion of the ground state population by the actinic pump on one molecule does not reduce the magnitude of the cascaded nonlinearity. Rather, increasing the intensity of the actinic pump (i.e., increasing ground state depletion for one of the molecules involved in the cascade) should increase the total signal intensity if cascades are dominant. The actinic pump-induced decrease in the signal intensity found in Figure 4.9 is therefore inconsistent with dominance of third-order cascades.

4.4.4. Dynamic Line Shapes of FSRS Signals Obtained by Six-Wave Mixing

In this section, the sensitivity and data acquisition rate of our method are demonstrated by measuring decay profiles of vibrational resonances in metMb. We also compare FSRS signals acquired in the five-beam geometry with cascaded responses simulated using experimental four-wave mixing signals. Simulations of this type were instrumental in identifying signatures of cascades in off-resonant experiments conducted on pure liquids. We also employed similar approach in a recent multidimensional resonance Raman study of triiodide.[35]

FSRS signals acquired for metMb in the five-beam geometry are presented in Figure 4.10. These data represent the average of two different data sets. In each data set, the τ_1 delay is scanned 30 times in 15 minutes, and 200 points are acquired in each scan. Inspection of the contour plot makes clear that all vibrational resonances fully decay within 10 ps. Figure 4.10(b) overlays distributions of relaxation times obtained for modes at 670, 1120, 1370, and 1600 cm^{-1} using the maximum entropy method (MEM).[53] Analysis by MEM is motivated by avoidance of assumptions about the shapes of decay profiles. Although powerful, the MEM is not often used in analysis of femtosecond transients, because it requires exceptionally high signal-to-noise ratios. The 670 and 1370-cm^{-1} resonances represent in-plane modes that are located on the

147

tetrapyrrole moiety, whereas many of the weaker resonances in the 1000-1300 cm^{-1} and 1400-1650 cm^{-1} wavenumber ranges are localized on the vinyl substituents.[44] Intensities of the resonances in the 1000-1300 cm^{-1} range are enhanced in the present experiments (compared to spontaneous Raman or traditional FSRS), because the intensity of the Stokes pulse maximizes in this range (see Figure 4.2).
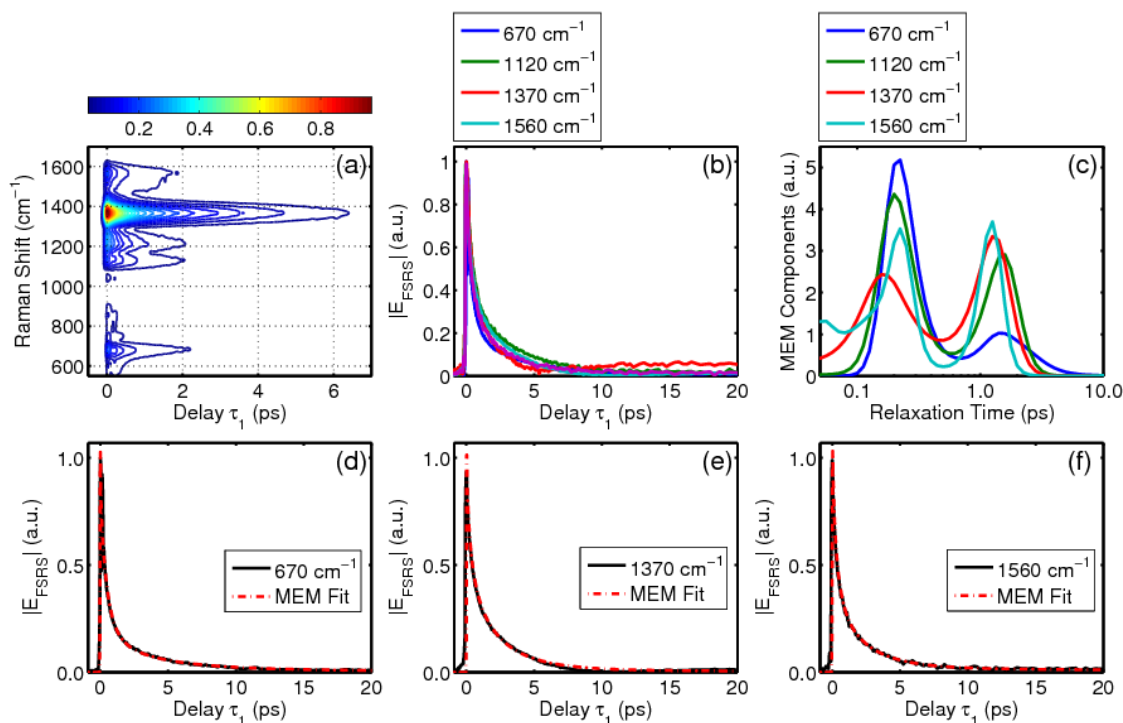
Figure 4.10. *(a) Contour plot of signal field magnitude, $|E_{FSRS}|$, obtained for metMb in the five-beam geometry. (b) Temporal decay profiles for vibrational resonances detected in FSRS response. (c) Distributions of relaxation times for various resonances are obtained using the maximum entropy method. (d)-(f) FSRS signal field magnitudes are overlaid with fits conducted using the maximum entropy method.*

Chergui and co-workers have recently identified two relaxation pathways in metMb that possess nearly equal efficiencies.[23] One pathway repopulates the ground state by way of sub-ps internal conversion from a high-energy charge transfer state, whereas the second pathway proceeds through a number of intermediate iron spin states. Importantly, transient electronic resonances associated with both pathways overlap with the frequencies of the laser pulses

employed in this work (see Figure 4.2). The FSRS experiments described in this section should therefore be sensitive to excited state relaxation even though the nonlinear response near 430 nm possesses significant contributions from the bleach of the Soret band.

The MEM analysis displayed in Figure 10(c) reveals peaks in the kinetic distributions near 0.22 ps and 1.4 ps for all vibrational modes. The peaks in the distributions centered near 0.22 ps encompass the time scales associated with two processes: (i) back-electron transfer between Fe^{2+} and the porphyrin; (ii) ground state recovery via a high-energy charge-separated excited state.[23] The peaks in the MEM distributions centered near 1.4 ps may reflect contributions from the second relaxation pathway, wherein an intermediate iron spin state (with S=1/2) is depopulated with a time constant of 1.1 ps. It is also possible that vibrational cooling dynamics contribute to this second peak in the MEM distribution.[54]

The relative amplitudes of the two peaks in the MEM distributions are fairly similar for the resonances associated with the vinyl substituents (1120 and 1560 cm^{-1}). However, the vibrational modes located on the tetrapyrrole (670 and 1370 cm^{-1}) differ markedly in the relative amplitudes of the two peaks, with the 670 cm^{-1} mode possessing a dominant 0.22-ps component. The signal intensity observed for a particular mode in FSRS reflects the dynamic resonance Raman cross section, which is governed by the *difference* in nuclear geometries associated with the pair of electronic states that comprise the resonance (i.e., difference in potential energy gradients). It is possible that the differences in the relaxation rates observed for various resonances reflect mode-specific details the internal conversion mechanisms in the system. That is, at short delay times, before a significant amount of vibrational cooling has occurred, the non-equilibrium distributions of vibrational quanta found in metMb may reflect the propensities for particular coordinates to act as "promoting modes" in the internal conversion processes.
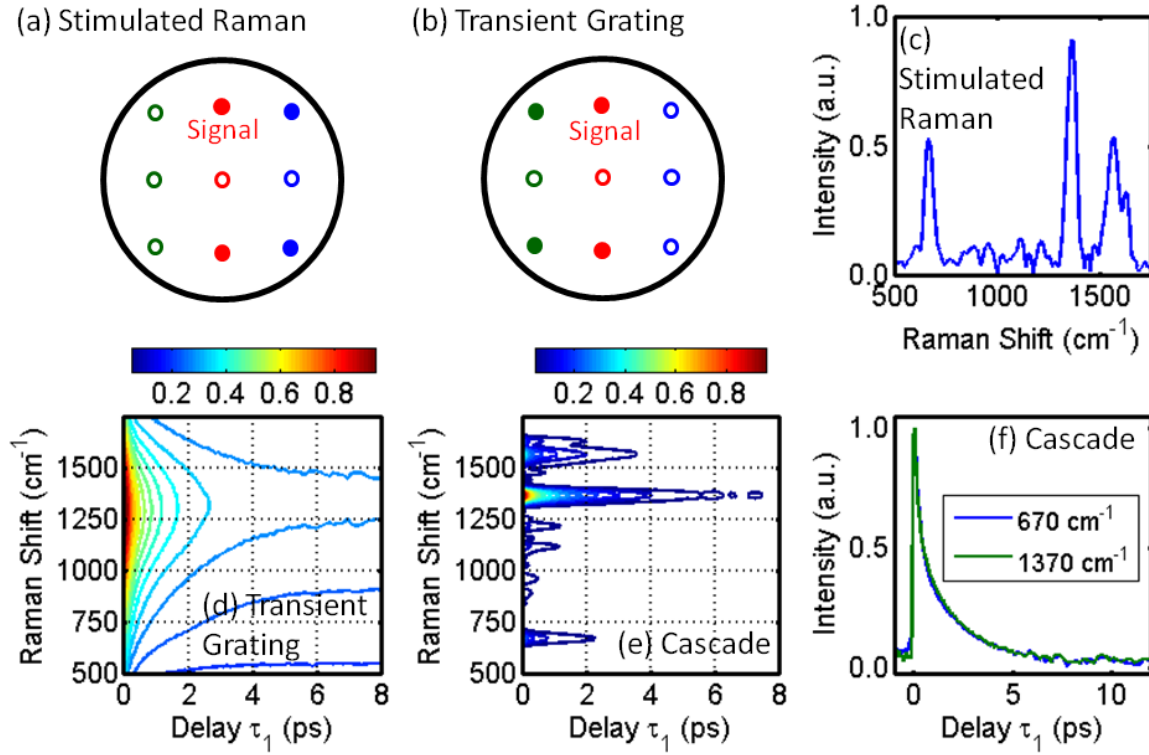
Figure 4.11. *Laser beam geometries used to acquire (a) stimulated Raman and (b) transient grating signals shown in (c) and (d), respectively. Beams represented with solid circles reach the sample, whereas those represented with open circles are blocked with a mask. (e) The two four-wave mixing signals are combined to simulate the cascaded response. (f) Unlike the FSRS signals plotted in Figure 4.10, all vibrational resonances decay with indistinguishable temporal profiles in the simulated cascade. Signal magnitudes for the 670 and 1370-cm^{-1} vibrational resonances are shown as examples.*

As a final experimental test for cascaded nonlinearities, we compare signals simulated with experimental four-wave mixing responses to those presented in Figure 4.11. This empirical approach does not require knowledge of the form of the optical response function or associated parameters. We assume only that the cascaded process combines a transient grating response (involving the actinic pump and Stokes) with a stimulated Raman response (involving the Raman pump and Stokes). This assumption is consistent with calculated phase mismatch factors discussed below. Both of these four-wave mixing responses, which are denoted here as $S_{TG}(\omega_t)$ and $S_{SRS}(\omega_t)$, are readily measured by blocking the appropriate beams in the interferometer

shown in Figure 4.3. The cascaded signal field is then generated with the product,

$$S_{CAS}\left(\tau_1,\omega_t\right)=S_{TG}\left(\tau_1,\omega_t\right)S_{SRS}\left(\omega_t\right).$$

The two four-wave mixing responses, $S_{TG}\left(\tau_1,\omega_t\right)$ and $S_{SRS}\left(\omega_t\right)$, and the cascade,

$S_{CAS}\left(\tau_1,\omega_t\right)$, are shown in Figure 4.11. The four-wave mixing Raman spectrum, $S_{SRS}\left(\omega_t\right)$,

appears similar to the six-wave mixing FSRS spectrum (at a fixed delay time), which is to be

expected because the same Franck-Condon active modes contribute to both nonlinearities. In

agreement with recent work on metMb,[23] the signal, $S_{TG}\left(\tau_1,\omega_t\right)$, decays within a few

picoseconds. The simulated cascade, $S_{CAS}\left(\tau_1,\omega_t\right)$, obtained by combining $S_{TG}\left(\tau_1,\omega_t\right)$ and

$S_{SRS}\left(\omega_t\right)$ exhibits negligible changes in the Raman spectrum during the relaxation process (i.e.,

the overall amplitude changes but the spectrum does not). Time-invariant Raman spectra are

inconsistent with the mode-specific transients displayed in Figure 4.10.

In summary, the present analysis suggests that cascades radiated in the 600-1700-cm[-1]

range in metMb will possess Raman spectra that are insensitive to the delay time. In other words,

the relative amplitudes of the various peaks will be insensitive to the delay time. Such delay-

independent Raman spectra are inconsistent with the measured FSRS signals shown in Figure

4.10. More generally, we anticipate that cascades will be distinguishable from direct processes in

related heme proteins, where the relative magnitudes and frequencies of the peaks are known to

evolve during the vibrational cooling process.[16]

4.5. Theoretical Analysis of Relative Magnitudes of Resonant FSRS Signals and Cascades

In this section, we use model calculations to compare direct fifth-order and cascaded

third-order signal strengths for a model system that approximates metMb. All experimental tests

conducted above are consistent with dominance of the direct fifth-order signal. The calculations

presented here address the likelihood that this result will generalize to a wider variety of systems and experimental conditions.

4.5.1. Background

Cascades of third-order nonlinearities are generated in all spectroscopies that are fifth-order in the nonlinear polarization (e.g., 2D Raman, pump-repump-probe, visible pump-2DIR probe, etc). Third-order cascades are not unique to experiments that employ five incoming laser beams. In fact, phase-matching conditions for cascades are generally enhanced relative to the direct fifth-order response in geometries that employ few laser beams with small crossing angles.[55] Phase-matching efficiencies become essential design criteria when the intrinsic magnitudes of direct fifth-order signals are small compared to those associated with cascaded third-order processes.[29] Of course, laser beam geometries can be chosen purely as a matter of convenience if the direct signal is known to dominate the response. For example, the proven negligibility of third-order cascades has motivated simplified three-beam approaches in 3D-IR experiments.[56-57]

Cascades are known to significantly challenge off-resonant fifth-order Raman spectroscopies conducted on pure liquids and concentrated mixtures.[28-30] High sample concentrations are one reason why cascades are so dominant in these systems. Another reason is that the direct fifth-order signal is forbidden for harmonic systems in which the polarizability depends linearly on the vibrational coordinate (i.e., lowest-order approximations).[31-33] Reliance on higher-order effects for signal generation is particularly problematic, because the cascades are not subject to such restrictions. We have recently discussed why electronically resonant conditions generally make the direct fifth-order response dominant in systems with Franck-Condon active modes.[35] The key is that all displaced modes (harmonic and anharmonic) may contribute to the signal without non-Condon effects in resonant FSRS.[36]
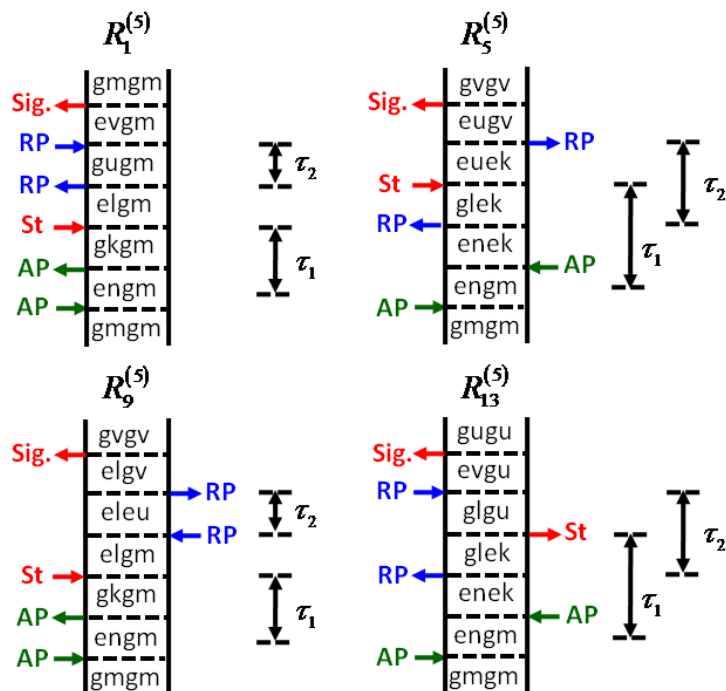
Figure 4.12. *Double- sided Feynman diagrams associated with four classes of terms in the FSRS response function. The terms are classified according to whether or not they evolve in ground or excited state populations during the delay times, τ_1 and τ_2. The laser pulses associated with each field-matter interaction are indicated in the figure in the same color-code employed in Figure 4.2.*

4.5.2. Response Functions

The FSRS response for a system in which resonance enhancement is dominated by a single pair of electronic states possesses 16 response functions (see Supplementary Material).[47] The response functions can be divided into four classes based on whether or not the system is in the ground or excited state during the two population times (see Figure 4.12 for one member of each class). An earlier theoretical description of FSRS has grouped terms in a related way.[58] In metMb, excited state populations may contribute at sub-picosecond delay times (i.e., before internal conversion is complete), whereas dynamics on the picosecond time scale primarily reflect vibrational cooling in the electronic ground state.[21-25] We consider all terms here as the goal is simply to estimate relative signal strengths for direct and cascaded responses.

It is instructive to consider one of the polarization components in the FSRS response. The polarization component associated with the $R_1^{(5)}$ diagram in Figure 4.12 is given by

$$P_1^{(5)}(\omega_t) = i \frac{N \xi_{AP}^2 \xi_{RP}^2 \xi_{St} |\mu_{eg}|^6}{\hbar^5} \sum_{mnkluv} B_m \langle n|m \rangle \langle n|k \rangle \langle l|k \rangle \langle l|u \rangle \langle v|u \rangle \langle v|m \rangle$$
$$\times L_{en,gm}(\omega_{AP}) D_{gk,gm}(\tau_1) L_{el,gm}(\omega_t) J_{gu,gm}(\omega_t - \omega_{RP}) L_{ev,gm}(\omega_t) \qquad (4.10)$$

where ξ_j are the electric field amplitudes associated with the three types of laser pulses (actinic pump, Raman pump, Stokes), N is the number density, μ_{eg} is the electronic transition dipole for the Soret band, B_m is the Boltzmann population of level m, $\langle n|m \rangle$ is a vibrational overlap integral (with excited state index in the bra),[59] and the summation is carried out with respect to dummy indices for vibrational energy levels. The functions, $L_{en,gm}(\omega)$, are Lorentzian line shapes associated with resonances between vibronic levels in electronic states g and ℓ, whereas $D_{gk,gm}(\tau_1)$ describes vibrational wavepacket motion induced by the actinic pump in the delay time, τ_1 (see Section 4.8.1). The function,

$$J_{gu,gm}(\omega_t - \omega_{RP}) = \frac{\exp(-\Lambda_{RP}\tau_2)}{(\omega_t - \omega_{RP} + \omega_{um}) + i(\Gamma_{vib} - \Lambda_{RP})}, \qquad (4.11)$$

provides insight into aspects of the signal that are unique to the present approach. The denominator suggests that the line width of the resonance is reduced by introducing a time delay between Raman pump pulses (i.e., Γ_{vib} and Λ_{RP} have opposite signs). However, the numerator makes clear that such enhancement in spectral resolution comes at the expense of signal intensity; the magnitude of the polarization decreases exponentially with τ_2.
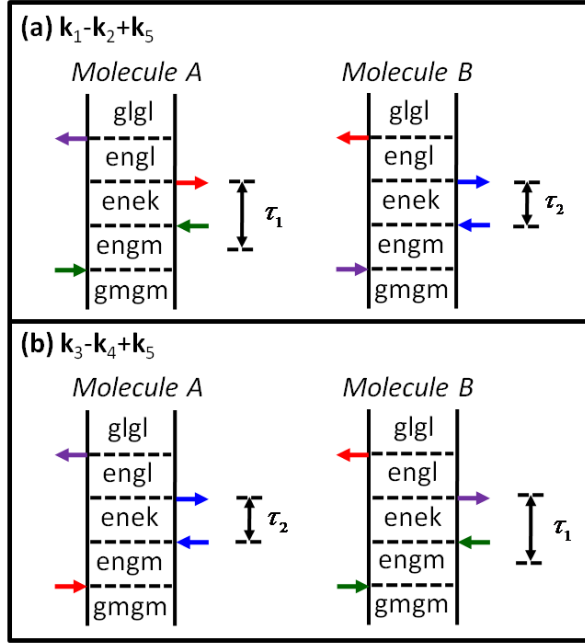
Figure 4.13. *Feynman diagrams associated with the nonlinearities on the two molecules involved in third-order cascades with intermediate phase-matching conditions (a) k_1-k_2+k_5 and (b) k_3-k_4+k_5. Field-matter interactions are color-coded as follows: actinic pump is green; Raman pump is blue; Stokes is red; cascaded signal field is red; the field radiated at the intermediate step in the cascade is purple.*

In the present laser beam geometries, we consider third-order cascades with intermediate phase-matching conditions, k_1-k_2+k_5 and k_3-k_4+k_5. Additional cascades are possible (e.g., k_2-k_1+k_4) but possess much smaller phase-matching efficiencies. The polarization components related to the cascaded nonlinearities are summarized in Supplemental section 4.7.2. The two types of cascades essentially permute coherent Stokes Raman scattering (CSRS) and pump-probe (PP) responses on the two molecules involved in the process (see Figure 4.13). For example, third-order polarization components associated with these two types of nonlinear responses are given by

$$P_{1,PP}^{(3)}(\omega_t) = i\frac{N\xi_{AP}^2\xi_{St}\left|\mu_{eg}\right|^4}{\hbar^3}\sum_{mnkl} B_m\langle n|m\rangle\langle k|m\rangle\langle k|l\rangle\langle n|l\rangle L_{en,gm}(\omega_{AP})D_{en,ek}(\tau_1)L_{en,gl}(\omega_t),\ (4.12)$$

and

$$P_{1,CSRS}^{(3)}(\omega_t) = -\frac{N\xi_{RP}^2\xi_{St}|\mu_{eg}|^4}{\hbar^3}\sum_{mnkl}B_m\langle n|m\rangle\langle k|m\rangle\langle k|l\rangle\langle n|l\rangle L_{en,gm}(\omega_t),$$
$$\times J_{en,ek}(\omega_t - \omega_{RP})L_{en,gl}(\omega_t) \qquad (4.13)$$

where we have derived these expressions under the same assumptions used to describe the direct fifth-order response (see Supplementary Material).[47] The cascaded signal field is proportional to the product of $P_{1,PP}^{(3)}(\omega_t)$ and $P_{1,CSRS}^{(3)}(\omega_t)$.

The above formulas highlight three key issues that govern relative magnitudes of direct and cascaded responses:

(i) The cascaded signal field scales as the square of concentration, whereas the field radiated by the fifth-order polarization is linear in concentration. This is one reason why cascades are generally negligible at optical densities employed under resonant conditions in transmissive geometries. For example, the concentration of CS_2, in which cascades are dominant, is roughly 80,000 times larger than that employed here.

(ii) The direct and cascaded responses respectively include 3 and 4 resonant electronic line shape functions, $L_{en,gm}(\omega)$. The direct fifth-order signal field therefore becomes more dominant as the electronic dephasing rate increases.[35] This aspect of the nonlinear response favors the direct fifth-order signal in condensed phases at ambient temperatures, where line widths are generally greater than 1000 cm^{-1}.

(iii) The direct and cascaded polarization components involve sums of products of 8 and 6 vibrational overlap integrals, respectively. The direct fifth-order signal field becomes more dominant as the mode displacement increases because the integrals are all less than 1 and decrease as the mode displacement increases. In related work, we found that this effect becomes

quite pronounced in systems with extremely large displacements (displacements greater than 3).[35]

4.5.3. Model Calculations

In this section, we evaluate the ratio between the cascaded third-order and direct fifth-order signal magnitudes, $\left|E_{cas}^{(5)}(\omega_t)\right| / \left|E_{direct}(\omega_t)\right|$, which are defined in appendices A and B. These model calculations are motivated by knowledge of how the relative signal strengths depend on properties of the model system and the frequencies of the incident pulses. Insights derived from these calculations do not assume an optimal parameterization for metMb. Rather, parameters are scanned over wide ranges to explore general effects that apply not only to metMB but also to other heme proteins with similar optical properties. Figure 4.14 presents spectra computed with a displaced 1370-cm^{-1} mode, where the actinic and Raman pump frequencies, ω_{AP} and ω_{RP}, are taken to be equal to the electronic resonance frequency, ω_{eg}. The vibrational resonances appear on a frequency-dependent baseline, which is consistent with the model developed by Ernsting and co-workers.[3] We consider a system with a single harmonic mode to keep the number of parameters manageable. For fundamental transitions, we find that the ratio, $\left|E_{cas}(\omega_t)\right| / \left|E_{direct}^{(5)}(\omega_t)\right|$, is insensitive to the number of vibrational modes in the system.
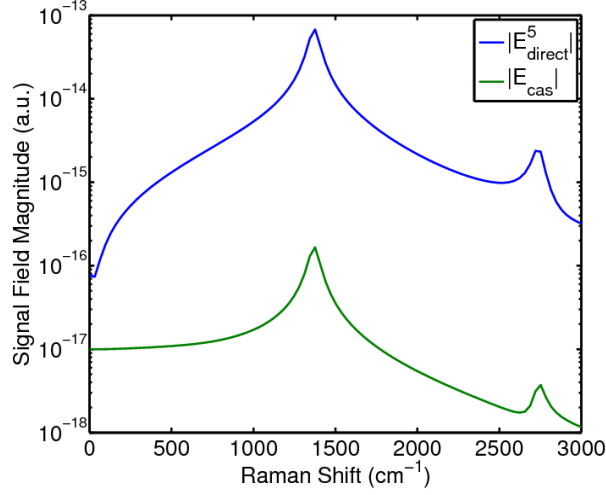
Figure 4.14. *Absolute values of signal spectra computed using the models presented in appendices A and B and the parameters in Tables 4.1 and 4.2. The system possesses a single 1370-cm^{-1} harmonic mode with a displacement of 0.35 (a reasonable estimate for metMb).[42] The frequency of the actinic pump pulse is set equal to the electronic resonance frequency, $\omega_{AP} = \omega_{eg}$. This calculation assumes that the five-beam geometry is employed (cascades are 4 times weaker in the four-beam geometry).*

We begin by exploring the parameter space of the mode frequency and displacement in

Figure 4.15(a). The ratios between $\left| E_{cas}^{(5)}(\omega_t) \right|$ and $\left| E_{direct}(\omega_t) \right|$ are computed at values of the

Raman shift, $\omega_{RP} - \omega_t$, equal to the mode frequency (i.e., at the peak of the fundamental

transition). The calculations predict extremely small ratios (<0.01) at frequencies near the 1370

cm^{-1} mode. The ratio, $\left| E_{cas}(\omega_t) \right| / \left| E_{direct}^{(5)}(\omega_t) \right|$, increases as the vibrational frequency decreases,

but $\left| E_{direct}^{(5)}(\omega_t) \right|$ remains dominant down to the lowest frequency probed in this work (i.e., the

670-cm^{-1} mode). The calculation is carried out over a wide range of mode displacements in order

to establish behaviors that will generalize to other systems. Displacements for the 670-cm^{-1} and

1370-cm^{-1} modes are near 0.25 and 0.35, respectively.[54]

The laser detuning and mode displacement are varied for the 670 and 1370-cm^{-1} modes in

Figures 4.15(b) and 4.15(c). The calculations suggest greater dominance of $\left| E_{direct}^{(5)}(\omega_t) \right|$ when

the actinic and Raman pump beams are tuned to the low-frequency side of the electronic resonance (i.e., $\omega_{AP} < \omega_{eg}$ and $\omega_{RP} < \omega_{eg}$). Notably, the ratio remains small when the beams are within the approximate 1500-cm^{-1} linewidth of the electronic transition ($2\Gamma_{eg}$). Regions of the plots most relevant to the present application to metMb are indicated with boxes. The calculations predict that $\left| E_{direct}^{(5)}(\omega_t) \right|$ remains dominant for displacements between 0 and 1.

The present model system approximates the response of metMb when photoexcited in the region of the Soret band. Inclusion of additional excited states in the model (e.g., higher-energy spin states of iron) is unlikely to affect the ratio because of their relatively small magnitudes. Increases in $\left| E_{cas}(\omega_t) \right|$ and $\left| E_{direct}^{(5)}(\omega_t) \right|$ are largely offset when new classes of signal components are introduced (e.g., resonances between excited states), because terms with nearly equal weights must then be added to both types of fields. Perhaps the most important issue is that $\left| E_{direct}^{(5)}(\omega_t) \right|$ and $\left| E_{cas}(\omega_t) \right|$ always consist of sums of products of 6 and 8 vibrational overlap integrals, respectively. The terms in $\left| E_{cas}(\omega_t) \right|$ will generally be smaller than those in $\left| E_{direct}^{(5)}(\omega_t) \right|$, because each of the overlap integrals in the product is less than 1. The direct response, $\left| E_{direct}^{(5)}(\omega_t) \right|$, can become many orders of magnitude larger than $\left| E_{cas}(\omega_t) \right|$ in systems with extremely large mode displacements.[35] This, together with the low sample concentrations typically employed in transmissive laser beam geometries suggests that third-order cascades are unlikely to outcompete the resonant FSRS response in most systems.
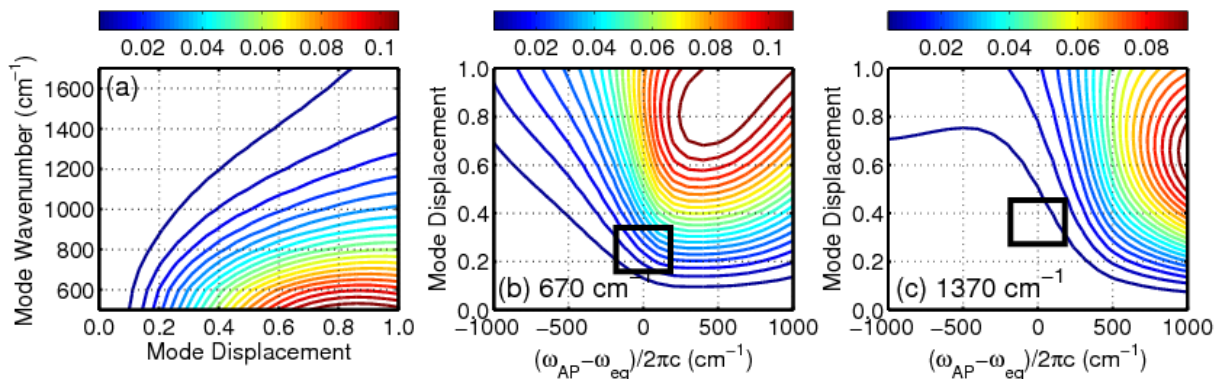
Figure 4.15. *(a) The ratio,* $\left|E_{cas}(\omega_t)\right|/\left|E_{direct}^{(5)}(\omega_t)\right|$*, is computed for a system with a single harmonic mode under electronically resonant conditions,* $\omega_{AP} = \omega_{eg}$*. The ratio is computed at the value of the Raman Shift equal to the mode frequency (i.e., at the peak of the vibrational resonance). (b) The ratio,* $\left|E_{cas}(\omega_t)\right|/\left|E_{direct}^{(5)}(\omega_t)\right|$*, is computed for a 670- cm⁻¹ mode at various dimensionless displacements and detuning factors,* $\omega_{AP} - \omega_{eg}$*. (c) The ratio,* $\left|E_{cas}(\omega_t)\right|/\left|E_{direct}^{(5)}(\omega_t)\right|$*, is computed for a 1370-cm⁻¹ mode at various dimensionless mode displacements and detuning factors,* $\omega_{AP} - \omega_{eg}$*. Boxes are drawn in the regions of the plots relevant to myoglobin in panels (b) and (c).*

4.6. Concluding Remarks

Four and five-beam implementations of FSRS have been used in this work to significantly reduce the background of residual laser light and lower-order nonlinearities that would be present in the three-beam geometry carried out with the same laser pulses. The background-free nature of the five-beam geometry supports excellent signal-to-noise ratios and short data acquisition times. As with any experimental technique, the present method possesses strengths and limitations that are important to take into account when deciding on an approach. The fast data acquisition time and sensitivity achieved by the present method comes at the expense of nonlinearities that are more complicated than those associated with spontaneous Raman probes. This is one reason why time-resolved spontaneous Raman spectroscopy may be preferred for studies of relaxation dynamics in heme proteins that are slower than 0.7 ps.[16] We

envision that the power of the present method may be fully exploited in studies of low-frequency vibrational coherences in τ_1, and their anharmonic couplings to vibrational resonances in τ_2 (i.e., multidimensional analogues of third-order vibrational coherences studies).[54] Hybrid FSRS/2D Photon Echo pulse sequences may also be implemented in a five-beam geometry.

Significant contributions from cascaded nonlinearities have been ruled out with control experiments based on the signal phase, concentration dependence, and spectroscopic line shapes. In addition, we have developed a model to explore how the propensity for cascades depends on parameters of the system, the frequencies of the incoming beams, and the laser beam geometry. Our calculations suggest that third-order cascades are less than 5% of the signal in the entire vibrational frequency range examined in this study. The present work (and our related study of I_3^- by our group)[35] suggests that cascades are unlikely to be problematic at the optical densities typically employed in transmissive beam geometries. In such experiments, concentrations are typically tens of thousands of times lower than those associated with the pure liquids and concentrated mixtures in which cascades are known to dominate.[28-30] Moreover, Franck-Condon active modes will always dominate the direct fifth-order response under electronically resonant conditions (i.e., the direct response is "allowed" under resonant conditions). Together, the control experiments and model calculations presented here suggest promise for multidimensional resonance Raman investigations of heme proteins.

4.7. Supplemental Information

4.7.1. Direct Fifth-Order Signal Field

The direct fifth-order polarization possesses 16 components when a single electronic resonance dominates the optical response. One of these polarization components is given in Equation 4.10. The remaining 15 polarization components are

$$P_2^{(5)}(\omega_t) = i\frac{N\xi_{AP}^2\xi_{RP}^2\xi_{St}\left|\mu_{eg}\right|^6}{\hbar^5}\sum_{mnkluv}B_m\langle n|m\rangle\langle n|k\rangle\langle l|m\rangle\langle l|u\rangle\langle v|k\rangle\langle v|u\rangle,$$
$$\times L_{en,gm}(\omega_{AP})D_{gk,gm}(\tau_1)L_{gk,el}(-\omega_{RP})J_{gk,gu}(\omega_t-\omega_{RP})L_{ev,gu}(\omega_t) \qquad (4.14)$$

$$P_3^{(5)}(\omega_t) = i\frac{N\xi_{AP}^2\xi_{RP}^2\xi_{St}\left|\mu_{eg}\right|^6}{\hbar^5}\sum_{mnkluv}B_m\langle n|m\rangle\langle n|k\rangle\langle l|k\rangle\langle l|u\rangle\langle v|m\rangle\langle v|u\rangle,$$
$$\times L_{gm,en}(-\omega_{AP})D_{gm,gk}(\tau_1)L_{gm,el}(-\omega_{RP})J_{gm,gu}(\omega_t-\omega_{RP})L_{ev,gu}(\omega_t) \qquad (4.15)$$

$$P_4^{(5)}(\omega_t) = i\frac{N\xi_{AP}^2\xi_{RP}^2\xi_{St}\left|\mu_{eg}\right|^6}{\hbar^5}\sum_{mnkluv}B_m\langle n|m\rangle\langle n|k\rangle\langle l|m\rangle\langle l|u\rangle\langle v|u\rangle\langle v|k\rangle,$$
$$\times L_{gm,en}(-\omega_{AP})D_{gm,gk}(\tau_1)L_{el,gk}(\omega_t)J_{gu,gk}(\omega_t-\omega_{RP})L_{ev,gk}(\omega_t) \qquad (4.16)$$

$$P_5^{(5)}(\omega_t) = i\frac{N\xi_{AP}^2\xi_{RP}^2\xi_{St}\left|\mu_{eg}\right|^6}{\hbar^5}\sum_{mnkluv}B_m\langle n|m\rangle\langle k|m\rangle\langle n|l\rangle\langle u|l\rangle\langle k|v\rangle\langle u|v\rangle,$$
$$\times L_{en,gm}(\omega_{AP})D_{en,ek}(\tau_1)L_{gl,ek}(-\omega_{RP})J_{eu,ek}(\omega_t-\omega_{RP})L_{eu,gv}(\omega_t) \qquad (4.17)$$

$$P_6^{(5)}(\omega_t) = i\frac{N\xi_{AP}^2\xi_{RP}^2\xi_{St}\left|\mu_{eg}\right|^6}{\hbar^5}\sum_{mnkluv}B_m\langle n|m\rangle\langle k|m\rangle\langle k|l\rangle\langle u|l\rangle\langle u|v\rangle\langle n|v\rangle,$$
$$\times L_{en,gm}(\omega_{AP})D_{en,ek}(\tau_1)L_{en,gl}(\omega_t)J_{en,eu}(\omega_t-\omega_{RP})L_{en,gv}(\omega_t) \qquad (4.18)$$

$$P_7^{(5)}(\omega_t) = i\frac{N\xi_{AP}^2\xi_{RP}^2\xi_{St}\left|\mu_{eg}\right|^6}{\hbar^5}\sum_{mnkluv}B_m\langle n|m\rangle\langle k|m\rangle\langle k|l\rangle\langle u|l\rangle\langle n|v\rangle\langle u|v\rangle,$$
$$\times L_{gm,en}(-\omega_{AP})D_{ek,en}(\tau_1)L_{gl,en}(-\omega_{RP})J_{eu,en}(\omega_t-\omega_{RP})L_{eu,gv}(\omega_t) \qquad (4.19)$$

$$P_8^{(5)}(\omega_t) = i\frac{N\xi_{AP}^2\xi_{RP}^2\xi_{St}\left|\mu_{eg}\right|^6}{\hbar^5}\sum_{mnkluv}B_m\langle n|m\rangle\langle k|m\rangle\langle n|l\rangle\langle u|l\rangle\langle u|v\rangle\langle k|v\rangle,$$
$$\times L_{gm,en}(-\omega_{AP})D_{ek,en}(\tau_1)L_{ek,gl}(\omega_t)J_{ek,eu}(\omega_t-\omega_{RP})L_{ek,gv}(\omega_t) \qquad (4.20)$$

$$P_9^{(5)}(\omega_t) = i\frac{N\xi_{AP}^2\xi_{RP}^2\xi_{St}\left|\mu_{eg}\right|^6}{\hbar^5}\sum_{mnkluv}B_m\langle n|m\rangle\langle n|k\rangle\langle l|k\rangle\langle u|m\rangle\langle u|v\rangle\langle l|v\rangle,$$
$$\times L_{en,gm}(\omega_{AP})D_{gk,gm}(\tau_1)L_{el,gm}(\omega_t)J_{el,eu}(\omega_t-\omega_{RP})L_{el,gv}(\omega_t) \qquad (4.21)$$

$$P_{10}^{(5)}(\omega_t) = i\frac{N\xi_{AP}^2\xi_{RP}^2\xi_{St}\left|\mu_{eg}\right|^6}{\hbar^5}\sum_{mnkluv} B_m\langle n|m\rangle\langle n|k\rangle\langle l|m\rangle\langle u|k\rangle\langle l|v\rangle\langle u|v\rangle, \qquad (4.22)$$
$$\times L_{en,gm}(\omega_{AP})D_{gk,gm}(\tau_1)L_{gk,el}(-\omega_{RP})J_{eu,el}(\omega_t-\omega_{RP})L_{eu,gv}(\omega_t)$$

$$P_{11}^{(5)}(\omega_t) = i\frac{N\xi_{AP}^2\xi_{RP}^2\xi_{St}\left|\mu_{eg}\right|^6}{\hbar^5}\sum_{mnkluv} B_m\langle n|m\rangle\langle n|k\rangle\langle l|m\rangle\langle u|k\rangle\langle u|v\rangle\langle l|v\rangle, \qquad (4.23)$$
$$\times L_{gm,en}(-\omega_{AP})D_{gm,gk}(\tau_1)L_{el,gk}(\omega_t)J_{el,eu}(\omega_t-\omega_{RP})L_{el,gv}(\omega_t)$$

$$P_{12}^{(5)}(\omega_t) = i\frac{N\xi_{AP}^2\xi_{RP}^2\xi_{St}\left|\mu_{eg}\right|^6}{\hbar^5}\sum_{mnkluv} B_m\langle n|m\rangle\langle n|k\rangle\langle l|k\rangle\langle u|m\rangle\langle l|v\rangle\langle u|v\rangle, \qquad (4.24)$$
$$\times L_{gm,en}(-\omega_{AP})D_{gm,gk}(\tau_1)L_{gm,el}(-\omega_{RP})J_{eu,el}(\omega_t-\omega_{RP})L_{eu,gv}(\omega_t)$$

$$P_{13}^{(5)}(\omega_t) = i\frac{N\xi_{AP}^2\xi_{RP}^2\xi_{St}\left|\mu_{eg}\right|^6}{\hbar^5}\sum_{mnkluv} B_m\langle n|m\rangle\langle k|m\rangle\langle n|l\rangle\langle k|u\rangle\langle v|l\rangle\langle v|u\rangle, \qquad (4.25)$$
$$\times L_{en,gm}(\omega_{AP})D_{en,ek}(\tau_1)L_{gl,ek}(-\omega_{RP})J_{gl,gu}(\omega_t-\omega_{RP})L_{ev,gu}(\omega_t)$$

$$P_{14}^{(5)}(\omega_t) = i\frac{N\xi_{AP}^2\xi_{RP}^2\xi_{St}\left|\mu_{eg}\right|^6}{\hbar^5}\sum_{mnkluv} B_m\langle n|m\rangle\langle k|m\rangle\langle k|l\rangle\langle n|u\rangle\langle v|u\rangle\langle v|l\rangle, \qquad (4.26)$$
$$\times L_{en,gm}(\omega_{AP})D_{en,ek}(\tau_1)L_{en,gl}(\omega_t)J_{gu,gl}(\omega_t-\omega_{RP})L_{ev,gl}(\omega_t)$$

$$P_{15}^{(5)}(\omega_t) = i\frac{N\xi_{AP}^2\xi_{RP}^2\xi_{St}\left|\mu_{eg}\right|^6}{\hbar^5}\sum_{mnkluv} B_m\langle n|m\rangle\langle k|m\rangle\langle k|l\rangle\langle n|u\rangle\langle v|l\rangle\langle v|u\rangle, \qquad (4.27)$$
$$\times L_{gm,en}(-\omega_{AP})D_{ek,en}(\tau_1)L_{gl,en}(-\omega_{RP})J_{gl,gu}(\omega_t-\omega_{RP})L_{ev,gu}(\omega_t)$$

$$P_{16}^{(5)}(\omega_t) = i\frac{N\xi_{AP}^2\xi_{RP}^2\xi_{St}\left|\mu_{eg}\right|^6}{\hbar^5}\sum_{mnkluv} B_m\langle n|m\rangle\langle k|m\rangle\langle n|l\rangle\langle k|u\rangle\langle v|u\rangle\langle v|l\rangle. \qquad (4.28)$$
$$\times L_{gm,en}(-\omega_{AP})D_{ek,en}(\tau_1)L_{ek,gl}(\omega_t)J_{gu,gl}(\omega_t-\omega_{RP})L_{ev,gl}(\omega_t)$$

The functions $D_{gk,gm}(\tau_1)$ and $L_{en,gm}(\omega)$ are written as[60]

$$D_{gk,gm}(\tau_1) = \frac{2\Lambda_{AP}}{\omega_{km}^2+\Lambda_{AP}^2}\theta(\tau_1)\exp\left(-i\omega_{km}\tau_1-\Gamma_{vib}\tau_1\right) \qquad (4.29)$$

and

$$L_{en,gm}(\omega) = \frac{1}{\omega - \omega_{eg} - \omega_{nm} + i\Gamma_{eg}} \; . \tag{4.30}$$

The vibrational line shape function, $J_{gu,gm}(\omega_t - \omega_{RP})$, is defined in Equation 4.11.

The direct fifth-order signal field is expressed in terms of these polarization components as[60]

$$E_{direct}^{(5)}(\omega_t) = \frac{1}{7}\left(\frac{i\omega_t l}{2\varepsilon_0 n(\omega_t)c}\right)\sum_{j=1}^{16} P_j^{(5)}(\omega_t)\operatorname{sinc}\left(\frac{\Delta k_{direct}^{(5)}l}{2}\right)\exp\left(i\frac{\Delta k_{direct}^{(5)}l}{2}\right), \tag{4.31}$$

where the factor of 1/7 represents the orientational average for all-parallel electric field polarizations[56] and the wavevector mismatch, $\Delta k_{direct}^{(5)}$, is given for the four and five beam geometries in Tables 4.2 and 4.3.

4.7.2. Cascaded Third-Order Signal Field

In this supplemental section, we obtain an expression for the signal field generated by third-order cascades with intermediate phase-matching conditions, $\mathbf{k}_1$-$\mathbf{k}_2$+$\mathbf{k}_5$ and $\mathbf{k}_3$-$\mathbf{k}_4$+$\mathbf{k}_5$. The two processes essentially permute the type of nonlinearity that occurs on the two molecules involved in the cascade. A pump-probe-like response precedes a coherent Stokes Raman scattering (CSRS) process in cascade 1, whereas the sequence is reversed in cascade 2. Below, we present polarization components for each process then combine them in an expression for the cascaded signal field. The formulas are obtained under the same approximations as the fifth-order polarization and thus can be compared on the same footing (see Supplementary Material).[47]

The pump-probe-like polarization components are

$$P_{1,PP}^{(3)}(\omega_t) = i \frac{N\xi_{AP}^2 \xi_{St} |\mu_{eg}|^4}{\hbar^3} \sum_{mnkl} B_m \langle n|m\rangle \langle k|m\rangle \langle k|l\rangle \langle n|l\rangle L_{en,gm}(\omega_{AP}) D_{en,ek}(\tau_1) L_{en,gl}(\omega_t), \quad (4.32)$$

$$P_{2,PP}^{(3)}(\omega_t) = i \frac{N\xi_{AP}^2 \xi_{St} |\mu_{eg}|^4}{\hbar^3} \sum_{mnkl} B_m \langle n|m\rangle \langle k|m\rangle \langle n|l\rangle \langle k|l\rangle L_{gm,en}(-\omega_{AP}) D_{ek,en}(\tau_1) L_{ek,gl}(\omega_t), \quad (4.33)$$

$$P_{3,PP}^{(3)}(\omega_t) = i \frac{N\xi_{AP}^2 \xi_{St} |\mu_{eg}|^4}{\hbar^3} \sum_{mnkl} B_m \langle n|m\rangle \langle n|k\rangle \langle l|k\rangle \langle l|m\rangle L_{en,gm}(\omega_{AP}) D_{gk,gm}(\tau_1) L_{el,gm}(\omega_t), \quad (4.34)$$

$$P_{4,PP}^{(3)}(\omega_t) = i \frac{N\xi_{AP}^2 \xi_{St} |\mu_{eg}|^4}{\hbar^3} \sum_{mnkl} B_m \langle n|m\rangle \langle n|k\rangle \langle l|m\rangle \langle l|k\rangle L_{gm,en}(-\omega_{AP}) D_{gm,gk}(\tau_1) L_{el,gk}(\omega_t). \quad (4.35)$$

The CSRS polarization components are

$$\begin{aligned}P_{1,CSRS}^{(3)}(\omega_t) = &-\frac{N\xi_{RP}^2 \xi_{St} |\mu_{eg}|^4}{\hbar^3} \sum_{mnkl} B_m \langle n|m\rangle \langle k|m\rangle \langle k|l\rangle \langle n|l\rangle L_{en,gm}(\omega_t) \\ &\times J_{en,ek}(\omega_t - \omega_{RP}) L_{en,gl}(\omega_t)\end{aligned} \quad (4.36)$$

$$\begin{aligned}P_{2,CSRS}^{(3)}(\omega_t) = &-\frac{N\xi_{RP}^2 \xi_{St} |\mu_{eg}|^4}{\hbar^3} \sum_{mnkl} B_m \langle n|m\rangle \langle k|m\rangle \langle n|l\rangle \langle k|l\rangle L_{gm,en}(-\omega_{RP}) \\ &\times J_{ek,en}(\omega_t - \omega_{RP}) L_{ek,gl}(\omega_t)\end{aligned} \quad (4.37)$$

$$\begin{aligned}P_{3,CSRS}^{(3)}(\omega_t) = &-\frac{N\xi_{RP}^2 \xi_{St} |\mu_{eg}|^4}{\hbar^3} \sum_{mnkl} B_m \langle n|m\rangle \langle n|k\rangle \langle l|k\rangle \langle l|m\rangle L_{en,gm}(\omega_t) \\ &\times J_{gk,gm}(\omega_t - \omega_{RP}) L_{el,gm}(\omega_t)\end{aligned} \quad (4.38)$$

$$\begin{aligned}P_{4,CSRS}^{(3)}(\omega_t) = &-\frac{N\xi_{RP}^2 \xi_{St} |\mu_{eg}|^4}{\hbar^3} \sum_{mnkl} B_m \langle n|m\rangle \langle n|k\rangle \langle l|m\rangle \langle l|k\rangle L_{gm,en}(-\omega_{RP}) \\ &\times J_{gm,gk}(\omega_t - \omega_{RP}) L_{el,gk}(\omega_t)\end{aligned} \quad (4.39)$$

The total signal field generated by the two cascades can be written as

$$E_{cas}(\omega_t) = \frac{1}{25}\left(\frac{i\omega_t l}{2\varepsilon_0 n(\omega_t)c}\right)^2 \sum_{m=1}^{4}\sum_{n=1}^{4}\xi_{St}^{-1}P_{m,PP}^{(3)}(\omega_t)P_{n,CSRS}^{(3)}(\omega_t)f_{cas}(\Delta k_1,\Delta k_2), \tag{4.40}$$

where the phase matching function is given by[60]

$$f_{cas}(\Delta k_1,\Delta k_2) = \sum_{j=1}^{2}\text{sinc}\left(\frac{\Delta k_{jA}l}{2}\right)\text{sinc}\left(\frac{\Delta k_{jB}l}{2}\right)\exp\left[i\frac{(\Delta k_{jA}+\Delta k_{jB})l}{2}\right]. \tag{4.41}$$

The factor of 1/25 represents the product of orientational averages for all-parallel electric field polarizations[61] and the wavevector mismatches, Δk_{jA} and Δk_{jB}, are given for each of the experimental geometries in Tables 4.2 and 4.3.

Table 4.1. *Parameters of Theoretical Model*

Parameter	Value
$(\omega_{AP}-\omega_{eg})/2\pi c$	varied
ω_{RP}	ω_{AP}
d	varied
Γ_{vib}/c	10 cm^{-1}
Γ_{eg}/c	750 cm^{-1}
μ_{eg}	8.8 D
N	1.2×10^{23} m^{-3}
$\omega_t/2\pi c$	23250 cm^{-1}
$n(\omega_t)$	1.39
l	0.22 mm

Table 4.2. *Wavevector Mismatch in the Five-Beam Geometry*

Nonlinearity	$\Delta k_{direct}^{(n)}$ (cm^{-1})	Δk_A (cm^{-1})	Δk_B (cm^{-1})	[a],[b]Efficiency
Direct Fifth-Order (FSRS)	-215	------	------	0.123
Cascade #1 ($\mathbf{k}_1$-$\mathbf{k}_2$+$\mathbf{k}_5$ intermediate)	------	-18	-197	0.069
Cascade #2 ($\mathbf{k}_3$-$\mathbf{k}_4$+$\mathbf{k}_5$ intermediate)	------	-412	196	0.005

[a] The efficiency is computed using $\mathrm{sinc}\left(\dfrac{\Delta k_{direct}^{(n)} l}{2}\right)$ and $\mathrm{sinc}\left(\dfrac{\Delta k_A l}{2}\right)\mathrm{sinc}\left(\dfrac{\Delta k_B l}{2}\right)$ for direct and cascaded processes, respectively.
[b] Path length, l, is 0.022 cm.

Table 4.3. *Wavevector Mismatch in the Four-Beam Geometry*

Nonlinearity	$\Delta k_{direct}^{(n)}$ (cm^{-1})	Δk_A (cm^{-1})	Δk_B (cm^{-1})	[a],[b]Efficiency
Direct Fifth-Order (FSRS)	-198	----------	----------	0.123
Direct Third-Order (CSRS)	-225	----------	---------------	0.128
Cascade #1 ($\mathbf{k}_1$-$\mathbf{k}_2$+$\mathbf{k}_5$ intermediate)	----------	-215	-215	0.015
Cascade #2 ($\mathbf{k}_3$-$\mathbf{k}_4$+$\mathbf{k}_5$ intermediate)	----------	-215	-180	-0.002

[a] The efficiency is computed using $\mathrm{sinc}\left(\dfrac{\Delta k_{direct}^{(n)} l}{2}\right)$ and $\mathrm{sinc}\left(\dfrac{\Delta k_A l}{2}\right)\mathrm{sinc}\left(\dfrac{\Delta k_B l}{2}\right)$ for direct and cascaded processes, respectively.
[b] Path length, l, is 0.022 cm.

4.7.3. Distinguishing the Broadband and FSRS Responses

The present experiments must contend with an intense broadband (pump-repump-probe) response because all laser pulses are electronically resonant with the Soret band. Many traditional FSRS applications because the Raman pump and Stokes pulses are tuned into resonance with a photoproduct (often where the equilibrium system is transparent). We suppress this broadband response by introducing a delay between the two Raman pump pulses. This enforces the desired order of field-matter interactions; the final interaction occurs with the

Raman pump and Stokes pulses in the FSRS and pump-repump-probe nonlinearities, respectively.

Figure 4.16 compares FSRS signals acquired with $\tau_2 = 0$ and 290 fs. The types of terms in the response function responsible for both signal components are also presented. The FSRS resonances are not visible when $\tau_2 = 0$ fs because of the dominant pump-repump-probe response. Notably, such a delay between Raman pump interactions cannot be achieved in a traditional three-beam geometry. The measurement obtained with $\tau_2 = 0$ fs reflects the ratio in FSRS and broadband responses that would be observed in a three-beam geometry with the same laser pulses.
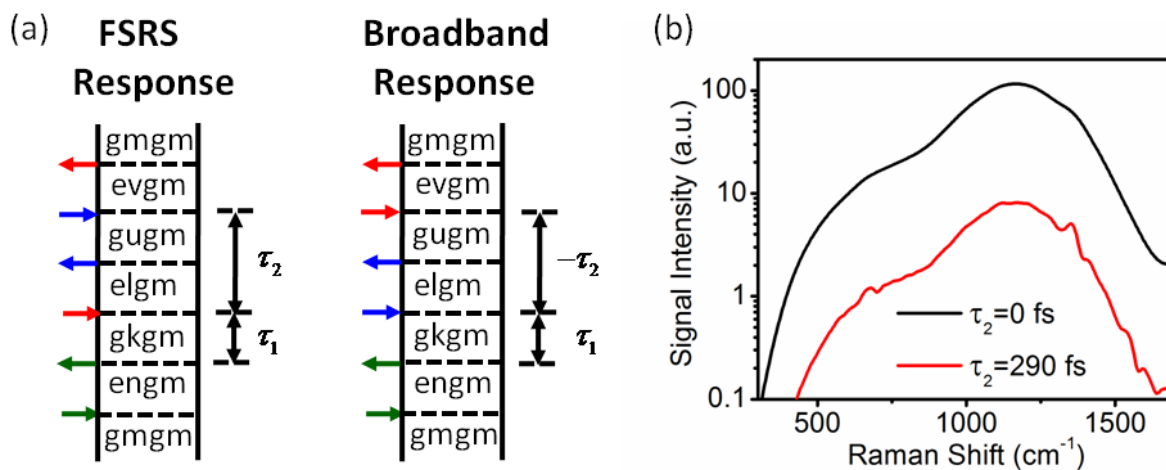
Figure 4.16. (a) Examples of Feynman diagrams associated with the desired FSRS and undesired broadband responses. The indices, g and ℓ, represent the ground and excited electronic states, whereas dummy indices (m, n, k, l, u, and v) denote vibrational levels. Green, blue, and red arrows represent the actinic pump, Raman pump, and Stokes pulses, respectively. (b) The FSRS component of the response of metMb increases as the delay τ_2 increases (the delay, τ_1, is 0.5 ps here). This effect can be understood by inspection of the Feynman diagrams, which suggest that the FSRS response will increase as the delay τ_2 increases.

REFERENCES

1. Kukura, P.; McCamant, D. W.; Mathies, R. A., Femtosecond stimulated Raman spectroscopy. *Annu. Rev. Phys. Chem.* **2007,** *58*, 461-488.

2. Frontiera, R. R.; Dasgupta, J.; Mathies, R. A., Probing interfacial electron transfer in coumarin 343 sensitized TiO_2 nanoparticles with femtosecond stimulated Raman. *J. Am. Chem. Soc.* **2009,** *131* (43), 15630-15632.

3. Weigel, A.; Dobryakov, A.; Klaumunzer, B.; Sajadi, M.; Saalfrank, P.; Ernsting, N. P., Femtosecond stimulated Raman spectroscopy of flavin after optical excitation. *J. Phys. Chem. B* **2011,** *115* (13), 3656-3680.

4. Yu, W.; Zhou, J.; Bragg, A. E., Exciton conformational dynamics of poly(3-hexylthiophene) (P3HT) in solution from time-resolved resonant-Raman spectroscopy. *J. Phys. Chem. Lett.* **2012,** *3* (10), 1321-1328.

5. Kraack, J. P.; Wand, A.; Buckup, T.; Motzkus, M.; Ruhman, S., Mapping multidimensional excited state dynamics using pump-impulsive-vibrational-spectroscopy and pump-degenerate-four-wave-mixing. *Phys. Chem. Chem. Phys.* **2013,** *15* (34), 14487-14501.

6. Kraack, J. P.; Buckup, T.; Motzkus, M., Coherent high-frequency vibrational dynamics in the excited electronic state of all-trans retinal derivatives. *J. Phys. Chem. Lett.* **2013,** *4* (3), 383-7.

7. Pontecorvo, E.; Ferrante, C.; Elles, C. G.; Scopigno, T., Spectrally tailored narrowband pulses for femtosecond stimulated Raman spectroscopy in the range 330-750 nm. *Opt. Express* **2013,** *21* (6), 6866-72.

8. Rhinehart, J. M.; Challa, J. R.; McCamant, D. W., Multimode charge-transfer dynamics of 4-(dimethylamino)benzonitrile probed with ultraviolet femtosecond stimulated Raman spectroscopy. *J. Phys. Chem. B* **2012,** *116* (35), 10522-34.

9. Fang, C.; Frontiera, R. R.; Tran, R.; Mathies, R. A., Mapping GFP structure evolution during proton transfer with femtosecond Raman spectroscopy. *Nature* **2009,** *462* (7270), 200-204.

10. Oscar, B. G.; Liu, W.; Zhao, Y.; Tang, L.; Wang, Y.; Campbell, R. E.; Fang, C., Excited-state structural dynamics of a dual-emission calmodulin-green fluorescent protein sensor for calcium ion imaging. *Proc. Natl. Acad. Sci. U. S. A.* **2014,** *111* (28), 10191-6.

11. Provencher, F.; Berube, N.; Parker, A. W.; Greetham, G. M.; Towrie, M.; Hellmann, C.; Cote, M.; Stingelin, N.; Silva, C.; Hayes, S. C., Direct observation of ultrafast long-range charge separation at polymer-fullerene heterojunctions. *Nat. Commun.* **2014,** *5*, 4288.

12. Wende, T.; Liebel, M.; Schnedermann, C.; Pethick, R. J.; Kukura, P., Population-controlled impulsive vibrational spectroscopy: Background- and baseline-free Raman spectroscopy of excited electronic states. *J. Phys. Chem. A* **2014,** *118* (43), 9976-9984.

13. Mukamel, S.; Biggs, J. D., Communication: Comment on the effective temporal and spectral resolution of impulsive stimulated Raman signals. *J. Chem. Phys.* **2011,** *134* (16), 161101.

14. McCamant, D. W., Re-evaluation of rhodopsin's relaxation kinetics determined from femtosecond stimulated Raman lineshapes. *J. Phys. Chem. B* **2011,** *115* (29), 9299-9305.

15. Dorfman, K. E.; Fingerhut, B. P.; Mukamel, S., Time-resolved broadband Raman spectroscopies: A unified six-wave-mixing representation. *J. Chem. Phys.* **2013,** *139* (12), 124113.

16. Kruglik, S. G.; Lambry, J.-C.; Martin, J.-L.; Vos, M. H.; Negrerie, M., Sub-picosecond Raman spectrometer for time-resolved studies of structural dynamics in heme proteins. *J. Raman Spectrosc.* **2011,** *42* (3), 265-275.

17. McCamant, D. W.; Kukura, P.; Yoon, S.; Mathies, R. A., Femtosecond broadband stimulated Raman spectroscopy: Apparatus and methods. *Rev. Sci. Instrum.* **2004,** *75* (11), 4971-4980.

18. Kovalenko, S. A.; Dobryakov, A. L.; Ernsting, N. P., An efficient setup for femtosecond stimulated Raman spectroscopy. *Rev. Sci. Instrum.* **2011,** *82* (6), 063102.

19. Grumstrup, E. M.; Chen, Z.; Vary, R. P.; Moran, A. M.; Schanze, K. S.; Papanikolas, J. M., Frequency modulated femtosecond stimulated Raman spectroscopy of ultrafast energy transfer in a donor-acceptor copolymer. *J. Phys. Chem. B* **2013,** *117* (27), 8245-8255.

20. McCamant, D. W., Femtosecond stimulated Raman spectroscopy of ultrafast biophysical reaction dynamics. Ph.D. Dissertation, University of California, Berkeley, 2004.

21. Petrich, J. W.; Poyart, C.; Martin, J. L., Photophysics and reactivity of heme proteins: a femtosecond absorption study of hemoglobin, myoglobin, and protoheme. *Biochemistry* **2002,** *27* (11), 4049-4060.

22. Ye, X.; Demidov, A.; Rosca, F.; Wang, W.; Kumar, A.; Ionascu, D.; Zhu, L.; Barrick, D.; Wharton, D.; Champion, P. M., Investigations of heme protein absorption line shapes, vibrational relaxation, and resonance Raman scattering on ultrafast time scales. *J. Phys. Chem. A* **2003,** *107* (40), 8156-8165.

23. Consani, C.; Aubock, G.; Bram, O.; van Mourik, F.; Chergui, M., A cascade through spin states in the ultrafast haem relaxation of met-myoglobin. *J. Chem. Phys.* **2014,** *140* (2), 025103.

24.   Martin, J. L.; Vos, M. H., Femtosecond biology. *Annu Rev. Biophys. Biomol. Struct.* **1992,** *21*, 199-222.

25.   Vos, M. H., Ultrafast dynamics of ligands within heme proteins. *Biochim. Biophys. Acta.* **2008,** *1777* (1), 15-31.

26.   Ivanecky, J. E.; Wright, J. C., An investigation of the origins and efficiencies of higher-order nonlinear spectroscopic processes. *Chem. Phys. Lett.* **1993,** *206* (5-6), 437-444.

27.   Ulness, D. J.; Kirkwood, J. C.; Albrecht, A. C., Competitive events in fifth order time resolved coherent Raman scattering: Direct versus sequential processes. *J. Chem. Phys.* **1998,** *108* (10), 3897-3902.

28.   Blank, D. A.; Kaufman, L. J.; Fleming, G. R., Fifth-order two-dimensional Raman spectra of CS_2 are dominated by third-order cascades. *J. Chem. Phys.* **1999,** *111* (7), 3105-3114.

29.   Kubarych, K. J.; Milne, C. J.; Lin, S.; Astinov, V.; Miller, R. J. D., Diffractive optics-based six-wave mixing: Heterodyne detection of the full $\chi(5)$ tensor of liquid CS_2. *J. Chem. Phys.* **2002,** *116* (5), 2016-2042.

30.   Wilson, K. C.; Lyons, B.; Mehlenbacher, R.; Sabatini, R.; McCamant, D. W., Two-dimensional femtosecond stimulated Raman spectroscopy: Observation of cascading Raman signals in acetonitrile. *J. Chem. Phys.* **2009,** *131* (21), 214502.

31.   Tokmakoff, A.; Lang, M. J.; Larsen, D. S.; Fleming, G. R.; Chernyak, V.; Mukamel, S., Two-dimensional Raman spectroscopy of vibrational interactions in liquids. *Phys. Rev. Lett.* **1997,** *79* (14), 2702-2705.

32.   Jansen, T. l. C.; Snijders, J. G.; Duppen, K., Interaction induced effects in the nonlinear Raman response of liquid CS_2: A finite field nonequilibrium molecular dynamics approach. *J. Chem. Phys.* **2001,** *114* (24), 10910-10921.

33.   Mehlenbacher, R. D.; Lyons, B.; Wilson, K. C.; Du, Y.; McCamant, D. W., Theoretical analysis of anharmonic coupling and cascading Raman signals observed with femtosecond stimulated Raman spectroscopy. *J. Chem. Phys.* **2009,** *131* (24), 244512.

34.   Cina, J. A.; Kovac, P. A., How fissors works: observing vibrationally adiabatic conformational change through femtosecond stimulated Raman spectroscopy. *J. Phys. Chem. A* **2013,** *117* (29), 6084-6095.

35.   Molesky, B. P.; Giokas, P. G.; Guo, Z.; Moran, A. M., Multidimensional resonance Raman spectroscopy by six-wave mixing in the deep UV. *J. Chem. Phys.* **2014,** *141* (11), 114202.

36.   Tanimura, Y.; Okumura, K., First-, third-, and fifth-order resonant spectroscopy of an anharmonic displaced oscillators system in the condensed phase. *J. Chem. Phys.* **1997,** *106* (6), 2078-2095.

37.   van Veldhoven, E.; Khurmi, C.; Zhang, X.; Berg, M. A., Time-resolved optical spectroscopy with multiple population dimensions: a general method for resolving dynamic heterogeneity. *Chemphyschem* **2007,** *8* (12), 1761-1765.

38.   Berg, M. A., Multidimensional incoherent time-resolved spectroscopy and complex kinetics. *Adv. Chem. Phys.* **2012,** *150*, 1.

39.   Underwood, D. F.; Blank, D. A., Measuring the change in the intermolecular Raman spectrum during dipolar solvation. *J. Phys. Chem. A* **2005,** *109* (15), 3295-3306.

40.   Moran, A. M.; Nome, R. A.; Scherer, N. F., Field-resolved measurement of reaction-induced spectral densities by polarizability response spectroscopy. *J. Chem. Phys.* **2007,** *127* (18), 184505.

41.   Park, S.; Kim, J.; Scherer, N. F., Two-dimensional measurements of the solvent structural relaxation dynamics in dipolar solvation. *Phys. Chem. Chem. Phys.* **2012,** *14* (22), 8116-8122.

42.   Bangcharoenpaurpong, O.; Schomacker, K. T.; Champion, P. M., Resonance Raman investigation of myoglobin and hemoglobin. *J. Am. Chem. Soc.* **1984,** *106* (19), 5688-5698.

43.   Moran, A. M.; Nome, R. A.; Scherer, N. F., Field-resolved coherent Raman spectroscopy of high frequency vibrational resonances. *J. Phys. Chem. A* **2006,** *110* (38), 10925-8.

44.   Hu, S.; Smith, K. M.; Spiro, T. G., Assignment of protoheme resonance Raman spectrum by heme labeling in myoglobin. *J. Am. Chem. Soc.* **1996,** *118* (50), 12638-12646.

45.   Lepetit, L.; Chériaux, G.; Joffre, M., Linear techniques of phase measurement by femtosecond spectral interferometry for applications in spectroscopy. *J. Opt. Soc. Am. B* **1995,** *12* (12), 2467.

46.   Hoffman, D. P.; Valley, D.; Ellis, S. R.; Creelman, M.; Mathies, R. A., Optimally shaped narrowband picosecond pulses for femtosecond stimulated Raman spectroscopy. *Opt. Express* **2013,** *21* (18), 21685-21692.

47.   See supplementary material at http://dx.doi.org/10.1063/1.4914095 E-JCPSA6-142-001596for further discussion of the delay, τ_2, and derivations of formulas used to compute direct fifth-order and cascaded third-order signals. .

48.   Laaser, J. E.; Xiong, W.; Zanni, M. T., Time-domain SFG spectroscopy using mid-IR pulse shaping: practical and intrinsic advantages. *J. Phys. Chem. B* **2011,** *115* (11), 2536-2546.

49.   Womick, J. M.; Miller, S. A.; Moran, A. M., Probing the dynamics of intraband electronic coherences in cylindrical molecular aggregates. *J. Phys. Chem. A* **2009,** *113* (24), 6587-6598.

50. Ding, F.; Fulmer, E. C.; Zanni, M. T., Heterodyned fifth-order two-dimensional IR spectroscopy: third-quantum states and polarization selectivity. *J. Chem. Phys.* **2005,** *123* (9), 94502.

51. Garrett-Roe, S.; Hamm, P., Purely absorptive three-dimensional infrared spectroscopy. *J. Chem. Phys.* **2009,** *130* (16), 164510.

52. Busby, E.; Carroll, E. C.; Chinn, E. M.; Chang, L.; Moulé, A. J.; Larsen, D. S., Excited-state self-trapping and ground-state relaxation dynamics in poly(3-hexylthiophene) resolved with broadband pump–dump–probe spectroscopy. *J. Phys. Chem. Lett.* **2011,** *2* (21), 2764-2769.

53. Kumar, A. T. N.; Zhu, L.; Christian, J. F.; Demidov, A. A.; Champion, P. M., On the rate distribution analysis of kinetic data using the maximum entropy method: Applications to myoglobin relaxation on the nanosecond and femtosecond timescales. *J. Phys. Chem. B* **2001,** *105* (32), 7847-7856.

54. Rosca, F.; Kumar, A. T. N.; Ye, X.; Sjodin, T.; Demidov, A. A.; Champion, P. M., Investigations of coherent vibrational oscillations in myoglobin. *J. Phys. Chem. A* **2000,** *104* (18), 4280-4290.

55. Dunlap, B.; Wilson, K. C.; McCamant, D. W., Phase-matching and dilution effects in two-dimensional femtosecond stimulated Raman spectroscopy. *J. Phys. Chem. A* **2013,** *117* (29), 6205-6216.

56. Fulmer, E. C.; Ding, F.; Zanni, M. T., Heterodyned fifth-order 2D-IR spectroscopy of the azide ion in an ionic glass. *J. Chem. Phys.* **2005,** *122* (3), 34302.

57. Mukherjee, S. S.; Skoff, D. R.; Middleton, C. T.; Zanni, M. T., Fully absorptive 3D IR spectroscopy using a dual mid-infrared pulse shaper. *J. Chem. Phys.* **2013,** *139* (14), 144205.

58. Sun, Z.; Lu, J.; Zhang, D. H.; Lee, S. Y., Quantum theory of (femtosecond) time-resolved stimulated Raman scattering. *J. Chem. Phys.* **2008,** *128* (14), 144114.

59. Myers, A. B.; Mathies, R. A.; Tannor, D. J.; Heller, E. J., Excited state geometry changes from preresonance Raman intensities: Isoprene and hexatriene. *J. Chem. Phys.* **1982,** *77* (8), 3857-3866.

60. Mukamel, S., *Principles of Nonlinear Optical Spectroscopy*. Oxford University Press: New York, 1999.

61. Hochstrasser, R. M., Two-dimensional IR-spectroscopy: polarization anisotropy effects. *Chem. Phys.* **2001,** *266* (2-3), 273-284.

CHAPTER 5. TWO-DIMENSIONAL RESONANCE RAMAN SPECTROSCOPY OF OXYGEN- AND WATER-LIGATED MYOGLOBIN[3]

5.1. Introduction

Once the specialization of a small number of experimental groups, multidimensional laser spectroscopies have become fairly widespread in the past 20 years with applications spanning the traditional disciplines of chemistry, biology, and physics.[1-10] The development of multi-dimensional techniques is rooted in the picosecond coherent Raman spectroscopies of the late 1970's and early 1980's.[11-14] At the time, it was unclear whether or not traditional (one-dimensional) coherent Raman measurements could distinguish between homogeneous and inhomogeneous line broadening mechanisms.[15-17] Theoretical work showed that higher-order (multidimensional) methods were indeed required to obtain such information,[18-20] and early success was achieved in Raman echo experiments (i.e., eight-wave mixing).[21] Several experimental groups took up the challenge of conducting six-wave mixing experiments in the mid-1990's but met substantial technical challenges.[22-27] Success in six-wave mixing measurements was achieved after years of exhaustive efforts.[27-28] Difficulties encountered in these pioneering works significantly slowed further development of multidimensional Raman techniques. However, interest in this class of experiments has been reinitiated by related methods that are used to study molecular photochemistries.[29-40]

---

[3] This chapter previously appeared as an article in the Journal of Chemical Physics. The original citation is as follows: Molesky, B. P.; Guo, Z.; Cheshire, T. P.; Moran, A. M., Two-dimensional resonance Raman spectroscopy of oxygen- and water-ligated myoglobins. *J. Chem. Phys.* **2016**, 145 (3), 034203. Copyright (2016) American Institute of Physics.

In this paper, we present two-dimensional resonance Raman (2DRR) measurements that blend different types of higher-order Raman spectroscopies. The multi-beam aspect of the experiment illustrated in Figure 5.1 is similar in nature to earlier off-resonant 2D Raman work,[27-28] whereas the combination of narrowband and broadband pulses is inspired by Femtosecond Stimulated Raman Spectroscopy (FSRS).[30, 32] As depicted in Figure 5.1, the experiment begins when an actinic pump pulse initiates vibrational motion of the system in the variable delay, τ_1. Fourier transformation with respect to τ_1 constitutes the first dimension of the 2DRR spectrum. Vibrational motion is re-initiated by time-coincident Raman pump and Stokes pulses before a second Raman pump pulse induces signal emission. The second dimension of the 2DRR spectrum is obtained by dispersing the signal pulse on an array detector. The approach is distinct from traditional three-pulse FSRS in that (i) residual laser light does not travel in the same direction as the signal beam and (ii) a fixed delay, τ_2, is used to suppress the intense broadband pump-repump-probe response.[41] The data acquisition rate and sensitivity of our method facilitate detection of the 2DRR response, which is generally less that 5% of the total fifth-order signal. Traditional three-beam FSRS offers other advantages such as automatic heterodyne detection and straightforward implementation of two-color experiments.[30]

175
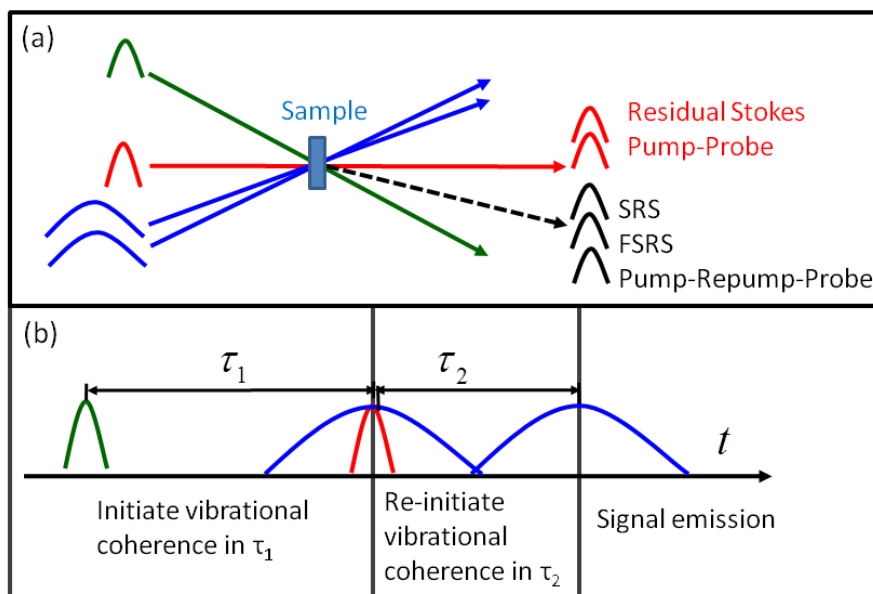
Figure 5.1. (a) A four-beam FSRS geometry is used in this work to eliminate the portion of the background associated with residual Stokes light and a pump-probe response. The color code is as follows: the actinic pump is green, the Raman pump is blue, and the Stokes pulse is red. (b) Vibrational coherences in τ_1 are resolved by numerically Fourier transforming the signal with respect to the delay time. Time-coincident Raman pump and Stokes pulse then initiate a second set of vibrational coherences, which are resolved by dispersing the signal pulse on an array detector. The fixed time delay, τ_2, is used to suppress the broadband pump-repump-probe response of the solution.

Measurements and model calculations are conducted for both metmyoglobin (metMb) and oxymyoglobin (MbO_2) in order to establish signatures of inhomogeneous line broadening and anharmonic coupling in 2DRR spectra. The charge of the iron atom is +3 (ferric) and +2 (ferrous) in metMb and MbO_2, respectively. Of course, the two systems also differ in whether water (metMB) or oxygen (MbO_2) is coordinated on the distal side of the heme group. Sub-100-fs photodissociation of oxygen is induced following photoexcitation in the visible spectral range in MbO_2, whereas metMb relaxes to the ground electronic state by way of non-radiative processes on the picosecond time scale.[42-47] In analogy with other 2D methods, the present 2DRR measurements reveal heterogeneity within the ensembles for the two systems. The 220-cm^{-1} iron-histidine stretching mode is of particular interest because of its prominence in MbO_2, where the

heme moiety transitions from a planar to non-planar geometry following photodissociation.[48] In addition, vibrational modes associated with the propionic acid side chains may provide insight into energy exchange between the heme and aqueous solvent.[49-52] Line broadening mechanisms of these modes are intimately connected to such vibrational energy exchange, because they reflect fluctuations in the geometries.

The present work builds upon a variety of experimental approaches that we have developed for conducting 2DRR experiments in recent years.[41, 53-54] An earlier report of the technique employed in this work focused primarily on experimental issues.[41] Control experiments were used to show that the response of metMb exhibits the anticipated (correct) dependence on sample concentration and on the intensities of the incoming beams. The susceptibility of the experiment to cascaded four-wave mixing responses was an issue of primary concern, because these undesired nonlinearities present significant challenges in off-resonant 2D Raman experiments.[26-28, 55-56] It was also shown that cascades of four-wave mixing signals are negligible under our experimental conditions. Calculations suggest the selection rules that enhance cascaded signal intensity under electronically off-resonant conditions are obviated when all pulses are electronically resonant with the system. In effect, the direct and cascaded signals compete on the same footing when all laser beams are tuned into electronic resonance. The cascaded signal is weaker than the direct response with optical densities of metMb less than 1.0, because it involves two more field-matter interactions (i.e., it is a higher-order process in this respect). Our analysis suggests that the direct response of myoglobin will also dominate in a conventional three-beam FSRS geometry. That is, it may generally be possible to conduct 2DRR spectroscopy without beam geometries cleverly designed to induce phase mismatch in third-order nonlinearities.

5.2. Experimental Methods

5.2.1. Sample Preparation

Myoglobin from horse skeletal muscle (Sigma-Aldrich) is dissolved in 0.1-M sodium phosphate buffer at a pH of 7.0. The metMb solutions are centrifuged at 6000 revolutions per minute for 15 minutes before each experiment to optimize the optical quality. To convert metMb to MbO_2, 10-fold molar excess of sodium hydrosulfite is added to reduce metMb. Air is then bubbled through the solution for 15 minutes until it is bright red in color. Attainment of a high quality MbO_2 sample is confirmed by comparison of the sample's linear absorption to the known spectrum of MbO_2. The primary metric is the peak position of the Soret band, which is located at 409 and 418 nm for metMb and MbO_2, respectively.[57] Spontaneous Raman spectra are also used to confirm the position of the most intense in-plane bond stretching vibration (i.e., an oxidation state marker band). The vibrational frequencies of this mode are close to 1373 and 1356 cm^{-1} for metMb and MbO_2 , respectively.[58-59] In all experiments, the 0.2-mM sample of myoglobin is flowed through a wire-guided jet with a thickness of 220 μm, where the reservoir volume is 50 mL.[60] Absorbance spectra are measured before and after experiments to confirm the absence of sample degradation.

5.2.2. Spectroscopic Measurements

In this section, we summarize key aspects of the experimental approach, which is described at length in Reference [41]. As in earlier work, we employ laser pulses which are all resonant with the Soret bands of metMb and MbO_2 (see Figure 5.2). The narrowband Raman pump pulses are generated by sending 70-fs, 410-nm second harmonic pulses through a 4F spectral filter consisting of two 2400-g/mm gratings and two 25-cm focal length lenses. Pulses with spectral widths of 50 cm^{-1} are obtained by placing a slit with a 890-μm width at the 2F plane. Broadband actinic pump and Stokes pulses are produced by focusing a 90-μJ, 410-nm

second harmonic beam into a 75-cm long hollow core fiber filled with 1.0 atm of argon gas. The spectrally broadened output of the fiber is compressed using fused-silica prisms separated by 50 cm to achieve an instrument response of 20 fs over full the spectral range corresponding to Raman shifts of 200-1500 cm^{-1} (413-437 nm).
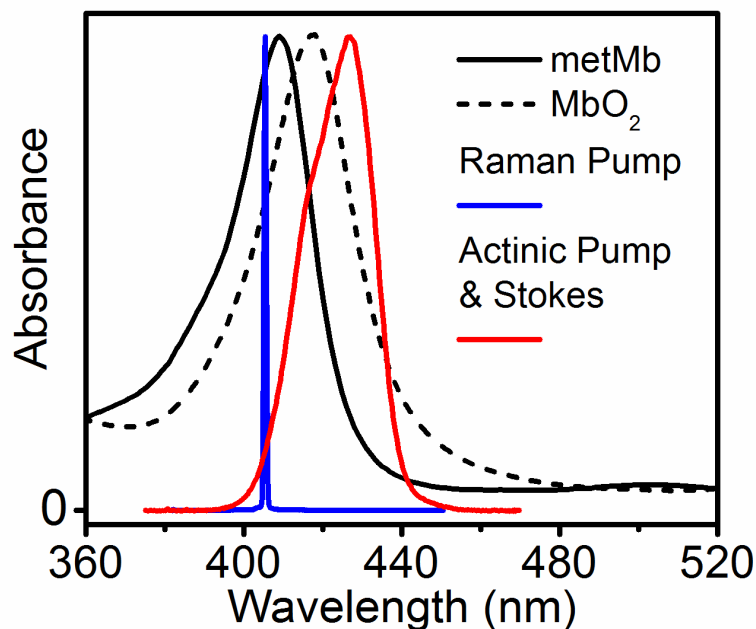
Figure 5.2. *Laser spectra are overlaid on the linear absorbance spectra of (a) metMb and (b) MbO₂ in aqueous buffer solution at pH=7.0.*

Experiments are conducted with the diffractive optic-based interferometer shown in Figure 5.3. All beams are focused onto the diffractive optic with a 50-cm focal length spherical mirror. Approximately 25% of each incident beam is diffracted into each of the three diffraction orders (0 and +/-1). The 20-cm focal length imaging mirror is rotated off-axis by approximately 5° (i.e., the minimum amount). The actinic pump and Raman pump beams cross at approximately 6.9° in the diffractive optic and are bisected by the Stokes beam. The angle between the +1 and -1 diffraction orders of the Raman pump beams is 6.9°. The angle between +1 and -1 diffraction orders of the actinic pump and Stokes beams is 7.2°; the actinic pump and Stokes pulses have the

same spectrum (see Figure 5.2). Pulse energies of the actinic pump and Stokes pulses are 100 nJ each. The pulse energy of each Raman pump is 150 nJ. The FWHM spot sizes of all laser beams are 200 μm at the sample position.
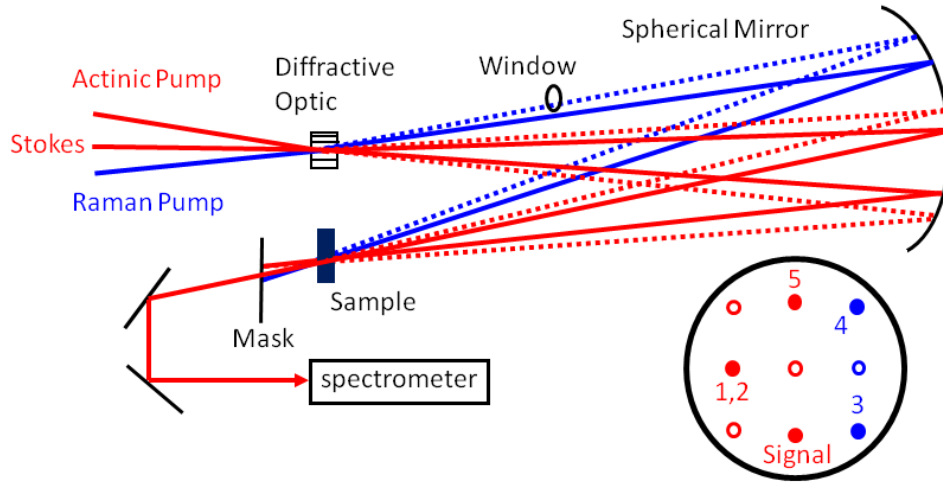
Figure 5.3. *Diffractive optic-based interferometer used for 2DRR measurements. The transparent fused silica window delays pulse 3 by 290 fs with respect to pulse 4 (delay τ_2 in Figure 5.1). A four-beam geometry is used to detect the signal radiated in the direction, k_1-$k_2+k_3-k_4+k_5$; the wavevectors k_1 and k_2 cancel each other. The 2DRR signal is obtained by measuring differences with and without the actinic pump (beam 1,2). Beams represented with solid circles reach the sample, whereas those represented with open circles are blocked with a mask.*

We employ a four-beam geometry in which the signal is associated with the difference produced by the actinic pump beam.[41] The four-wave mixing "background" generated by the Raman pump and Stokes pulses is not difficult to subtract, because it is only 10-20 times larger than the desired fifth-order response. We find that the background is most effectively removed by subtracting spectra acquired at negative delay times (far from the rise of the FSRS signal near τ_1 =-10 ps). An alternate approach in which the actinic pump beam is chopped at every delay point results in poor signal quality because of the longer data acquisition time. Despite its smaller background, we opt not to use the five-beam geometry described in Reference [41], because it is more difficult to maintain alignment day-to-day. In addition, color tunable actinic pump beams

may be employed in the four-beam geometry, and such experiments are presently being pursued with the same experimental setup.[54]

Signals are detected using a back-illuminated CCD array (Princeton Instruments PIXIS 100B) mounted on a 0.3-meter spectrograph with a 1200-g/mm grating. The signal beam is focused to a spot size of 100 μm at the entrance to the spectrograph to obtain hardware-limited spectral resolution of approximately 10 cm^{-1}. Ultimately, the resolution of the measurement is limited by the 50-cm^{-1} spectral width of the Raman pump beam. The total FSRS response produces roughly 1000 counts on the detector at each delay point with an integration time of 100 ms. The vibrational coherences associated with the 2DRR component of the response are all less than 5% of the total signal. The delay, τ_1, of the actinic pump is scanned 100 times, and the signal is averaged to optimize the data quality.

5.3. Simulations of 2DRR Spectra

The development of 2DRR spectroscopy is still at an early stage despite a long history of off-resonant 2D Raman work. As mentioned above, signal generation is allowed and forbidden for harmonic systems in resonant and off-resonant experiments, respectively. The implications of this difference in selection rules for information content has not yet been established. To this end, we begin this section by examining signatures of inhomogeneous broadening and anharmonicity in 2DRR spectra for a pair of vibrational modes. The 2DRR spectrum of myoglobin is then simulated using parameters derived from earlier spontaneous resonance Raman experiments. Insights gained from these calculations will be used to interpret experimental signals in Section 5.4.

5.3.1. Signatures of Inhomogeneous Broadening in 2DRR Spectra

The ability to distinguish inhomogeneous and homogeneous line broadening mechanisms motivated the first multidimensional Raman experiments conducted in the late 1980's and early 1990's.[18, 21] The spectroscopic signatures are much like those associated with 2D photon echo experiments, where heterogeneity gives rise to a difference between the diagonal and anti-diagonal widths.[1, 8, 61-62] Inhomogeneous line broadening is a signature of correlation between the resonance frequencies detected in the two frequency dimensions.[63-64] Unlike Raman echo experiments,[21] the present (fifth-order) 2DRR experiments do not yield the time scale at which correlation decays, because an intermediate "waiting time" cannot be scanned.[18] Rather, we are able to detect the amount of correlation present in the system on the time-scale of the inverse of the vibrational line width.

Spectroscopic signatures are most easily established with calculations based on two vibrational modes and a single electronic resonance. The model developed in Reference [41] can be adapted for this purpose (see Section 5.7.1). We take the mode frequencies to be 400 cm^{-1} and 1100 cm^{-1} in order to produce well-resolved vibrational resonances. Resolution of the various 2DRR peaks also requires that the two mode frequencies and their overtones are well-separated. For example, the overtone of the 400-cm^{-1} mode at 800 cm^{-1} must be well-separated from the fundamental mode frequency at 1100 cm^{-1}. The dimensionless displacement of each mode is set equal to 0.75 so that all key resonances can be observed on the same linear scale for the signal magnitude.

Heterogeneity is introduced by convoluting the signal field defined in Section 5.7.1 with a Gaussian function,

$$S(\omega_1, \omega_2) = \int_{-\infty}^{\infty} \int_{-\infty}^{\infty} G(\eta_a, \eta_b) E_{2DRR}^{(5)}(\omega_1, \omega_2) d\eta_a d\eta_b \ , \tag{5.1}$$

Where

$$G(\eta_a, \eta_b) = \frac{1}{2\pi\sigma_a\sigma_b\sqrt{1-\rho^2}} \times$$
$$\exp\left\{-\frac{1}{2(1-\rho^2)}\left[\frac{(\varpi_a+\eta_a)^2}{\sigma_a^2} - 2\rho\frac{(\varpi_a+\eta_a)(\varpi_b+\eta_b)}{\sigma_a\sigma_b} + \frac{(\varpi_b+\eta_b)^2}{\sigma_b^2}\right]\right\} \qquad (5.2)$$

Here, η_a is the deviation of the harmonic mode frequency, a, from its mean value, ϖ_a (in cm^{-1}) whereas σ_a is the width of the inhomogeneous distribution. The inter-mode correlation parameter, ρ, ranges from the fully anti-correlated (-1) to fully correlated (+1) limits.[63-64] The signal field depends on ϖ_a and ϖ_b through the vibrational Hamiltonian of the system (see Section 5.7.2).

The calculations in Figure 5.4 are conducted in the anti-correlated (ρ =-0.75), uncorrelated (ρ =0), and correlated (ρ =+0.75) regimes. Of course, the diagonal peaks exhibit correlated line shapes for all cases, because the inhomogeneous widths, σ_a and σ_b, are nonzero. Notably, this signature of inhomogeneous line broadening cannot be derived from one-dimensional Raman spectroscopy (e.g., third-order stimulated Raman and spontaneous Raman measurements). For diagonal 2DRR peaks, the anti-diagonal width is related to homogeneous broadening, whereas the diagonal width represents the combination of homogeneous and inhomogeneous widths. Unlike the diagonal peaks, the orientations and relative intensities of the cross peaks depend on the correlation parameter, ρ; the cross peaks possess an anti-diagonal and diagonal slant when the correlation parameter is negative and positive, respectively. The cross peaks exhibit a fairly "round" line shape for the uncorrelated limit in Figure 5.4(b). These spectroscopic signatures are much like those established in 2D infrared experiments.[1, 8, 61-62] The

relative intensities of the cross peaks are largest when ρ is positive because of cancellations between terms with opposite signs in $G\left(\eta_a, \eta_b\right)$.
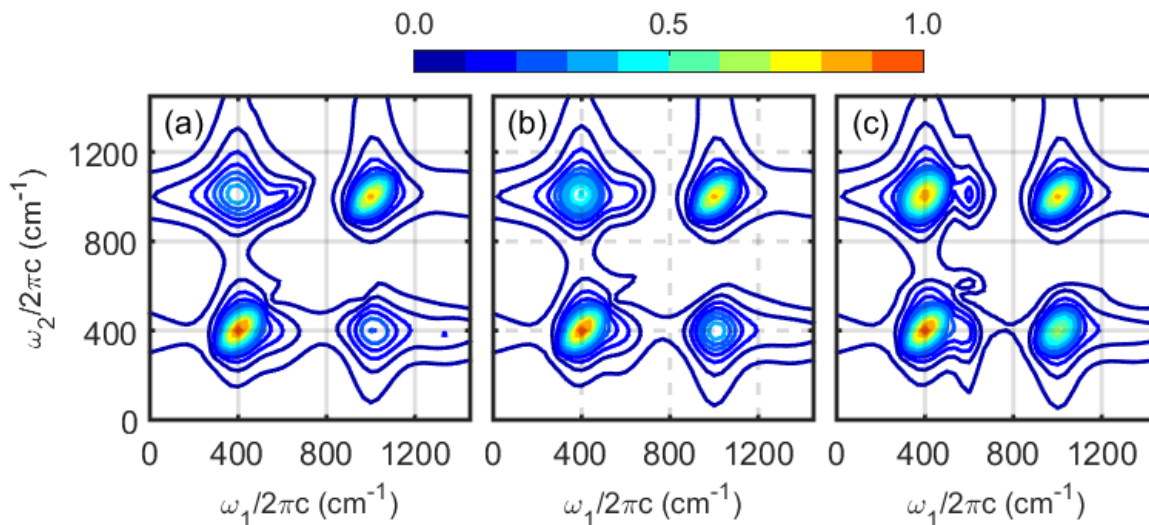
Figure 5.4. *2DRR spectra computed for a pair of harmonic oscillators with inhomogeneous line broadening. The spectra are computed by combining Equations 5.1 and 5.23 with the parameters given in Table 5.1. The correlation parameter, ρ, is set equal to (a) -0.75, (b) 0.0, and (c) 0.75. The diagonal peaks always exhibit correlated line shapes, whereas the orientations and intensities of the off-diagonal peaks depend on the correlation parameter, ρ.*

5.3.2. Signatures of Anharmonicity in 2DRR Spectra

Signal generation is allowed in off-resonant 2D Raman experiments only if the modes are anharmonic or the polarizability scales nonlinearly with the vibrational coordinates.[19-20] Thus, success in detecting the signal constitutes unambiguous evidence of a non-trivial behavior. Of course, this aspect of the off-resonant nonlinearity also means that the signal will generally be small and that artifacts such as cascades can readily contaminate the signals.[27-28] As noted in our previous work, 2DRR spectroscopy is "easier" to conduct than off-resonant 2D Raman experiments, because signal generation is allowed for harmonic modes. Unfortunately, this also means that any pair of harmonic Franck-Condon active modes will generate a 2DRR cross peak,

thereby complicating signal interpretation. We investigate signatures of anharmonicity in 2DRR spectra in this section.
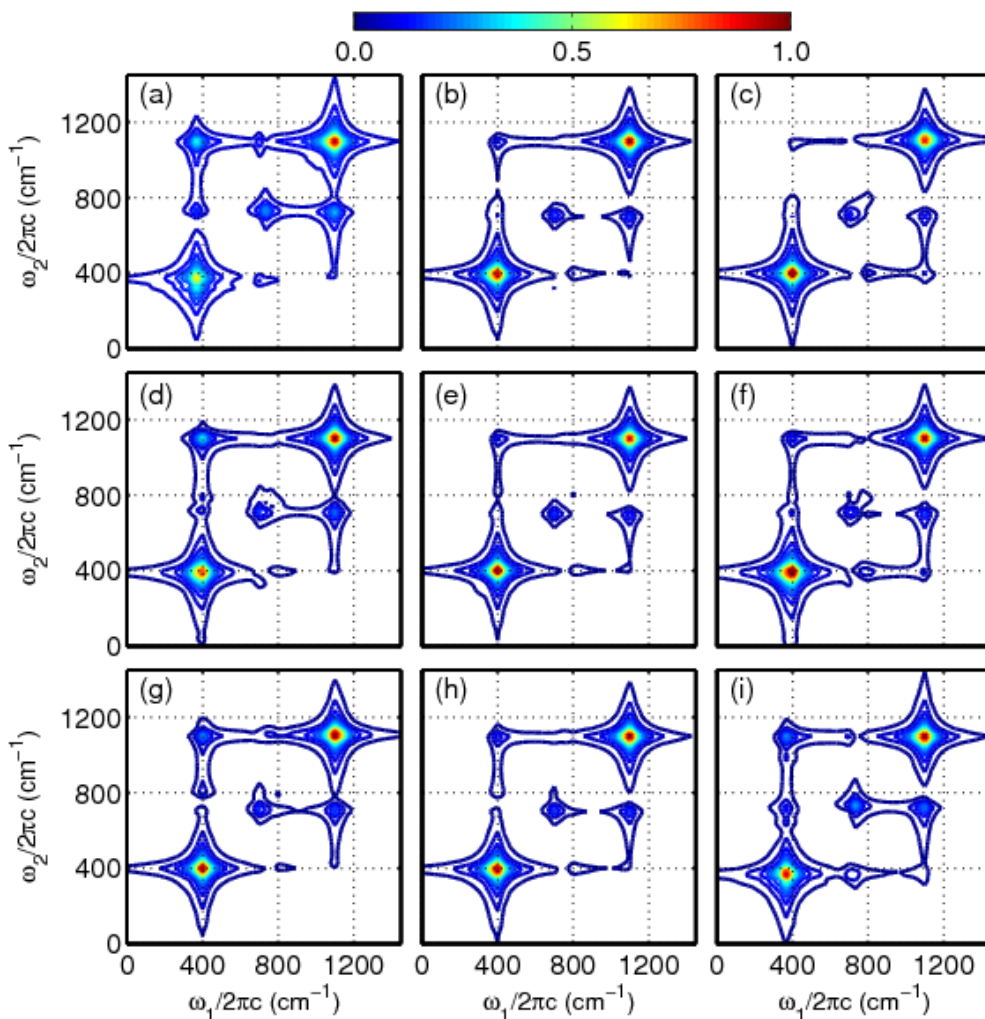
Figure 5.5. *2DRR spectra computed with the anharmonic vibrational Hamiltonian described in Section 5.7.2 and the parameters in Table 5.1. The diagonal cubic expansion coefficients are set equal to -5 (first row), 0 (second row), and 5 cm^{-1} (third row). The off-diagonal expansion coefficients are set equal to -5 (first column), 0 (second column), and 5 cm^{-1} (third column). The response of a harmonic system is shown in panel (e). These calculations suggest that anharmonic coupling promotes intensity borrowing effects via the transformation of Franck-Condon overlap integrals from the harmonic to anharmonic basis set (see Equation 5.26). For many of the parameter sets, anharmonicity causes the intensity of the cross peak above the diagonal to increase relative to that of the cross peak below the diagonal. This effect is most pronounced in the left column.*

As in Section 5.3.1, calculations are conducted for a pair of vibrational modes and single electronic resonance. However, we treat only homogeneous line broadening here in order to focus on the effects of anharmonicity. Cubic force constants are added to a harmonic vibrational Hamiltonian as described in Section 5.7.2. The two normal modes mix through cubic force constants that depend on two coordinates. These "off-diagonal" cubic expansion coefficients are denoted as U_{122}, U_{212}, U_{221}, U_{211}, U_{121}, and U_{112}. In contrast, the "diagonal" cubic expansion coefficients, U_{111} and U_{222}, primarily shift the resonances to lower frequencies.

In Figure 5.5, the off-diagonal expansion coefficients are all set equal to three values (-5, 0, and 5 cm^{-1}) to illustrate the effects that these terms have on 2DRR spectra. New resonances are not generated; however, the peak intensities are affected by an intensity borrowing effect that originates in the transformation of Franck-Condon overlap integrals from the harmonic to anharmonic basis sets (see Equation 5.26). Calculations are also carried out for three values of the diagonal expansion coefficients (-5, 0, and 5 cm^{-1}). In general, the cross peak intensities above the diagonal increase relative to the cross peak below the diagonal for the anharmonic systems (see Figures 5.5(a), 5.5(d), 5g, and 5.5(i)). In general, differences between 2DRR spectra for the anharmonic and harmonic (see Figure 5.5(e)) systems are fairly subtle, which suggests limited potential of the 2DRR technique to reveal anharmonic couplings in the present a quasi-degenerate (one-color) configuration.

For FSRS signals represented in the traditional way (τ_1 and ω_2 in our notation), it has been shown that anharmonic coupling between modes may cause the vibrational resonance frequencies in ω_2 to oscillate with respect to τ_1 in ring-opening[65] and proton photodissociation[66] reactions. The present model does not predict such dynamics, because the non-oscillatory

component of the signal dominates the response under one-color conditions. In previous 2DRR studies of the photodissociation reaction of triiodide, we observed anharmonicity-induced oscillations in the vibrational resonance frequencies under two-color conditions.[53-54] Although signatures of anharmonicity are more readily derived from two-color 2DRR experiments, it will still be true that cross peaks are generated for all pairs of Franck-Condon actives modes (whether they are harmonic or not). Simulated 2DRR spectra will be useful for identifying genuine evidence of anharmonicity.

5.3.3. Predicted 2DRR Spectrum of Myoglobin

Calculations presented in Sections 5.3.1 and 5.3.2 provide basic insights into 2DRR signal interpretation. The simulations suggest that signatures of inhomogeneous line broadening will be fairly obvious, whereas unambiguous evidence of anharmonicity will be difficult to derive from experimental data (particularly in one-color experiments). It will be useful to "estimate" how the 2DRR spectrum of myoglobin should be expected to appear based on earlier work. To this end, the parameters needed to simulate the 2DRR spectrum for a one-color experiment can be obtained from earlier fits to the spontaneous Raman excitation profiles for the Soret band.[67] Notably, these fits are carried out in a basis of harmonic modes.

In Figure 5.6, we present a 2DRR spectrum computed in the homogeneous limit of line broadening using the parameters given in Table 5.2. The four most dominant vibrational modes are included in the model. A peak associated with each mode appears on the diagonal. The most intense cross peak is found at $\omega_1/2\pi c = 220$ cm^{-1} (iron-histidine stretch) and $\omega_2/2\pi c = 1356$ cm^{-1} (in-plane stretch of heme); the cross peak intensity above the diagonal is greater than that found for the corresponding cross peak below the diagonal. The model additionally suggests that the intensity of the cross peak above the diagonal increases with respect to the peak below the

diagonal as the dimensionless displacements increase. The spectrum in Figure 5.6 exhibits weak off-diagonal peaks that are shifted down the ω_2 axis from the 674-cm^{-1} and 1356-cm^{-1} diagonal peaks by 220 cm^{-1}. These off-diagonal peaks represent sequences in which the system evolves in a coherence at the fundamental 674-cm^{-1} or 1356-cm^{-1} frequency τ_1 and an inter-mode coherence in τ_2. Finally, we remark that the calculations presented in Figure 5.6, which employ large mode displacements, exhibit a peak associated with an inter-mode vibrational coherence on the diagonal (at $\omega_1/2\pi c = \omega_2/2\pi c = 454$ cm^{-1}). Detection of this type of resonance requires two modes with significant displacements.

Overall, the calculations presented in Figures 5.4-5.6 suggest that line broadening mechanisms will be the primary information to be derived from 2DRR spectra for myoglobin. Signatures of anharmonicity are likely to be ambiguous in the present quasi-degenerate (one-color) experiments, because the response is allowed for harmonic modes. Moreover, the fairly small potential energy surface displacements found in myoglobin should make most cross peaks difficult to detect.[67]
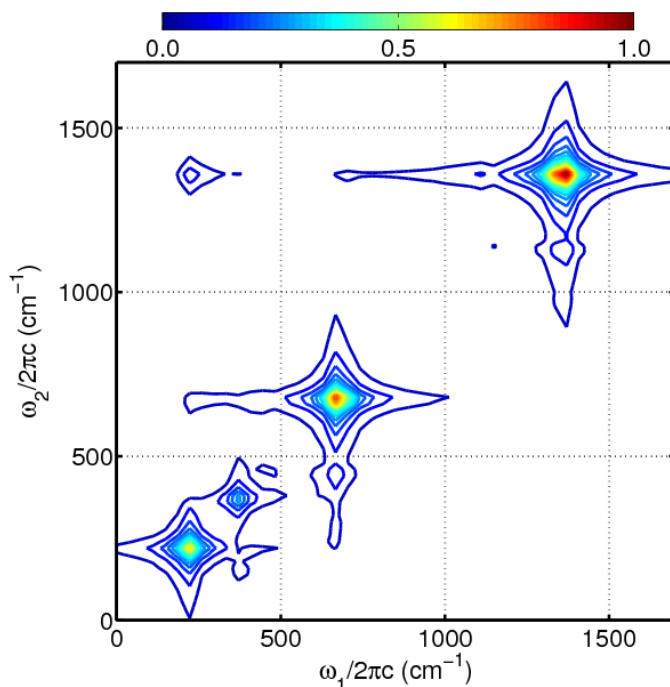
Figure 5.6. *2DRR spectrum of myoglobin computed using parameters obtain by fitting spontaneous resonance Raman excitation profiles.[67] The spectrum is dominated by resonances on the diagonal. The most dominant cross peak is associated with the iron-histidine stretch (* $\omega_1 / 2\pi c = 220\ cm^{-1}$*) and in-plane stretching mode (* $\omega_2 / 2\pi c = 1356\ cm^{-1}$*). The spectra are computed by combining Equation 5.23 with the parameters in Table 5.2.*

5.4. Results and Discussion

5.4.1. Isolation of 2DRR Signal Components

In this section, we show how the 2DRR response is extracted from the total signal. To begin, the procedure used to obtain the FSRS-like representation of the signal at various delay times, τ_1, was described at length in earlier work.[41] Examples of such FSRS-like signals are shown in Figures 5.7(a) and 5.7(d). The novel aspect of this study is that we carry out a Fourier transformation with respect to τ_1 to generate a 2DRR spectrum. The main challenge in doing so is that the coherent signal component of interest must be separated from the much larger incoherent fifth-order response. Below, we discuss issues particular to this aspect of the data analysis.
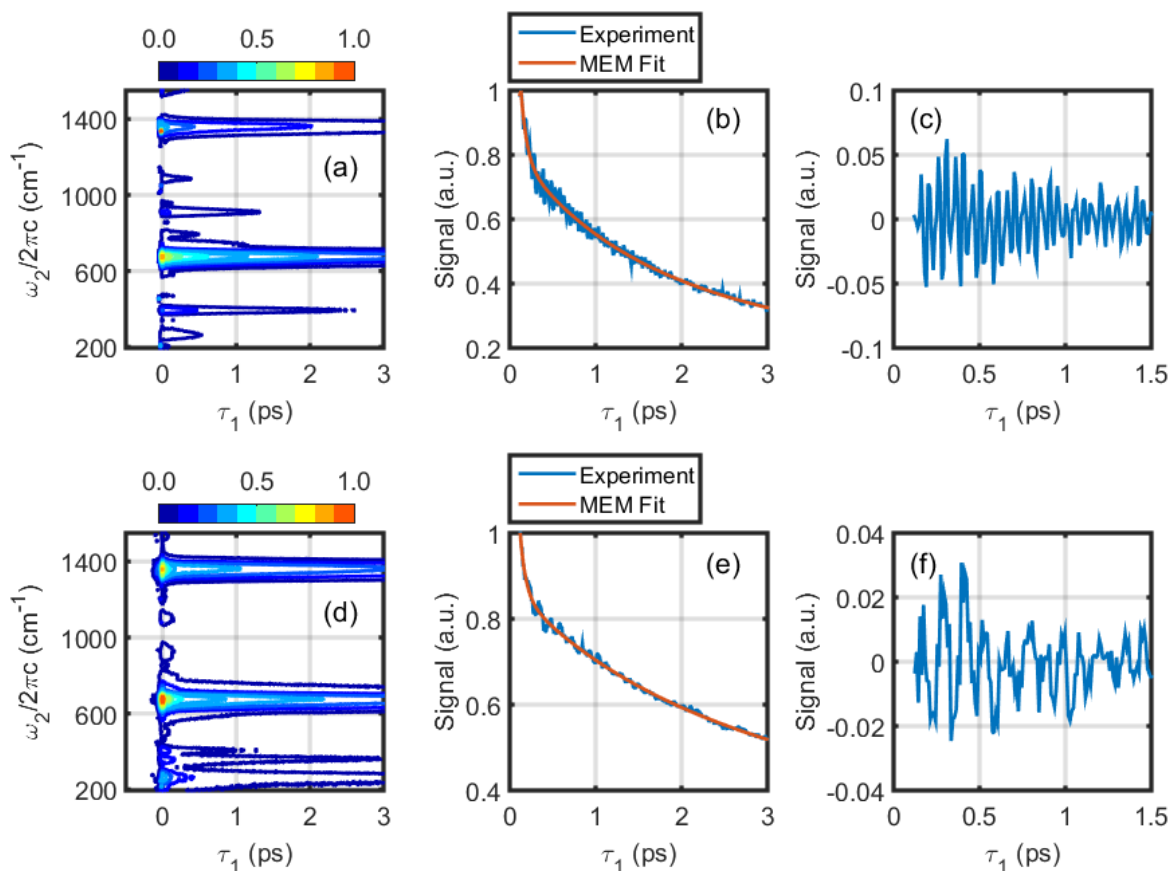
Figure 5.7. *Signals obtained for (a) metMb and (d) MbO₂ in a FSRS-like representation. At each point in ω_2, the incoherent baseline is generated using the maximum entropy method. Shown here are slices of the signals for (b) the 670-cm⁻¹ mode of metMb and (e) the 370-cm⁻¹ mode of MbO₂. Coherent residuals are obtained by subtracting incoherent MEM baselines from the total signals for (b) metMb and (e) MbO₂. The coherent residuals are presented for (c) metMb and (f) MbO₂.*

To illustrate the method of data analysis, we begin by examining time-dependent Raman spectra obtained for both metMb and MbO₂ in Figure 5.7. In both cases, peaks are observed near 220 cm⁻¹, 370 cm⁻¹, 675 cm⁻¹, and 1356 cm⁻¹. The in-plane bond stretching mode is a particularly useful marker for the oxidation state of the heme. The vibrational wavenumber is 1356 cm⁻¹ in MbO₂ and 1373 cm⁻¹ in metMB.[59] The 220-cm⁻¹ resonance corresponds to the iron-histidine stretch on the proximal side of the heme group. The 370-cm⁻¹ mode represents double bond (methylene) stretching local to the propionic acid side chains (see Figure 5.8). Finally, the 670

and 1356-cm^{-1} (or 1373-cm^{-1}) modes correspond to deformation and bond-stretching motions localized on the tetrapyrrole moiety, respectively. The intensity of the 220 cm^{-1} mode varies significantly between systems, because photodissociation is initiated only in MbO_2. That is, there is a significant excited state potential energy gradient for the iron-histidine stretch in MbO_2, because the iron moves out of plane following photodissociation.
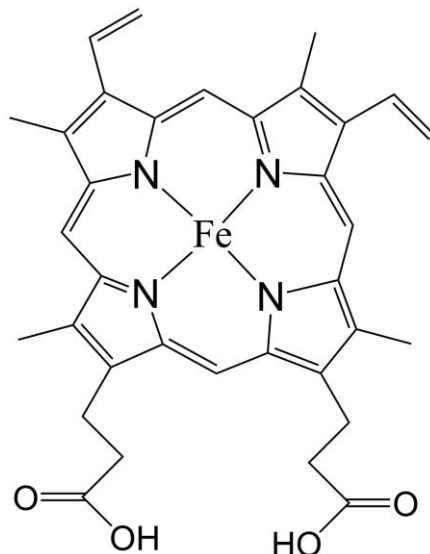
Figure 5.8. *Molecular structure of iron protoporphyrin-IX.*

Oscillatory signal components in τ_1 are isolated by subtracting incoherent baselines generated using the maximum entropy method (MEM), which suppresses low-frequency artifacts that may arise when baselines are produced using a small number of exponential functions.[68] In Figures 5.7(b) and 5.7(e), we overlay example MEM fits with signals obtained for both metMb and MbO_2; residuals are plotted in Figures 5.7(c) and 5.7(f). The analysis is carried out beginning at a delay time of 0.1 ps in τ_1 to remove contributions from the region of pulse overlap. The 2DRR spectra shown in Figure 5.9 are obtained by repeating this procedure at every

point in ω_2 (i.e., every pixel on CCD array), then carrying out a Fourier transformation with respect to τ_1,

$$S(\omega_1,\omega_2) = \int S(\tau_1,\omega_2)\exp(i\omega_1\tau_1 - \alpha\tau_1)d\tau_1, \qquad (5.3)$$

where $S(\tau_1,\omega_2)$ is the baseline-subtracted signal, $S(\omega_1,\omega_2)$ is the 2DRR spectrum, and α is a time constant used to suppress contributions from delay times at which the oscillations have decayed below the noise level. In the present work we set α equal to 1.4 ps^{-1}.

The 2DRR spectra of both systems shown in Figure 5.9 exhibit diagonal peaks near 220 cm^{-1}, 370 cm^{-1}, 674 cm^{-1}, and 1356 cm^{-1} (close to 1373 cm^{-1} in metMb).[59, 67] The peaks near 1356 cm^{-1} are relatively weak, because the 24-fs period of this mode is slightly larger than the 19-fs instrument response width at this particular value of the Raman shift. Two cross peaks are located above the diagonal. The cross peaks at $\omega_1/2\pi c$=50 cm^{-1} and $\omega_2/2\pi c$=674 cm^{-1} reflect motion along the doming coordinate in τ_1. Cross peaks are also located near $\omega_1/2\pi c$=370 cm^{-1} and $\omega_2/2\pi c$=1356 cm^{-1}. It is interesting that only one cross peak is found in the slice of the 2D spectrum near $\omega_2/2\pi c$=1356 cm^{-1}; cross peaks near $\omega_1/2\pi c$=674 cm^{-1} and $\omega_2/2\pi c$=1356 cm^{-1} are below the detection threshold despite the significant intensity of the diagonal peak at 674 cm^{-1}. This aspect of the spectrum is consistent with the simulation in Figure 5.6. In this calculation, an intense cross peak is generated above the diagonal near $\omega_1/2\pi c$=220 cm^{-1} and $\omega_2/2\pi c$=1356 cm^{-1}, but not at $\omega_1/2\pi c$=674 cm^{-1} and $\omega_2/2\pi c$=1356 cm^{-1}. The measurement in Figure 5.9 differs from Figure 5.6 in that off-diagonal peaks are not detected 220 cm^{-1} below diagonal peaks in ω_2 (e.g., at $\omega_1/2\pi c$=674 cm^{-1} and $\omega_2/2\pi c$=454 cm^{-1}). The key issue is that

the iron-histidine stretch is less intense than the prediction based on a fit to the spontaneous

Raman excitation profile.[67]

Cross peaks are detected below the diagonal near $\omega_1/2\pi c = 990$ cm^{-1} and $\omega_2/2\pi c = 674$

cm^{-1}. We tentatively suggest that a Franck-Condon active vinyl stretching mode is responsible

for the 990-cm^{-1} of this peak in the first dimension.[59] The absence of a diagonal peak at $\omega_1/2\pi c$

$= \omega_2/2\pi c = 990$ cm^{-1} could be explained by the weaker Franck-Condon activity of this mode. It is

unclear why a cross peak is not also detected at $\omega_1/2\pi c = 674$ cm^{-1} and $\omega_2/2\pi c = 990$ cm^{-1}. One

possibility is that anharmonicity redistributes intensities among cross peaks as demonstrated in

Figure 5.5. *The calculation presented in Figure 5.6 captures many aspects of the measured*

2DRR spectra in Figure 5.9; however, knowledge of the anharmonic couplings may be the key to

precisely reproducing peak intensities. The calculations presented in Figure 5.5 suggest that

intensity borrowing effects may be observed with relatively modest anharmonic couplings.
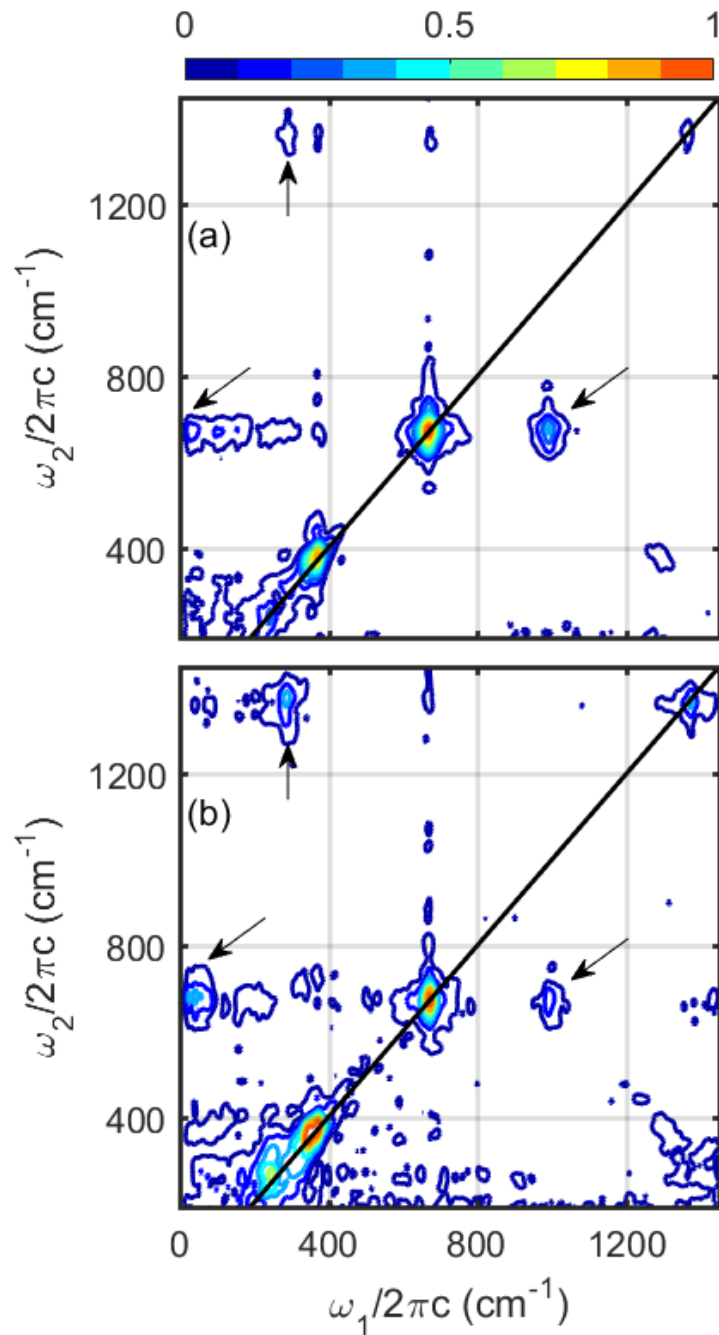
Figure 5.9. *Experimental 2DRR spectra for (a) metMb and (b) MbO₂ are generated by Fourier transforming the coherent residuals with respect to τ_1 at each point in ω_2 (i.e., at each pixel in CCD detector). For both systems, diagonal peaks are detected near 220, 370, 674, and 1356 cm⁻¹ (close to 1373 cm⁻¹ in metMb). Arrows are used to identify cross peaks.*

5.4.2. Analysis of Spectral Line Shapes

      The ability to distinguish inhomogeneous and homogeneous line broadening mechanisms motivated the first multidimensional Raman experiments.[18, 21] As in 2D infrared spectroscopy, information about the line broadening mechanism can be read directly from the line shape. Inhomogenous broadening will cause peaks to elongate on the diagonal of the 2DRR spectrum; the diagonal width will then be greater than the anti-diagonal width. Correlated line shapes may be observed when spectral diffusion of a vibrational resonance frequency is much slower than the time-scale of the inverse line width (roughly 1 picosecond). In this section, we characterize the 2DRR line shapes shown in Figure 5.9. The present analysis is limited to the region of the spectrum between 200 and 800 cm^{-1} in both dimensions, because we find no evidence of inhomogeneous line broadening elsewhere.
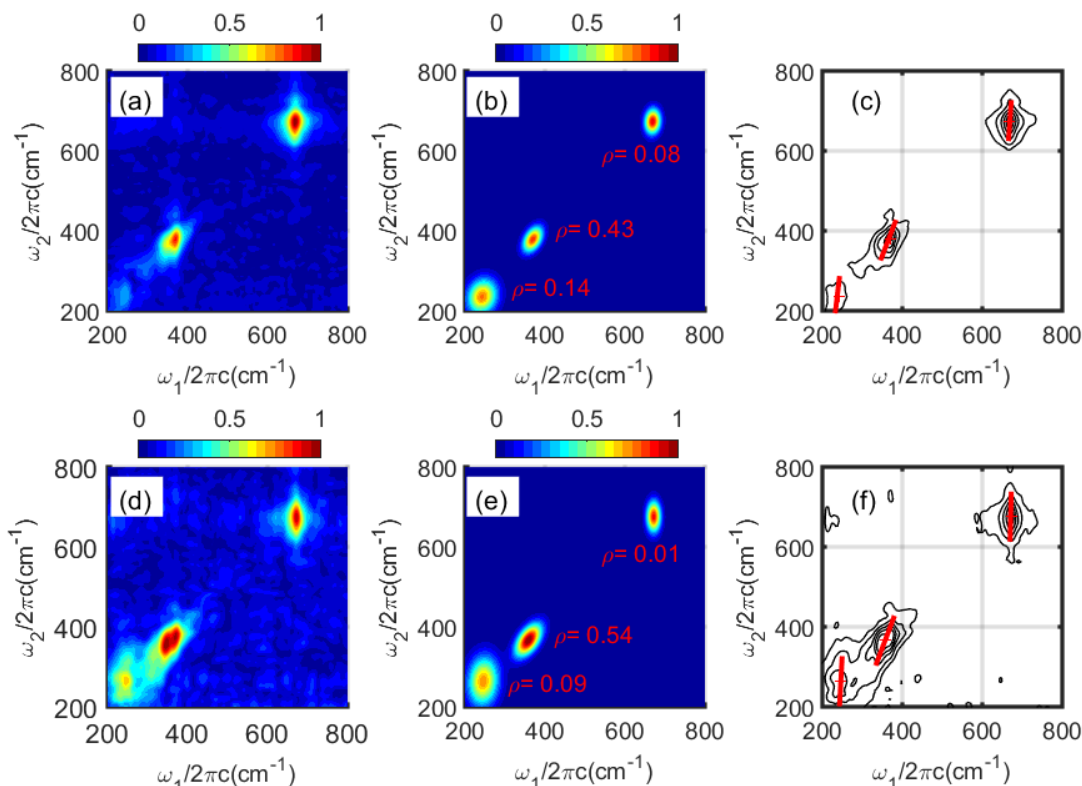
Figure 5.10. *Line shapes of diagonal peaks are examined in lower-frequency regions of 2DRR spectra obtained for (a) metMb and (b) MbO$_2$. Peaks are fit to two-dimensional Gaussians with correlation parameters in panels (c) and (d) (see Equation 5.2). The parameter, ρ, ranges between the uncorrelated (ρ =0) and fully correlated (ρ =1) limits for diagonal peaks. A correlation parameter greater than 0 is a signature of inhomogeneous line broadening. In panels (e) and (f), the slope consistent with each correlation parameter is overlaid on the experimental data to offer an additional perspective. For both systems, the 370-cm^{-1} methylene deformation mode local to the propionic acid side chains exhibits the greatest amount of heterogeneity (wavenumber near 370 cm^{-1}).*

In Figure 5.10, all peaks are fit to two-dimensional Gaussian line shapes of the form given in Equation 5.2. The correlation parameter, ρ, generally ranges from the fully anti-correlated (ρ =-1) to fully correlated (ρ =+1) limits. However, ρ should not be less than zero for diagonal peaks. This form of the 2D Gaussian function takes into account the difference in frequency resolution associated with the two dimensions. The correlation parameters must be equal to zero if the line broadening mechanisms are fully homogeneous. With inspiration from 2D infrared spectroscopy, slopes obtained with a linear regression analysis are overlaid on

various peaks in Figures 5.10(c) and 5.10(f). The slopes are useful for inspection of the data but are less rigorous than the 2D Gaussian fits, because they are affected by frequency resolution.

The iron-histidine stretching mode near 220-cm^{-1} exhibits a smaller amount of heterogeneity; the correlation parameter is 0.14 in metMb and 0.09 in MbO$_2$. For both systems, the greatest amount of heterogeneity is associated with the 370-cm^{-1} methylene deformation mode local to the propionic acid groups. The correlation parameter for this mode is 0.43 in metMb and 0.54 in MbO$_2$. We hypothesize that this heterogeneity originates in fluctuations of the "floppy" propionic acid side chains. That is, the 2DRR data suggest that rigidity of the macrocycle suppresses heterogeneity in higher frequency modes such at the in-plane deformation near 674 cm^{-1}.

5.4.3. Computational Analysis of Line Broadening Mechanism

In this section, computational models are used to explore the effects that motions of the propionic acid side chains have on the vibrational frequency of the 370-cm^{-1} methylene deformation mode. In particular, we are interested in how the magnitudes of the fluctuations compare to characteristic frequencies in the spectral densities (i.e., spectra of vibrational freqeuncy fluctuations). These comparisons will provide insights into the line broadening mechanisms. It is relatively straightforward to model fluctuations in the geometries of the proteins with classical molecular dynamics (MD) simulations; however, the vibrational frequencies should be calculated at a higher level of theory. Here, we use *ab initio* maps to parameterize the vibrational frequencies associated with side chain geometries extracted from MD simulations. Similar approaches have been used to interpret 2D infrared experiments conducted on proteins and pure liquids.[69-72]

Fluctuations in the geometries of the proteins are modeled with MD simulations based on the GROMACS96 force field[73-75] To prepare the systems, heavy atoms in the proteins were

restrained and an energy minimization (steepest descent method) was implemented to relax the solvent around the protein. This was followed by two equilibration steps in the isothermal-isochoric and isothermal-isobaric ensembles for a total of 400 ps. Simulations were run for 1 ns with 2 fs steps. The *ab initio* maps are constructed by first optimizing the geometries of the isolated hemes at the B3LYP/6-311G(2d,3p) level.[76] The equilibrium dihedral angles associated with the propionic acid side chains are $\Phi_L = 81.3°$ and $\Phi_R = 81.1°$ for metMb and $\Phi_L = 94.4°$ and $\Phi_R = 109°$ for MbO$_2$ (see Figure 5.11). The *ab initio* maps are produced by varying the two dihedral angles (in steps of 5°) over the full ranges covered by the MD simulations while holding all other coordinates fixed at the values corresponding to the equilibrium geometries. In doing so, it is assumed that the frequency of the methylene deformation mode local to the propionic acid side chains is primarily affected by the "floppy" coordinates of the side chain. The vibrational modes are computed at each geometry, and the methylene deformation mode is identified by (i) large-amplitude motion of the methylene bonds near the propionic acid side chain and (ii) the scalar product with the normal mode calculated at the equilibrium geometry. The resulting maps of vibrational frequencies are presented in Figures 5.11(b) and 5.11(e). With these maps, the vibrational frequency is readily generated at each step in the MD trajectory by extracting the two dihedral angles. Segments of the trajectories are presented in Figures 5.11(c) and 5.11(f). Scatter plots of the dihedral angles suggest that fluctuations in these coordinates are fairly evenly distributed about the equilibrium geometry (see Supplementary Material).[77]
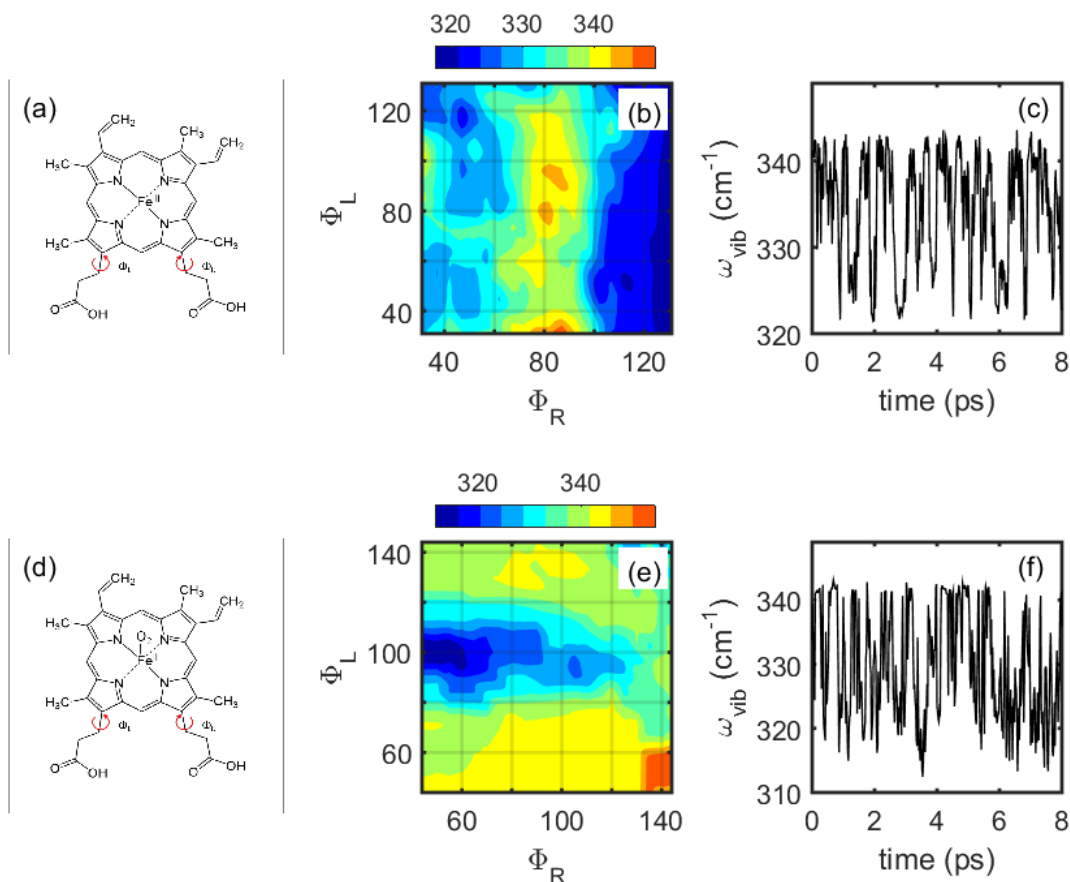
Figure 5.11. *Dihedral angles associated with the propionic acid chains are defined for the heme in (a) metMb and (d) MbO$_2$. The vibrational frequency of the methylene deformation mode local to the propionic acid side chains is computed as a function of the two dihedral angles for (b) metMb and (e) MbO$_2$. These ab initio maps are used to parameterize the vibrational frequencies associated with molecular dynamics simulations. Segments of the trajectories for vibrational frequencies are shown for (c) metMb and (f) MbO$_2$.*

MD trajectories of vibrational frequencies for metMB and MbO$_2$ yield standard deviations of 5.9 and 7.0 cm^{-1}, respectively. These standard deviations correspond to FWHM line widths of 13.9 and 16.5 cm^{-1} under the assumption of Gaussian line shapes. These line widths are smaller than those found in the 2DRR measurements shown in Figure 5.9 because of finite spectral resolution. In order to obtain further insight into the line broadening mechanism, time-correlation functions associated with the MD trajectories are Fourier transformed to produce the spectral densities shown in Figure 5.12.[78-79] The spectral densities show how the fluctuation

amplitudes are distributed in the frequency domain. The simulations suggest that the fluctuations in the vibrational frequencies are dominated by thermal motion below 10 cm^{-1}; however, higher-frequency components with magnitudes up to 10% of the maximum value are found in both systems.

The line broadening mechanism can be interpreted by comparing the fluctuation amplitudes (5.9 cm^{-1} in metMb and 7.0 cm^{-1} in MbO$_2$) to the characteristic frequencies of thermal motion (i.e., dominant part of spectral density). In the homogeneous limit, the fluctuation amplitude must be small compared to the characteristic frequency, whereas the opposite applies in the inhomogeneous limit.[78] The spectral densities computed with MD simulations have decayed to roughly 50% of their maximum values at frequencies corresponding to the 5.9 and 7.0-cm^{-1} fluctuation amplitudes computed for metMb and MbO$_2$. Thus, the calculations suggests that the line broadening of both systems reside between the homogeneous and inhomogeneous limits. The correlation parameters of 0.43 and 0.54 determined from experimental data for metMb and MbO$_2$ are consistent with the line broadening regime predicted by the MD simulations (see Figure 5.10).
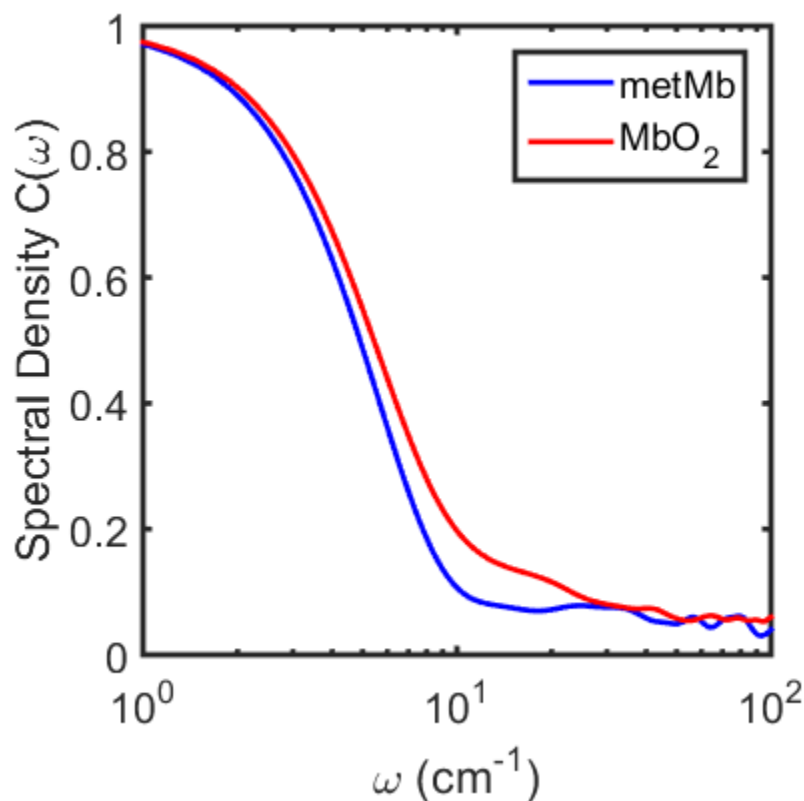
Figure 5.12. *Spectral densities of the methylene deformation modes obtained from molecular dynamics simulations. The spectral densities decay to less than 50% of the maximum values at frequencies corresponding to the fluctuation amplitudes (5.9 and 7.0 cm⁻¹ for metMb and MbO₂).* *These calculations are consistent with an intermediate line broadening regime.*

5.4.4. Implications for the Vibrational Cooling Mechanism

The propionic acid groups are known to dominate vibrational energy exchange of the

heme with its surrounding environment. Hochstrasser first proposed this mechanism in 1994, and

MD simulations contributed further support several years later.[49-51] In 2006, the role of the

propionic acid groups was finally confirmed by a direct experimental test in which vibrational

cooling rates were compared for the native protein and a mutant.[52] These earlier works suggest

that the propionic acid side chains are an effective gateway for vibrational energy transfer,

because they hydrogen bond with the aqueous solvent. In contrast, the porphyrin macrocycle is

enclosed in a hydrophobic pocket devoid of solvent. The surrounding protein matrix is less

effective than the solvent in exchanging vibrational energy with the porphyrin despite close to 90 van der Waals contacts.[80] This behavior underscores the important role of hydrogen bonds in accelerating solute-to-solvent vibrational energy transfer.[81]

The experimental data and computational simulations presented in Figures 5.10-5.12 suggest that the 2DRR line shapes of the methylene deformation modes reflect heterogeneity in the geometries of the side chains. It is interesting to consider whether or not heterogeneity in the structure translates into heterogeneity in the vibrational cooling rate. This issue cannot be directly addressed with 2DRR spectroscopy. However, Berg and co-workers have shown that such information about incoherent dynamics can be derived from six-wave mixing experiments.[82-83] We are presently using a related pump-repump-probe approach to examine heterogeneity in vibrational cooling rates in heme proteins.

5.5. Concluding Remarks

In summary, we have conducted quasi-degenerate (one-color) 2DRR spectroscopy experiments on oxygen- and water-ligated myoglobin. The experimental technique developed in Reference [41] has been leveraged to produce 2D resonance Raman spectra. For both systems, we find that the greatest amount of heterogeneity is associated with the methylene deformation mode local to the propionic acid side chains. The computational model presented in Section 5.4.3 yields distributions with standard deviations of 5.9 and 7.0 cm^{-1} for metMb and MbO$_2$, respectively. It is interesting to consider whether or not the vibrational cooling rate of the heme varies as a consequence of heterogeneity in the propionic acid groups. This issue will be addressed in future work using pump-repump-probe spectroscopy.

The calculations in Section 5.3 suggest that two key points must be considered when interpreting 2DRR signals. First, 2DRR experiments do not necessarily yield information about anharmonic mode couplings, because the signal is allowed for harmonic systems. The absence of

a signal for harmonic systems is one of the primary motivations for conducting electronically off-resonant 2D Raman experiments.[19, 27-28, 55-56] Thus, a tradeoff between information content and susceptibility to experimental artifacts is made when 2D Raman experiments are conducted under electronically resonant conditions. A two-color implementation of 2DRR spectroscopy may expand the range of scientific questions that can be addressed, but does not change this essential aspect of the signal generation mechanism.[54] Second, 2DRR experiments can be used to characterize vibrational line broadening mechanisms in a straightforward way. As in 2D infrared experiments, inhomogeneous line broadening is made clear by inspection of the 2DRR signal. Notably, the line broadening mechanism cannot be directly determined from traditional (third-order) coherent Raman or spontaneous Raman spectroscopies.[18]

5.6. Supplemental Information

5.6.1. Response Function

The fifth-order polarization possesses 16 components when a single electronic resonance dominates the optical response.[41] The 2DRR spectra in this work are calculated by Fourier transforming the polarization components presented in Reference [41] with respect to the delay time, τ_1. The frequency dimension, ω_2, is equal to the difference between the detection frequency, ω_t, and the frequency of the narrowband Raman pump, ω_{RP}. The summations below are restricted to eliminate population terms from the dimensions, ω_1 and ω_2. The 16 polarization components are

$$P_1^{(5)}(\omega_1, \omega_2) = -\frac{N\xi_{AP}^2\xi_{RP}^2\xi_{St}|\mu_{eg}|^6}{\hbar^5} \sum_{\substack{mnkluv \\ k \neq m, u \neq m}} B_m \langle n|m\rangle\langle n|k\rangle\langle l|k\rangle\langle l|u\rangle\langle v|u\rangle\langle v|m\rangle$$
$$\times L_{en,gm}(\omega_{AP}) D_{gk,gm}(\omega_1) L_{el,gm}(\omega_t) J_{gu,gm}(\omega_2) L_{ev,gm}(\omega_t) \quad , \quad (5.4)$$

$$P_2^{(5)}(\omega_1,\omega_2) = -\frac{N\xi_{AP}^2\xi_{RP}^2\xi_{St}\left|\mu_{eg}\right|^6}{\hbar^5}\sum_{\substack{mnkluv\\k\neq m,u\neq k}}B_m\langle n|m\rangle\langle n|k\rangle\langle l|m\rangle\langle l|u\rangle\langle v|k\rangle\langle v|u\rangle$$
$$\times L_{en,gm}\left(\omega_{AP}\right)D_{gk,gm}\left(\omega_1\right)L_{gk,el}\left(-\omega_{RP}\right)J_{gk,gu}\left(\omega_2\right)L_{ev,gu}\left(\omega_t\right)$$
(5.5)

$$P_3^{(5)}(\omega_1,\omega_2) = -\frac{N\xi_{AP}^2\xi_{RP}^2\xi_{St}\left|\mu_{eg}\right|^6}{\hbar^5}\sum_{\substack{mnkluv\\k\neq m,u\neq m}}B_m\langle n|m\rangle\langle n|k\rangle\langle l|k\rangle\langle l|u\rangle\langle v|m\rangle\langle v|u\rangle$$
$$\times L_{gm,en}\left(-\omega_{AP}\right)D_{gm,gk}\left(\omega_1\right)L_{gm,el}\left(-\omega_{RP}\right)J_{gm,gu}\left(\omega_2\right)L_{ev,gu}\left(\omega_t\right)$$
(5.6)

$$P_4^{(5)}(\omega_1,\omega_2) = -\frac{N\xi_{AP}^2\xi_{RP}^2\xi_{St}\left|\mu_{eg}\right|^6}{\hbar^5}\sum_{\substack{mnkluv\\k\neq m,u\neq k}}B_m\langle n|m\rangle\langle n|k\rangle\langle l|m\rangle\langle l|u\rangle\langle v|u\rangle\langle v|k\rangle$$
$$\times L_{gm,en}\left(-\omega_{AP}\right)D_{gm,gk}\left(\omega_1\right)L_{el,gk}\left(\omega_t\right)J_{gu,gk}\left(\omega_2\right)L_{ev,gk}\left(\omega_t\right)$$
(5.7)

$$P_5^{(5)}(\omega_1,\omega_2) = -\frac{N\xi_{AP}^2\xi_{RP}^2\xi_{St}\left|\mu_{eg}\right|^6}{\hbar^5}\sum_{\substack{mnkluv\\k\neq n,u\neq k}}B_m\langle n|m\rangle\langle k|m\rangle\langle n|l\rangle\langle u|l\rangle\langle k|v\rangle\langle u|v\rangle$$
$$\times L_{en,gm}\left(\omega_{AP}\right)D_{en,ek}\left(\omega_1\right)L_{gl,ek}\left(-\omega_{RP}\right)J_{eu,ek}\left(\omega_2\right)L_{eu,gv}\left(\omega_t\right)$$
(5.8)

$$P_6^{(5)}(\omega_1,\omega_2) = -\frac{N\xi_{AP}^2\xi_{RP}^2\xi_{St}\left|\mu_{eg}\right|^6}{\hbar^5}\sum_{\substack{mnkluv\\k\neq n,u\neq n}}B_m\langle n|m\rangle\langle k|m\rangle\langle k|l\rangle\langle u|l\rangle\langle u|v\rangle\langle n|v\rangle$$
$$\times L_{en,gm}\left(\omega_{AP}\right)D_{en,ek}\left(\omega_1\right)L_{en,gl}\left(\omega_t\right)J_{en,eu}\left(\omega_2\right)L_{en,gv}\left(\omega_t\right)$$
(5.9)

$$P_7^{(5)}(\omega_1,\omega_2) = -\frac{N\xi_{AP}^2\xi_{RP}^2\xi_{St}\left|\mu_{eg}\right|^6}{\hbar^5}\sum_{\substack{mnkluv\\k\neq n,u\neq n}}B_m\langle n|m\rangle\langle k|m\rangle\langle k|l\rangle\langle u|l\rangle\langle n|v\rangle\langle u|v\rangle$$
$$\times L_{gm,en}\left(-\omega_{AP}\right)D_{ek,en}\left(\omega_1\right)L_{gl,en}\left(-\omega_{RP}\right)J_{eu,en}\left(\omega_2\right)L_{eu,gv}\left(\omega_t\right)$$
(5.10)

$$P_8^{(5)}(\omega_1,\omega_2) = -\frac{N\xi_{AP}^2\xi_{RP}^2\xi_{St}\left|\mu_{eg}\right|^6}{\hbar^5}\sum_{\substack{mnkluv\\k\neq n,u\neq k}}B_m\langle n|m\rangle\langle k|m\rangle\langle n|l\rangle\langle u|l\rangle\langle u|v\rangle\langle k|v\rangle$$
$$\times L_{gm,en}\left(-\omega_{AP}\right)D_{ek,en}\left(\omega_1\right)L_{ek,gl}\left(\omega_t\right)J_{ek,eu}\left(\omega_2\right)L_{ek,gv}\left(\omega_t\right)$$
(5.11)

$$P_9^{(5)}(\omega_1, \omega_2) = -\frac{N\xi_{AP}^2\xi_{RP}^2\xi_{St}|\mu_{eg}|^6}{\hbar^5} \sum_{\substack{mnkluv \\ k \neq m, u \neq l}} B_m \langle n|m\rangle\langle n|k\rangle\langle l|k\rangle\langle u|m\rangle\langle u|v\rangle\langle l|v\rangle$$

$$\times L_{en,gm}(\omega_{AP}) D_{gk,gm}(\omega_1) L_{el,gm}(\omega_t) J_{el,eu}(\omega_2) L_{el,gv}(\omega_t) \qquad , \quad (5.12)$$

$$P_{10}^{(5)}(\omega_1, \omega_2) = -\frac{N\xi_{AP}^2\xi_{RP}^2\xi_{St}|\mu_{eg}|^6}{\hbar^5} \sum_{\substack{mnkluv \\ k \neq m, u \neq l}} B_m \langle n|m\rangle\langle n|k\rangle\langle l|m\rangle\langle u|k\rangle\langle l|v\rangle\langle u|v\rangle$$

$$\times L_{en,gm}(\omega_{AP}) D_{gk,gm}(\omega_1) L_{gk,el}(-\omega_{RP}) J_{eu,el}(\omega_2) L_{eu,gv}(\omega_t) \qquad , . \quad (5.13)$$

$$P_{11}^{(5)}(\omega_1, \omega_2) = -\frac{N\xi_{AP}^2\xi_{RP}^2\xi_{St}|\mu_{eg}|^6}{\hbar^5} \sum_{\substack{mnkluv \\ k \neq m, u \neq l}} B_m \langle n|m\rangle\langle n|k\rangle\langle l|m\rangle\langle u|k\rangle\langle u|v\rangle\langle l|v\rangle$$

$$\times L_{gm,en}(-\omega_{AP}) D_{gm,gk}(\omega_1) L_{el,gk}(\omega_t) J_{el,eu}(\omega_2) L_{el,gv}(\omega_t) \qquad , \quad (5.14)$$

$$P_{12}^{(5)}(\omega_1, \omega_2) = -\frac{N\xi_{AP}^2\xi_{RP}^2\xi_{St}|\mu_{eg}|^6}{\hbar^5} \sum_{\substack{mnkluv \\ k \neq m, u \neq l}} B_m \langle n|m\rangle\langle n|k\rangle\langle l|k\rangle\langle u|m\rangle\langle l|v\rangle\langle u|v\rangle$$

$$\times L_{gm,en}(-\omega_{AP}) D_{gm,gk}(\omega_1) L_{gm,el}(-\omega_{RP}) J_{eu,el}(\omega_2) L_{eu,gv}(\omega_t) \qquad , \quad (5.15)$$

$$P_{13}^{(5)}(\omega_1, \omega_2) = -\frac{N\xi_{AP}^2\xi_{RP}^2\xi_{St}|\mu_{eg}|^6}{\hbar^5} \sum_{\substack{mnkluv \\ k \neq n, u \neq l}} B_m \langle n|m\rangle\langle k|m\rangle\langle n|l\rangle\langle k|u\rangle\langle v|l\rangle\langle v|u\rangle$$

$$\times L_{en,gm}(\omega_{AP}) D_{en,ek}(\omega_1) L_{gl,ek}(-\omega_{RP}) J_{gl,gu}(\omega_2) L_{ev,gu}(\omega_t) \qquad , \quad (5.16)$$

$$P_{14}^{(5)}(\omega_1, \omega_2) = -\frac{N\xi_{AP}^2\xi_{RP}^2\xi_{St}|\mu_{eg}|^6}{\hbar^5} \sum_{\substack{mnkluv \\ k \neq n, u \neq l}} B_m \langle n|m\rangle\langle k|m\rangle\langle k|l\rangle\langle n|u\rangle\langle v|u\rangle\langle v|l\rangle$$

$$\times L_{en,gm}(\omega_{AP}) D_{en,ek}(\omega_1) L_{en,gl}(\omega_t) J_{gu,gl}(\omega_2) L_{ev,gl}(\omega_t) \qquad , \quad (5.17)$$

$$P_{15}^{(5)}(\omega_1, \omega_2) = -\frac{N\xi_{AP}^2\xi_{RP}^2\xi_{St}|\mu_{eg}|^6}{\hbar^5} \sum_{\substack{mnkluv \\ k \neq n, u \neq l}} B_m \langle n|m\rangle\langle k|m\rangle\langle k|l\rangle\langle n|u\rangle\langle v|l\rangle\langle v|u\rangle$$

$$\times L_{gm,en}(-\omega_{AP}) D_{ek,en}(\omega_1) L_{gl,en}(-\omega_{RP}) J_{gl,gu}(\omega_2) L_{ev,gu}(\omega_t) \qquad , \quad (5.18)$$

$$P_{16}^{(5)}(\omega_1,\omega_2) = -\frac{N\xi_{AP}^2\xi_{RP}^2\xi_{St}|\mu_{eg}|^6}{\hbar^5}\sum_{\substack{mnkluv\\k\neq n,u\neq l}}B_m\langle n|m\rangle\langle k|m\rangle\langle n|l\rangle\langle k|u\rangle\langle v|u\rangle\langle v|l\rangle$$

$$\times L_{gm,en}(-\omega_{AP})D_{ek,en}(\omega_1)L_{ek,gl}(\omega_t)J_{gu,gl}(\omega_2)L_{ev,gl}(\omega_t) \qquad (5.19)$$

The electronic line shape function, $L_{en,gm}(\omega)$, is written as

$$L_{en,gm}(\omega) = \frac{1}{\omega - \omega_{eg} - \omega_{nm} + i\Gamma_{eg}} . \qquad (5.20)$$

The vibrational line shape functions, $D_{gk,gm}(\omega_1)$ and $J_{gu,gm}(\omega_2)$, are given by

$$D_{gk,gm}(\omega_1) = \frac{2\Lambda_{AP}}{\omega_{km}^2 + \Lambda_{AP}^2} \cdot \frac{1}{(\omega_1 - \omega_{km}) + i\Gamma_{vib}} \qquad (5.21)$$

and

$$J_{gu,gm}(\omega_2) = \frac{\exp[i\omega\tau_2 - \Lambda_{RP}\tau_2]}{(\omega_2 - \omega_{um}) + i(\Gamma_{vib} - \Lambda_{RP})} . \qquad (5.22)$$

The fifth-order 2DRR signal field is expressed in terms of these polarization components as

$$E_{2DRR}^{(5)}(\omega_1,\omega_1) = \frac{1}{7}\left(\frac{i\omega_t l}{2\varepsilon_0 n(\omega_t)c}\right)\sum_{j=1}^{16}P_j^{(5)}(\omega_1,\omega_1) , \qquad (5.23)$$

where perfect phase-matching has been assumed and the factor of 1/7 represents the orientational average for all-parallel electric field polarizations.[84]

5.6.2. Anharmonic Vibrational Hamiltonian

All calculations conducted in this work are based on the following vibrational Hamiltonian,[85]

$$H = \sum_j\left[\frac{\hbar\omega_j}{2}\left(2a_j^\dagger a_j + 1\right) + U_{jjj}\left(3a_j^\dagger + 3a_j\right)\right] + \sum_{jkl}U_{jkl}\left(a_j^\dagger a_k^\dagger a_l^\dagger + 3a_j^\dagger a_k^\dagger a_l\right.$$
$$\left. + 3a_j^\dagger a_k a_l + a_j a_k a_l\right) \qquad (5.24)$$

where the cubic expansion coefficients are given by

$$U_{jkl} = \frac{1}{3!\sqrt{2^3 m^3 \omega^3 \hbar^{-3}}} \left(\frac{\partial^3 V}{\partial q_j \partial q_k \partial q_l} \right)_0.$$ (5.25)

The basis set is taken to be uncoupled at second-order for this Hamiltonian. Therefore, normal modes are recovered if the cubic expansion coefficients are set equal to zero. This is the most natural basis set for the present study, because the calculations in Section 5.3 make use of fitting parameters obtained in a basis of normal modes.[67] Vibrational wavefunctions are obtained by diagonalizing the Hamiltonian in a basis of harmonic oscillators (up to the 20 vibrational quanta in each mode results in good convergence).

The vibrational overlap integrals needed to evaluate the response functions are written as

$$\langle n|m \rangle = \sum_{\alpha\beta} \varphi_{n\alpha}\varphi_{m\beta} \langle \alpha|\beta \rangle,$$ (5.26)

where $\varphi_{n\alpha}$ is the expansion coefficient for harmonic basis function α and the anharmonic vibrational wavefunction, n.

5.6.3. Parameters Used in the Model

Table 5.1. *Parameters of Theoretical Model for System with Two Vibrational Modes*

[a]Parameter	Value
$\omega_{eg}/2\pi c$	23250 cm^{-1}
ω_{AP} & ω_{RP}	set equal to ω_{eg}
[b]ϖ_a	400 cm^{-1}
[b]ϖ_b	1100 cm^{-1}
[c]d_a	0.75
[c]d_b	0.75
Γ_{vib}/c	10 cm^{-1}
Γ_{eg}/c	750 cm^{-1}
μ_{eg}	8.8 D
[d]σ_a & σ_b	35 cm^{-1}

[a] The number density (N), refractive index ($n(\omega_t)$), and path length (l) do not affect these results because normalized intensities are displayed (see Equation 5.22).

[b] The parameter, ϖ_j, is the wavenumber for mode j, $\varpi_j = \omega_j/2\pi c$.

[c] The parameter, d_j, is the dimensionless potential energy minimum displacement for mode j.

[d] Inhomogeneous line broadening is included only for the calculations shown in Figure 5.5 (see Equations 5.1 and 5.2).

Table 5.2. *Parameters of Model Based on Empirical Fit of Spontaneous Raman Signals*

[a]Parameter	Value
$\omega_{eg}/2\pi c$	23250 cm^{-1}
ω_{AP} & ω_{RP}	set equal to ω_{eg}
[b]ϖ_1	220 cm^{-1}
[b]ϖ_2	370 cm^{-1}
[b]ϖ_3	674 cm^{-1}
[b]ϖ_4	1356 cm^{-1}
[c]d_1	0.47
[c]d_2	0.20
[c]d_3	0.26
[c]d_4	0.34
Γ_{vib}/c	10 cm^{-1}
Γ_{eg}/c	750 cm^{-1}
μ_{eg}	8.8 D

[a] The number density (N), refractive index ($n(\omega_t)$), and path length (l) do not affect these results because normalized intensities are displayed (see Equation 5.22).

[b] The parameter, ϖ_j, is the wavenumber for mode j, $\varpi_j = \omega_j/2\pi c$.

[c] The parameter, d_j, is the dimensionless potential energy minimum displacement for mode j.

REFERENCES

1. Asplund, M. C.; Zanni, M. T.; Hochstrasser, R. M., Two-dimensional infrared spectroscopy of peptides by phase-controlled femtosecond vibrational photon echoes. *Proc. Natl. Acad. Sci. U. S. A.* **2000,** *97* (15), 8219-8224.

2. Golonzka, O.; Khalil, M.; Demirdoven, N.; Tokmakoff, A., Vibrational anharmonicities revealed by coherent two-dimensional infrared spectroscopy. *Phys. Rev. Lett.* **2001,** *86* (10), 2154-2157.

3. Jonas, D. M., Two-dimensional femtosecond spectroscopy. *Annu. Rev. Phys. Chem.* **2003,** *54*, 425-463.

4. Brixner, T.; Mancal, T.; Stiopkin, I. V.; Fleming, G. R., Phase-stabilized two-dimensional electronic spectroscopy. *J. Chem. Phys.* **2004,** *121* (9), 4221-4236.

5. Cowan, M. L.; Ogilvie, J. P.; Miller, R. J. D., Two-dimensional spectroscopy using diffractive optics based phased-locked photon echoes. *Chem. Phys. Lett.* **2004,** *386* (1-3), 184-189.

6. Ogilvie, J. P.; Kubarych, K. J., Multidimensional electronic and vibrational spectroscopy: An ultrafast probe of molecular relaxation and reaction dynamics. *Adv. At., Mol., Opt. Phys.* **2009,** *57*, 249-321.

7. Pakoulev, A. V.; Block, S. B.; Yurs, L. A.; Mathew, N. A.; Kornau, K. M.; Wright, J. C., Multiply resonant coherent multidimensional spectroscopy: implications for materials science. *J. Phys. Chem. Lett.* **2010,** *1* (5), 822-828.

8. Hamm, P.; Zanni, M., *Concepts and methods of 2D infrared spectroscopy*. Cambridge University Press: New York, 2011.

9. Wright, J. C., Multiresonant coherent multidimensional spectroscopy. *Annu. Rev. Phys. Chem.* **2011,** *62*, 209-230.

10. Slenkamp, K. M.; Lynch, M. S.; Van Kuiken, B. E.; Brookes, J. F.; Bannan, C. C.; Daifuku, S. L.; Khalil, M., Investigating vibrational anharmonic couplings in cyanide-bridged transition metal mixed valence complexes using two-dimensional infrared spectroscopy. *J. Chem. Phys.* **2014,** *140* (8), 084505.

11. Laubereau, A.; Kaiser, W., Vibrational dynamics of liquids and solids investigated by picosecond light pulses. *Rev. Mod. Phys.* **1978,** *50* (3), 607-665.

12. Hesp, B. H.; Wiersma, D. A., Vibrational relaxation in neat crystals of naphthalene by picosecond cars. *Chem. Phys. Lett.* **1980,** *75* (3), 423-426.

13. Velsko, S.; Trout, J.; Hochstrasser, R. M., Quantum beating of vibrational factor group components in molecular solids[a)]. *J. Chem. Phys.* **1983,** *79* (5), 2114-2120.

14. Schosser, C. L.; Dlott, D. D., A picosecond CARS study of vibron dynamics in molecular crystals: Temperature dependence of homogeneous and inhomogeneous linewidths. *J. Chem. Phys.* **1984,** *80* (4), 1394-1406.

15. Laubereau, A.; Wochner, G.; Kaiser, W., Ultrafast coherent excitation and probing of molecular vibrations with isotopic substructure. *Phys. Rev. A* **1976,** *13* (6), 2212-2225.

16. Oxtoby, D. W., Picosecond phase relaxation experiments: A microscopic theory and a new interpretation. *J. Chem. Phys.* **1981,** *74* (10), 5371-5376.

17. George, S. M.; Harris, A. L.; Berg, M.; Harris, C. B., Picosecond studies of the temperature dependence of homogeneous and inhomogeneous vibrational linewidth broadening in liquid acetonitrile. *J. Chem. Phys.* **1984,** *80* (1), 83-94.

18. Loring, R. F.; Mukamel, S., Selectivity in coherent transient Raman measurements of vibrational dephasing in liquids. *J. Chem. Phys.* **1985,** *83* (5), 2116-2128.

19. Tanimura, Y.; Mukamel, S., Two-dimensional femtosecond vibrational spectroscopy of liquids. *J. Chem. Phys.* **1993,** *99* (12), 9496-9511.

20. Jansen, T. l. C.; Snijders, J. G.; Duppen, K., Interaction induced effects in the nonlinear Raman response of liquid CS_2: A finite field nonequilibrium molecular dynamics approach. *J. Chem. Phys.* **2001,** *114* (24), 10910-10921.

21. Berg, M.; Vanden Bout, D. A., Ultrafast Raman Echo Measurements of Vibrational Dephasing and the Nature of Solvent-Solute Interactions. *Acc. Chem. Res.* **1997,** *30* (2), 65-71.

22. Ivanecky, J. E.; Wright, J. C., An investigation of the origins and efficiencies of higher-order nonlinear spectroscopic processes. *Chem. Phys. Lett.* **1993,** *206* (5-6), 437-444.

23. Tominaga, K.; Yoshihara, K., Fifth-order nonlinear spectroscopy on the low-frequency modes of liquid CS_2. *J. Chem. Phys.* **1996,** *104* (12), 4419-4426.

24. Steffen, T.; Duppen, K., Time resolved four- and six-wave mixing in liquids. II. Experiments. *J. Chem. Phys.* **1997,** *106* (10), 3854-3864.

25. Tokmakoff, A.; Lang, M. J.; Larsen, D. S.; Fleming, G. R.; Chernyak, V.; Mukamel, S., Two-Dimensional Raman Spectroscopy of Vibrational Interactions in Liquids. *Phys. Rev. Lett.* **1997,** *79* (14), 2702-2705.

26. Blank, D. A.; Kaufman, L. J.; Fleming, G. R., Fifth-order two-dimensional Raman spectra of CS_2 are dominated by third-order cascades. *J. Chem. Phys.* **1999,** *111* (7), 3105-3114.

27. Kubarych, K. J.; Milne, C. J.; Lin, S.; Astinov, V.; Miller, R. J. D., Diffractive optics-based six-wave mixing: Heterodyne detection of the full $\chi(5)$ tensor of liquid CS_2. *J. Chem. Phys.* **2002,** *116* (5), 2016-2042.

28.   Kaufman, L. J.; Heo, J.; Ziegler, L. D.; Fleming, G. R., Heterodyne-detected fifth-order nonresonant Raman scattering from room temperature CS_2. *Phys. Rev. Lett.* **2002,** *88* (20), 207402.

29.   Fujiyoshi, S.; Takeuchi, S.; Tahara, T., Time-resolved impulsive stimulated Raman scattering from excited-state polyatomic molecules in solution. *J. Phys. Chem. A* **2003,** *107* (4), 494-500.

30.   McCamant, D. W.; Kukura, P.; Yoon, S.; Mathies, R. A., Femtosecond broadband stimulated Raman spectroscopy: Apparatus and methods. *Rev. Sci. Instrum.* **2004,** *75* (11), 4971-4980.

31.   Underwood, D. F.; Blank, D. A., Measuring the change in the intermolecular Raman spectrum during dipolar solvation. *J. Phys. Chem. A* **2005,** *109* (15), 3295-3306.

32.   Kukura, P.; McCamant, D. W.; Mathies, R. A., Femtosecond stimulated Raman spectroscopy. *Annu. Rev. Phys. Chem.* **2007,** *58*, 461-488.

33.   Moran, A. M.; Nome, R. A.; Scherer, N. F., Field-resolved measurement of reaction-induced spectral densities by polarizability response spectroscopy. *J. Chem. Phys.* **2007,** *127* (18), 184505.

34.   Marek, M. S.; Buckup, T.; Motzkus, M., Direct observation of a dark state in lycopene using pump-DFWM. *J. Phys. Chem. B* **2011,** *115* (25), 8328-8337.

35.   Kraack, J. P.; Wand, A.; Buckup, T.; Motzkus, M.; Ruhman, S., Mapping multidimensional excited state dynamics using pump-impulsive-vibrational-spectroscopy and pump-degenerate-four-wave-mixing. *Phys. Chem. Chem. Phys.* **2013,** *15* (34), 14487-14501.

36.   Weigel, A.; Dobryakov, A.; Klaumunzer, B.; Sajadi, M.; Saalfrank, P.; Ernsting, N. P., Femtosecond stimulated Raman spectroscopy of flavin after optical excitation. *J. Phys. Chem. B* **2011,** *115* (13), 3656-3680.

37.   Yu, W.; Zhou, J.; Bragg, A. E., Exciton conformational dynamics of poly(3-hexylthiophene) (P3HT) in solution from time-resolved resonant-Raman spectroscopy. *J. Phys. Chem. Lett.* **2012,** *3* (10), 1321-1328.

38.   Park, S.; Kim, J.; Scherer, N. F., Two-dimensional measurements of the solvent structural relaxation dynamics in dipolar solvation. *Phys. Chem. Chem. Phys.* **2012,** *14* (22), 8116-8122.

39.   Grumstrup, E. M.; Chen, Z.; Vary, R. P.; Moran, A. M.; Schanze, K. S.; Papanikolas, J. M., Frequency modulated femtosecond stimulated Raman spectroscopy of ultrafast energy transfer in a donor-acceptor copolymer. *J. Phys. Chem. B* **2013,** *117* (27), 8245-8255.

40. Ruchira Silva, W.; Frontiera, R. R., Excited state structural evolution during charge-transfer reactions in betaine-30. *Phys. Chem. Chem. Phys.* **2016,** *18* (30), 20290-20297.

41. Molesky, B. P.; Guo, Z.; Moran, A. M., Femtosecond stimulated Raman spectroscopy by six-wave mixing. *J. Chem. Phys.* **2015,** *142* (21), 212405.

42. Petrich, J. W.; Poyart, C.; Martin, J. L., Photophysics and reactivity of heme proteins: a femtosecond absorption study of hemoglobin, myoglobin, and protoheme. *Biochemistry* **2002,** *27* (11), 4049-4060.

43. Franzen, S.; Kiger, L.; Poyart, C.; Martin, J.-L., Heme photolysis occurs by ultrafast excited state metal-to-ring charge transfer. *Biophys. J.* **2001,** *80* (5), 2372-2385.

44. Ye, X.; Demidov, A.; Rosca, F.; Wang, W.; Kumar, A.; Ionascu, D.; Zhu, L.; Barrick, D.; Wharton, D.; Champion, P. M., Investigations of heme protein absorption line shapes, vibrational relaxation, and resonance Raman scattering on ultrafast time scales. *J. Phys. Chem. A* **2003,** *107* (40), 8156-8165.

45. Martin, J. L.; Vos, M. H., Femtosecond biology. *Annu. Rev. Biophys. Biomol. Struct.* **1992,** *21*, 199-222.

46. Vos, M. H., Ultrafast dynamics of ligands within heme proteins. *Biochim. Biophys. Acta.* **2008,** *1777* (1), 15-31.

47. Consani, C.; Aubock, G.; Bram, O.; van Mourik, F.; Chergui, M., A cascade through spin states in the ultrafast haem relaxation of met-myoglobin. *J. Chem. Phys.* **2014,** *140* (2), 025103.

48. Champion, P. M.; Rosca, F.; Ionascu, D.; Cao, W.; Ye, X., Rapid timescale processes and the role of electronic surface coupling in the photolysis of diatomic ligands from heme proteins. *Faraday Discuss.* **2004,** *127*, 123.

49. Tian, Y.; Wu, C.; Fendler, J. H., Fluorescence activation and surface-state reactions of size-quantized cadmium sulfide particles in Langmuir-Blodgett films. *J. Phys. Chem.* **1994,** *98* (18), 4913-4918.

50. Sagnella, D. E.; Straub, J. E., Directed energy "funneling" mechanism for heme cooling following ligand photolysis or direct excitation in solvated carbonmonoxy myoglobin. *J. Phys. Chem. B* **2001,** *105* (29), 7057-7063.

51. Bu, L.; Straub, J. E., Vibrational energy relaxation of "tailored" hemes in myoglobin following ligand photolysis supports energy funneling mechanism of heme "cooling". *J. Phys. Chem. B* **2003,** *107* (38), 10634-10639.

52.   Gao, Y.; Koyama, M.; El-Mashtoly, S. F.; Hayashi, T.; Harada, K.; Mizutani, Y.; Kitagawa, T., Time-resolved Raman evidence for energy 'funneling' through propionate side chains in heme 'cooling' upon photolysis of carbonmonoxy myoglobin. *Chem. Phys. Lett.* **2006,** *429* (1-3), 239-243.

53.   Molesky, B. P.; Giokas, P. G.; Guo, Z.; Moran, A. M., Multidimensional resonance Raman spectroscopy by six-wave mixing in the deep UV. *J. Chem. Phys.* **2014,** *141* (11), 114202.

54.   Guo, Z.; Molesky, B. P.; Cheshire, T. P.; Moran, A. M., Elucidation of reactive wavepackets by two-dimensional resonance Raman spectroscopy. *J. Chem. Phys.* **2015,** *143* (12), 124202.

55.   Wilson, K. C.; Lyons, B.; Mehlenbacher, R.; Sabatini, R.; McCamant, D. W., Two-dimensional femtosecond stimulated Raman spectroscopy: Observation of cascading Raman signals in acetonitrile. *J. Chem. Phys.* **2009,** *131* (21), 214502.

56.   Mehlenbacher, R. D.; Lyons, B.; Wilson, K. C.; Du, Y.; McCamant, D. W., Theoretical analysis of anharmonic coupling and cascading Raman signals observed with femtosecond stimulated Raman spectroscopy. *J. Chem. Phys.* **2009,** *131* (24), 244512.

57.   Ye, X.; Demidov, A.; Champion, P. M., Measurements of the photodissociation quantum yields of MbNO and MbO_2 and the vibrational relaxation of the six-coordinate heme species. *J. Am. Chem. Soc.* **2002,** *124* (20), 5914-5924.

58.   Morikis, D.; Sage, J. T.; Rizos, A. K.; Champion, P. M., Resonance Raman studies of myoglobin single crystals. *J. Am. Chem. Soc.* **1988,** *110* (19), 6341-6342.

59.   Hu, S.; Smith, K. M.; Spiro, T. G., Assignment of protoheme resonance Raman spectrum by heme labeling in myoglobin. *J. Am. Chem. Soc.* **1996,** *118* (50), 12638-12646.

60.   Tauber, M. J.; Mathies, R. A.; Chen, X.; Bradforth, S. E., Flowing liquid sample jet for resonance Raman and ultrafast optical spectroscopy. *Rev. Sci. Instrum.* **2003,** *74* (11), 4958-4960.

61.   Cho, M., Coherent two-dimensional optical spectroscopy. *Chem. Rev.* **2008,** *108* (4), 1331-1418.

62.   Fayer, M. D., Dynamics of liquids, molecules, and proteins measured with ultrafast 2D IR vibrational echo chemical exchange spectroscopy. *Annu. Rev. Phys. Chem.* **2009,** *60*, 21-38.

63.   Demirdöven, N.; Khalil, M.; Golonzka, O.; Tokmakoff, A., Correlation effects in the two-dimensional vibrational spectroscopy of coupled vibrations. *J. Phys. Chem. A* **2001,** *105* (34), 8025-8030.

64.   Venkatramani, R.; Mukamel, S., Correlated line broadening in multidimensional vibrational spectroscopy. *J. Chem. Phys.* **2002,** *117* (24), 11089-11101.

65. Valley, D. T.; Hoffman, D. P.; Mathies, R. A., Reactive and unreactive pathways in a photochemical ring opening reaction from 2D femtosecond stimulated Raman. *Phys. Chem. Chem. Phys.* **2015,** *17* (14), 9231-9240.

66. Wang, Y.; Liu, W.; Tang, L.; Oscar, B.; Han, F.; Fang, C., Early time excited-state structural evolution of pyranine in methanol revealed by femtosecond stimulated Raman spectroscopy. *J. Phys. Chem. A* **2013,** *117* (29), 6024-6042.

67. Bangcharoenpaurpong, O.; Schomacker, K. T.; Champion, P. M., Resonance Raman investigation of myoglobin and hemoglobin. *J. Am. Chem. Soc.* **1984,** *106* (19), 5688-5698.

68. Kumar, A. T. N.; Zhu, L.; Christian, J. F.; Demidov, A. A.; Champion, P. M., On the rate distribution analysis of kinetic data using the maximum entropy method: Applications to myoglobin relaxation on the nanosecond and femtosecond timescales. *J. Phys. Chem. B* **2001,** *105* (32), 7847-7856.

69. Corcelli, S. A.; Lawrence, C. P.; Skinner, J. L., Combined electronic structure/molecular dynamics approach for ultrafast infrared spectroscopy of dilute HOD in liquid H_2O and D_2O. *J. Chem. Phys.* **2004,** *120* (17), 8107-8117.

70. Hayashi, T.; la Cour Jansen, T.; Zhuang, W.; Mukamel, S., Collective solvent coordinates for the infrared spectrum of HOD in D_2O based on an ab initio electrostatic map. *J. Phys. Chem. A* **2005,** *109* (1), 64-82.

71. la Cour Jansen, T.; Knoester, J., A transferable electrostatic map for solvation effects on amide I vibrations and its application to linear and two-dimensional spectroscopy. *J. Chem. Phys.* **2006,** *124* (4), 044502.

72. Wang, J.; Zhuang, W.; Mukamel, S.; Hochstrasser, R., Two-dimensional infrared spectroscopy as a probe of the solvent electrostatic field for a twelve residue peptide. *J. Phys. Chem. B* **2008,** *112* (19), 5930-5937.

73. Van Der Spoel, D.; Lindahl, E.; Hess, B.; Groenhof, G.; Mark, A. E.; Berendsen, H. J., GROMACS: Fast, flexible, and free. *J. Comput. Chem.* **2005,** *26* (16), 1701-1718.

74. Pronk, S.; Pall, S.; Schulz, R.; Larsson, P.; Bjelkmar, P.; Apostolov, R.; Shirts, M. R.; Smith, J. C.; Kasson, P. M.; van der Spoel, D.; Hess, B.; Lindahl, E., GROMACS 4.5: A high-throughput and highly parallel open source molecular simulation toolkit. *Bioinformatics* **2013,** *29* (7), 845-854.

75. Vanommeslaeghe, K.; Hatcher, E.; Acharya, C.; Kundu, S.; Zhong, S.; Shim, J.; Darian, E.; Guvench, O.; Lopes, P.; Vorobyov, I.; Mackerell, A. D., Jr., CHARMM general force field: A force field for drug-like molecules compatible with the CHARMM all-atom additive biological force fields. *J. Comput. Chem.* **2010,** *31* (4), 671-690.

76. Frisch, M. J.; Trucks, G. W.; Schlegel, H. B.; Scuseria, G. E.; Robb, M. A.; Cheeseman, J. R.; Scalmani, G.; Barone, V.; Mennucci, B.; Petersson, G. A.; Nakatsuji, H.; Caricato,

M.; Li, X.; Hratchian, H. P.; Izmaylov, A. F.; Bloino, J.; Zheng, G.; Sonnenberg, J. L.; Hada, M.; Ehara, M.; Toyota, K.; Fukuda, R.; Hasegawa, J.; Ishida, M.; Nakajima, T.; Honda, Y.; Kitao, O.; Nakai, H.; Vreven, T.; Montgomery, J. A., Jr.; Peralta, J. E.; Ogliaro, F.; Bearpark, M.; Heyd, J. J.; Brothers, E.; Kudin, K. N.; Staroverov, V. N.; Kobayashi, R.; Normand, J.; Raghavachari, K.; Rendell, A.; Burant, J. C.; Iyengar, S. S.; Tomasi, J.; Cossi, M.; Rega, N.; Millam, J. M.; Klene, M.; Knox, J. E.; Cross, J. B.; Bakken, V.; Adamo, C.; Jaramillo, J.; Gomperts, R.; Stratmann, R. E.; Yazyev, O.; Austin, A. J.; Cammi, R.; Pomelli, C.; Ochterski, J. W.; Martin, R. L.; Morokuma, K.; Zakrzewski, V. G.; Voth, G. A.; Salvador, P.; Dannenberg, J. J.; Dapprich, S.; Daniels, A. D.; Farkas, Ö.; Foresman, J. B.; Ortiz, J. V.; Cioslowski, J.; Fox, D. J. *Gaussian 09*, 2009.

77.   See supplementary material at http://dx.doi.org/10.1063/1.4958625 E-JCPSA6-145-044627 for further discussion of signatures of anharmonicity in 2DRR spectra and additional output of the molecular dynamics simulations.

78.   Mukamel, S., *Principles of Nonlinear Optical Spectroscopy*. Oxford University Press: New York, 1999.

79.   Nitzan, A., *Chemical Dynamics in Condensed Phases: Relaxation, Transfer And Reactions In Condensed Molecular Systems*. Oxford University Press: New York, 2006.

80.   Miller, R. J., Vibrational energy relaxation and structural dynamics of heme proteins. *Annu. Rev. Phys. Chem.* **1991,** *42*, 581-614.

81.   Middleton, C. T.; Cohen, B.; Kohler, B., Solvent and solvent isotope effects on the vibrational cooling dynamics of a DNA base derivative. *J. Phys. Chem. A* **2007,** *111* (42), 10460-7.

82.   van Veldhoven, E.; Khurmi, C.; Zhang, X.; Berg, M. A., Time-resolved optical spectroscopy with multiple population dimensions: a general method for resolving dynamic heterogeneity. *Chemphyschem* **2007,** *8* (12), 1761-1765.

83.   Khurmi, C.; Berg, M. A., Parallels between multiple population-period transient spectroscopy and multidimensional coherence spectroscopies. *J. Chem. Phys.* **2008,** *129* (6), 064504.

84.   Ding, F.; Fulmer, E. C.; Zanni, M. T., Heterodyned fifth-order two-dimensional IR spectroscopy: third-quantum states and polarization selectivity. *J. Chem. Phys.* **2005,** *123* (9), 94502.

85.   Moran, A. M.; Dreyer, J.; Mukamel, S., Ab initiosimulation of the two-dimensional vibrational spectrum of dicarbonylacetylacetonato rhodium(I). *J. Chem. Phys.* **2003,** *118* (3), 1347-1355.

CHAPTER 6. IMAGING CARRIER DIFFUSION IN PEROVSKITES WITH A DIFFRACTIVE OPTIC-BASED TRANSIENT ABSORPTION MICROSCOPE[4]

6.1. Introduction

Organohalide perovskites carry many advantages for use in solar cells and other optoelectronic devices.[1-3] They can be processed from solution[4] and have absorbance spectra that are readily tuned with control of the halide ratio[5] and metal cation.[6] Long diffusion lengths[7-8] and low susceptibility to trap-assisted recombination[9-10] have also been demonstrated, which is a remarkable result considering the flexibility of the ionic lattice.[11] Slow vibrational cooling, which occurs on the time scale of 100 picoseconds, is one source of enhanced carrier transport in perovskites.[3, 12-14] The extent to which grain boundaries and many-body decay processes influence carrier transport is also under investigation.[8, 15-16]

Carrier mobilities in organohalide perovskites have been determined using a variety of methods. Conventional (indirect) measurements of carrier diffusivities yield values (0.02-0.16 cm^2/s)[7, 13, 17] that are an order of magnitude smaller than those obtained in a more direct manner with transient absorption microscopy (0.05-1.77 cm^2/s).[14, 18-20] Discrepancies in the diffusion coefficients determined using these two approaches are thought to represent the influence of grain boundaries.[20] In the conventional approach, an electron (PCBM) or hole quencher (Spiro-OMeTAD) is placed in contact with the perovskite. Diffusion coefficients can then be determined under the assumption that electron transfer is instantaneous when an electron reaches

---

the interface with the quencher. While the conventional approach is often effective, the rate of electron transfer and the quenching efficiency can vary significantly at different locations on heterogeneous interfaces.[21] Such a breakdown in assumptions may lead to an underestimation of diffusion coefficients. By contrast, carrier diffusion within individual grains can be directly imaged with transient absorption microscopy, thereby eliminating contributions from grain boundaries when the laser is focused to a spot size smaller than an individual grain.

Ultrafast transient absorption microscopy is a relatively new approach for studying carrier diffusion in nanoparticles and films.[14, 18-20, 22-26] Systems under investigation include silicon nanowires,[23] metal dichalcogenides,[25] perovskite thin films,[14, 18, 20] and various organic semiconductors.[22] In these types of experiments, the pump beam is typically focused to a sub-μm spot size and a probe beam is raster scanned in order to image carrier diffusion. Laser systems with MHz repetition rates are best-suited to such point-by-point methods for image construction. In an alternate approach that is more appropriate for laser systems with kHz repetition rates, an entire femtosecond time-resolved image is obtained in a wide-field geometry without scanning the position of a laser beam.[27-28] Unfortunately, wide-field imaging is not well-suited for studies of carrier diffusion because the pump and probe beams are focused to large spot sizes on the sample. A method that combines wide-field imaging with the initiation of a localized distribution of carriers (on the μm length scale) is better-suited for laser systems with kHz repetition rates.

In this work, we describe a diffractive optic-based, wide-field method for conducting transient absorption microscopy. In order to directly image carrier diffusion in organohalide perovskite systems, the pump and probe beams, which counter-propagate through the microscope objective, and are focused to 0.7-μm and 150-μm spot sizes on the sample surface, respectively. Up to 41 transient absorption experiments are conducted in parallel using an array

of pump laser beams generated with a diffractive optic. This multi-beam approach facilitates the rapid attainment of statistical information. The capabilities of the instrument are demonstrated with measurements conducted on lead iodide perovskite films and single crystals. This choice of systems is motivated by two goals. The first goal is to analyze the effects of grain boundaries on the diffusivities and relaxation processes. The second goal is to establish a fitting procedure that accounts for the dependence of the excited state lifetime on the position-dependent laser intensity.

6.2. Experimental Methods

6.2.1. Sample Preparation

Methylammonium lead iodide perovskite films were prepared based on previously reported methods.[29] Dimethylformamide (DMF) was obtained from Sigma-Aldrich, lead iodide was purchased from Alfa Aesar, methylammonium iodide (MAI) was obtained from Solaronix, and isopropanol (Optima grade) was purchased from Fisher Scientific. All materials were used without further purification.

FTO (Sigma-Aldrich; ~13 Ω/sq, approx. 1.1 cm^2) substrates were cleaned via sonication for 20 minutes in a series of four solvents: Contrex AP glassware detergent in deionized water, deionized water, acetone, and isopropanol. Substrates were dried in a stream of nitrogen gas following the isopropanol wash.

Pre-cleaned FTO substrates and a lead iodide solution (0.83 M in DMF) were preheated at 90°C for 30 minutes immediately before film deposition. Perovskites films were prepared using a two-step fabrication process. First, 50 µL of the pre-heated lead iodide solution was deposited onto the preheated substrate by spin coating at 6000 RPM for 20 seconds (3000 RPM/second acceleration). Immediately following the spin coating, 200 µL of MAI solution (10 mg/mL in isopropanol) was deposited on top of the lead iodide layer and allowed to soak into the

film for 10 seconds. Excess solvent was spun off the film using the previously described spin cycle. The perovskite films were then annealed at 90°C for 40 minutes.

The perovskite crystal was prepared with a space-limiting method reported elsewhere.[30] First, 461 mg of lead iodide and 159 mg of MAI were dissolved in 0.75 mL γ-Butyrolactone (from Sigma-Aldrich) and heated at 60 °C. A drop of the precursor solution was then deposited onto a glass slide (Fisher Scientific, pre-cleaned and used as received) and covered with a second identical slide. Thin perovskite crystals were then grown between the glass slides at 120 °C for 2 hours.

6.2.2. Transient Absorption Microscopy
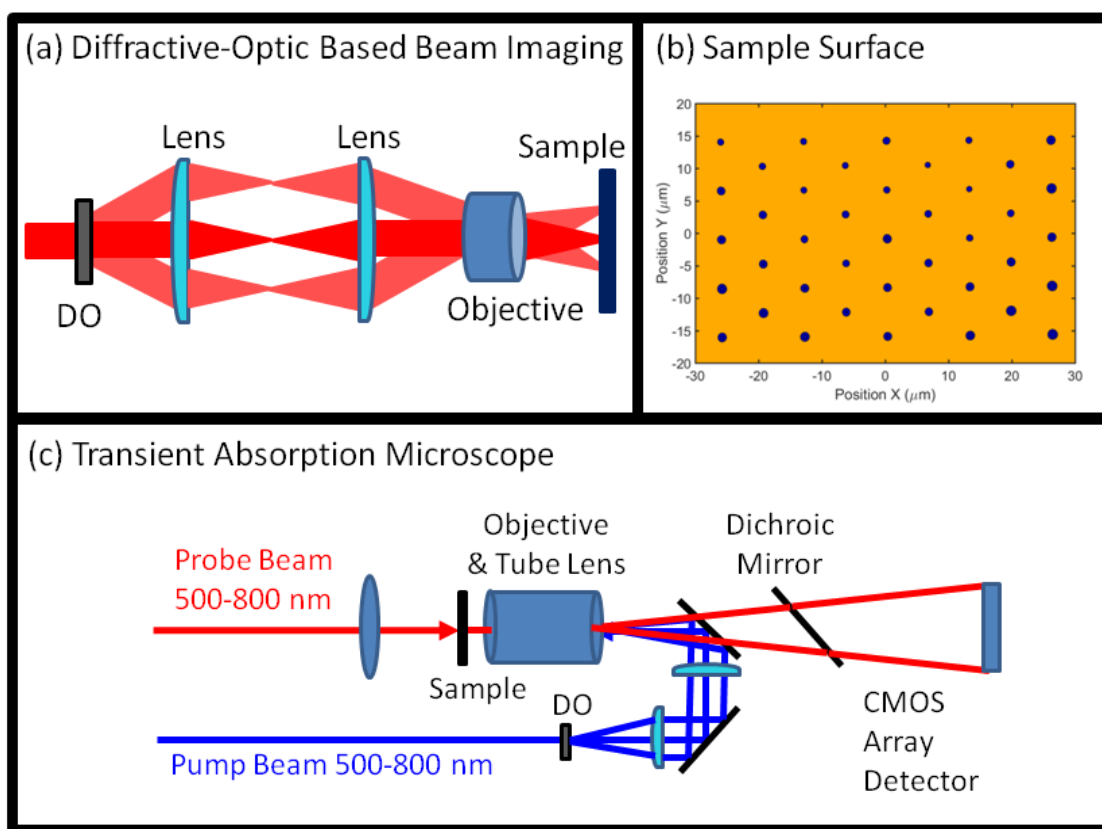
Figure 6.1. *Transient absorption microscopy experiments are conducted with a diffractive optic-based, wide-field microscope. (a) A diffractive optic is used to generate an array of pump beams which focus at different places on the sample. (b) Array of 41 pump laser beams is focused onto the sample surface. (c) Counter-propagating pump and probe beams are focused to FWHM spot sizes of 0.7 and 150 μm, respectively.*

All experiments are conducted with a 45-fs, 4-mJ Coherent Libra laser system with a 1-kHz repetition rate. Continuum pump and probe pulses are produced by focusing 1.5 mJ of the 800 nm fundamental beam into a 2-m long tube filled with argon gas to induce continuum generation. The continuum is then divided into pump and the probe beams with a 70:30 beam splitter. The two laser beams are passed through all-reflective 4F setups, which are based on 1200 g/mm gratings and 20-cm focal length mirrors. Motorized slits at the Fourier planes are used to filter the desired portions of the pump and probe spectra. The spectrally filtered pulses have 250-fs durations and 5-nm widths. The continuum beams are then relayed into the microscope setup shown in Figure 6.1(c). Pulse energies are controlled with neutral density filters.

The operations performed by the diffractive-optic based microscope are illustrated in Figure 6.1(a). Three beams are shown for clarity; however, arbitrary beam patterns can be generated by customizing the diffractive optic.[31-32] The pump is split into 41 beams with the diffractive optic (Holoeye) employed in this work (see Figure 6.1(b)). The two lenses placed before the microscope objective have 10- and 2.5-cm focal lengths, which reduce the angles between beams by 75%. The pump beams are then focused onto the sample with a microscope objective (Olympus). The infinity-corrected microscope objective has a magnification of 40x, a numerical aperture of 0.95, and a working distance of 0.18 mm. The tube lens located between the objective and the detector is also infinity-corrected and has an 18-cm focal length. With this objective, the FWHM spot size of each pump beam is 0.7 µm on the sample surface. The probe beam, which has a fluence of approximately 15 µJ/cm^2 at the sample, is focused to a spot size of 150 µm from the opposite side of the microscope objective using a 10-cm focal length lens. Therefore, the probe intensity for a spot at one of the corners of the array of pump beams is 11%

less than that of the central beam (see Figure 6.1(b)). Of course, a difference of 11% is irrelevant in transient absorption experiments because differential absorption is independent of the probe intensity.

The CMOS detector is 12-bit with a 1024×1280 array of pixels and 915 Hz maximum frame rate (Phantom Miro C110). The detector is synchronized to the laser system at 1 kHz. An optical chopper, which is placed in the path of the pump beam, cycles the instrument between the pump-on, S_1, and pump-off, S_2, conditions at 500 Hz. Differential absorption is then computed as $\Delta A = \log(S_1) - \log(S_2)$. Each differential absorption image is averaged over a total of 100 images in a single scan of the delay line. The delay line is scanned 30 times during each experiment.
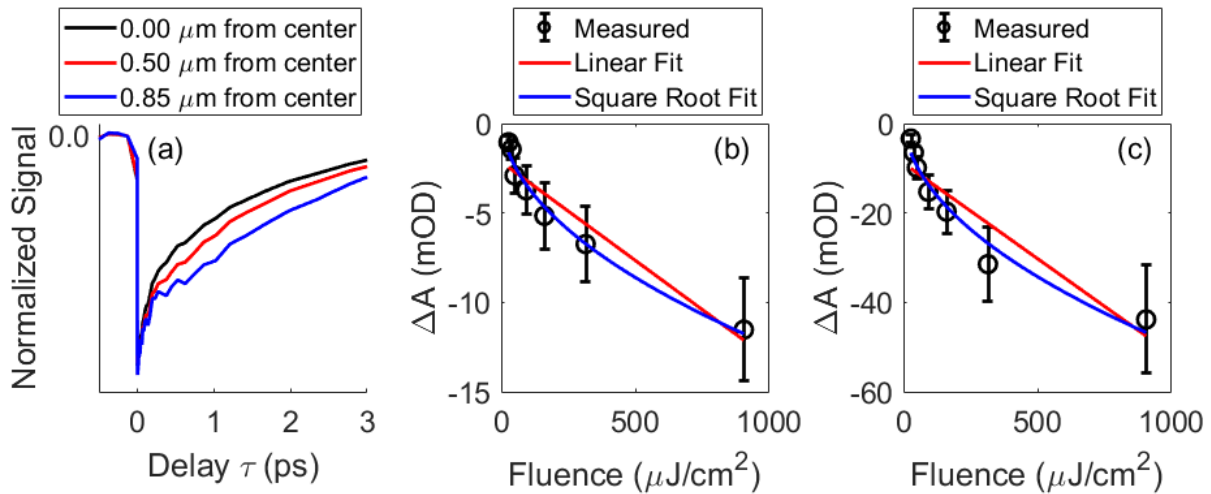
Figure 6.2. *Control experiments are conducted to establish a model for signal processing. (a) The decay rate decreases with distance from the center of one of the pump beams because of the decrease in laser fluence. Transient absorption signals measured at 760 nm for the (b) film and (c) crystal exhibit square root dependencies on the fluence of the pump beam (pump is at 570 nm).*

6.3. Signal Processing

Sensitivity of the photoluminescence quantum yield to the incident light intensity has been demonstrated in previous studies of organohalide perovskites.[33-36] The quantum yield of light emission is compared to the spatially-averaged intensity (i.e., averaged over the beam profile) of the incident laser beam in these measurements. In the present experiments, it is important to account for variation of the carrier lifetimes across the Gaussian beam profile. As expected, we find that the lifetime is shortest in the center of the pump beam and increases at points displaced from the peak of the intensity distribution (see Figure 6.2(a)). Such variation of the lifetime promotes a delay-dependent expansion in the width of the signal spot that is unrelated to carrier diffusion. Incorporating this process into the algorithm for signal interpretation is important because the carrier diffusivity will be overestimated if the intensity dependence of the lifetime is not taken into account.

The relaxation dynamics under investigation exhibit a clear dependence on the pump intensity as evidenced by variation of the lifetime within the laser spot. We account for such many-body relaxation processes with the modified diffusion equation,

$$\frac{\partial N}{\partial \tau} = D_0 \frac{\partial^2 N}{\partial x^2} - \frac{N}{\tau_1} - \frac{N^2}{\tau_2}, \tag{6.1}$$

where x is a spatial coordinate (a one-dimensional slice through the peak of a two-dimensional Gaussian intensity distribution), N is the density of electronic excitations, D_0 is a diffusion constant, τ_1 is the single-body carrier lifetime, τ_2 and is a two-body relaxation time.

Data processing involves calculating full-width-half-maxima of the signal spots at each delay point. The signal intensity is first normalized to 1 for each one-dimensional slice of the signal. On the left (smaller x value) side of the peak, two successive data points (x_1, y_1), (x_2, y_2)

are located at a signal intensity of 0.5. The half-width-half-maximum coordinate on this side of

the peak is then calculated with linear interpolation,

$$HWHM_{left} = (0.5 - y_1) \cdot \frac{x_2 - x_1}{y_2 - y_1} + x_1.$$ (6.2)
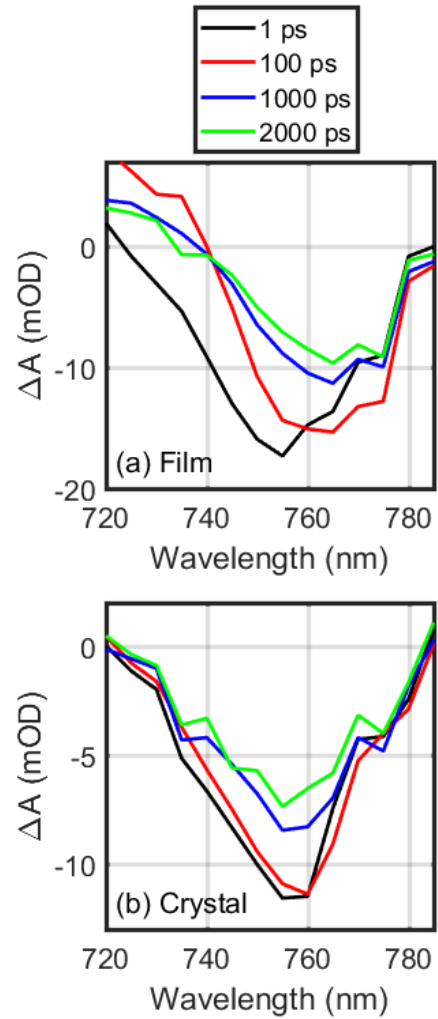
Figure 6.3. Transient absorption spectra measured for the perovskite (a) film and (b) crystal with a 570-nm pump wavelength. Imaging for both systems is conducted with at probe wavelength of 760 nm.

The relation between the signal intensity $S(x,\tau)$ and carrier density $N(x,\tau)$ must be known in order to fit the data. We have confirmed that the signal scales as the square root of $N(x,\tau)$,

$$S(x,\tau) = A\sqrt{N(x,\tau)},\qquad(6.3)$$

where A is a linear scaling parameter determined in the fitting process (see Figures 6.2(b) and 6.2(c)). When interactions between electronic excitations are significant, such scaling is anticipated for signal components in which the system evolves in an excited state population during the delay time, τ (e.g., stimulated emission in Figure 6.3).[14, 37] The initial condition required to solve Equation 6.1 is given by

$$N(x,0) = \left(\frac{S(x,0)}{A}\right)^2.\qquad(6.4)$$

The boundary condition for the differential equation is

$$N(\pm\infty,0) = 0.\qquad(6.5)$$

The least squares method is used to fit the data and obtain the parameters D_0, A, τ_1, and τ_2.

6.4. Results and Discussion

Both the film and crystal exhibit intense stimulated emission resonances near 760 nm as shown in Figure 6.3. Evidence for excitons has been presented for perovskites with crystalline domains in recent literature;[26, 38] however, we do not observe signatures of excitons in this crystal (i.e., no excited state absorption in the 700-800 nm range). The transient absorption spectrum of the film red-shifts at delay times less than 10 ps, whereas the peak of the signal is essentially independent of the delay time for the crystal. This difference between the spectra is partly due to a larger excited state absorption response in the film at detection wavelengths less

than 740 nm. In order to compare both systems on similar footing, images are constructed with

signal detection at 760 nm. The dynamics of interest occur on the nanosecond time scale and are

therefore insensitive to the ultrafast red-shift in the signal spectrum of the film.
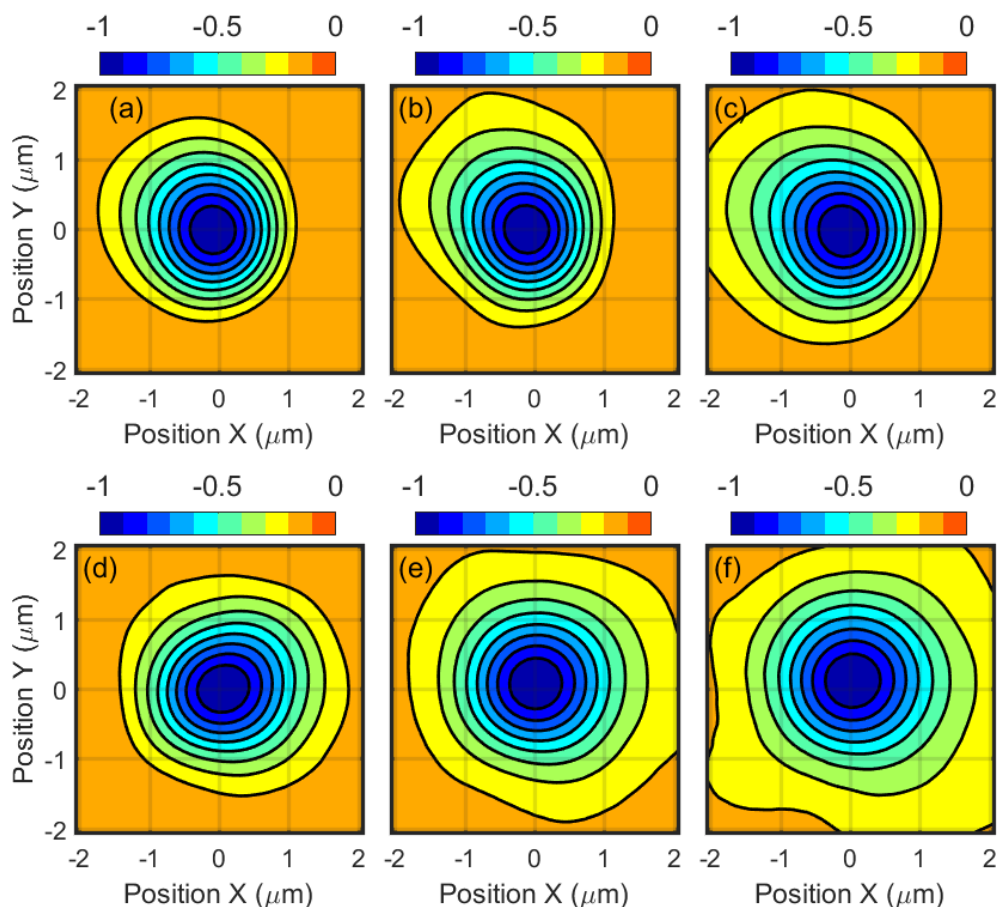
Figure 6.4. Transient absorption signals measured with 570-nm pump beam and 760-nm probe beam with a pump fluence of 40 μJ/cm². Images measured for a perovskite film at delay times of (a) 1 ps, (b) 500 ps, and (c) 1000 ps. Images measured for a perovskite single crystal at delay times of (d) 1 ps, (e) 500 ps, and (f) 1000 ps. The sizes of the signal spots expand as the delay time increases because of carrier diffusion and intensity dependence of the carrier lifetimes.

Transient absorption images measured for the perovskite film and crystal are presented in

Figure 6.4. In both systems, the signal spots expand as the delay time increases due to carrier

diffusion and/or intensity dependence of the carrier lifetimes. These two processes cannot be

distinguished by inspection. Rather, it is necessary to vary the intensities of the pump beams and

fit the intensity distributions of the signals. In addition, the shape of the signal intensity is maintained as time evolves for carrier diffusion, whereas the peak of the signal "flattens" when intensity dependence of the excited state lifetimes takes hold. While Equation 6.1 is sufficient for such line shape analysis, conclusions about the influence of the pump intensity on the widths of the signal spots should be corroborated with measurements in which the intensity of the pump is varied over a wide range.
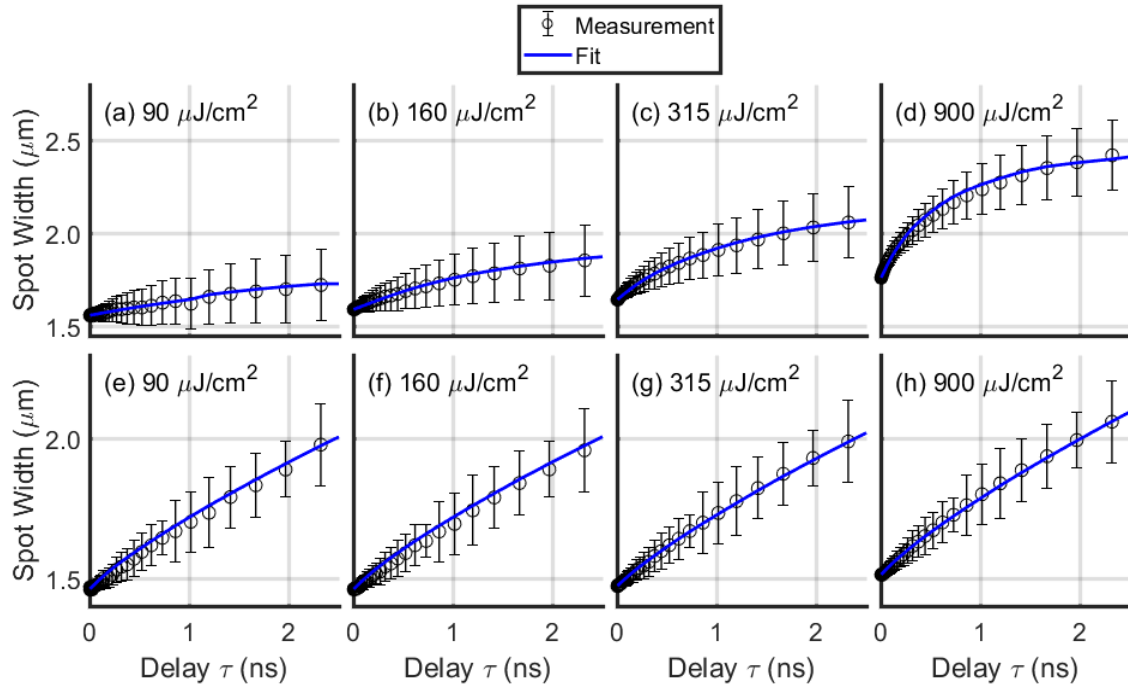
Figure 6.5. *Full-width-half-maximum spot widths measured for a methylammonium lead iodide perovskite film (top row) and single crystal (bottom row). The data are fit with Equation 6.1 (blue line). These data suggest that dynamics in the film and crystal are associated with fluence-dependent carrier lifetimes and carrier diffusion, respectively.*

Dynamics in the spatial widths of the transient absorption signal spots are displayed in Figure 6.5. Equation 6.1 adequately describes the dynamics in the spot widths for both samples at all pump fluences. In the film, the magnitude of the expansion in the signals' spot widths becomes larger as the pump fluence increases, whereas the spot widths are fairly insensitive to the pump fluence in the crystal. The behavior of the film suggests that the spot widths increase

primarily because the carrier lifetimes are shortest in the center of the signal spot (see Figure

6.2(a)). This fluence-dependent effect on the spot widths is associated with the two-body

contribution to the relaxation time, τ_2. In contrast, the delay-dependent increases in the spot

widths determined for the crystal are insensitive to the fluence of the pump, which indicates that

carrier diffusion is responsible for the dynamics.
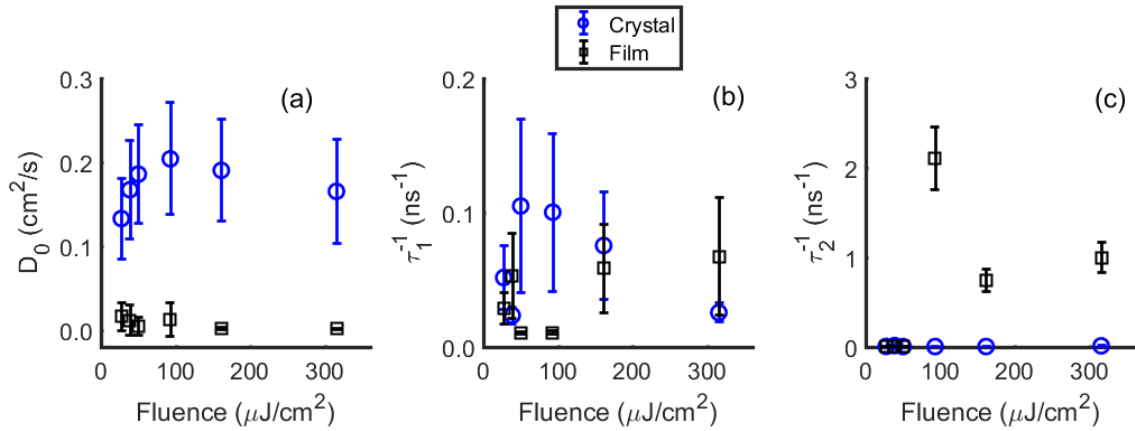
Figure 6.6. *Statistical analyses of fitting parameters for perovskite film and single crystal: (a)
diffusion coefficients, D_0; (b) single-body relaxation rate, τ_1^{-1}; (c) two-body relaxation rate,
τ_2^{-1}. The uncertainty intervals represent two standard deviations. These data confirm the
negligibility of carrier diffusion in the perovskite film. In contrast, expansion of the signal spots
observed for the perovskite crystal is dominated by carrier diffusion.*

The fitting parameters obtained for the perovskite film and crystal are compared in Figure

6.6. The error bars span ranges equal to two standard deviations. The parameters are obtained by

fitting the transient absorption dynamics at each spot on the sample surface with Equation 6.1.

The means and standard deviations for each of the parameters are then calculated for 41 and 33

spots for the film and crystal, respectively. Fewer laser spots are processed for the crystal

because of light scattering at defects.

The diffusion coefficients, D_0, determined for the single crystal are near 0.20 cm²/s for

most pump fluences, whereas those obtained for the film are close to 0.01 cm²/s. Diffusivities of

the carriers in the film are below the lower limit of the range of values reported in earlier studies $(0.02\text{-}0.16 \text{ cm}^2/\text{s})$.[7, 13, 17] In contrast, the diffusion coefficients determined for the crystal are within the range of those reported in recent transient absorption microscopy measurements conducted on individual grains $(0.05\text{-}1.77 \text{ cm}^2/\text{s})$.[14, 18-20] The smaller diffusivities determined for carriers in the film are consistent with the dynamics in the spot widths displayed in Figure 6.5. Notably, the parameters, D_0 and τ_2, are governed by dynamics in the shapes of the signal spots (i.e., the peak of the signal spot "flattens" when two-body dynamics contribute). For this reason, Figures 6.5 and 6.6 represent independent ways to differentiate diffusion and intensity dependence of the carrier lifetimes.

Our data suggests that the difference in diffusion coefficients, D_0, obtained for the film and crystal are associated with grain boundaries. The grain sizes in the film are on the order of 0.2 μm, which is smaller than 0.7-μm spot sizes of the pump laser. Thus, the experimental measurements are sensitive to inter-grain carrier diffusion processes in the film (i.e., insensitive to diffusion within the grains). This may explain why the diffusion constants for the film derived from our measurements are smaller than those reported in recent transient absorption microscopies.[14, 18, 20]

6.5. Conclusion

In summary, the present approach for conducting transient absorption microscopy solves several technical challenges associated with the use of a 1-kHz laser system. First, the data acquisition time is minimized by employing a wide-field geometry in which the pump and probe beams counter-propagate through the sample. The pump beams are focused to spot sizes with FWHM of 0.7 μm, whereas the spot size of the probe beam is 150 μm. In this configuration, an entire image of the sample can be obtained in less than one second without raster scanning

individual laser beams on the sample surface. Second, a diffractive optic is used to generate an array of 41 pump beams. Conducting many transient absorption experiments in parallel allows statistics to be quickly compiled.

The capabilities of the instrument are demonstrated with applications to a methylammonium lead iodide perovskite film and crystal. Our data suggests that carrier diffusion in the film is essentially negligible on the nanosecond time-scale, whereas the diffusion coefficients in the crystal are approximately 0.2 cm^2/s. Measurements conducted at multiple pulse energies are required to distinguish between two mechanisms for delay-dependent expansions in the spot widths: carrier diffusion and intensity-dependence of the carrier lifetimes. We conclude that the spot widths expand in the film because of intensity-dependence of the carrier lifetimes rather than carrier diffusion. These differences between the film and crystal are attributed to the presence of grain boundaries in the film.

REFERENCES

1.   Lee, M. M.; Teuscher, J.; Miyasaka, T.; Murakami, T. N.; Snaith, H. J., Efficient hybrid solar cells based on meso-superstructured organometal halide perovskites. *Science* **2012,** *338* (6107), 643-647.

2.   Kim, H. S.; Lee, C. R.; Im, J. H.; Lee, K. B.; Moehl, T.; Marchioro, A.; Moon, S. J.; Humphry-Baker, R.; Yum, J. H.; Moser, J. E.; Gratzel, M.; Park, N. G., Lead iodide perovskite sensitized all-solid-state submicron thin film mesoscopic solar cell with efficiency exceeding 9%. *Sci. Rep.* **2012,** *2*, 591.

3.   Yang, Y.; Ostrowski, D. P.; France, R. M.; Zhu, K.; van de Lagemaat, J.; Luther, J. M.; Beard, M. C., Observation of a hot-phonon bottleneck in lead-iodide perovskites. *Nat. Photonics* **2015,** *10* (1), 53-59.

4.   Burschka, J.; Pellet, N.; Moon, S. J.; Humphry-Baker, R.; Gao, P.; Nazeeruddin, M. K.; Gratzel, M., Sequential deposition as a route to high-performance perovskite-sensitized solar cells. *Nature* **2013,** *499* (7458), 316-319.

5.   Fang, Y.; Dong, Q.; Shao, Y.; Yuan, Y.; Huang, J., Highly narrowband perovskite single-crystal photodetectors enabled by surface-charge recombination. *Nat. Photonics* **2015,** *9* (10), 679-686.

6.   Hao, F.; Stoumpos, C. C.; Cao, D. H.; Chang, R. P. H.; Kanatzidis, M. G., Lead-free solid-state organic-inorganic halide perovskite solar cells. *Nat. Photonics* **2014,** *8* (6), 489-494.

7.   Stranks, S. D.; Eperon, G. E.; Grancini, G.; Menelaou, C.; Alcocer, M. J.; Leijtens, T.; Herz, L. M.; Petrozza, A.; Snaith, H. J., Electron-hole diffusion lengths exceeding 1 micrometer in an organometal trihalide perovskite absorber. *Science* **2013,** *342* (6156), 341-344.

8.   Dong, Q.; Fang, Y.; Shao, Y.; Mulligan, P.; Qiu, J.; Cao, L.; Huang, J., Electron-hole diffusion lengths > 175 µm in solution-grown $CH_3NH_3PbI_3$ single crystals. *Science* **2015,** *347* (6225), 967-970.

9.   Kim, J.; Lee, S. H.; Lee, J. H.; Hong, K. H., The Role of Intrinsic Defects in Methylammonium Lead Iodide Perovskite. *J. Phys. Chem. Lett.* **2014,** *5* (8), 1312-1317.

10.   Saidaminov, M. I.; Abdelhady, A. L.; Murali, B.; Alarousu, E.; Burlakov, V. M.; Peng, W.; Dursun, I.; Wang, L.; He, Y.; Maculan, G.; Goriely, A.; Wu, T.; Mohammed, O. F.; Bakr, O. M., High-quality bulk hybrid perovskite single crystals within minutes by inverse temperature crystallization. *Nat. Commun.* **2015,** *6*, 7586.

11.   Wu, X.; Trinh, M. T.; Niesner, D.; Zhu, H.; Norman, Z.; Owen, J. S.; Yaffe, O.; Kudisch, B. J.; Zhu, X. Y., Trap states in lead iodide perovskites. *J. Am. Chem. Soc.* **2015,** *137* (5), 2089-2096.

12. Niesner, D.; Zhu, H.; Miyata, K.; Joshi, P. P.; Evans, T. J.; Kudisch, B. J.; Trinh, M. T.; Marks, M.; Zhu, X. Y., Persistent energetic electrons in methylammonium lead iodide perovskite thin films. *J. Am. Chem. Soc.* **2016,** *138* (48), 15717-15726.

13. Savenije, T. J.; Ponseca, C. S., Jr.; Kunneman, L.; Abdellah, M.; Zheng, K.; Tian, Y.; Zhu, Q.; Canton, S. E.; Scheblykin, I. G.; Pullerits, T.; Yartsev, A.; Sundstrom, V., Thermally activated exciton dissociation and recombination control the carrier dynamics in organometal halide perovskite. *J. Phys. Chem. Lett.* **2014,** *5* (13), 2189-2194.

14. Guo, Z.; Wan, Y.; Yang, M.; Snaider, J.; Zhu, K.; Huang, L., Long-range hot-carrier transport in hybrid perovskites visualized by ultrafast microscopy. *Science* **2017,** *356* (6333), 59-62.

15. Nie, W.; Tsai, H.; Asadpour, R.; Blancon, J. C.; Neukirch, A. J.; Gupta, G.; Crochet, J. J.; Chhowalla, M.; Tretiak, S.; Alam, M. A.; Wang, H. L.; Mohite, A. D., High-efficiency solution-processed perovskite solar cells with millimeter-scale grains. *Science* **2015,** *347* (6221), 522-525.

16. Reid, O. G.; Yang, M.; Kopidakis, N.; Zhu, K.; Rumbles, G., Grain-size-limited mobility in methylammonium lead iodide perovskite thin films. *ACS Energy Lett.* **2016,** *1* (3), 561-565.

17. Xing, G.; Mathews, N.; Sun, S.; Lim, S. S.; Lam, Y. M.; Gratzel, M.; Mhaisalkar, S.; Sum, T. C., Long-range balanced electron- and hole-transport lengths in organic-inorganic $CH_3NH_3PbI_3$. *Science* **2013,** *342* (6156), 344-347.

18. Guo, Z.; Manser, J. S.; Wan, Y.; Kamat, P. V.; Huang, L., Spatial and temporal imaging of long-range charge transport in perovskite thin films by ultrafast microscopy. *Nat. Commun.* **2015,** *6*, 7471.

19. Tian, W.; Zhao, C.; Leng, J.; Cui, R.; Jin, S., Visualizing carrier diffusion in individual single-crystal organolead halide perovskite nanowires and nanoplates. *J. Am. Chem. Soc.* **2015,** *137* (39), 12458-12461.

20. Hill, A. H.; Smyser, K. E.; Kennedy, C. L.; Massaro, E. S.; Grumstrup, E. M., Screened charge carrier transport in methylammonium lead iodide perovskite thin films. *J. Phys. Chem. Lett.* **2017,** *8* (5), 948-953.

21. Zigler, D. F.; Morseth, Z. A.; Wang, L.; Ashford, D. L.; Brennaman, M. K.; Grumstrup, E. M.; Brigham, E. C.; Gish, M. K.; Dillon, R. J.; Alibabaei, L.; Meyer, G. J.; Meyer, T. J.; Papanikolas, J. M., Disentangling the physical processes responsible for the kinetic complexity in interfacial electron transfer of excited Ru(II) polypyridyl dyes on TiO_2. *J. Am. Chem. Soc.* **2016,** *138* (13), 4426-4438.

22. Wong, C. Y.; Penwell, S. B.; Cotts, B. L.; Noriega, R.; Wu, H.; Ginsberg, N. S., Revealing exciton dynamics in a small-molecule organic semiconducting film with subdomain transient absorption microscopy. *J. Phys. Chem. C* **2013,** *117* (42), 22111-22122.

23. Gabriel, M. M.; Grumstrup, E. M.; Kirschbrown, J. R.; Pinion, C. W.; Christesen, J. D.; Zigler, D. F.; Cating, E. E.; Cahoon, J. F.; Papanikolas, J. M., Imaging charge separation and carrier recombination in nanowire p-i-n junctions using ultrafast microscopy. *Nano Lett.* **2014,** *14* (6), 3079-3087.

24. Johns, P.; Yu, K.; Devadas, M. S.; Hartland, G. V., Role of resonances in the transmission of surface plasmon polaritons between nanostructures. *ACS Nano* **2016,** *10* (3), 3375-3381.

25. Yuan, L.; Wang, T.; Zhu, T.; Zhou, M.; Huang, L., Exciton dynamics, transport, and annihilation in atomically thin two-dimensional semiconductors. *J. Phys. Chem. Lett.* **2017,** *8* (14), 3371-3379.

26. Nah, S.; Spokoyny, B.; Stoumpos, C.; Soe, C. M. M.; Kanatzidis, M.; Harel, E., Spatially segregated free-carrier and exciton populations in individual lead halide perovskite grains. *Nat. Photonics* **2017,** *11* (5), 285-288.

27. Baiz, C. R.; Schach, D.; Tokmakoff, A., Ultrafast 2D IR microscopy. *Opt. Express* **2014,** *22* (15), 18724-18735.

28. Ostrander, J. S.; Serrano, A. L.; Ghosh, A.; Zanni, M. T., Spatially Resolved two-dimensional infrared spectroscopy via wide-field microscopy. *ACS Photonics* **2016,** *3* (7), 1315-1323.

29. Bi, D.; Moon, S.-J.; Häggman, L.; Boschloo, G.; Yang, L.; Johansson, E. M. J.; Nazeeruddin, M. K.; Grätzel, M.; Hagfeldt, A., Using a two-step deposition technique to prepare perovskite ($CH_3NH_3PbI_3$) for thin film solar cells based on ZrO_2 and TiO_2 mesostructures. *RSC Adv.* **2013,** *3* (41), 18762.

30. Bao, C.; Chen, Z.; Fang, Y.; Wei, H.; Deng, Y.; Xiao, X.; Li, L.; Huang, J., Low-noise and large-linear-dynamic-range photodetectors based on hybrid-perovskite thin-single-crystals. *Adv. Mater.* **2017,** *29* (39).

31. Polin, M.; Ladavac, K.; Lee, S. H.; Roichman, Y.; Grier, D. G., Optimized holographic optical traps. *Opt. Express* **2005,** *13* (15), 5831.

32. Lohmann, A. W.; Paris, D. P., Binary fraunhofer holograms, generated by computer. *Appl. Opt.* **1967,** *6* (10), 1739-1748.

33. Stranks, S. D.; Burlakov, V. M.; Leijtens, T.; Ball, J. M.; Goriely, A.; Snaith, H. J., Recombination kinetics in organic-inorganic perovskites: Excitons, free charge, and subgap states. *Phys. Rev. Appl.* **2014,** *2* (3).

34. Manser, J. S.; Kamat, P. V., Band filling with free charge carriers in organometal halide perovskites. *Nat. Photonics* **2014,** *8* (9), 737-743.

35. Yamada, Y.; Nakamura, T.; Endo, M.; Wakamiya, A.; Kanemitsu, Y., Photocarrier recombination dynamics in perovskite $CH_3NH_3PbI_3$ for solar cell applications. *J. Am. Chem. Soc.* **2014,** *136* (33), 11610-11613.

36. Yamada, Y.; Yamada, T.; Phuong le, Q.; Maruyama, N.; Nishimura, H.; Wakamiya, A.; Murata, Y.; Kanemitsu, Y., Dynamic optical properties of $CH_3NH_3PbI_3$ single crystals as revealed by one- and two-photon excited photoluminescence measurements. *J. Am. Chem. Soc.* **2015,** *137* (33), 10456-10459.

37. Jain, S. C.; McGregor, J. M.; Roulston, D. J., Band-gap narrowing in novel III-V semiconductors. *J. Appl. Phys.* **1990,** *68* (7), 3747-3749.

38. Grancini, G.; Srimath Kandada, A. R.; Frost, J. M.; Barker, A. J.; De Bastiani, M.; Gandini, M.; Marras, S.; Lanzani, G.; Walsh, A.; Petrozza, A., Role of Microstructure in the Electron-Hole Interaction of Hybrid Lead-Halide Perovskites. *Nat. Photonics* **2015,** *9* (10), 695-701.

CHAPTER 7. CONCLUDING REMARKS

The works in this dissertation have developed two diffractive optical element (DOE) based spectroscopy techniques: two-dimensional resonance Raman (2DRR) spectroscopy and multiplex wide-field transient absorption microscopy. 2DRR provides new insights into fast chemical reactions involving simple molecules or even complex proteins. Specifically, this work has revealed the correlation between vibrational coherence in the reactant and product, as well as investigated the heterogeneity in protein conformations responsible for dissipating energy to the surroundings. Besides 2DRR, multiplex wide-field transient absorption microscopy is capable of imaging the entire area of interest in one shot and conducting a large number of transient absorption measurements in parallel. Statistical information is available after only one experiment, which is essential for highly heterogeneous samples. Chapter 1 discussed the scientific background and motivation driving the demands of new spectroscopy methods in this dissertation. Chapter 2 introduced the basic theories related to DOE-based spectroscopies and detailed the instrumental setups applied in the rest of this dissertation.

The DOE-based 2DRR was firstly applied to a small molecule model system, triiodide, in Chapter 3. The measurement assigned the nuclear motions of the reactant and product into separate dimensions without ambiguity and established a positive correlation between vibrational coherences, indicating that the nonequilibrium bond length of triiodide determines the vibrational coherence frequency of diiodide. To further validate this assertion, a simulation based on a theoretical model that treats the reaction as a 'coherence transfer transition' was found to match the experimentally measured signals.

In Chapter 4, the focus was shifted to a more complicated system, the photo-dissociation of ligands in myoglobin—protein that possesses many active vibrational coordinates. As a derivative of 2DRR applied above, a femtosecond stimulated Raman spectroscopy (FSRS) pulse sequence is implemented in the DOE-based six-wave-mixing interferometer, which eliminates the low-order nonlinearities and collects the background-free fifth-order signal. This approach significantly shortens the data acquisition time and improves the signal-to-noise ratio. The Raman response of the photo-excited heme throughout the fingerprint region was detected in the frequency dimension while the evolution of vibrations was measured in the time domain. The agreement in time scales of the vibrational cooling between our results and reports made by Chergui and coworkers[1] demonstrates the effectiveness of this approach. As another contribution to the field of spectroscopy, carefully controlled experiments were conducted to rule out the possibility of cascades, which are a technical issue that produced many artifacts in previously performed off-resonance two-dimensional Raman spectroscopies. A publication containing the work in Chapter 4 was an Editor's Choice in the Journal of Chemical Physics for the year 2015.[2]

Further study of myoglobin in Chapter 5 relies on the high-quality data measured with the approach detailed in Chapter 4. Fourier transform of the vibrational coherence in the time-dimension yields the 2DRR spectra, which is sensitive to signatures of different line broadening mechanisms. The measurement together with simulation suggests that the greatest amount of heterogeneity is contributed by the methylene deformation mode, which is local to the propionic acid side chains. Because they serve as the gateways mediating fast energy dissipation from the heme,[2-6] variation in these side chains may play critical roles in such process.

Besides studying photo-dissociation reactions in triiodide and myoglobin, 2DRR should be sensitive to other photo-induced reactions where a non-radiative electronic transition occurs at

the same time scale as the nuclear vibrations. This technique could bring new insights for processes including energy transfer in photosynthetic complexes[7-12], charge transfer in electron transport chain chromophores,[13-14] charge transfer at the molecule-semiconductor interfaces,[15-17] electron migration in polymer-fullerene blends,[18] and even the chemistry comprising the initial steps of vision.[19-20] 2DRR correlates the vibrational coherence in the reactant and product with clear assignment of the signal origins and distinguishes the static and dynamic line broadening mechanisms.

As the next step of applying DOE in spectroscopy, a multiplex excitation transient absorption microscopy technique was developed in Chapter 6. The data acquisition time is minimized by employing counter-propagating pump and probe beams, which facilitates wide-field detection and generates the whole image on the camera within one laser shot. More importantly, the DOE splits the pump into many segments and makes it possible to simultaneously measure multiple spots on a heterogeneous sample. The obtained averaged properties together with variation reflect the intrinsic nature of a sample without bias, which is essential for nanomaterials.

To demonstrate the ability of the DOE-based microscope, carrier diffusion in methylammonium lead-iodide perovskite films and crystals were measured. By applying a diffusion model with two-body relaxation process, our analysis suggests that the diffusivities in crystals are at least one order of magnitude larger than in films. The differences between the systems are attributed to the presence of grain boundaries in the films. (Modify this paragraph according to the updated version of the microscopy paper).

The DOE-based microscope can also be applied to other newly-emerging materials, such as two-dimensional (2D) Ruddlesden–Popper perovskites. 2D perovskites refer to few-layer

perovskite sheets surrounded by layers of organic cations, in which the thickness of the organic layer determines the degree of quantum confinement.[21-22] Because of the tunability and higher stability comparing to its three-dimensional counterpart, low-dimensional perovskite films, which is a mixture of different thickness, have been implemented in solar cells[23-25] and LEDs.[26-30] For solar cells, these benefits were obtained at a price of low power conversion efficiency due to the low carrier mobility inside or between the quantum-confined layers.[31-37] On one hand, the latter has been improved by building preferential layer alignment perpendicular to the film substrate[34]. Besides, recent reports indicated that a statistically ordered layer distribution and a suitable bandgap alignment engineering facilitate ultrafast carrier or energy transfer between the layers thus enhance the performances of 2D perovskite devices.[38-44] (Also cite our JCP and Liang Yan's paper here). On the other hand, there is still no direct measurement of the carrier transport inside individual 2D perovskite grain, where the excitons diffusion could be remarkably different from the bulk as observed in transition metal dichalcogenides.[45-47] Stronger exciton many-body interactions[31, 48] and exciton-phonon interactions[49-51] are the possible factors affecting carrier mobility in 2D perovskites. Applying the DOE-based microscopy could provide a solid-base to analyze the mechanisms involved in exciton diffusion process.

In summary, we developed two DOE-based spectroscopy techniques: two-dimensional resonance Raman spectroscopy and wide-field transient absorption microscopy. We demonstrated the validity of these techniques by applying them on simple systems, like triiodide, complicated biological samples, like the protein myoglobin, and a newly-emerging semiconductor, lead halide perovskites.

REFERENCES

1. Consani, C.; Aubock, G.; Bram, O.; van Mourik, F.; Chergui, M., A cascade through spin states in the ultrafast haem relaxation of met-myoglobin. *J. Chem. Phys.* **2014**, 140 (2), 025103.

2. Molesky, B. P.; Guo, Z.; Moran, A. M., Femtosecond stimulated Raman spectroscopy by six-wave mixing. *J. Chem. Phys.* **2015**, 142 (21), 212405.

3. Gao, Y.; Koyama, M.; El-Mashtoly, S. F.; Hayashi, T.; Harada, K.; Mizutani, Y.; Kitagawa, T., Time-resolved Raman evidence for energy 'funneling' through propionate side chains in heme 'cooling' upon photolysis of carbonmonoxy myoglobin. C*hem. Phys. Lett.* **2006**, 429 (1-3), 239-243.

4. Koyama, M.; Neya, S.; Mizutani, Y., Role of heme propionates of myoglobin in vibrational energy relaxation. *Chem. Phys. Lett. 2006*, 430 (4-6), 404-408.

5. Lian, T.; Locke, B.; Kholodenko, Y.; Hochstrasser, R. M., Energy flow from solute to solvent probed by femtosecond ir spectroscopy: Malachite green and heme protein solutions. *J. of Phys. Chem.* **1994**, 98 (45), 11648-11656.

6. Sagnella, D. E.; Straub, J. E., Directed energy "funneling" mechanism for heme cooling following ligand photolysis or direct excitation in solvated carbonmonoxy myoglobin. *J. Phys. Chem. B* **2001**, 105 (29), 7057-7063.

7. Fuller, F. D.; Pan, J.; Gelzinis, A.; Butkus, V.; Senlik, S. S.; Wilcox, D. E.; Yocum, C. F.; Valkunas, L.; Abramavicius, D.; Ogilvie, J. P., Vibronic coherence in oxygenic photosynthesis. *Nat. Chem.* **2014**, 6 (8), 706-711.

8. Womick, J. M.; Moran, A. M., Vibronic enhancement of exciton sizes and energy transport in photosynthetic complexes. *J. Phys. Chem. B* **2011**, 115 (6), 1347-1356.

9. Christensson, N.; Kauffmann, H. F.; Pullerits, T.; Mancal, T., Origin of long-lived coherences in light-harvesting complexes. *J. Phys. Chem. B* **2012**, 116 (25), 7449-54.

10. Kolli, A.; O'Reilly, E. J.; Scholes, G. D.; Olaya-Castro, A., The fundamental role of quantized vibrations in coherent light harvesting by cryptophyte algae. *J. Chem. Phys.* **2012**, 137 (17), 174109.

11. Chin, A. W.; Prior, J.; Rosenbach, R.; Caycedo-Soler, F.; Huelga, S. F.; Plenio, M. B., The role of non-equilibrium vibrational structures in electronic coherence and recoherence in pigment–protein complexes. *Nat. Phys.* **2013**, 9 (2), 113-118.

12. Fujihashi, Y.; Fleming, G. R.; Ishizaki, A., Impact of environmentally induced fluctuations on quantum mechanically mixed electronic and vibrational pigment states in photosynthetic energy transfer and 2D electronic spectra. *J. Chem. Phys.* **2015**, 142 (21), 212403.

13. Liebl, U.; Lipowski, G.; Negrerie, M.; Lambry, J. C.; Martin, J. L.; Vos, M. H., Coherent reaction dynamics in a bacterial cytochrome c oxidase. *Nature* **1999**, 401 (6749), 181-184.

14. Treuffet, J.; Kubarych, K. J.; Lambry, J. C.; Pilet, E.; Masson, J. B.; Martin, J. L.; Vos, M. H.; Joffre, M.; Alexandrou, A., Direct observation of ligand transfer and bond formation in cytochrome c oxidase by using mid-infrared chirped-pulse upconversion. *Proc. Natl. Acad. Sci. U. S. A.* **2007**, 104 (40), 15705-15710.

15. Tisdale, W. A.; Williams, K. J.; Timp, B. A.; Norris, D. J.; Aydil, E. S.; Zhu, X. Y., Hot-electron transfer from semiconductor nanocrystals. *Science* **2010**, 328 (5985), 1543-1547.

16. Zimmermann, C.; Willig, F.; Ramakrishna, S.; Burfeindt, B.; Pettinger, B.; Eichberger, R.; Storck, W., Experimental fingerprints of vibrational wave-packet motion during ultrafast heterogeneous electron transfer. *J. Phys. Chem. B* **2001**, 105 (38), 9245-9253.

17. Guo, Z.; Giokas, P. G.; Cheshire, T. P.; Williams, O. F.; Dirkes, D. J.; You, W.; Moran, A. M., Ultrafast Spectroscopic Signatures of Coherent Electron-Transfer Mechanisms in a Transition Metal Complex. *J. Phys. Chem. A* **2016**, 120 (29), 5773-5790.

18. Song, Y.; Clafton, S. N.; Pensack, R. D.; Kee, T. W.; Scholes, G. D., Vibrational coherence probes the mechanism of ultrafast electron transfer in polymer-fullerene blends. *Nat. Commun.* **2014**, 5, 4933.

19. Polli, D.; Altoe, P.; Weingart, O.; Spillane, K. M.; Manzoni, C.; Brida, D.; Tomasello, G.; Orlandi, G.; Kukura, P.; Mathies, R. A.; Garavelli, M.; Cerullo, G., Conical intersection dynamics of the primary photoisomerization event in vision. *Nature* **2010**, 467 (7314), 440-443.

20. Johnson, P. J.; Halpin, A.; Morizumi, T.; Prokhorenko, V. I.; Ernst, O. P.; Miller, R. J., Local vibrational coherences drive the primary photochemistry of vision. *Nat. Chem.* **2015**, 7 (12), 980-986.

21. Stoumpos, C. C.; Cao, D. H.; Clark, D. J.; Young, J.; Rondinelli, J. M.; Jang, J. I.; Hupp, J. T.; Kanatzidis, M. G., Ruddlesden–Popper hybrid lead iodide perovskite 2D homologous semiconductors. *Chem. Mater.* **2016**, 28 (8), 2852-2867.

22. Stoumpos, C. C.; Soe, C. M. M.; Tsai, H.; Nie, W.; Blancon, J.-C.; Cao, D. H.; Liu, F.; Traoré, B.; Katan, C.; Even, J.; Mohite, A. D.; Kanatzidis, M. G., High members of the 2D Ruddlesden-Popper halide perovskites: Synthesis, optical properties, and solar cells of $(CH_3(CH_2)_3NH_3)_2(CH_3NH_3)_4Pb_5I_{16}$. *Chem* **2017**, 2 (3), 427-440.

23. Cao, D. H.; Stoumpos, C. C.; Yokoyama, T.; Logsdon, J. L.; Song, T.-B.; Farha, O. K.; Wasielewski, M. R.; Hupp, J. T.; Kanatzidis, M. G., Thin films and solar cells based on semiconducting two-dimensional Ruddlesden–Popper $(CH_3(CH_2)_3NH_3)_2(CH_3NH_3)_{n-1}Sn_nI_{3n+1}$ perovskites. *ACS Energy Lett.* **2017**, 2 (5), 982-990.

24. Smith, I. C.; Hoke, E. T.; Solis-Ibarra, D.; McGehee, M. D.; Karunadasa, H. I., A layered hybrid perovskite solar-cell absorber with enhanced moisture stability. *Angew. Chem.* **2014**, 126 (42), 11414-11417.

25. Cao, D. H.; Stoumpos, C. C.; Farha, O. K.; Hupp, J. T.; Kanatzidis, M. G., 2D homologous perovskites as light-absorbing materials for solar cell applications. *J. Am. Chem. Soc.* **2015**, 137 (24), 7843-7850.

26. Chen, Z.; Zhang, C.; Jiang, X. F.; Liu, M.; Xia, R.; Shi, T.; Chen, D.; Xue, Q.; Zhao, Y. J.; Su, S.; Yip, H. L.; Cao, Y., High-performance color-tunable perovskite light emitting devices through structural modulation from bulk to layered film. *Adv. Mater.* **2017**, 29 (8).

27. Cheng, L.; Cao, Y.; Ge, R.; Wei, Y.-Q.; Wang, N.-N.; Wang, J.-P.; Huang, W., Sky-blue perovskite light-emitting diodes based on quasi-two-dimensional layered perovskites. *Chin. Chem. Lett.* **2017**, 28 (1), 29-31.

28. Jia, G.; Shi, Z. J.; Xia, Y. D.; Wei, Q.; Chen, Y. H.; Xing, G. C.; Huang, W., Super air stable quasi-2D organic-inorganic hybrid perovskites for visible light-emitting diodes. *Opt. Express* **2018**, 26 (2), A66-A74.

29. Kumar, S.; Jagielski, J.; Kallikounis, N.; Kim, Y. H.; Wolf, C.; Jenny, F.; Tian, T.; Hofer, C. J.; Chiu, Y. C.; Stark, W. J.; Lee, T. W.; Shih, C. J., Ultrapure green light-emitting diodes using two-dimensional formamidinium perovskites: Achieving recommendation 2020 color coordinates. *Nano. Lett.* **2017**, 17 (9), 5277-5284.

30. Li, M.; Gao, Q.; Liu, P.; Liao, Q.; Zhang, H.; Yao, J.; Hu, W.; Wu, Y.; Fu, H., Amplified spontaneous emission based on 2D Ruddlesden-Popper perovskites. *Adv. Funct. Mater.* **2018**, 1707006.

31. Milot, R. L.; Sutton, R. J.; Eperon, G. E.; Haghighirad, A. A.; Martinez Hardigree, J.; Miranda, L.; Snaith, H. J.; Johnston, M. B.; Herz, L. M., Charge-carrier dynamics in 2d hybrid metal-halide perovskites. *Nano Lett.* **2016**, 16 (11), 7001-7007.

32. Peng, W.; Yin, J.; Ho, K. T.; Ouellette, O.; De Bastiani, M.; Murali, B.; El Tall, O.; Shen, C.; Miao, X.; Pan, J.; Alarousu, E.; He, J. H.; Ooi, B. S.; Mohammed, O. F.; Sargent, E.; Bakr, O. M., Ultralow self-doping in two-dimensional hybrid perovskite single crystals. *Nano Lett.* **2017**, 17 (8), 4759-4767.

33. Johnston, M. B.; Herz, L. M., Hybrid Perovskites for photovoltaics: Charge-carrier recombination, diffusion, and radiative efficiencies. *Acc. Chem. Res.* **2016**, 49 (1), 146-154.

34. Tsai, H.; Nie, W.; Blancon, J. C.; Stoumpos, C. C.; Asadpour, R.; Harutyunyan, B.; Neukirch, A. J.; Verduzco, R.; Crochet, J. J.; Tretiak, S.; Pedesseau, L.; Even, J.; Alam, M. A.; Gupta, G.; Lou, J.; Ajayan, P. M.; Bedzyk, M. J.; Kanatzidis, M. G., High-

efficiency two-dimensional Ruddlesden-Popper perovskite solar cells. *Nature* **2016**, 536 (7616), 312-316.

35.   Kagan, C. R., Organic-inorganic hybrid materials as semiconducting channels in thin-film field-effect transistors. *Science* **1999**, 286 (5441), 945-947.

36.   Cao, D. H.; Stoumpos, C. C.; Farha, O. K.; Hupp, J. T.; Kanatzidis, M. G., 2D homologous perovskites as light-absorbing materials for solar cell applications. *J. Am. Chem. Soc.* **2015**, 137 (24), 7843-7850.

37.   Noh, J. H.; Im, S. H.; Heo, J. H.; Mandal, T. N.; Seok, S. I., Chemical management for colorful, efficient, and stable inorganic-organic hybrid nanostructured solar cells. *Nano Lett.* **2013**, 13 (4), 1764-1769.

38.   Shang, Q.; Wang, Y.; Zhong, Y.; Mi, Y.; Qin, L.; Zhao, Y.; Qiu, X.; Liu, X.; Zhang, Q., Unveiling structurally engineered carrier dynamics in hybrid quasi-two-dimensional perovskite thin films toward controllable emission. *J. Phys. Chem. Lett.* **2017**, 8 (18), 4431-4438.

39.   Liu, J.; Leng, J.; Wu, K.; Zhang, J.; Jin, S., Observation of internal photoinduced electron and hole separation in hybrid two-dimentional perovskite films. *J. Am. Chem. Soc.* **2017**, 139 (4), 1432-1435.

40.   Yuan, M.; Quan, L. N.; Comin, R.; Walters, G.; Sabatini, R.; Voznyy, O.; Hoogland, S.; Zhao, Y.; Beauregard, E. M.; Kanjanaboos, P.; Lu, Z.; Kim, D. H.; Sargent, E. H., Perovskite energy funnels for efficient light-emitting diodes. *Nat. Nanotechnol.* **2016**, 11 (10), 872-877.

41.   Wang, N.; Cheng, L.; Ge, R.; Zhang, S.; Miao, Y.; Zou, W.; Yi, C.; Sun, Y.; Cao, Y.; Yang, R.; Wei, Y.; Guo, Q.; Ke, Y.; Yu, M.; Jin, Y.; Liu, Y.; Ding, Q.; Di, D.; Yang, L.; Xing, G.; Tian, H.; Jin, C.; Gao, F.; Friend, R. H.; Wang, J.; Huang, W., Perovskite light-emitting diodes based on solution-processed self-organized multiple quantum wells. *Nat. Photonics* **2016**, 10 (11), 699-704.

42.   Proppe, A. H.; Quintero-Bermudez, R.; Tan, H.; Voznyy, O.; Kelley, S. O.; Sargent, E. H., Synthetic control over quantum well width distribution and carrier migration in low-dimensional perovskite photovoltaics. *J. Am. Chem. Soc.* **2018**, 140 (8), 2890-2896.

43.   Quan, L. N.; Zhao, Y.; Garcia de Arquer, F. P.; Sabatini, R.; Walters, G.; Voznyy, O.; Comin, R.; Li, Y.; Fan, J. Z.; Tan, H.; Pan, J.; Yuan, M.; Bakr, O. M.; Lu, Z.; Kim, D. H.; Sargent, E. H., Tailoring the energy landscape in quasi-2D halide perovskites enables efficient green-light emission. *Nano Lett.* **2017**, 17 (6), 3701-3709.

44.   Williams, O. F.; Guo, Z.; Hu, J.; Yan, L.; You, W.; Moran, A. M., Energy transfer mechanisms in layered 2D perovskites. *J. Chem. Phys.* **2018**, 148 (13), 134706.

45.   Wang, R.; Ruzicka, B. A.; Kumar, N.; Bellus, M. Z.; Chiu, H.-Y.; Zhao, H., Ultrafast and spatially resolved studies of charge carriers in atomically thin molybdenum disulfide. *Phys. Rev. B* **2012**, 86 (4).

46.   Gabriel, M. M.; Grumstrup, E. M.; Kirschbrown, J. R.; Pinion, C. W.; Christesen, J. D.; Zigler, D. F.; Cating, E. E.; Cahoon, J. F.; Papanikolas, J. M., Imaging charge separation and carrier recombination in nanowire p-i-n junctions using ultrafast microscopy. *Nano Lett.* **2014**, 14 (6), 3079-3087.

47.   Shi, H.; Yan, R.; Bertolazzi, S.; Brivio, J.; Gao, B.; Kis, A.; Jena, D.; Xing, H. G.; Huang, L., Exciton dynamics in suspended monolayer and few-layer MoS_2 2D crystals. *ACS Nano* **2013**, 7 (2), 1072-1080.

48.   Wu, X.; Trinh, M. T.; Zhu, X. Y., Excitonic many-body interactions in two-dimensional lead iodide perovskite quantum wells. *J. Phys. Chem. C* **2015**, 119 (26), 14714-14721.

49.   Gauthron, K.; Lauret, J. S.; Doyennette, L.; Lanty, G.; Al Choueiry, A.; Zhang, S. J.; Brehier, A.; Largeau, L.; Mauguin, O.; Bloch, J.; Deleporte, E., Optical spectroscopy of two-dimensional layered $(C_6H_6C_2H_4-NH_3)_2-PbI_4$ perovskite. *Opt. Express* **2010**, 18 (6), 5912-5919.

50.   Tanino, H.; Rühle, W. W.; Takahashi, K., Time-resolved photoluminescence study of excitonic relaxation in one-dimensional systems. *Phys. Rev. B* 1988, 38 (17), 12716-12719.

51.   Dohner, E. R.; Jaffe, A.; Bradshaw, L. R.; Karunadasa, H. I., Intrinsic white-light emission from layered hybrid perovskites. *J. Am. Chem. Soc.* **2014**, 136 (38), 13154-13157.

Figure A1. *Fenyman diagrams associated with dominant 2DRR nonlinearities. Blue and red arrows represent pulses resonant with triiodide and diiodide, respectively. The indices r and $r*$ represent the ground and excited electronic states of the triiodide reactant, whereas p and $p*$ correspond to the diiodide photoproduct. Vibrational levels associated with these electronic states are specified by dummy indices (m, n, j, k, l, u, v, w). Each row represents a different class of terms: (i) both dimensions correspond to triiodide in terms 1-4; (ii) both dimensions correspond to diiodide in terms 5-8; (iii) vibrational resonances of triiodide and diiodide appear in separate dimensions in terms 9-12. The intervals shaded in blue represent a non-radiative transfer of vibronic coherence from triiodide to diiodide.*

A.1. Derivation of Formula for the Two-Dimensional Resonance Raman Signal Field

The Feynman diagrams presented in Figure A1 include dummy indices for vibrational levels (m, n, j, k, l, u, v, w) associated with the ground and excited electronic states of the reactant (r and r^*) and product (p and p^*). Response functions are written in the Condon approximation, where the integral over electronic and nuclear degrees of freedom in the transition dipole is separated into a product of integrals. For example, an interaction that couples vibrational level m in the ground electronic state of the reactant and vibrational level n in the excited electronic state contributes the product, $\mu_{r^*r} \langle n|m \rangle$, to the response function, where μ_{r^*r} is the electronic transition dipole of the reactant and $\langle n|m \rangle$ is a vibrational overlap integral. We use a notation in which the index for the excited state vibrational energy level is always written in the bra.[1]

Under the assumption that the photodissociation time scale is short compared to the vibrational period, the time interval, t_{PD}, can be eliminated from consideration. The response functions corresponding to the fifth-order diagrams in Figure A1 can then be written as

$$R_1^{(5)}(t_1, t_2, t_3, t_4, t_5) = |\mu_{r^*r}|^6 \sum_{mnjklu} B_m \langle n|m \rangle \langle n|j \rangle \langle k|j \rangle \langle k|l \rangle \langle u|l \rangle \langle u|m \rangle L_{r^*n,rm}(t_1)$$
$$\times L_{rj,rm}(t_2) L_{r^*k,rm}(t_3) L_{rl,rm}(t_4) L_{r^*u,rm}(t_5) \tag{A1}$$

$$R_2^{(5)}(t_1, t_2, t_3, t_4, t_5) = |\mu_{r^*r}|^6 \sum_{mnjklu} B_m \langle n|m \rangle \langle n|j \rangle \langle k|m \rangle \langle k|l \rangle \langle u|j \rangle \langle u|l \rangle L_{r^*n,rm}(t_1)$$
$$\times L_{rj,rm}(t_2) L_{rj,r^*k}(t_3) L_{rj,rl}(t_4) L_{r^*u,rl}(t_5) \tag{A2}$$

$$R_3^{(5)}(t_1, t_2, t_3, t_4, t_5) = |\mu_{r^*r}|^6 \sum_{mnjklu} B_m \langle n|m \rangle \langle n|j \rangle \langle k|j \rangle \langle k|l \rangle \langle u|m \rangle \langle u|l \rangle L_{rm,r^*n}(t_1)$$
$$\times L_{rm,rj}(t_2) L_{rm,r^*k}(t_3) L_{rm,rl}(t_4) L_{r^*u,rl}(t_5) \tag{A3}$$

$$R_4^{(5)}\left(t_1,t_2,t_3,t_4,t_5\right)=\left|\mu_{r*r}\right|^6\sum_{mnjklu}B_m\left\langle n|m\right\rangle\left\langle n|j\right\rangle\left\langle k|m\right\rangle\left\langle k|l\right\rangle\left\langle u|l\right\rangle\left\langle u|j\right\rangle L_{rm,r*n}\left(t_1\right)$$
$$\times L_{rm,rj}\left(t_2\right)L_{r*k,rj}\left(t_3\right)L_{rl,rj}\left(t_4\right)L_{r*u,rj}\left(t_5\right) \tag{A4}$$

$$R_5^{(5)}\left(t_1,t_2,t_3,t_4,t_5\right)=\left|\mu_{r*r}\right|^2\left|\mu_{p*p}\right|^4\sum_{mnjkluvw}B_m\left\langle n|m\right\rangle\left\langle j|m\right\rangle\left\langle u|k\right\rangle\left\langle u|v\right\rangle\left\langle w|v\right\rangle\left\langle w|l\right\rangle$$
$$\times L_{r*n,rm}\left(t_1\right)L_{pk,pl}\left(t_2\right)L_{p*u,pl}\left(t_3\right)L_{pv,pl}\left(t_4\right)L_{p*w,pl}\left(t_5\right) \tag{A5}$$

$$R_6^{(5)}\left(t_1,t_2,t_3,t_4,t_5\right)=\left|\mu_{r*r}\right|^2\left|\mu_{p*p}\right|^4\sum_{mnjkluvw}B_m\left\langle n|m\right\rangle\left\langle j|m\right\rangle\left\langle u|k\right\rangle\left\langle u|v\right\rangle\left\langle w|v\right\rangle\left\langle w|l\right\rangle$$
$$\times L_{rm,r*n}\left(t_1\right)L_{pk,pl}\left(t_2\right)L_{p*u,pl}\left(t_3\right)L_{pv,pl}\left(t_4\right)L_{p*w,pl}\left(t_5\right) \tag{A6}$$

$$R_7^{(5)}\left(t_1,t_2,t_3,t_4,t_5\right)=\left|\mu_{r*r}\right|^2\left|\mu_{p*p}\right|^4\sum_{mnjkluvw}B_m\left\langle n|m\right\rangle\left\langle j|m\right\rangle\left\langle u|l\right\rangle\left\langle u|v\right\rangle\left\langle w|k\right\rangle\left\langle w|v\right\rangle$$
$$\times L_{r*n,rm}\left(t_1\right)L_{pk,pl}\left(t_2\right)L_{pk,p*u}\left(t_3\right)L_{pk,pv}\left(t_4\right)L_{p*w,pv}\left(t_5\right) \tag{A7}$$

$$R_8^{(5)}\left(t_1,t_2,t_3,t_4,t_5\right)=\left|\mu_{r*r}\right|^2\left|\mu_{p*p}\right|^4\sum_{mnjkluvw}B_m\left\langle n|m\right\rangle\left\langle j|m\right\rangle\left\langle u|l\right\rangle\left\langle u|v\right\rangle\left\langle w|k\right\rangle\left\langle w|v\right\rangle$$
$$\times L_{rm,r*n}\left(t_1\right)L_{pk,pl}\left(t_2\right)L_{pk,p*u}\left(t_3\right)L_{pk,pv}\left(t_4\right)L_{p*w,pv}\left(t_5\right) \tag{A8}$$

$$R_9^{(5)}\left(t_1,t_2,t_3,t_4,t_5\right)=\left|\mu_{r*r}\right|^2\left|\mu_{p*p}\right|^2\sum_{mnjkluvw}B_m\left\langle n|m\right\rangle\left\langle n|j\right\rangle\left\langle k|j\right\rangle\left\langle l|m\right\rangle\left\langle w|u\right\rangle\left\langle w|v\right\rangle$$
$$\times L_{r*n,rm}\left(t_1\right)L_{rj,rm}\left(t_2\right)L_{r*k,rm}\left(t_3\right)L_{pu,pv}\left(t_4\right)L_{p*w,pv}\left(t_5\right) \tag{A9}$$

$$R_{10}^{(5)}\left(t_1,t_2,t_3,t_4,t_5\right)=\left|\mu_{r*r}\right|^4\left|\mu_{p*p}\right|^2\sum_{mnjkluvw}B_m\left\langle n|m\right\rangle\left\langle n|j\right\rangle\left\langle k|m\right\rangle\left\langle l|j\right\rangle\left\langle w|u\right\rangle\left\langle w|v\right\rangle$$
$$\times L_{rm,r*n}\left(t_1\right)L_{rm,rj}\left(t_2\right)L_{r*k,rj}\left(t_3\right)L_{pu,pv}\left(t_4\right)L_{p*w,pv}\left(t_5\right) \tag{A10}$$

$$R_{11}^{(5)}\left(t_1,t_2,t_3,t_4,t_5\right)=\left|\mu_{r*r}\right|^4\left|\mu_{p*p}\right|^2\sum_{mnjkluvw}B_m\left\langle n|m\right\rangle\left\langle n|j\right\rangle\left\langle k|m\right\rangle\left\langle l|j\right\rangle\left\langle w|u\right\rangle\left\langle w|v\right\rangle$$
$$\times L_{r*n,rm}\left(t_1\right)L_{rj,rm}\left(t_2\right)L_{rj,r*k}\left(t_3\right)L_{pu,pv}\left(t_4\right)L_{p*w,pv}\left(t_5\right) \tag{A11}$$

$$R_{12}^{(5)}\left(t_1,t_2,t_3,t_4,t_5\right)=\left|\mu_{r*r}\right|^4\left|\mu_{p*p}\right|^2\sum_{mnjkluvw}B_m\left\langle n|m\right\rangle\left\langle n|j\right\rangle\left\langle k|j\right\rangle\left\langle l|m\right\rangle\left\langle w|u\right\rangle\left\langle w|v\right\rangle$$
$$\times L_{rm,r*n}\left(t_1\right)L_{rm,rj}\left(t_2\right)L_{rm,r*k}\left(t_3\right)L_{pu,pv}\left(t_4\right)L_{p*w,pv}\left(t_5\right) \tag{A12}$$

In the above equations, the propagation functions corresponding to vibronic (in t_1, t_3, or t_5) and

purely vibrational (in t_2 or t_4) coherences are respectively given by[2]

$$L_{r*m,rn}(t) = \theta(t)\exp\left(-i\omega_{r*r}t - i\omega_{mn}t - \Gamma_{r*r}t\right) \qquad (A13)$$

and

$$L_{rm,rn}(t) = \theta(t)\exp\left(-i\omega_{mn}t - \Gamma_{vib}t\right) , \qquad (A14)$$

where $\theta(t)$ is a Heaviside step function. It is assumed in Equation (A13) that electronic

dephasing is much faster than vibrational dephasing (i.e., $\Gamma_{r*r} >> \Gamma_{vib}$).

We next obtain the 12 components of the fifth-order polarization by convoluting the

response functions with the external electric fields. The component of the fifth-order polarization

corresponding to the R_1 term is given by

$$P_1^{(5)}(t) = N\left(\frac{i}{\hbar}\right)^5 \int_0^\infty dt_5 \int_0^\infty dt_4 \int_0^\infty dt_3 \int_0^\infty dt_2 \int_0^\infty dt_1 R_1^{(5)}\left(t_1,t_2,t_3,t_4,t_5\right) E_{UV}(t-t_5)E_{UV}^*(t+\tau_2-t_5-t_4)$$

$$E_{UV}(t+\tau_2-t_5-t_4-t_3)E_{UV}^*(t+\tau_1+\tau_2-t_5-t_4-t_3-t_2) \qquad \qquad , (A15)$$

$$E_{UV}(t+\tau_1+\tau_2-t_5-t_4-t_3-t_2-t_1)$$

where N is the number density and τ_j are the pulse delay times defined in the manuscript.

Pulses with the subscripts *UV* and *VIS* are taken to interact with triiodide and diiodide,

respectively. Attainment of analytic expressions is facilitated by use of double-sided exponential

electric field envelopes,

$$E_j(t) = \xi_j \exp\left(-i\omega_j t - \Lambda_j |t|\right) , \qquad (A16)$$

where ξ_j is the (real) electric field amplitude, Λ_j is the HWHM spectral width, and ω_j is the

carrier frequency of the laser pulse (the index, j, signifies either the "pump" or "probe"), which

we take to be resonant with the triiodide reactant. The polarization component, $P_1^{(5)}(t)$, can now

be rewritten as

$$P_1^{(5)}(t) = N\xi_{UV}^5 \exp(-i\omega_{UV}t)\left(\frac{i}{\hbar}\right)^5 \int_0^\infty dt_5 \int_0^\infty dt_4 \int_0^\infty dt_3 \int_0^\infty dt_2 \int_0^\infty dt_1 R_1^{(5)}(t_1,t_2,t_3,t_4,t_5)$$

$$\times \exp\left[i\omega_{UV}t_1 + i\omega_{UV}t_3 + i\omega_{UV}t_5\right]$$

$$\times \exp\left[-\Lambda_{UV}\left|t - t_5\right| - \Lambda_{UV}\left|t + \tau_2 - t_5 - t_4\right| - \Lambda_{UV}\left|t + \tau_2 - t_5 - t_4 - t_3\right|\right]$$

$$\times \exp\left[-\Lambda_{UV}\left|t + \tau_1 + \tau_2 - t_5 - t_4 - t_3 - t_2\right| - \Lambda_{UV}\left|t + \tau_1 + \tau_2 - t_5 - t_4 - t_3 - t_2 - t_1\right|\right]$$

(A17)

We use a "doorway wavepacket" to filter vibrational coherences with frequencies that exceed the bandwidth of the pump pulse.[2] To this end, we introduce the change of variables, $t' = t + \tau_1 - t_2$ and $t'' = t + \tau_2 - t_4$. The polarization component is then given by

$$P_1^{(5)}(t) = N\xi_{UV}^5 \left(\frac{i}{\hbar}\right)^5 \int_0^\infty dt_5 \int_{-\infty}^\infty dt'' \int_0^\infty dt_3 \int_{-\infty}^\infty dt' \int_0^\infty dt_1 R_1^{(5)}\left(t_1, t + \tau_1 - t', t_3, t + \tau_2 - t'', t_5\right)$$

$$\times \exp\left[i\omega_{UV}t_1 + i\omega_{UV}t_3 + i\omega_{UV}t_5 - i\omega_{UV}t\right]$$

$$\times \exp\left[-2\Lambda_{UV}\left|t''\right| - 2\Lambda_{UV}\left|t'\right|\right]$$

(A18)

Here, we have assumed that (i) $t_2 \approx \tau_1$ in order to carry out the integral over t' and (ii) the pulse durations are short compared to the delay times to make the upper limits of the integrals over t' and t'' infinite. The time intervals, t_1, t_3, and t_5, have also been removed from the arguments of the laser pulses under the assumption that the pulse durations are long compared to the electronic dephasing time. We next introduce the approximation, $t = t_5$,

$$P_1^{(5)}(\omega_1, \omega_2) = N\xi_{UV}^5 \left(\frac{i}{\hbar}\right)^5 \int_0^\infty dt \int_0^\infty d\tau_2 \int_0^\infty d\tau_1 \int_{-\infty}^\infty dt'' \int_0^\infty dt_3 \int_{-\infty}^\infty dt' \int_0^\infty dt_1 R_1^{(5)}\left(t_1, \tau_1 - t', t_3, \tau_2 - t'', t\right)$$

$$\times \exp\left[i\omega_{UV}t_1 + i\omega_{UV}t_3 + i\omega_1\tau_1 + i\omega_2\tau_2 + i\omega_t t - 2\Lambda_{UV}\left|t''\right| - 2\Lambda_{UV}\left|t'\right|\right]$$

(A19)

and Fourier transform the expression with respect to τ_1, τ_2, and t. Evaluation of the seven integrals in Equation (A19) yields

$$P_1^{(5)}(\omega_1,\omega_2) = -\frac{N\xi_{UV}^5 |\mu_{r*r}|^6}{\hbar^5} \sum_{mnjklu} B_m \langle n|m\rangle\langle n|j\rangle\langle k|j\rangle\langle k|l\rangle\langle u|l\rangle\langle u|m\rangle,$$
$$\times L_{r*n,rm}(\omega_{UV}) D_{rj,rm}(\omega_1) L_{r*k,rm}(\omega_{UV}) D_{rl,rm}(\omega_2) L_{r*u,rm}(\omega_t) \tag{A20}$$

where the line shape of the electronic resonance is given by

$$L_{r*n,rm}(\omega) = -i \int_0^\infty L_{r*n,rm}(t) \exp(i\omega t) dt = \frac{1}{\omega - \omega_{r*r} - \omega_{nm} + i\Gamma_{r*r}}. \tag{A21}$$

The spectroscopic line shape associated with the doorway wavepacket is written as

$$D_{rk,rm}(\omega) = -i \int_{-\infty}^\infty dt \exp\left(i\omega_{km}t - \Gamma_{vib}|t| - 2\Lambda_{UV}|t|\right) \int_0^\infty dt L_{rk,rm}(\tau) \exp(i\omega\tau)$$
$$= \frac{2\Gamma_{vib} + 4\Lambda_{UV}}{\omega_{km}^2 + \left(\Gamma_{vib} + 2\Lambda_{UV}\right)^2} \left(\frac{1}{\omega - \omega_{km} + i\Gamma_{vib}}\right) \tag{A22}$$

We obtain the following 11 polarization components by following the same procedure

$$P_2^{(5)}(\omega_1,\omega_2) = -\frac{N\xi_{UV}^5 |\mu_{r*r}|^6}{\hbar^5} \sum_{mnjklu} B_m \langle n|m\rangle\langle n|j\rangle\langle k|m\rangle\langle k|l\rangle\langle u|j\rangle\langle u|l\rangle,$$
$$\times L_{r*n,rm}(\omega_{UV}) D_{rj,rm}(\omega_1) L_{rj,r*k}(-\omega_{UV}) D_{rj,rl}(\omega_2) L_{r*u,rl}(\omega_t) \tag{A23}$$

$$P_3^{(5)}(\omega_1,\omega_2) = -\frac{N\xi_{UV}^5 |\mu_{r*r}|^6}{\hbar^5} \sum_{mnjklu} B_m \langle n|m\rangle\langle n|j\rangle\langle k|j\rangle\langle k|l\rangle\langle u|m\rangle\langle u|l\rangle,$$
$$\times L_{rm,r*n}(-\omega_{UV}) D_{rm,rj}(\omega_1) L_{rm,r*k}(-\omega_{UV}) D_{rm,rl}(\omega_2) L_{r*u,rl}(\omega_t) \tag{A24}$$

$$P_4^{(5)}(\omega_1,\omega_2) = -\frac{N\xi_{UV}^5 |\mu_{r*r}|^6}{\hbar^5} \sum_{mnjklu} B_m \langle n|m\rangle\langle n|j\rangle\langle k|m\rangle\langle k|l\rangle\langle u|l\rangle\langle u|j\rangle,$$
$$\times L_{rm,r*n}(-\omega_{UV}) D_{rm,rj}(\omega_1) L_{r*k,rj}(\omega_{UV}) D_{rl,rj}(\omega_2) L_{r*u,rj}(\omega_t) \tag{A25}$$

$$P_5^{(5)}(\omega_1,\omega_2) = -\frac{N\xi_{UV}^2 \xi_{VIS}^3 |\mu_{r*r}|^2 |\mu_{p*p}|^4}{\hbar^5} \sum_{mnjkluvw} B_m \langle n|m\rangle\langle j|m\rangle\langle u|k\rangle\langle u|v\rangle\langle w|v\rangle\langle w|l\rangle,$$
$$\times L_{r*n,rm}(\omega_{UV}) D_{pk,pl}(\omega_1) L_{p*u,pl}(\omega_{VIS}) D_{pv,pl}(\omega_2) L_{p*w,pl}(\omega_t) \tag{A26}$$

$$P_6^{(5)}(\omega_1,\omega_2) = -\frac{N\xi_{UV}^2\xi_{VIS}^3\left|\mu_{r*r}\right|^2\left|\mu_{p*p}\right|^4}{\hbar^5}\sum_{mnjkluvw}B_m\langle n|m\rangle\langle j|m\rangle\langle u|k\rangle\langle u|v\rangle\langle w|v\rangle\langle w|l\rangle,$$
$$\times L_{rm,r*n}(-\omega_{UV})D_{pk,pl}(\omega_1)L_{p*u,pl}(\omega_{VIS})D_{pv,pl}(\omega_2)L_{p*w,pl}(\omega_t)$$
(A27)

$$P_7^{(5)}(\omega_1,\omega_2) = -\frac{N\xi_{UV}^2\xi_{VIS}^3\left|\mu_{r*r}\right|^2\left|\mu_{p*p}\right|^4}{\hbar^5}\sum_{mnjkluvw}B_m\langle n|m\rangle\langle j|m\rangle\langle u|l\rangle\langle u|v\rangle\langle w|k\rangle\langle w|v\rangle,$$
$$\times L_{r*n,rm}(\omega_{UV})D_{pk,pl}(\omega_1)L_{pk,p*u}(-\omega_{VIS})D_{pk,pv}(\omega_2)L_{p*w,pv}(\omega_t)$$
(A28)

$$P_8^{(5)}(\omega_1,\omega_2) = -\frac{N\xi_{UV}^2\xi_{VIS}^3\left|\mu_{r*r}\right|^2\left|\mu_{p*p}\right|^4}{\hbar^5}\sum_{mnjkluvw}B_m\langle n|m\rangle\langle j|m\rangle\langle u|l\rangle\langle u|v\rangle\langle w|k\rangle\langle w|v\rangle,$$
$$\times L_{rm,r*n}(-\omega_{UV})D_{pk,pl}(\omega_1)L_{pk,p*u}(-\omega_{VIS})D_{pk,pv}(\omega_2)L_{p*w,pv}(\omega_t)$$
(A29)

$$P_9^{(5)}(\omega_1,\omega_2) = -\frac{N\xi_{UV}^4\xi_{VIS}\left|\mu_{r*r}\right|^4\left|\mu_{p*p}\right|^2}{\hbar^5}\sum_{mnjkluvw}B_m\langle n|m\rangle\langle n|j\rangle\langle k|j\rangle\langle l|m\rangle\langle w|u\rangle\langle w|v\rangle,$$
$$\times L_{r*n,rm}(\omega_{UV})D_{rj,rm}(\omega_1)L_{r*k,rm}(\omega_{UV})D_{pu,pv}(\omega_2)L_{p*w,pv}(\omega_t)$$
(A30)

$$P_{10}^{(5)}(\omega_1,\omega_2) = -\frac{N\xi_{UV}^4\xi_{VIS}\left|\mu_{r*r}\right|^4\left|\mu_{p*p}\right|^2}{\hbar^5}\sum_{mnjkluvw}B_m\langle n|m\rangle\langle n|j\rangle\langle k|m\rangle\langle l|j\rangle\langle w|u\rangle\langle w|v\rangle,$$
$$\times L_{rm,r*n}(-\omega_{UV})D_{rm,rj}(\omega_1)L_{r*k,rj}(\omega_{UV})D_{pu,pv}(\omega_2)L_{p*w,pv}(\omega_t)$$
(A31)

$$P_{11}^{(5)}(\omega_1,\omega_2) = -\frac{N\xi_{UV}^4\xi_{VIS}\left|\mu_{r*r}\right|^4\left|\mu_{p*p}\right|^2}{\hbar^5}\sum_{mnjkluvw}B_m\langle n|m\rangle\langle n|j\rangle\langle k|m\rangle\langle l|j\rangle\langle w|u\rangle\langle w|v\rangle,$$
$$\times L_{r*n,rm}(\omega_{UV})D_{rj,rm}(\omega_1)L_{rj,r*k}(-\omega_{UV})D_{pu,pv}(\omega_2)L_{p*w,pv}(\omega_t)$$
(A32)

$$P_{12}^{(5)}(\omega_1,\omega_2) = -\frac{N\xi_{UV}^4\xi_{VIS}\left|\mu_{r*r}\right|^4\left|\mu_{p*p}\right|^2}{\hbar^5}\sum_{mnjkluvw}B_m\langle n|m\rangle\langle n|j\rangle\langle k|j\rangle\langle l|m\rangle\langle w|u\rangle\langle w|v\rangle.$$
$$\times L_{rm,r*n}(-\omega_{UV})D_{rm,rj}(\omega_1)L_{rm,r*k}(-\omega_{UV})D_{pu,pv}(\omega_2)L_{p*w,pv}(\omega_t)$$
(A33)

A.2. Dominance of the Direct 2DRR Response Over Third-Order Cascades

Fifth-order coherent Raman spectroscopies conducted under off-resonant conditions are susceptible to artifacts known as cascades.[3-7] A cascade is a sequence in which the four-wave mixing signal field generated by one molecule induces a four-wave mixing response on a second molecule. The second molecule then radiates a signal field in the same direction as the fifth-order signal of interest. Cascades are problematic under off-resonant conditions, because they can be many orders of magnitude more intense than the direct fifth-order response. It is thought that selection rules primarily govern this mismatch in signal intensities.[7-9] That is, two-quantum transitions involved in the direct fifth-order process are forbidden in harmonic systems when the polarizability scales linearly in the vibrational coordinate. In contrast, third-order cascades are allowed in harmonic systems, which gives them a significant advantage over the fifth-order process. Cascades require this difference in selection rules to dominate over the direct fifth-order response, because they are higher-order in the sense that they involve two more field-matter interactions than the direct process (i.e., this extra factor of the polarizability operator suppresses the relative intensity of the cascaded response).

Cascades were ruled out in our previous all-UV 2DRR study of triiodide using control experiments based on the signal phase, concentration dependence of the signal intensity, and the relative phases of the vibrations detected in four and six-wave mixing signals.[8] The direct 2DRR response should be even more dominant in the present study because lower-frequency laser beams are employed. Moreover, the direct response is favored in the present experiments for the same reasons discussed at length in Reference [8]. In pump-repump-probe experiments, inspection of the signal phase is a particularly convenient way to check for cascades, because third and fifth-order signals possess a readily detected sign difference.[4-5] In contrast, cascades have the same sign as the direct third-order response. To illustrate this point, we present (third-order)

pump-probe and (fifth-order) pump-repump-probe signals acquired for triiodide in Figure A2. The two signals have opposite signs as expected for the direct response. Compared to the all-UV approach taken in Reference [8], the phase difference for vibrational motion is not as straightforward to predict in the present two-color experiments because of sensitivity to the complex photodissociation process. Nonetheless, in Figure A2b, we compare the third-order signal to a slice of the fifth-order signal in τ_2 (at $\tau_1=0$) at a signal detection wavenumber of 20,000 cm^{-1} (500 nm). The analysis carried out in Reference [8] suggests that a phase shift near 180° is expected for the direct fifth-order response under these conditions. This prediction is consistent with the measurement shown in Figure A2b.

Our work suggests that contributions from cascades will generally be negligible in systems such as triiodide, where the excited state potential energy surface displacement is extremely large.[8] In essence, Franck-Condon activity eliminates the problematic selection rules found under off-resonant conditions (see Figure 14 in Reference [8]). We emphasize that the direct response is not necessarily predicted to dominate in systems with modest mode displacements (i.e., dimensionless displacements below 1), which are typically found in larger molecules. However, in a recent study of metmyoglobin, we still found that the direct fifth-order nonlinearity is at least 10 times larger than the cascaded response in dilute solution.[10] It is worth noting that experiments in which the final four field-matter interactions are off-resonant with the equilibrium system are much less susceptible to cascades than our earlier all-resonant approaches.[8, 10] In such a two-color configuration, the fifth-order response will be fully (electronically) resonant, whereas one of the four-wave mixing responses involved in a cascade must be (electronically) off-resonant (see Figure 3.7 and terms 5-8 in Figure 3.2 of in Chapter 3 of this dissertation). Pulse sequences in which the final four field-matter interactions are off-

resonant with the equilibrium system are typically used in other types of optical pump-Raman probe experiments.[11-16]
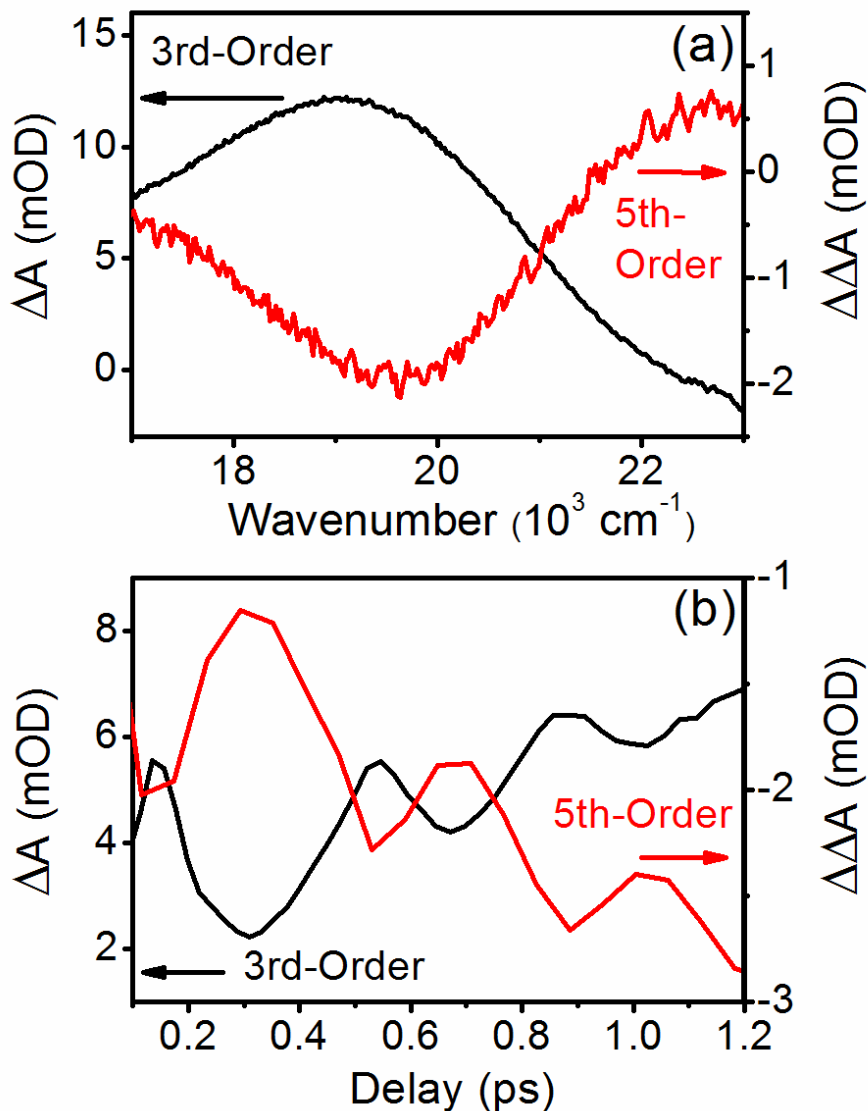
Figure A2. *Comparison of signal phases obtained for third-order (pump-probe) and fifth-order (pump-repump-probe) signals. (a) Pump-probe (delay of 0.5 ps) and pump-repump-probe ($\tau_1 = \tau_2 = 0.5$ ps) signals have similar line shapes but opposite signs. This sign-difference suggests that the pump-repump-probe signal is dominated by the desired fifth-order nonlinearity (i.e., not third-order cascades). (b) Oscillations in pump-probe and pump-repump-probe signals are compared with signal detection at 20,000 cm^{-1} (500 nm). This is a slice of the pump-repump-probe signal in τ_2 with the delay, τ_1, fixed at 0 ps. A relative phase-shift near 180º suggests that the oscillatory component of the pump-repump-probe signal is dominated by the direct fifth order nonlinearity.[8]*

REFERENCES

1. Myers, A. B.; Mathies, R. A.; Tannor, D. J.; Heller, E. J., Excited State Geometry Changes from Preresonance Raman Intensities: Isoprene and Hexatriene. *J. Chem. Phys.* **1982,** *77*, 3857-3866.

2. Mukamel, S., *Principles of Nonlinear Optical Spectroscopy*. Oxford University Press: New York, 1995.

3. Ivanecky III, J. E.; Wright, J. C., An investigation of the origins and efficiencies of higher-order nonlinear spectroscopic processes *Chem. Phys. Lett.* **1993,** *206*, 437-444.

4. Blank, D. A.; Kaufman, L. J.; Fleming, G. R., Fifth-order two-dimensional Raman spectra of CS_2 are dominated by third-order cascades *J. Chem. Phys.* **1999,** *111*, 3105-3114.

5. Kubarych, K. J.; Milne, C. J.; Lin, S.; Astinov, V.; Miller, R. J. D., Diffractive optics-based six-wave mixing: Heterodyne detection of the full $\chi^{(5)}$ tensor of liquid CS_2. *J. Chem. Phys.* **2002,** *116*, 2016-2042.

6. Wilson, K. C.; Lyons, B.; Mehlenbacher, R.; Sabatini, R.; McCamant, D. W., Two-dimensional femtosecond stimulated Raman spectroscopy: Observation of cascading Raman signals in acetonitrile *J. Chem. Phys.* **2009,** *131*, 214502.

7. Ulness, D. J.; Kirkwood, J. C.; Albrecht, A. C., Competitive events in fifth order time resolved coherent raman scattering: Direct versus sequential processes. *J. Chem. Phys.* **1998,** *108*, 3897-3902.

8. Molesky, B. P.; Giokas, P. G.; Guo, Z.; Moran, A. M., Multidimensional resonance Raman spectroscopy by six-wave mixing in the deep UV. *J. Chem. Phys.* **2014,** *114*, 114202.

9. Garret-Roe, S.; Hamm, P., Purely absorptive three-dimensional infrared spectroscopy *J. Chem. Phys.* **2009,** *130*, 164510.

10. Molesky, B. P.; Guo, Z.; Moran, A. M., Femtosecond stimulated Raman spectroscopy by six-wave mixing. *J. Chem. Phys.* **2015,** *142*, 212405.

11. Underwood, D. F.; Blank, D. A., Measuring the change in the intermolecular raman spectrum during dipolar solvation. *J. Phys. Chem. A* **2005,** *109*, 3295-3306.

12. Moran, A. M.; Nome, R. A.; Scherer, N. F., Field-resolved measurement of reaction-induced spectral densities by polarizability response spectroscopy. *J. Chem. Phys.* **2007,** *127*, 184505.

13. Marek, M. S.; Buckup, T.; Motzkus, M., Direct observation of a dark state in lycopene using pump-DFWM. *J. Phys. Chem. B* **2011,** *115*, 8328-8337.

14.   Rhinehart, J. M.; Challa, J. R.; McCamant, D. W., Multimode charge-transfer dynamics of 4-(dimethylamino)benzonitrile probed with ultraviolet femtosecond stimulated Raman spectroscopy. *J. Phys. Chem. B* **2012,** *116*, 10522-10534.

15.   Wang, Y.; Liu, W.; Tang, L.; Oscar, B.; Han, F.; Fang, C., Early time excited-state structural evolution of pyranine in methanol revealed by femtosecond stimulated Raman spectroscopy. *J. Phys. Chem. A* **2013,** *117*, 6024-6042.

16.   Valley, D. T.; Hoffman, D. P.; Mathies, R. A., Reactive and unreactive pathways in a photochemical ring opening reaction from 2D femtosecond stimulated Raman. *Phys. Chem. Chem. Phys.* **2015,** *17*, 9231-9240.
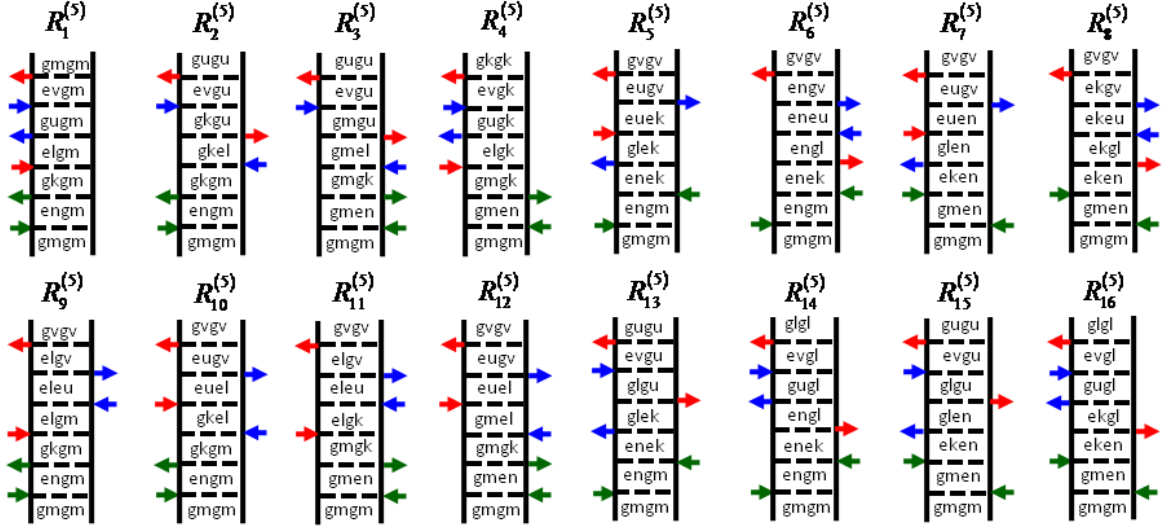
Figure B1. *Feynman diagrams associated with the direct fifth-order response. The indices, g and e, represent the ground and excited electronic states, whereas dummy indices (m, n, k, l, u, and v) denote vibrational levels. Green, blue, and red arrows represent the actinic pump, Raman pump, and Stokes pulses, respectively. We restrict the response function to these 16 terms under the assumption that the signal is primarily resonance-enhanced by the Soret band.*

B.1. Derivation of Formula for Direct Fifth-Order Signal Field

Here, we obtain formulas that can be used to compute the relative magnitudes of cascaded third-order and direct fifth-order signal fields. The Feynman diagrams presented in Figure B1 include dummy indices for vibrational levels (m, n, k, l, u, and v) associated with the ground and excited electronic states (g and e). Response functions are written in the Condon approximation, where the integral over electronic and nuclear degrees of freedom in the transition dipole is separated into a product of integrals. For example, an interaction that couples vibrational level m in the ground electronic state and vibrational level n in the excited electronic state contributes the product, $\mu_{eg} \langle n|m \rangle$, to the response function, where μ_{eg} is the electronic transition dipole and $\langle n|m \rangle$ is a vibrational overlap integral. We use a notation in which the excited state vibrational energy level is always written in the bra.[1]

The response functions corresponding to the fifth-order diagrams in Figure B1 can be written as

$$R_1^{(5)}\left(t_1,t_2,t_3,t_4,t_5\right)=\left|\mu_{eg}\right|^6\sum_{mnkluv}B_m\left\langle n|m\right\rangle\left\langle n|k\right\rangle\left\langle l|k\right\rangle\left\langle l|u\right\rangle\left\langle v|u\right\rangle\left\langle v|m\right\rangle L_{en,gm}\left(t_1\right)$$
$$\times L_{gk,gm}\left(t_2\right)L_{el,gm}\left(t_3\right)L_{gu,gm}\left(t_4\right)L_{ev,gm}\left(t_5\right) \quad\quad (B1)$$

$$R_2^{(5)}\left(t_1,t_2,t_3,t_4,t_5\right)=\left|\mu_{eg}\right|^6\sum_{mnkluv}B_m\left\langle n|m\right\rangle\left\langle n|k\right\rangle\left\langle l|m\right\rangle\left\langle l|u\right\rangle\left\langle v|k\right\rangle\left\langle v|u\right\rangle L_{en,gm}\left(t_1\right)$$
$$\times L_{gk,gm}\left(t_2\right)L_{gk,el}\left(t_3\right)L_{gk,gu}\left(t_4\right)L_{ev,gu}\left(t_5\right) \quad\quad (B2)$$

$$R_3^{(5)}\left(t_1,t_2,t_3,t_4,t_5\right)=\left|\mu_{eg}\right|^6\sum_{mnkluv}B_m\left\langle n|m\right\rangle\left\langle n|k\right\rangle\left\langle l|k\right\rangle\left\langle l|u\right\rangle\left\langle v|m\right\rangle\left\langle v|u\right\rangle L_{gm,en}\left(t_1\right)$$
$$\times L_{gm,gk}\left(t_2\right)L_{gm,el}\left(t_3\right)L_{gm,gu}\left(t_4\right)L_{ev,gu}\left(t_5\right) \quad\quad (B3)$$

$$R_4^{(5)}\left(t_1,t_2,t_3,t_4,t_5\right)=\left|\mu_{eg}\right|^6\sum_{mnkluv}B_m\left\langle n|m\right\rangle\left\langle n|k\right\rangle\left\langle l|m\right\rangle\left\langle l|u\right\rangle\left\langle v|u\right\rangle\left\langle v|k\right\rangle L_{gm,en}\left(t_1\right)$$
$$\times L_{gm,gk}\left(t_2\right)L_{el,gk}\left(t_3\right)L_{gu,gk}\left(t_4\right)L_{ev,gk}\left(t_5\right) \quad\quad (B4)$$

$$R_5^{(5)}\left(t_1,t_2,t_3,t_4,t_5\right)=\left|\mu_{eg}\right|^6\sum_{mnkluv}B_m\left\langle n|m\right\rangle\left\langle k|m\right\rangle\left\langle n|l\right\rangle\left\langle u|l\right\rangle\left\langle k|v\right\rangle\left\langle u|v\right\rangle L_{en,gm}\left(t_1\right)$$
$$\times L_{en,ek}\left(t_2\right)L_{gl,ek}\left(t_3\right)L_{eu,ek}\left(t_4\right)L_{eu,gv}\left(t_5\right) \quad\quad (B5)$$

$$R_6^{(5)}\left(t_1,t_2,t_3,t_4,t_5\right)=\left|\mu_{eg}\right|^6\sum_{mnkluv}B_m\left\langle n|m\right\rangle\left\langle k|m\right\rangle\left\langle k|l\right\rangle\left\langle u|l\right\rangle\left\langle u|v\right\rangle\left\langle n|v\right\rangle L_{en,gm}\left(t_1\right)$$
$$\times L_{en,ek}\left(t_2\right)L_{en,gl}\left(t_3\right)L_{en,eu}\left(t_4\right)L_{en,gv}\left(t_5\right) \quad\quad (B6)$$

$$R_7^{(5)}\left(t_1,t_2,t_3,t_4,t_5\right)=\left|\mu_{eg}\right|^6\sum_{mnkluv}B_m\left\langle n|m\right\rangle\left\langle k|m\right\rangle\left\langle k|l\right\rangle\left\langle u|l\right\rangle\left\langle n|v\right\rangle\left\langle u|v\right\rangle L_{gm,en}\left(t_1\right)$$
$$\times L_{ek,en}\left(t_2\right)L_{gl,en}\left(t_3\right)L_{eu,en}\left(t_4\right)L_{eu,gv}\left(t_5\right) \quad\quad (B7)$$

$$R_8^{(5)}\left(t_1,t_2,t_3,t_4,t_5\right)=\left|\mu_{eg}\right|^6\sum_{mnkluv}B_m\left\langle n|m\right\rangle\left\langle k|m\right\rangle\left\langle n|l\right\rangle\left\langle u|l\right\rangle\left\langle u|v\right\rangle\left\langle k|v\right\rangle L_{gm,en}\left(t_1\right)$$
$$\times L_{ek,en}\left(t_2\right)L_{ek,gl}\left(t_3\right)L_{ek,eu}\left(t_4\right)L_{ek,gv}\left(t_5\right) \quad\quad (B8)$$

$$R_9^{(5)}\left(t_1,t_2,t_3,t_4,t_5\right)=\left|\mu_{eg}\right|^6\sum_{mnkluv}B_m\left\langle n|m\right\rangle\left\langle n|k\right\rangle\left\langle l|k\right\rangle\left\langle u|m\right\rangle\left\langle u|v\right\rangle\left\langle l|v\right\rangle L_{en,gm}\left(t_1\right)$$
$$\times L_{gk,gm}\left(t_2\right)L_{el,gm}\left(t_3\right)L_{el,eu}\left(t_4\right)L_{el,gv}\left(t_5\right) \quad\quad (B9)$$

$$R_{10}^{(5)}\left(t_1,t_2,t_3,t_4,t_5\right)=\left|\mu_{eg}\right|^6\sum_{mnkluv}B_m\langle n|m\rangle\langle n|k\rangle\langle l|m\rangle\langle u|k\rangle\langle l|v\rangle\langle u|v\rangle L_{en,gm}\left(t_1\right)$$
$$\times L_{gk,gm}\left(t_2\right)L_{gk,el}\left(t_3\right)L_{eu,el}\left(t_4\right)L_{eu,gv}\left(t_5\right) \qquad \text{(B10)}$$

$$R_{11}^{(5)}\left(t_1,t_2,t_3,t_4,t_5\right)=\left|\mu_{eg}\right|^6\sum_{mnkluv}B_m\langle n|m\rangle\langle n|k\rangle\langle l|m\rangle\langle u|k\rangle\langle u|v\rangle\langle l|v\rangle L_{gm,en}\left(t_1\right)$$
$$\times L_{gm,gk}\left(t_2\right)L_{el,gk}\left(t_3\right)L_{el,eu}\left(t_4\right)L_{el,gv}\left(t_5\right) \qquad \text{(B11)}$$

$$R_{12}^{(5)}\left(t_1,t_2,t_3,t_4,t_5\right)=\left|\mu_{eg}\right|^6\sum_{mnkluv}B_m\langle n|m\rangle\langle n|k\rangle\langle l|k\rangle\langle u|m\rangle\langle l|v\rangle\langle u|v\rangle L_{gm,en}\left(t_1\right)$$
$$\times L_{gm,gk}\left(t_2\right)L_{gm,el}\left(t_3\right)L_{eu,el}\left(t_4\right)L_{eu,gv}\left(t_5\right) \qquad \text{(B12)}$$

$$R_{13}^{(5)}\left(t_1,t_2,t_3,t_4,t_5\right)=\left|\mu_{eg}\right|^6\sum_{mnkluv}B_m\langle n|m\rangle\langle k|m\rangle\langle n|l\rangle\langle k|u\rangle\langle v|l\rangle\langle v|u\rangle L_{en,gm}\left(t_1\right)$$
$$\times L_{en,ek}\left(t_2\right)L_{gl,ek}\left(t_3\right)L_{gl,gu}\left(t_4\right)L_{ev,gu}\left(t_5\right) \qquad \text{(B13)}$$

$$R_{14}^{(5)}\left(t_1,t_2,t_3,t_4,t_5\right)=\left|\mu_{eg}\right|^6\sum_{mnkluv}B_m\langle n|m\rangle\langle k|m\rangle\langle k|l\rangle\langle n|u\rangle\langle v|u\rangle\langle v|l\rangle L_{en,gm}\left(t_1\right)$$
$$\times L_{en,ek}\left(t_2\right)L_{en,gl}\left(t_3\right)L_{gu,gl}\left(t_4\right)L_{ev,gl}\left(t_5\right) \qquad \text{(B14)}$$

$$R_{15}^{(5)}\left(t_1,t_2,t_3,t_4,t_5\right)=\left|\mu_{eg}\right|^6\sum_{mnkluv}B_m\langle n|m\rangle\langle k|m\rangle\langle k|l\rangle\langle n|u\rangle\langle v|l\rangle\langle v|u\rangle L_{gm,en}\left(t_1\right)$$
$$\times L_{ek,en}\left(t_2\right)L_{gl,en}\left(t_3\right)L_{gl,gu}\left(t_4\right)L_{ev,gu}\left(t_5\right) \qquad \text{(B15)}$$

$$R_{16}^{(5)}\left(t_1,t_2,t_3,t_4,t_5\right)=\left|\mu_{eg}\right|^6\sum_{mnkluv}B_m\langle n|m\rangle\langle k|m\rangle\langle n|l\rangle\langle k|u\rangle\langle v|u\rangle\langle v|l\rangle L_{gm,en}\left(t_1\right)$$
$$\times L_{ek,en}\left(t_2\right)L_{ek,gl}\left(t_3\right)L_{gu,gl}\left(t_4\right)L_{ev,gl}\left(t_5\right) \qquad \text{(B16)}$$

In the above equations, the propagation functions corresponding to vibronic (in t_1, t_3, or t_5) and

purely vibrational (in t_2 or t_4) coherences are respectively given by[2]

$$L_{em,gn}\left(t\right)=\theta\left(t\right)\exp\left(-i\omega_{eg}t-i\omega_{mn}t-\Gamma_{eg}t\right) \qquad \text{(B17)}$$

and

$$L_{gm,gn}\left(t\right)=\theta\left(t\right)\exp\left(-i\omega_{mn}t-\Gamma_{vib}t\right), \qquad \text{(B18)}$$

where $\theta(t)$ is a Heaviside step function. Equation (B17) assumes that electronic dephasing is fast compared to vibrational dephasing (i.e., $\Gamma_{eg} \gg \Gamma_{vib}$).

We next convolute the response functions and electric fields to obtain the 16 components of the fifth-order polarization. The component of the fifth-order polarization corresponding to the R_1 term is given by

$$
P_1^{(5)}(t) = N\left(\frac{i}{\hbar}\right)^5 \int_0^\infty dt_5 \int_0^\infty dt_4 \int_0^\infty dt_3 \int_0^\infty dt_2 \int_0^\infty dt_1 R_1^{(5)}\left(t_1,t_2,t_3,t_4,t_5\right) E_{RP}(t-t_5) E_{RP}^*(t+\tau_2-t_5-t_4)
$$
$$
E_{St}(t+\tau_2-t_5-t_4-t_3) E_{AP}^*(t+\tau_1+\tau_2-t_5-t_4-t_3-t_2) E_{AP}(t+\tau_1+\tau_2-t_5-t_4-t_3-t_2-t_1) \tag{B19}
$$

where N is the number density, τ_j are the pulse delay times defined in the manuscript, and subscripts are used to specify the three types of laser pulses (actinic pump, Raman pump, and Stokes pulses). Attainment of analytic expressions is facilitated by use of double-sided exponential electric field envelopes,

$$
E_j(t) = \xi_j \exp\left(-i\omega_j t - \Lambda_j |t|\right), \tag{B20}
$$

where ξ_j is the (real) electric field amplitude, Λ_j is the HWHM spectral width, and ω_j is the carrier frequency. The polarization component, $P_1^{(5)}(t)$, can now be rewritten as

$$
P_1^{(5)}(t) = N\xi_{AP}^2 \xi_{RP}^2 \xi_{St} \exp\left(-i\omega_{St}t\right)\left(\frac{i}{\hbar}\right)^5 \int_0^\infty dt_5 \int_0^\infty dt_4 \int_0^\infty dt_3 \int_0^\infty dt_2 \int_0^\infty dt_1 R_1^{(5)}\left(t_1,t_2,t_3,t_4,t_5\right)
$$
$$
\times \exp\left[i\omega_{AP}t_1 + i\omega_{St}t_3 + i\left(\omega_{St}-\omega_{RP}\right)t_4 + i\omega_{St}t_5\right]
$$
$$
\times \exp\left[-\Lambda_{RP}|t-t_5| - \Lambda_{RP}|t+\tau_2-t_5-t_4| - \Lambda_{St}|t+\tau_2-t_5-t_4-t_3|\right]
$$
$$
\times \exp\left[-\Lambda_{AP}|t+\tau_1+\tau_2-t_5-t_4-t_3-t_2| - \Lambda_{AP}|t+\tau_1+\tau_2-t_5-t_4-t_3-t_2-t_1|\right] \tag{B21}
$$

The 65-fs actinic pump pulse employed in this work cannot initiate vibrational coherences in the high-frequency, bond-stretching modes in the delay, τ_1. Therefore, we use a "doorway

wavepacket" to filter vibrational coherences with frequencies that exceed the bandwidth of the actinic pump pulse (i.e., this assumption is valid in the limit of non-overlapping actinic pump and Stokes pulses).[2] We introduce the change of variables, $t_2 = \tau_1 + t'$, to obtain

$$
\begin{aligned}
P_1^{(5)}(t) &= N\xi_{AP}^2 \xi_{RP}^2 \xi_{St} \exp\left(-i\omega_{St} t\right) \left(\frac{i}{\hbar}\right)^5 \int_0^\infty dt_5 \int_0^\infty dt_4 \int_0^\infty dt_3 \int_{-\infty}^\infty dt' \int_0^\infty dt_1 R_1^{(5)}\left(t_1, \tau_1 + t', t_3, t_4, t_5\right) \\
&\times \exp\left[i\omega_{AP} t_1 + i\omega_{St} t_3 + i\left(\omega_{St} - \omega_{RP}\right) t_4 + i\omega_{St} t_5\right] \\
&\times \exp\left[-\Lambda_{RP}|t| - \Lambda_{RP}|t + \tau_2 - t_4| - \Lambda_{St}|t + \tau_2 - t_4|\right] \\
&\times \exp\left[-2\Lambda_{AP}|t'|\right]
\end{aligned}
\qquad , \quad (B22)
$$

where we have eliminated t_1, t_3, and t_5 from the arguments of the pulse envelopes under the assumption that the pulse durations are long compared to the electronic dephasing time. Since we must carefully bookkeep on the phase-angle of the polarization, it should be noted that the infinite limits of the integral over t' yield a *real* Lorentzian function. We next introduce the approximation, $t_4 \approx t + \tau_2$,

$$
\begin{aligned}
P_1^{(5)}(t) &= N\xi_{AP}^2 \xi_{RP}^2 \xi_{St} \theta\left(t + \tau_2\right) \left(\frac{i}{\hbar}\right)^5 \int_0^\infty dt_5 \int_0^\infty dt_3 \int_{-\infty}^\infty dt' \int_0^\infty dt_1 R_1^{(5)}\left(t_1, \tau_1 + t', t_3, t + \tau_2, t_5\right) \\
&\times \exp\left[i\omega_{AP} t_1 + i\omega_{St} t_3 + i\left(\omega_{St} - \omega_{RP}\right) \tau_2 - i\omega_{RP} t + i\omega_{St} t_5 - \Lambda_{RP}|t| - 2\Lambda_{AP}|t'|\right]
\end{aligned}
\qquad , \quad (B23)
$$

under the assumption that $\Gamma_{eg} \gg \Gamma_{vib}$. Evaluation of the four integrals in Equation (B23) yields

$$
\begin{aligned}
P_1^{(5)}(t) &= \frac{N\xi_{AP}^2 \xi_{RP}^2 \xi_{St} |\mu_{eg}|^6}{\hbar^5} \theta\left(t + \tau_2\right) \sum_{mnkluv} B_m \langle n|m\rangle \langle n|k\rangle \langle l|k\rangle \langle l|u\rangle \langle v|u\rangle \langle v|m\rangle \\
&\times L_{en,gm}\left(\omega_{AP}\right) D_{gk,gm}\left(\tau_1\right) L_{el,gm}\left(\omega_{St}\right) L_{ev,gm}\left(\omega_{St}\right) \\
&\times \exp\left[i\left(\omega_{St} - \omega_{RP} - \omega_{um}\right) \tau_2 - i\left(\omega_{RP} + \omega_{um}\right) t - \Gamma_{vib}\left(t + \tau_2\right) - \Lambda_{RP}|t|\right]
\end{aligned}
\qquad , \quad (B24)
$$

where the line shape of the electronic resonance is given by

$$
L_{en,gm}\left(\omega\right) = -i\int_0^\infty L_{en,gm}\left(t\right)\exp\left(i\omega t\right) dt = \frac{1}{\omega - \omega_{eg} - \omega_{nm} + i\Gamma_{eg}} \qquad , \quad (B25)
$$

and the doorway wavepacket induced by the actinic pump pulse is written as

$$D_{gk,gm}(\tau_1) = L_{gk,gm}(\tau_1) \int_{-\infty}^{\infty} dt' \exp\left(-i\omega_{km}t' - \Gamma_{vib}|t'| - \Lambda_{AP}|t'|\right) = L_{gk,gm}(\tau_1) \frac{2\Lambda_{AP}}{\omega_{km}^2 + \Lambda_{AP}^2} . \qquad \text{(B26)}$$

The polarization component, $P_1^{(5)}(t)$, must be Fourier transformed to the frequency domain to account for dispersed detection. To this end, it is useful to consider the following integral,

$$\begin{aligned}
&i\int_{-\tau_2}^{\infty} dt\,\theta(t+\tau_2)\exp\left[i(\omega_t - \omega_{RP} - \omega_{um})t - \Gamma_{vib}t - \Lambda_{RP}|t|\right] \\
&= -i\int_0^{\tau_2} dt \exp\left[-i(\omega_t - \omega_{RP} - \omega_{um})t + \Gamma_{vib}t - \Lambda_{RP}t\right] \\
&+ i\int_0^{\infty} dt \exp\left[i(\omega_t - \omega_{RP} - \omega_{um})t - \Gamma_{vib}t - \Lambda_{RP}t\right]
\end{aligned} \qquad , \qquad \text{(B27)}$$

where ω_t is the frequency of light emission observed on the array detector. Evaluation of the sum of integrals in Equation (B27) yields

$$\begin{aligned}
&i\int_{-\tau_2}^{\infty} dt\,\theta(t+\tau_2)\exp\left[i(\omega_t - \omega_{RP} - \omega_{um})t - \Gamma_{vib}t - \Lambda_{RP}|t|\right] \\
&= i\frac{1 - \exp\left[-i(\omega_t - \omega_{RP} - \omega_{um})\tau_2 + \Gamma_{vib}\tau_2 - \Lambda_{RP}\tau_2\right]}{i(\omega_t - \omega_{RP} - \omega_{um}) - \Gamma_{vib} + \Lambda_{RP}} \\
&- i\frac{1}{i(\omega_t - \omega_{RP} - \omega_{um}) - \Gamma_{vib} - \Lambda_{RP}}
\end{aligned} \qquad , \qquad \text{(B28)}$$

where $\omega_t - \omega_{RP}$ is the Raman shift. The first and third terms in Equation (B28) cancel each other when $\Gamma_{vib} \ll \Lambda_{RP}$ (i.e., a reasonable approximation for the present experimental conditions) and we obtain

$$\begin{aligned}
&i\int_{-\tau_2}^{\infty} dt\,\theta(t+\tau_2)\exp\left[i(\omega_t - \omega_{RP} - \omega_{um})t - \Gamma_{vib}t - \Lambda_{RP}|t|\right] \\
&\approx -\frac{\exp\left[-i(\omega_t - \omega_{RP} - \omega_{um})\tau_2 - (\Lambda_{RP} - \Gamma_{vib})\tau_2\right]}{(\omega_t - \omega_{RP} - \omega_{um}) + i(\Gamma_{vib} - \Lambda_{RP})}
\end{aligned} \qquad . \qquad \text{(B29)}$$

Equation (B29) reveals a desirable line narrowing effect that originates in the difference between Γ_{vib} and Λ_{RP} in the denominator (i.e., the line widths of the vibrational resonances can be

narrower than the bandwidth of the Raman pump). The above equations can be combined to obtain

$$P_1^{(5)}(\omega_t) = i\frac{N\xi_{AP}^2\xi_{RP}^2\xi_{St}|\mu_{eg}|^6}{\hbar^5}\sum_{mnkluv} B_m\langle n|m\rangle\langle n|k\rangle\langle l|k\rangle\langle l|u\rangle\langle v|u\rangle\langle v|m\rangle$$
$$\times L_{en,gm}(\omega_{AP})D_{gk,gm}(\tau_1)L_{el,gm}(\omega_t)J_{gu,gm}(\omega_t-\omega_{RP})L_{ev,gm}(\omega_t) \qquad \text{(B30)}$$

where

$$J_{gu,gm}(\omega_t-\omega_{RP}) = \frac{\exp(-\Lambda_{RP}\tau_2)}{(\omega_t-\omega_{RP}-\omega_{um})+i(\Gamma_{vib}-\Lambda_{RP})}. \qquad \text{(B31)}$$

This expression sets ω_{St} equal to ω_t under the assumption of vibrationally resonant conditions,

$\omega_{St}-\omega_{RP}\approx\omega_{um}$ and $\omega_t-\omega_{RP}\approx\omega_{um}$. We obtain the following 15 polarization components by

following the same procedure

$$P_2^{(5)}(\omega_t) = i\frac{N\xi_{AP}^2\xi_{RP}^2\xi_{St}|\mu_{eg}|^6}{\hbar^5}\sum_{mnkluv} B_m\langle n|m\rangle\langle n|k\rangle\langle l|m\rangle\langle l|u\rangle\langle v|k\rangle\langle v|u\rangle$$
$$\times L_{en,gm}(\omega_{AP})D_{gk,gm}(\tau_1)L_{gk,el}(-\omega_{RP})J_{gk,gu}(\omega_t-\omega_{RP})L_{ev,gu}(\omega_t) \qquad \text{(B32)}$$

$$P_3^{(5)}(\omega_t) = i\frac{N\xi_{AP}^2\xi_{RP}^2\xi_{St}|\mu_{eg}|^6}{\hbar^5}\sum_{mnkluv} B_m\langle n|m\rangle\langle n|k\rangle\langle l|k\rangle\langle l|u\rangle\langle v|m\rangle\langle v|u\rangle$$
$$\times L_{gm,en}(-\omega_{AP})D_{gm,gk}(\tau_1)L_{gm,el}(-\omega_{RP})J_{gm,gu}(\omega_t-\omega_{RP})L_{ev,gu}(\omega_t) \qquad \text{(B33)}$$

$$P_4^{(5)}(\omega_t) = i\frac{N\xi_{AP}^2\xi_{RP}^2\xi_{St}|\mu_{eg}|^6}{\hbar^5}\sum_{mnkluv} B_m\langle n|m\rangle\langle n|k\rangle\langle l|m\rangle\langle l|u\rangle\langle v|u\rangle\langle v|k\rangle$$
$$\times L_{gm,en}(-\omega_{AP})D_{gm,gk}(\tau_1)L_{el,gk}(\omega_t)J_{gu,gk}(\omega_t-\omega_{RP})L_{ev,gk}(\omega_t) \qquad \text{(B34)}$$

$$P_5^{(5)}(\omega_t) = i\frac{N\xi_{AP}^2\xi_{RP}^2\xi_{St}|\mu_{eg}|^6}{\hbar^5}\sum_{mnkluv} B_m\langle n|m\rangle\langle k|m\rangle\langle n|l\rangle\langle u|l\rangle\langle k|v\rangle\langle u|v\rangle$$
$$\times L_{en,gm}(\omega_{AP})D_{en,ek}(\tau_1)L_{gl,ek}(-\omega_{RP})J_{eu,ek}(\omega_t-\omega_{RP})L_{eu,gv}(\omega_t) \qquad \text{(B35)}$$

$$P_6^{(5)}(\omega_t) = i\frac{N\xi_{AP}^2\xi_{RP}^2\xi_{St}|\mu_{eg}|^6}{\hbar^5}\sum_{mnkluv}B_m\langle n|m\rangle\langle k|m\rangle\langle k|l\rangle\langle u|l\rangle\langle u|v\rangle\langle n|v\rangle \qquad (B36)$$

$$\times L_{en,gm}(\omega_{AP})D_{en,ek}(\tau_1)L_{en,gl}(\omega_t)J_{en,eu}(\omega_t-\omega_{RP})L_{en,gv}(\omega_t)$$

$$P_7^{(5)}(\omega_t) = i\frac{N\xi_{AP}^2\xi_{RP}^2\xi_{St}|\mu_{eg}|^6}{\hbar^5}\sum_{mnkluv}B_m\langle n|m\rangle\langle k|m\rangle\langle k|l\rangle\langle u|l\rangle\langle n|v\rangle\langle u|v\rangle \qquad (B37)$$

$$\times L_{gm,en}(-\omega_{AP})D_{ek,en}(\tau_1)L_{gl,en}(-\omega_{RP})J_{eu,en}(\omega_t-\omega_{RP})L_{eu,gv}(\omega_t)$$

$$P_8^{(5)}(\omega_t) = i\frac{N\xi_{AP}^2\xi_{RP}^2\xi_{St}|\mu_{eg}|^6}{\hbar^5}\sum_{mnkluv}B_m\langle n|m\rangle\langle k|m\rangle\langle n|l\rangle\langle u|l\rangle\langle u|v\rangle\langle k|v\rangle \qquad (B38)$$

$$\times L_{gm,en}(-\omega_{AP})D_{ek,en}(\tau_1)L_{ek,gl}(\omega_t)J_{ek,eu}(\omega_t-\omega_{RP})L_{ek,gv}(\omega_t)$$

$$P_9^{(5)}(\omega_t) = i\frac{N\xi_{AP}^2\xi_{RP}^2\xi_{St}|\mu_{eg}|^6}{\hbar^5}\sum_{mnkluv}B_m\langle n|m\rangle\langle n|k\rangle\langle l|k\rangle\langle u|m\rangle\langle u|v\rangle\langle l|v\rangle \qquad (B39)$$

$$\times L_{en,gm}(\omega_{AP})D_{gk,gm}(\tau_1)L_{el,gm}(\omega_t)J_{el,eu}(\omega_t-\omega_{RP})L_{el,gv}(\omega_t)$$

$$P_{10}^{(5)}(\omega_t) = i\frac{N\xi_{AP}^2\xi_{RP}^2\xi_{St}|\mu_{eg}|^6}{\hbar^5}\sum_{mnkluv}B_m\langle n|m\rangle\langle n|k\rangle\langle l|m\rangle\langle u|k\rangle\langle l|v\rangle\langle u|v\rangle \qquad (B40)$$

$$\times L_{en,gm}(\omega_{AP})D_{gk,gm}(\tau_1)L_{gk,el}(-\omega_{RP})J_{eu,el}(\omega_t-\omega_{RP})L_{eu,gv}(\omega_t)$$

$$P_{11}^{(5)}(\omega_t) = i\frac{N\xi_{AP}^2\xi_{RP}^2\xi_{St}|\mu_{eg}|^6}{\hbar^5}\sum_{mnkluv}B_m\langle n|m\rangle\langle n|k\rangle\langle l|m\rangle\langle u|k\rangle\langle u|v\rangle\langle l|v\rangle \qquad (B41)$$

$$\times L_{gm,en}(-\omega_{AP})D_{gm,gk}(\tau_1)L_{el,gk}(\omega_t)J_{el,eu}(\omega_t-\omega_{RP})L_{el,gv}(\omega_t)$$

$$P_{12}^{(5)}(\omega_t) = i\frac{N\xi_{AP}^2\xi_{RP}^2\xi_{St}|\mu_{eg}|^6}{\hbar^5}\sum_{mnkluv}B_m\langle n|m\rangle\langle n|k\rangle\langle l|k\rangle\langle u|m\rangle\langle l|v\rangle\langle u|v\rangle \qquad (B42)$$

$$\times L_{gm,en}(-\omega_{AP})D_{gm,gk}(\tau_1)L_{gm,el}(-\omega_{RP})J_{eu,el}(\omega_t-\omega_{RP})L_{eu,gv}(\omega_t)$$

$$P_{13}^{(5)}(\omega_t) = i\frac{N\xi_{AP}^2\xi_{RP}^2\xi_{St}|\mu_{eg}|^6}{\hbar^5}\sum_{mnkluv}B_m\langle n|m\rangle\langle k|m\rangle\langle n|l\rangle\langle k|u\rangle\langle v|l\rangle\langle v|u\rangle \qquad (B43)$$

$$\times L_{en,gm}(\omega_{AP})D_{en,ek}(\tau_1)L_{gl,ek}(-\omega_{RP})J_{gl,gu}(\omega_t-\omega_{RP})L_{ev,gu}(\omega_t)$$

$$P_{14}^{(5)}(\omega_t) = i \frac{N \xi_{AP}^2 \xi_{RP}^2 \xi_{St} |\mu_{eg}|^6}{\hbar^5} \sum_{mnkluv} B_m \langle n|m \rangle \langle k|m \rangle \langle k|l \rangle \langle n|u \rangle \langle v|u \rangle \langle v|l \rangle$$
$$\times L_{en,gm}(\omega_{AP}) D_{en,ek}(\tau_1) L_{en,gl}(\omega_t) J_{gu,gl}(\omega_t - \omega_{RP}) L_{ev,gl}(\omega_t)$$
(B44)

$$P_{15}^{(5)}(\omega_t) = i \frac{N \xi_{AP}^2 \xi_{RP}^2 \xi_{St} |\mu_{eg}|^6}{\hbar^5} \sum_{mnkluv} B_m \langle n|m \rangle \langle k|m \rangle \langle k|l \rangle \langle n|u \rangle \langle v|l \rangle \langle v|u \rangle$$
$$\times L_{gm,en}(-\omega_{AP}) D_{ek,en}(\tau_1) L_{gl,en}(-\omega_{RP}) J_{gl,gu}(\omega_t - \omega_{RP}) L_{ev,gu}(\omega_t)$$
(B45)

$$P_{16}^{(5)}(\omega_t) = i \frac{N \xi_{AP}^2 \xi_{RP}^2 \xi_{St} |\mu_{eg}|^6}{\hbar^5} \sum_{mnkluv} B_m \langle n|m \rangle \langle k|m \rangle \langle n|l \rangle \langle k|u \rangle \langle v|u \rangle \langle v|l \rangle$$
$$\times L_{gm,en}(-\omega_{AP}) D_{ek,en}(\tau_1) L_{ek,gl}(\omega_t) J_{gu,gl}(\omega_t - \omega_{RP}) L_{ev,gl}(\omega_t)$$
(B46)

The direct fifth-order signal field is expressed in terms of these polarization components

as

$$E_{direct}^{(5)}(\omega_t) = \frac{1}{7} \left(\frac{i\omega_t l}{2\varepsilon_0 n(\omega_t) c} \right) \sum_{m=1}^{16} P_m^{(5)}(\omega_t) \operatorname{sinc}\left(\frac{\Delta k_{direct}^{(5)} l}{2} \right) \exp\left(i \frac{\Delta k_{direct}^{(5)} l}{2} \right)$$
(B47)

where the factor of 1/7 represents the orientational average for all-parallel electric field

polarizations.[3]

B.2. Derivation of Formula for Third-Order Cascaded Signal Field

The third-order response functions needed to compute cascaded nonlinearities can be

derived under the same approximations outlined above. Feynman diagrams for third-order

nonlinearities are presented in Figure B3. Response functions corresponding to these diagrams

can be written as

$$R_1^{(3)}(t_1, t_2, t_3) = |\mu_{eg}|^4 \sum_{mnkl} B_m \langle n|m \rangle \langle k|m \rangle \langle k|l \rangle \langle n|l \rangle L_{en,gm}(t_1) L_{en,ek}(t_2) L_{en,gl}(t_3)$$
(B48)

$$R_2^{(3)}(t_1, t_2, t_3) = |\mu_{eg}|^4 \sum_{mnkl} B_m \langle n|m \rangle \langle k|m \rangle \langle n|l \rangle \langle k|l \rangle L_{gm,en}(t_1) L_{ek,en}(t_2) L_{ek,gl}(t_3)$$
(B49)

$$R_3^{(3)}(t_1,t_2,t_3) = |\mu_{eg}|^4 \sum_{mnkl} B_m \langle n|m\rangle\langle n|k\rangle\langle l|k\rangle\langle l|m\rangle L_{en,gm}(t_1)L_{gk,gm}(t_2)L_{el,gm}(t_3) \quad , \quad \text{(B50)}$$

$$R_4^{(3)}(t_1,t_2,t_3) = |\mu_{eg}|^4 \sum_{mnkl} B_m \langle n|m\rangle\langle n|k\rangle\langle l|m\rangle\langle l|k\rangle L_{gm,en}(t_1)L_{gm,gk}(t_2)L_{el,gk}(t_3) \quad . \quad \text{(B51)}$$
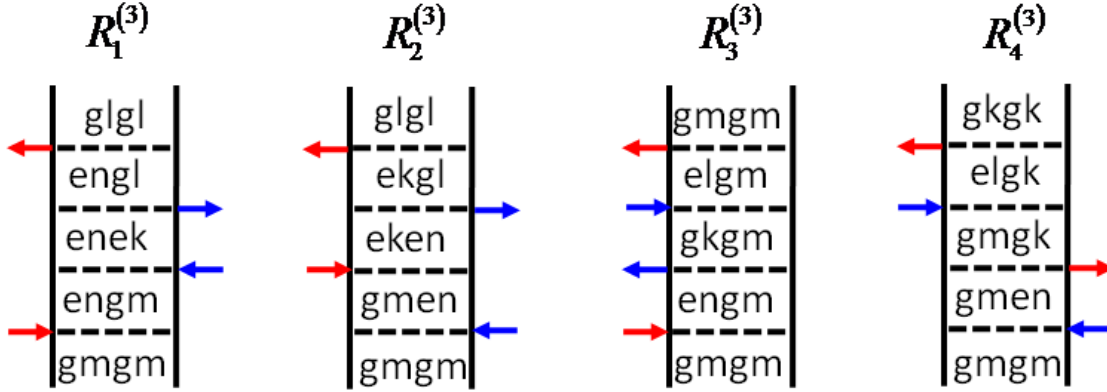

Figure B3. *Feynman diagrams associated with the direct third-order CSRS response. The indices, g and ℓ, represent the ground and excited electronic state, whereas dummy indices (m, n, k, and l) denote vibrational levels. Blue and red arrows represent the Raman pump and Stokes pulses, respectively.*

B.2.1. Direct Coherent Stokes Raman Scattering (CSRS) Signal Field Obtained with the Phase Matching Condition k3-k4+k5

We first consider the direct third-order CSRS signal field, which is compared to the direct fifth-order signal field in the four-beam geometry in section IIID of the manuscript. The CSRS polarization component associated with term, $F_1(t_1,t_2,t_3)$, is given by

$$P_{1,CSRS}^{(3)}(t) = N\left(\frac{i}{\hbar}\right)^3 \int_0^\infty dt_3 \int_0^\infty dt_2 \int_0^\infty dt_1 R_1^{(3)}(t_1,t_2,t_3) E_{RP}(t-t_5)E_{RP}^*(t+\tau_2-t_3-t_2)$$
$$\times E_{St}(t+\tau_2-t_3-t_2-t_1) \quad \text{(B52)}$$

Application of the approximations and procedure outlined above yields

$$P_{1,CSRS}^{(3)}(\omega_t) = -\frac{N\xi_{RP}^2\xi_{St}|\mu_{eg}|^4}{\hbar^3} \sum_{mnkl} B_m \langle n|m\rangle\langle k|m\rangle\langle k|l\rangle\langle n|l\rangle L_{en,gm}(\omega_t)$$
$$\times J_{en,ek}(\omega_t-\omega_{RP})L_{en,gl}(\omega_t) \quad . \quad \text{(B53)}$$

The polarization components for the three remaining terms are

$$P_{2,CSRS}^{(3)}(\omega_t) = -\frac{N\xi_{RP}^2\xi_{St}\left|\mu_{eg}\right|^4}{\hbar^3}\sum_{mnkl}B_m\left\langle n|m\right\rangle\left\langle k|m\right\rangle\left\langle n|l\right\rangle\left\langle k|l\right\rangle L_{gm,en}\left(-\omega_{RP}\right)$$
$$\times J_{ek,en}\left(\omega_t-\omega_{RP}\right)L_{ek,gl}\left(\omega_t\right)$$
(B54)

$$P_{3,CSRS}^{(3)}(\omega_t) = -\frac{N\xi_{RP}^2\xi_{St}\left|\mu_{eg}\right|^4}{\hbar^3}\sum_{mnkl}B_m\left\langle n|m\right\rangle\left\langle n|k\right\rangle\left\langle l|k\right\rangle\left\langle l|m\right\rangle L_{en,gm}\left(\omega_t\right)$$
$$\times J_{gk,gm}\left(\omega_t-\omega_{RP}\right)L_{el,gm}\left(\omega_t\right)$$
(B55)

$$P_{4,CSRS}^{(3)}(\omega_t) = -\frac{N\xi_{RP}^2\xi_{St}\left|\mu_{eg}\right|^4}{\hbar^3}\sum_{mnkl}B_m\left\langle n|m\right\rangle\left\langle n|k\right\rangle\left\langle l|m\right\rangle\left\langle l|k\right\rangle L_{gm,en}\left(-\omega_{RP}\right)$$
$$\times J_{gm,gk}\left(\omega_t-\omega_{RP}\right)L_{el,gk}\left(\omega_t\right)$$
(B56)

The third-order CSRS signal field is given by

$$E_{CSRS}^{(3)}(\omega_t) = \frac{1}{5}\left(\frac{i\omega_t l}{2\varepsilon_0 n(\omega_t)c}\right)\sum_{m=1}^4 P_{m,CSRS}^{(3)}(\omega_t)\operatorname{sinc}\left(\frac{\Delta k_{direct}^{(3)}l}{2}\right)\exp\left(i\frac{\Delta k_{direct}^{(3)}l}{2}\right)$$
(B57)

where the factor of 1/5 represents the orientational average for all-parallel electric field polarizations at third-order in perturbation theory.[4]

B.2.2. Cascades with Intermediate Phase-Matching Conditions $\mathbf{k_1}$-$\mathbf{k_2}$+$\mathbf{k_5}$ and $\mathbf{k_3}$-$\mathbf{k_4}$+$\mathbf{k_5}$

In this section, we obtain an expression for the signal field generated by third-order cascades with intermediate phase-matching conditions, $\mathbf{k_1}$-$\mathbf{k_2}$+$\mathbf{k_5}$ and $\mathbf{k_3}$-$\mathbf{k_4}$+$\mathbf{k_5}$, which we refer to as cascades 1 and 2, respectively. Figures B4 and B5 display all terms in the response functions associated with these types of cascades. The two processes essentially permute the type of nonlinearity that occurs on each molecule. A pump-probe-like response precedes a CSRS process in cascade 1, whereas the opposite is true for cascade 2. The polarization components for the CSRS process are given in Equations (B53)-(B56). Therefore, we must first derive equations related to the pump-probe response (actinic pump and Stokes probe).

The pump-probe-like polarization component associated with term, $F_1\left(t_1,t_2,t_3\right)$, is given by

$$P^{(3)}_{1,PP}(t) = N\left(\frac{i}{\hbar}\right)^3 \int_0^\infty dt_3 \int_0^\infty dt_2 \int_0^\infty dt_1 F_1\left(t_1,t_2,t_3\right) E_{St}(t-t_5)E^*_{AP}(t+\tau_2-t_3-t_2)$$
$$\times E_{AP}(t+\tau_2-t_3-t_2-t_1)$$

(B58)

Application of the procedure used to derive the fifth-order polarization components in section I yields

$$P^{(3)}_{1,PP}(\omega_t) = i\frac{N\xi^2_{AP}\xi_{St}\left|\mu_{eg}\right|^4}{\hbar^3}\sum_{mnkl}B_m\langle n|m\rangle\langle k|m\rangle\langle k|l\rangle\langle n|l\rangle L_{en,gm}\left(\omega_{AP}\right)D_{en,ek}\left(\tau_1\right)L_{en,gl}\left(\omega_t\right).$$ (B59)

Under the same approximations, the polarization components for the three remaining terms are

$$P^{(3)}_{2,PP}(\omega_t) = i\frac{N\xi^2_{AP}\xi_{St}\left|\mu_{eg}\right|^4}{\hbar^3}\sum_{mnkl}B_m\langle n|m\rangle\langle k|m\rangle\langle n|l\rangle\langle k|l\rangle L_{gm,en}\left(-\omega_{AP}\right)D_{ek,en}\left(\tau_1\right)L_{ek,gl}\left(\omega_t\right),$$ (B60)

$$P^{(3)}_{3,PP}(\omega_t) = i\frac{N\xi^2_{AP}\xi_{St}\left|\mu_{eg}\right|^4}{\hbar^3}\sum_{mnkl}B_m\langle n|m\rangle\langle n|k\rangle\langle l|k\rangle\langle l|m\rangle L_{en,gm}\left(\omega_{AP}\right)D_{gk,gm}\left(\tau_1\right)L_{el,gm}\left(\omega_t\right),$$ (B61)

$$P_{4,PP}^{(3)}(\omega_t) = i\frac{N\xi_{AP}^2\xi_{St}|\mu_{eg}|^4}{\hbar^3}\sum_{mnkl}B_m\langle n|m\rangle\langle n|k\rangle\langle l|m\rangle\langle l|k\rangle L_{gm,en}(-\omega_{AP})D_{gm,gk}(\tau_1)L_{el,gk}(\omega_t). \quad \text{(B62)}$$

The total signal field generated by the two cascades can be written as

$$E_{cas}(\omega_t) = \frac{1}{25}\left(\frac{i\omega_t l}{2\varepsilon_0 n(\omega_t)c}\right)^2\sum_{m=1}^4\sum_{n=1}^4\xi_{St}^{-1}P_{m,PP}^{(3)}(\omega_t)P_{n,CSRS}^{(3)}(\omega_t)f_{cas}(\Delta k_1,\Delta k_2) \quad , \quad \text{(B63)}$$

where the phase matching function is given by

$$f_{cas}(\Delta k_1,\Delta k_2) = \sum_{j=1}^2\mathrm{sinc}\left(\frac{\Delta k_{jA}l}{2}\right)\mathrm{sinc}\left(\frac{\Delta k_{jB}l}{2}\right)\exp\left[i\frac{(\Delta k_{jA}+\Delta k_{jB})l}{2}\right]. \quad \text{(B64)}$$

The factor of 1/25 represents the product of orientational averages for all-parallel electric field polarizations at third-order in perturbation theory.[4] Wavevector mismatches, Δk_{jA} and Δk_{jB}, associated with all direct and cascaded processes are given in Tables B1-B3. We consider the four and five-beam geometries employed in the manuscript in Tables B1 and B2. In Table B3, calculations are also carried out for a hypothetical three-beam geometry in which the actinic and Raman pump pulses cross at 6.9° and are bisected by the Stokes beam (i.e., traditional FSRS).

Table B1. *Wavevector Mismatch in the Five-Beam Geometry*

Nonlinearity	$\Delta k_{direct}^{(n)}$ (cm^{-1})	Δk_A (cm^{-1})	Δk_B (cm^{-1})	[a],[b]Efficiency
Direct Fifth-Order (FSRS)	-215	------	------	0.123
Direct Third-Order (CSRS)	-430	------	------	0.050
Cascade #1 ($\mathbf{k}_1$-$\mathbf{k}_2$+$\mathbf{k}_5$ intermediate)	------	-18	-197	0.069
Cascade #2 ($\mathbf{k}_3$-$\mathbf{k}_4$+$\mathbf{k}_5$ intermediate)	------	-412	196	0.005

[a] The efficiency is computed using $\mathrm{sinc}\left(\dfrac{\Delta k_{direct}^{(n)}l}{2}\right)$ and $\mathrm{sinc}\left(\dfrac{\Delta k_A l}{2}\right)\mathrm{sinc}\left(\dfrac{\Delta k_B l}{2}\right)$ for direct and cascaded processes, respectively.
[b] Path length, l, is 0.022 cm.

Table B2. *Wavevector Mismatch in the Four-Beam Geometry*

Nonlinearity	$\Delta k_{direct}^{(n)}$ (cm⁻¹)	Δk_A (cm⁻¹)	Δk_B (cm⁻¹)	[a],[b]Efficiency
Direct Fifth-Order (FSRS)	-198	----------	----------	0.123
Direct Third-Order (CSRS)	-225	----------	---------------	0.128
Cascade #1 ($\mathbf{k}_1$-$\mathbf{k}_2$+$\mathbf{k}_5$ intermediate)	----------	-215	-215	0.015
Cascade #2 ($\mathbf{k}_3$-$\mathbf{k}_4$+$\mathbf{k}_5$ intermediate)	----------	-215	-180	-0.002

[a] The efficiency is computed using $\mathrm{sinc}\left(\dfrac{\Delta k_{direct}^{(n)} l}{2}\right)$ and $\mathrm{sinc}\left(\dfrac{\Delta k_A l}{2}\right)\mathrm{sinc}\left(\dfrac{\Delta k_B l}{2}\right)$ for direct and cascaded

processes, respectively.
[b] Path length, l, is 0.022 cm.

Table B3. *Wavevector Mismatch in a (Hypothetical) Three-Beam Geometry*

Nonlinearity	$\Delta k_{direct}^{(n)}$ (cm⁻¹)	Δk_A (cm⁻¹)	Δk_B (cm⁻¹)	[a],[b]Efficiency
Direct Fifth-Order (FSRS)	0	------	------	1.000
Direct Third-Order (CSRS)	0	------	------	1.000
Cascade #1 ($\mathbf{k}_1$-$\mathbf{k}_2$+$\mathbf{k}_5$ intermediate)	------	0	0	1.000
Cascade #2 ($\mathbf{k}_3$-$\mathbf{k}_4$+$\mathbf{k}_5$ intermediate)	------	0	0	1.000

[a] The efficiency is computed using $\mathrm{sinc}\left(\dfrac{\Delta k_{direct}^{(n)} l}{2}\right)$ and $\mathrm{sinc}\left(\dfrac{\Delta k_A l}{2}\right)\mathrm{sinc}\left(\dfrac{\Delta k_B l}{2}\right)$ for direct and cascaded

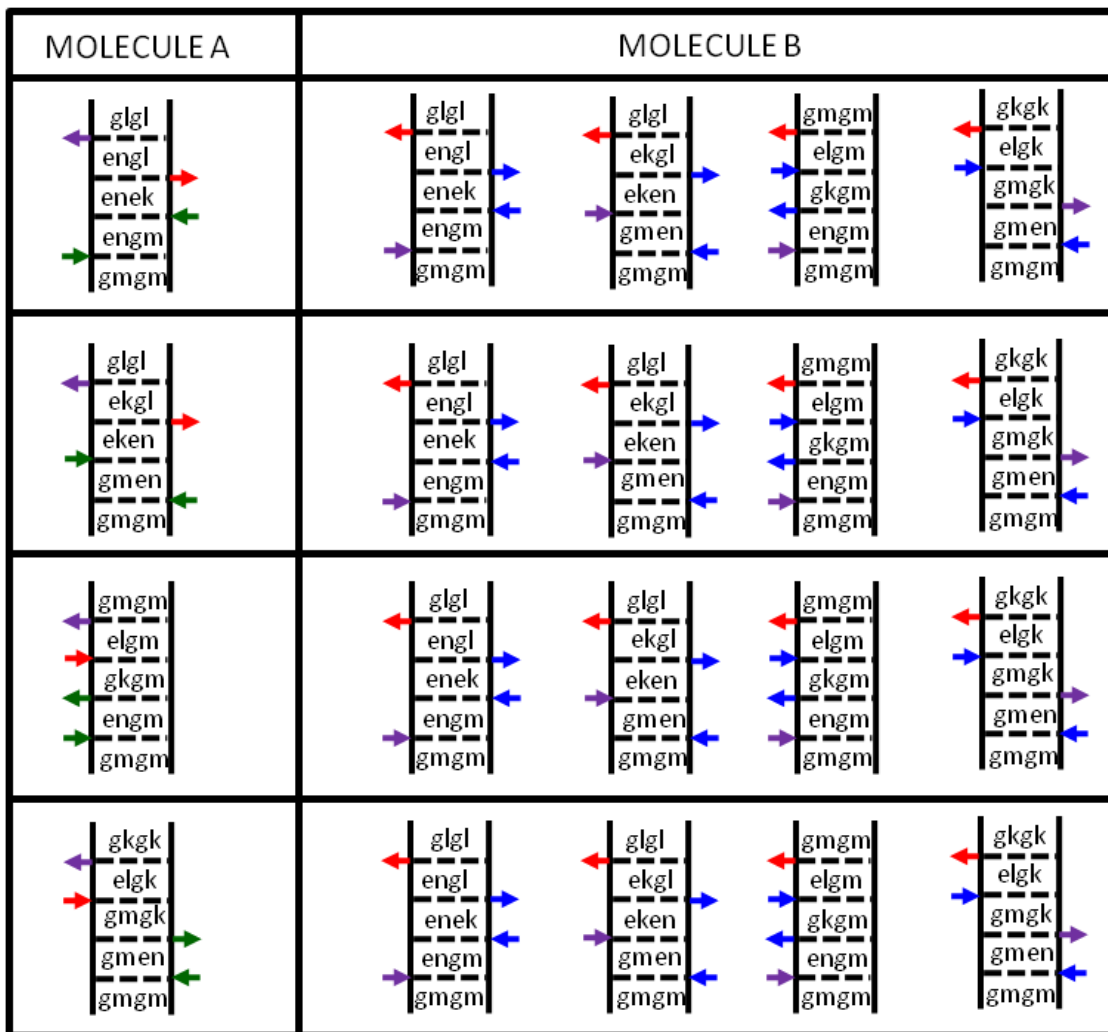processes, respectively.
[b] Path length, l, is 0.022 cm.

Figure B4. *Feynman diagrams associated with third-order cascades with the intermediate phase-matching condition $\mathbf{k}_1$-$\mathbf{k}_2$+$\mathbf{k}_5$ (referred to as cascade #1 in text). The indices, g and ℓ, represent the ground and excited electronic states, whereas dummy indices (m, n, k, l, u, and v) denote vibrational levels. Field-matter interactions are color-coded as follows: actinic pump is green; Raman pump is blue; Stokes is red; radiated signal field is red; the field radiated at the intermediate step in the cascade is purple. We restrict the response function to these terms (total of 16 products) under the assumption that the signal is primarily resonance-enhanced by the Soret band.*
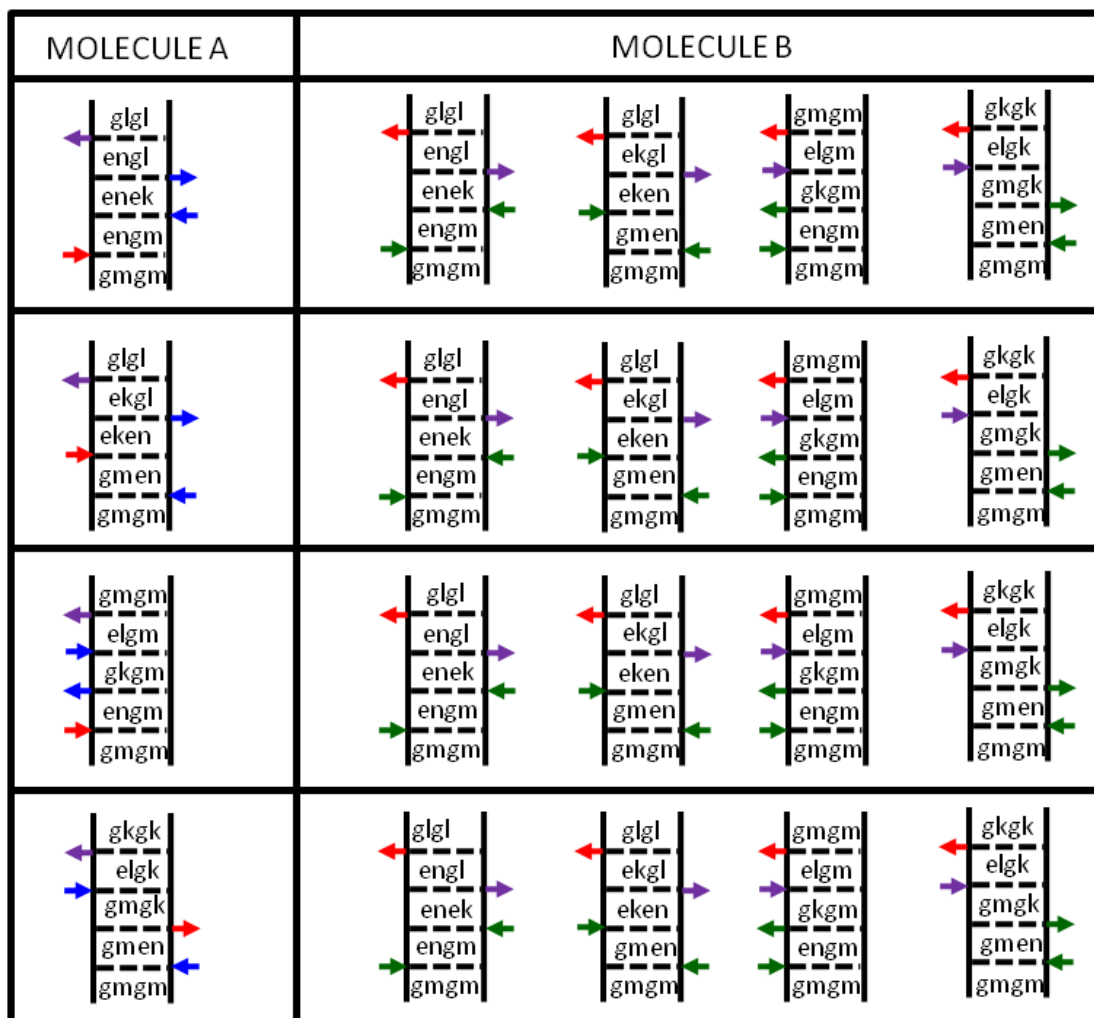
Figure B5. *Feynman diagrams associated with third-order cascades with the intermediate phase-matching condition k_3-k_4+k_5 (referred to as cascade #2 in text). The indices, g and ℓ, represent the ground and excited electronic states, whereas dummy indices (m, n, k, l, u, and v) denote vibrational levels. Field-matter interactions are color-coded as follows: actinic pump is green; Raman pump is blue; Stokes is red; radiated signal field is red; the field radiated at the intermediate step in the cascade is purple. We restrict the response function to these terms (total of 16 products) under the assumption that the signal is primarily resonance-enhanced by the Soret band.*

REFERENCES

1.	Myers, A. B.; Mathies, R. A.; Tannor, D. J.; Heller, E. J., Excited state geometry changes from preresonance raman intensities: Isoprene and hexatriene. *J. Chem. Phys.* **1982,** *77*, 3857-3866.

2.	Mukamel, S., *Principles of Nonlinear Optical Spectroscopy*. Oxford University Press: New York, 1995.

3.	Ding, F.; Fulmer, E. C.; Zanni, M. T., Heterodyned fifth-order two-dimensional IR spectroscopy: Third-quantum states and polarization selectivity *J. Chem. Phys.* **2005,** *123*, 094502.

4.	Hochstrasser, R. M., Two-dimensional IR-spectroscopy: Polarization anisotropy effects. *Chem. Phys.* **2001,** *266*, 273-284.

APPENDIX C: SUPPLEMENT TO "TWO-DIMENSIONAL RESONANCE RAMAN SPECTROSCOPY OF OXYGEN- AND WATER-LIGATED MYOGLOBIN"

C.1. Signatures of Anharmonicity in Time-Frequency Representation of 2DRR Signal

As discussed in the main text, anharmonic coupling between modes may cause the vibrational resonance frequencies in ω_2 to oscillate with respect to τ_1 for FSRS signals represented in the traditional way (τ_1 and ω_2 in our notation). Here, we examine this representation in our calculated signals. The first dimension may be expressed in the time domain by inverse Fourier transforming $E^{(5)}(\omega_1, \omega_2)$ with respect to τ_1. Analytic expressions for this representation, which we denote as $E^{(5)}(\tau_1, \omega_2)$, were given in Reference [1]. The mean vibrational frequencies in ω_2 are then Fourier transformed with respect to τ_1,

$$\sigma(\omega_1) = \int_{-\infty}^{\infty} \left[\frac{\int_{\alpha}^{\beta} \left| E^{(5)}(\tau_1, \omega_2) \right| \omega_2 d\omega_2}{\int_{\alpha}^{\beta} \left| E^{(5)}(\tau_1, \omega_2) \right| d\omega_2} \right] \exp(i\omega_1 \tau_1) d\tau_1. \tag{C1}$$

in order to produce a vibrational spectrum associated with the quantum beats in the resonance frequencies. The lower, α, and upper, β, limits of the integral over ω_2 are respectively set equal to 250 and 550 cm^{-1} for the 400-cm^{-1} mode. Limits of 950 and 1250 cm^{-1} are used for the 1100-cm^{-1} resonance in ω_2.

In Figure C1, we present vibrational spectra associated with quantum beats in the resonance frequencies. The harmonic system in panel (e) exhibits the most intense oscillations at the frequency corresponding to a coherence between the two modes (i.e., 700 cm^{-1} is the difference in wavenumbers. As in Reference [1], we find that oscillations in the mean vibrational resonance frequencies are observed even for a harmonic system (see Figures 11 and 12 in Reference [2]). Anharmonicity causes the relative amplitude of the quantum beat at 400 cm^{-1} to

increase; the effect is most pronounced in panels C1(a), C1(c), C1(g) and C1(i) (i.e., the parameters with the greatest amount of anharmonicity) These results suggest that the relative amplitudes of various spectral components carry the key information about anharmonicity in this representation. Quantum beats at difference frequencies occur even in the harmonic system. This conclusion is still valid if the real or imaginary parts of the fifth-order signal field enter Equation (C1). We process the absolute value of the signal field, $E^{(5)}\left(\tau_1, \omega_2\right)$, because the time evolution (in τ_1) between absorptive and dispersive line shapes (in ω_2) gives rise to artificially large oscillations in the mean resonance frequencies (in ω_2).
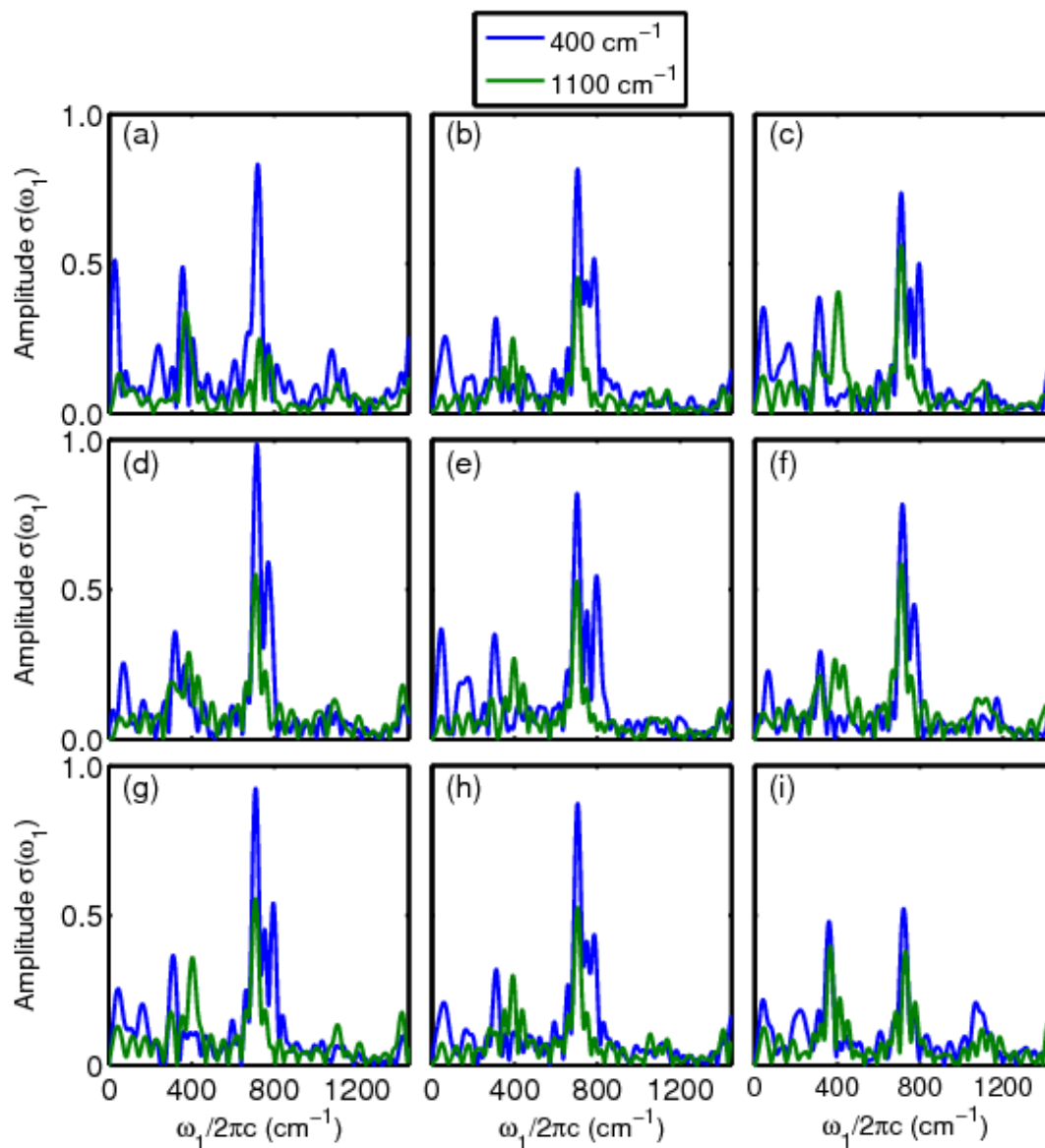
Figure C1. *Spectral components associated with oscillations of the mean vibrational resonance frequencies computed with an anharmonic vibrational Hamiltonian. The diagonal expansion coefficients are set equal to -5 (first row), 0 (second row), and 5 cm⁻¹ (third row). The off-diagonal expansion coefficients are set equal to -5 (first row), 0 (second row), and 5 cm⁻¹ (third row). All amplitudes are normalized to the maximum found for the 400-cm⁻¹ mode in the second row and first column. These calculations show that oscillations in the mean vibrational resonance frequencies occur primarily at the difference frequency in the harmonic system (see panel (e)). Anharmonicity increases the amplitude of oscillations at the fundamental frequencies of the vibrations.*

C.2. Fluctuations in the Geometries of the Propionic Acid Side Chains Produced with Molecular Dynamics Simulations and an Ab Initio Map

In this section, we present scatter plots for 5000 steps in the molecular dynamics trajectories of metMb and MbO_2, respectively. The structures fluctuate in a fairly symmetric manner with respect to the equilibrium geometries.
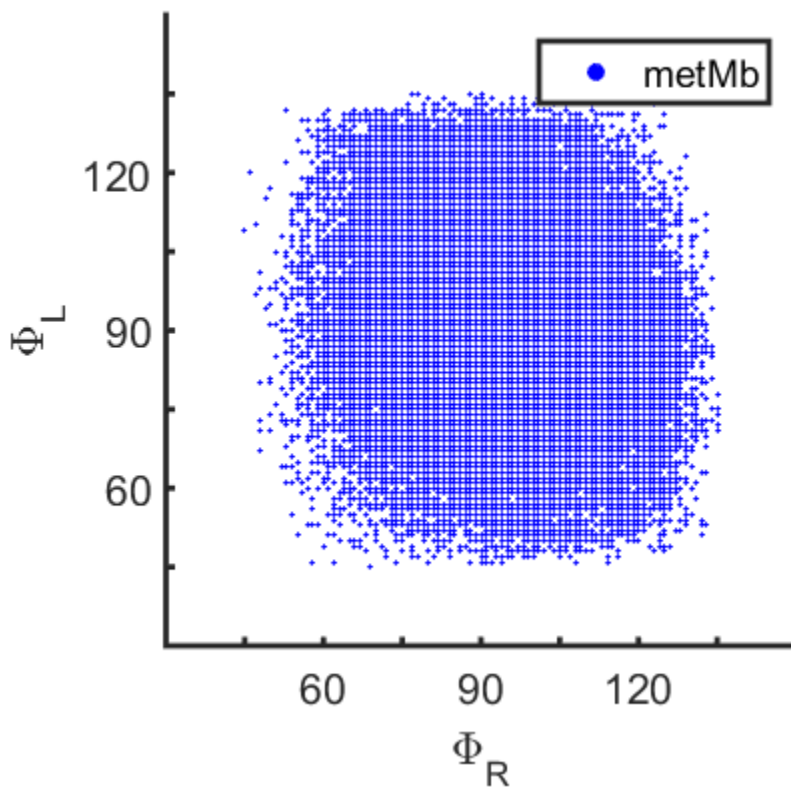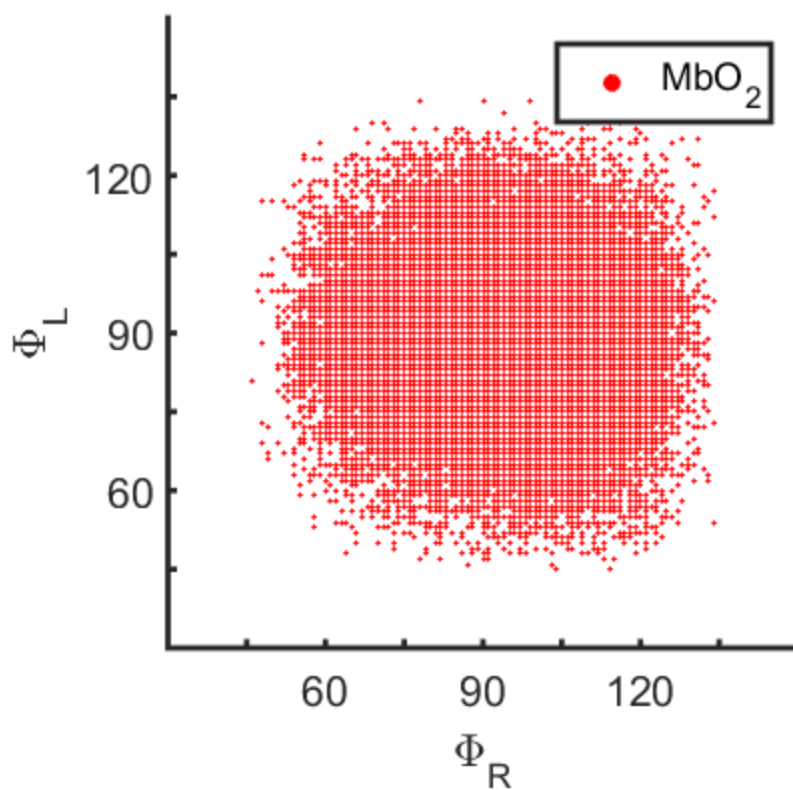

Figure C2. *Distribution of dihedral angles for 5000 steps of the molecular dynamics trajectory simulated for metMb. The equilibrium dihedral angles associated with the propionic acid side chains (see Figure 5.11 in Chapter 5 of this dissertation) are* $\Phi_L = 81.3°$ *and* $\Phi_R = 81.1°$.

Figure C3. *Distribution of dihedral angles for 5000 steps of the molecular dynamics trajectory simulated for MbO₂. The equilibrium dihedral angles associated with the propionic acid side chains (see Figure 5.11 in Chapter 5 of this dissertation) are* $\Phi_L = 94.4°$ *and* $\Phi_R = 109°$.

REFERENCES

1. Molesky, B. M.; Guo, Z.; Moran, A. M., Femtosecond stimulated Raman spectroscopy by six-wave mixing. *J. Chem. Phys.* **2015,** *142*, 212405.

2. Molesky, B. P.; Giokas, P. G.; Guo, Z.; Moran, A. M., Multidimensional resonance Raman spectroscopy by six-wave mixing in the deep UV. *J. Chem. Phys.* **2014,** *114*, 114202.

APPENDIX D: SUPPLEMENT TO "IMAGING CARRIER DIFFUSION IN PEROVSKITES WITH A DIFFRACTIVE OPTIC-BASED TRANSIENT ABSORPTION MICROSCOPE"
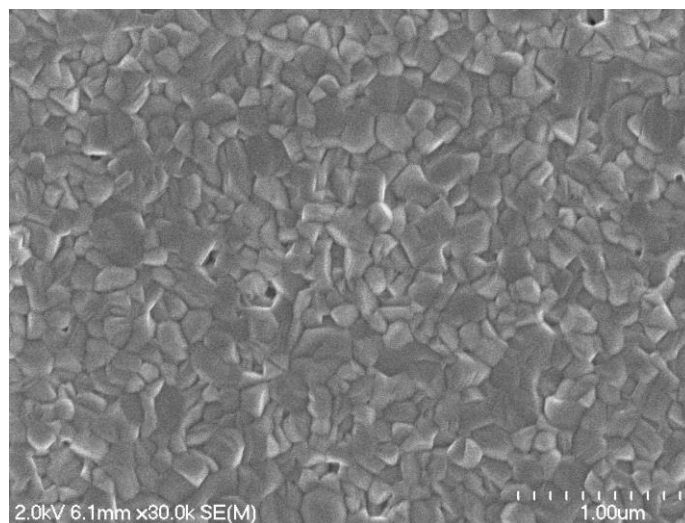
D1. SEM Image of Perovskite Film

Figure D1. *Individual grains are observed in this SEM image of a perovskite film.*
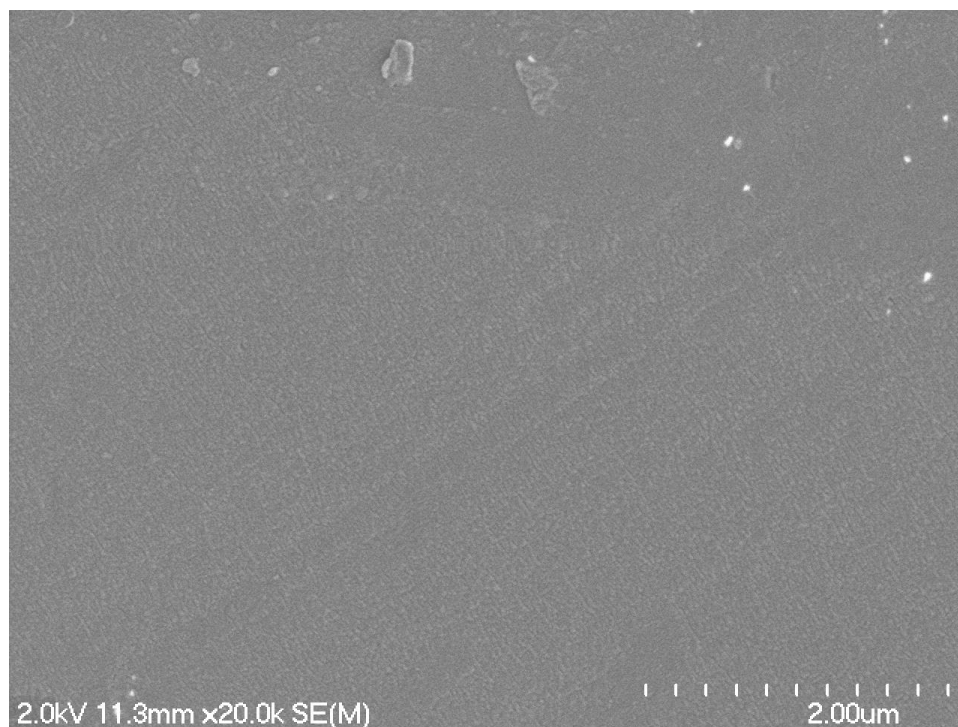
D2. SEM Image of Perovskite Single Crystal

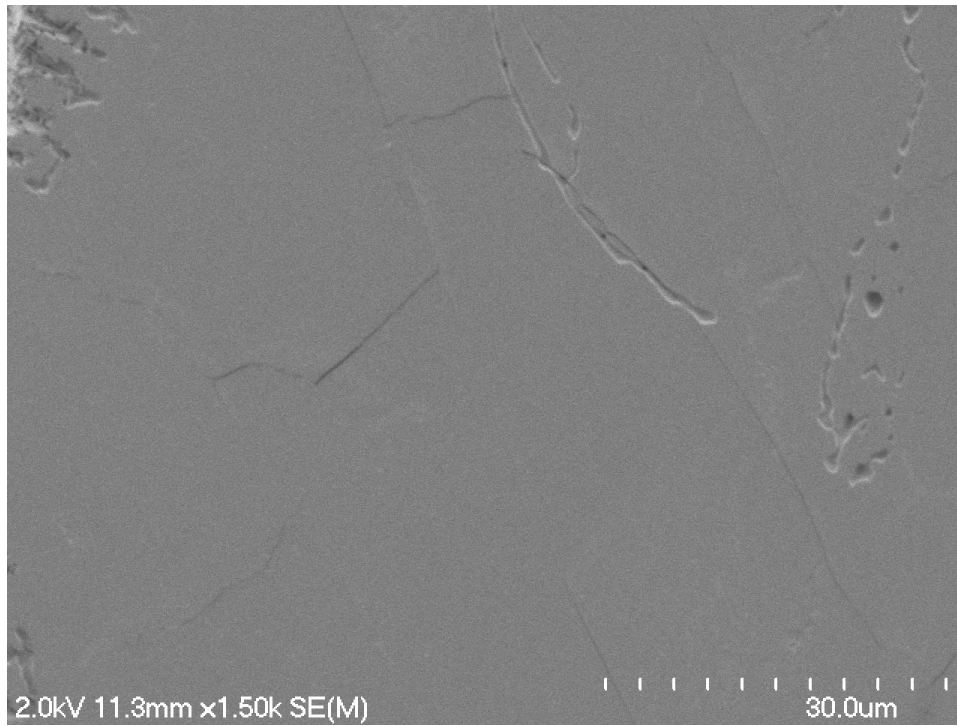**Figure D2.** *SEM image of perovskite single crystal.*

Figure D3. *SEM image of perovskite single crystal.*

D3. Summary of Fitting Parameters

Table D1. *Diffusion Coefficient D_0*

Fluence (μJ/cm^2)	Crystal D_0 (cm^2/s)	Film D_0 (cm^2/s)
95	0.268±0.0869	$2.80\times10^{-9}\pm6.84\times10^{-9}$
148	0.143±0.0546	0.00874±0.0127
233	0.178±0.0409	0.0465±0.0248
402	0.286±0.0702	0.0454±0.0305
782	0.263±0.0889	0.0360±0.0148
1590	0.271±0.0659	0.0733±0.0417
4018	0.282±0.0698	0.150±0.0886

Table D2. *Density-Independent Relaxation Time τ_1*

Fluence (μJ/cm^2)	Crystal τ_1 (ns)	Film τ_1 (ns)
95	0.676±0.234	3.39±1.13
148	1.18±1.16	7.75±2.65
233	1.15±0.476	10.7±6.60
402	1.58±0.763	10.8±10.3
782	1.27±0.537	10.5±9.03
1590	2.42±2.18	7.38±3.05
4018	10.3±22.4	5.47±2.42

Table D3. *Two-Body Relaxation Time τ_2*

Fluence (μJ/cm^2)	Crystal τ_2 (ns^2)	Film τ_2 (ns^2)
95	478±380	948±126
148	28.5±94.9	215±426
233	819±201	144±363
402	547±425	215±425
782	253±450	1.12±0.45
1590	4.64±2.03	1.28±0.217
4018	4.78±1.11	1.20±0.160

Table D4. *Constant Coefficient Relating the Signal Intensity and Density A*

Fluence (μJ/cm^2)	Crystal A	Film A
95	1.04±0.138	1.17±0.0568
148	0.853±0.0660	0.905±0.162
233	1.01±0.130	0.901±0.140
402	1.00±0.137	0.933±0.151
782	0.992±0.154	0.836±0.0146
1590	0.892±0.106	0.828±0.0153
4018	0.854±0.0470	0.824±0.0236